VOID GROWTH AND COALESCENCE STUDIED BY X-RAY COMPUTED TOMOGRAPHY

VOID GROWTH AND COALESCENCE STUDIED BY X-RAY COMPUTED TOMOGRAPHY

By

AKIHIDE HOSOKAWA, M.Eng., B.Eng.

A Thesis

Submitted to the School of Graduate Studies

in Partial Fulfilment of the Requirements

for the Degree

Doctor of Philosophy

McMaster University

Doctor of Philosophy (2010) McMaster University

(Materials Science and Engineering) Hamilton, Ontario

TITLE: Void Growth and Coalescence Studied by X-ray Computed Tomography

Author: Akihide Hosokawa

B.Eng.(Toyohashi University of Technology) 2004

M.Eng.(Toyohashi University of Technology) 2006

SUPERVISOR: Professor D. S. Wilkinson

NUMBER OF PAGES: xxi, 258

Abstract

Void growth and coalescence were investigated by means of *in situ* X-ray computed tomography coupled with tensile deformation. A variety of model materials were fabricated whereby artificial three dimensional void arrays were embedded in metal matrices. An ultra short-pulsed laser machining system and diffusion bonding technique were used to produce those model materials. Model materials containing a pair of round notches were also produced to investigate the effect of stress triaxiality. *In situ* X-ray tomography experiments successfully visualized the void growth and coalescence events in the model materials produced. The void growth behavior was quantitatively analyzed by measuring the principal diameters of the internal voids.

For several model materials, a new technique called continuous tomography was applied. The experiments were performed at the beamline ID15 of the European Synchrotron Radiation Facility (ESRF), France. This technique allows us to keep taking a series of tomographic scans during non-stop tensile deformation. This new technique enabled us to experimentally capture the plastic strains at the onset of void coalescence for the model materials. The onset of void coalescence here was defined as the point at which the lateral shrinkage of voids terminates. The captured plastic strains at the onset of void coalescence were compared for the first time ever with the existing void coalescence models which are essentially designed to predict the onset of coalescence instead of the simple linkage of voids.

Similar experiments were also conducted using a set of notched model materials at the same beamline ID15. A significant influence by the higher

stress triaxiality and the strain concentration induced by the notches on the void growth in these model materials was observed. This aspect was confirmed by the FE simulation performed. The captured linkage strains were used to assess the validity of the void coalescence models at a higher stress triaxiality.

Model materials made of Glidcop and brass were also tested using the same methodology. This set of experiments were performed at the beamline BL20XU of SPring-8, Japan. The results obtained from these samples suggested that the higher work hardening exponent in brass stabilized the plastic flow of the ligament while the lower work hardening exponent in the Glidcop materials significantly accelerated the linkage events. Nevertheless, the critical values of work hardening rate normalized by the current flow stresses were quite similar (lower than the critical value of localized necking) in individual materials (copper, Glidcop, brass) even if the plastic strains at linkage and coalescence events of the materials are different.

Acknowledgements

This thesis has been contributed by many people and I am very grateful for them. First, I would like to express my sincere gratitude to my supervisor Dr. David Wilkinson for his support, patience and guidance over the entire length of this project. I also thank my supervisory committee members, Dr. David Embury and Dr. John Preston. Without their encouragements and advices, this thesis would not have been completed.

Thanks also goes to Dr. Xiaohua Hu and Dr. Jidong Kang for their daily guidance.

Dr. Harold Haugen, Dr. Travis Crawford and Eugene Hsu are acknowledged for their support for the laser machining of my samples.

The support for the experiments at synchrotron radiation facilities must be also acknowledged. Dr. Eric Maire, Dr. Jerome Adrien, Dr. Damien Fabregue from INSA-Lyon and Dr. Marco Di Michiel from ESRF kindly helped my experiments performed at ESRF. When I arrived in France for this set of experiments, it was just the releasing week of Beaujolais Nouveau 2007. It is quite pleasant and unforgettable experience to drink a glass of Beaujolais at the cafeteria of INSA-Lyon on the third Thursday of November.

The experiments at SPring-8 were also supported by many people. Dr. Hiroyuki Toda, Dr. Masakazu Kobayashi, Tomoharu Niihara and Shinya Ito from Toyohashi University of Technology are acknowledged. I also appreciate the contribution by the beam scientists, Dr. Akihisa Takeuchi, Dr. Kentaro Uesugi and Dr. Yoshio Suzuki from SPring-8.

In addition, thanks goes to Doug Culley, John Rodda, Rob Lemmon and

Jim Garret for their support in my sample preparation processes and to Ed McCaffery for solving the computer related issues. Dr. Steve Koprich and Fred Pearson are acknowledged for supporting my experiments using electron microscopy.

Thanks also goes to Dr. Ke Han from The Florida State University for supplying the Glidcop sheets.

The colleagues in A206 are also acknowledged. Dr. Florent Lefevre-Schlick and Dr. Arnaud Weck helped me to start the graduate studies at McMaster University. Juan Kong gave me timely advices in terms of my FE calculations. Somaradi Khiev, Kendal Dunnett, Paul Okrutny helped me to get accustomed into the Canadian culture. Mike Nemcko helped me to check the spelling and grammatical errors of my thesis and gave me valuable comments.

Finally I would like to thank my family for their support and understanding.

Contents

List of Figures

List of Tables

Chapter 1

Introduction

Ductile fracture, which occurs after a significant amount of plastic deformation (Thomason, 1990), is a classical problem in materials science. It has technological significance in terms of both the integrity of engineering structures as well as the viability of manufacturing processes such as metal forming.

Fracture mechanisms at room temperature can be roughly classified into the three categories as shown in Figure 1.1. The first is brittle fracture either by cleavage or inter-granular fracture.

An antithetical mechanism is rupture or macroscopic shear . Rupture is an extremely ductile fracture mechanism that typically occurs by 100% reduction of the cross sectional area in inclusion-free materials. Shearing can happen as soon as the work hardening rate is saturated. This can happen either in a ductile or brittle manner, depending on when the material exhausts its work hardening capacity.

The current thesis project does not deal with either of these processes. Instead, we focus on the third mechanism (the middle one in the figure) which takes place through the three progressive processes of nucleation, growth and

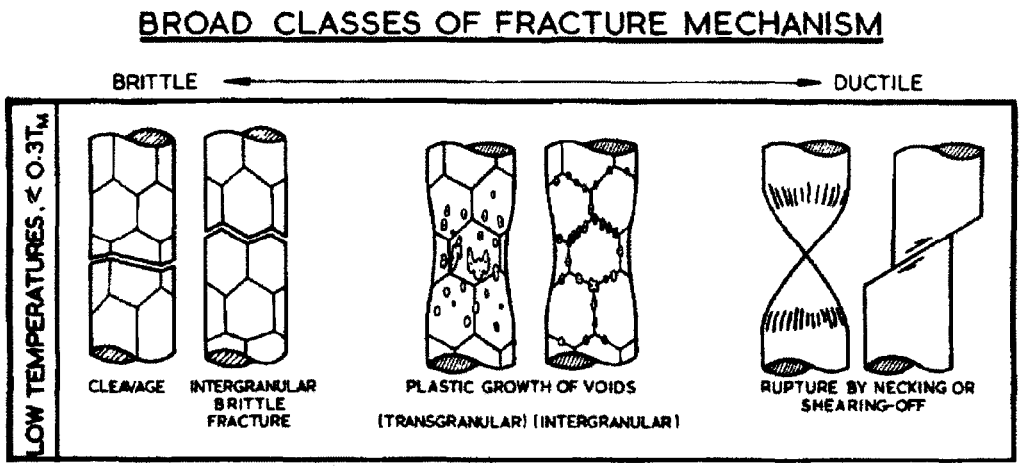

Figure 1.1: Classification of ductile fracture. (Ashby et al., 1979)

eventual coalescence of voids after a significant amount of plastic deformation. This is the most important ductile fracture mechanism since most of engineering materials contain various classes of inclusions or second phase particles that can serve as void nucleation sites. Particularly, void coalescence is the least understood part among the three processes, mainly due to its stochastic nature. One of the effective approaches to tackle this issue is to fabricate a class of model materials so that an artificial array of holes are located in the material. In situ observation of the hole array during tensile deformation enables researchers to investigate void coalescence in further detail.

In visualizing the voids embedded in a metal matrix, a significant contribution to this field is the development of X-ray computed tomography coupled with large scale synchrotron radiation facilities such as the European Synchrotron Radiation Facility (ESRF) and SPring-8. X-ray radiography and tomography were initially developed to inspect the internal structures of biological tissue (e.g. human body) in a non-destructive manner (Kak, 1988),

and the application of these techniques to metallic materials research was difficult due to the high absorption coefficients of metals. However, these so-called the third generation synchrotron facilities have led to overcoming this limitation, by virtue of their strong energy and high brilliance. Combination of X-ray tomography with such a strong and brilliant X-ray source with the model material approach is one of the most sophisticated means to obtain a set of experimental data that can be compared with the existing models, as demonstrated by Weck et al. (2008b).

Meanwhile, modeling work on void coalescence has regained considerable momentum in last two decades, driven in large part by the significant development of finite element modeling (FEM) methods and the increased speed of computation. Recent models based on FEM seem to provide extensive predictions even for quite complex situations. However, there is tremendous need for precise experimental data in order to validate these models in detail.

It is also worth emphasizing that the current thesis project aims to help understand fracture on the scale of the voids. This is in contrast to so-called *damage mechanics*. Damage is typically defined as the degradation of the macroscopic flow stress due to the internal cracking and void nucleation, growth and coalescence. On the scale of the voids however, the local effective stress in the ligament would never degrade. Instead of dealing with the deterioration in the effective stress of a porous solid, *this thesis primarily places an emphasis on the discussions on the instability of the plastic deformation of the ligament around voids.*

With the view to these points, the aims of the current thesis are summarized as below.

- To fabricate a series of model materials by modifying and improving the approach which was previously developed by Weck and Wilkinson.
- To visualize the internal void growth and coalescence/linkage of the voids in those model materials.
- To utilize the obtained experimental results in order to provide quantitative assessments for the existing void coalescence models in the literature.

This thesis consists of 8 chapters including this introduction. Chapter 2 presents a literature review on ductile fracture, and also provides a brief introduction to X-ray computed tomography with synchrotron radiation. Chapter 3 describes the work previously done at McMaster University on which the current thesis project is based. Chapter 4 explains the approach employed in the current project in order to investigate ductile fracture processes in a controlled manner. Chapter 5, 6 and 7 show the experimental results obtained, which are subject to comparison with the existing models in the literature. The conclusions drawn from the current project are summarized in Chapter 8.

Chapter 2

Literature review

Research on ductile fracture is longstanding and extensive. In this chapter, previous experimental investigations on ductile fracture will be presented as well as modeling work. In particular, the modeling of ductile fracture has been quite active because of the enormous development of computational materials science methods such as finite element modeling (FEM). The development of experimental techniques in the study of fracture is also remarkable, as represented by X-ray computed tomography using third generation synchrotron radiation facilities. Not only does technology currently allow for 3D image reconstruction but also the evolution of the structure over time can be investigated. The principle of tomographic reconstruction and some examples of experimental works that utilize X-ray tomography are presented as well.

2.1 Mechanisms and Mechanics of Ductile Fracture

2.1.1 Void nucleation

Pure metals, pulled in tension, can neck down to a point fracture or rupture with virtually 100% reduction in area (Callister, 2003) unless shear instability intervenes. This is because pure metals do not have any nucleation sites for microvoids, which are usually inclusions and second-phase particles within the matrix during plastic deformation (Thomason, 1990). Engineering materials generally have particles or inclusions within their matrix, and thus they play a role as nucleation sites for voids.

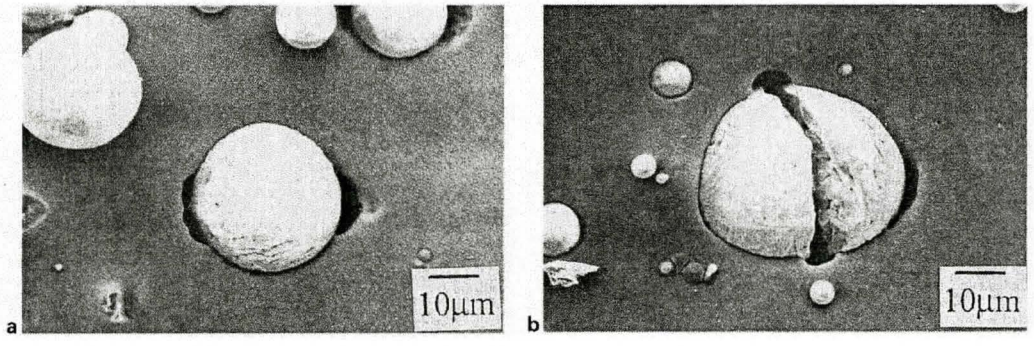

Figure 2.1: Two mechanisms of void nucleation around an inclusion (left) decohesion at matrix/inclusion interface (right) particle failure. Tensile load is horizontally applied. (Kanetake et al., 1995)

It is known that there are two types of mechanisms of void nucleation; decohesion of the particle/matrix interface and failure of particles themselves, both shown in Figure 2.1. This has been clarified with numerous experimental results. The relationships between various parameters and void nucleation are summarized in Table 2.1. The void nucleation strain tends to decrease with the increase of particle size, particle volume fraction and matrix strength.

Table 2.1: Influence of various parameters on void nucleation strain. Effects of void nucleation strain are given for an increase in parameters. ↑ and ↓ represent the increase and the decrease in void nucleation strain; → represents the nucleation strain is almost independent of the parameter.

Parameters	by particle cracking	by decohesion	Authors
Particle size	↓	↓	Llorca et al. (1993)
Aspect ratio			Lee et al. (1991)
			Brechet et al. (1991)
Inclusion volume fraction	↓	↓	Babout et al. (2001)
			Maire et al. (1995)
Matrix strength	↓	→	Babout et al. (2001)
Temperature	↑	↑	Zhao et al. (1994)
Hydrostatic pressure	↑	↑→	French and Weinrich (1974)
			Chen (1961)

Higher temperature results in the lower strength of the matrix, and as a result void nucleation strain improves. It is also noted that hydrostatic pressure suppresses void nucleation.

When attempting to model the nucleation of voids, one has to take into account particle size and shape. The size of particles can range from a few nm to 1 μm and more in practical materials (Thomason, 1990). Depending on the size of these particles, the required models for void nucleation are different. Dislocation models are required for the particles smaller than 1 μm since those small particles interact with individual dislocations. Continuum models are used for those particles larger than 1 μm since the stress elevation due to dislocations becomes negligible. Particles can also exhibit a wide variety from spherical form to lamellar or irregular angular forms, which must be taken into account in the models.

Let us examine the mechanisms of nucleation by particle/matrix decohesion. Decohesion of the particle/matrix interface occurs when the elastic strain energy released by the particle is at least equal to the newly created surface energy. However, this condition seems to be satisfied at the very initial stage of plastic deformation for particles in excess of 0.025 μm (Tanaka et al., 1970). Hence, it can be said that void nucleation by decohesion can occur when the normal stress at the particle/matrix interface reaches a critical value.

For the spheroidal particles smaller than 1 μm, strain-hardening around particles must be taken in to account using dislocation models. Brown and Stobbs (1976) showed that dislocation density around a particle is given by

$$\rho = \frac{1.7\varepsilon}{rb} \tag{2.1}$$

where ε is the maximum macroscopic strain, r the radius of a particle, b the Burger's vector. They also showed based on this equation that local flow stress is

$$\sigma_1 = \alpha\mu b\sqrt{\rho} = 1.3\alpha\mu\sqrt{\frac{\varepsilon b}{r}} \tag{2.2}$$

where μ is the shear modulus, α is a constant lying between 1/3 to 1/7. It is reported that the stress around particles increases by a factor of 4.2 approximately (Brown and Stobbs, 1976; Goods and Brown, 1979). Thus the elevated local stress on the particle interface is given by

$$\sigma_E = 5.46\alpha\mu\sqrt{\frac{\varepsilon b}{r}} \tag{2.3}$$

The maximum stress on the particle interface σ_T is therefore the sum of the elevated local stress σ_E and the macroscopic mean-normal stress σ_m and

the maximum deviatoric stress S_1;

$$\sigma_T = \sigma_E + \sigma_m + S_1 \tag{2.4}$$

The critical condition for void nucleation by decohesion is given by

$$\sigma_E + \sigma_m + S_1 = \sigma_C \tag{2.5}$$

where σ_C is the critical cohesive strength of the interface. After some approximation for the macroscopic flow stress and substitution of equation (2.3) into equation (2.5) this will give us the critical strain necessary to nucleate voids by particle decohesion in the form of,

$$\varepsilon_1^{nucleation} = Kr(\sigma_C - \sigma_m) \tag{2.6}$$

where K is a material constant that is determined by the shear modulus and volume fraction of the particles. On the other hand, strain-hardening effects around the particles become negligible for particles larger than 1 μm. This can be deduced from equation (2.3), as σ_E is proportional to the inverse of the square root of the particle size r. By considering both the non-hardening and linear-hardening elastic plastic flow around a rigid circular-cylindrical inclusion, Argon and his coworkers (Argon et al., 1975; Argon and Im, 1975) showed that the maximum radial stress at the inclusion interface is approximately 1.75 times higher than the yield shear stress of the plastic matrix, k. According to the von Mises yield criterion,

$$(\sigma_1 - \sigma_2)^2 + (\sigma_2 - \sigma_3)^2 + (\sigma_3 - \sigma_1)^2 = 2Y^2 = 6k^2 \tag{2.7}$$

Thus the uniaxial yield stress $Y = \sqrt{3}k$. The maximum radial tensile stress on the interface, σ_r^{max} , can be represented by

$$\sigma_r^{max} \cong \overline{\sigma} = \sqrt{\frac{1}{2}(\sigma_1 - \sigma_2)^2 + (\sigma_2 - \sigma_3)^2 + (\sigma_3 - \sigma_1)^2} \tag{2.8}$$

The mean normal stress σ_m does not bring any contribution to the deviatoric component and thus it is a quite good approximation for the maximum stress σ_r^{max} to superpose σ_m and $\overline{\sigma}$, i.e.,

$$\sigma_r^{max} = \sigma_m + \overline{\sigma} \tag{2.9}$$

The critical condition for void nucleation by decohesion at particle/matrix interface is represented by

$$\sigma_m + \overline{\sigma} = \sigma_C \tag{2.10}$$

The biggest difference in comparison with the criterion based on the dislocation model (i.e. equation (2.6)) is that equation (2.10) includes no parameter which depends on particle radius. This implies that void nucleation by decohesion can occur even if $\overline{\sigma}$ is small as long as σ_m is large enough.

The other important mechanism of void nucleation is particle failure. Particles in the matrix elongated in the direction of the maximum principal plastic-strain can lead to axial strain inside the particle due to the fiber-loading effect and premature cracking. If the bonding strength of matrix/inclusion interfaces is larger than the strength of particles, particle failure occurs but this is seldom the case. In most cases cavitation occurs by premature cracking and propagates to the failure. As was mentioned, damaged particles are frequently seen in practical materials such as steels prior to deformation. This is because

materials must undergo a series of hot or cold working production processes so that softer particles elongate in the direction of hot/cold working and the harder particles will get damaged. In the literature (Le Roy et al., 1981), these particles are classified into two types, namely the first population N_1, where particles are damage-free, and the second population N_2, where particles are damaged during the primary hot/cold working. For the relatively equiaxed particles among the second population of voids, the critical interface stress σ_f can be estimated approximately by the Griffith equation,

$$\sigma_f = A\sqrt{\frac{2E\gamma}{\pi c}} \tag{2.11}$$

where A is a geometrical constant, E the Young's modulus, γ the fracture surface energy and c the internal crack length.

It is helpful to illustrate the quantitative models in principal stress space. From equations (2.7) and (2.10), the critical condition for particle/matrix decohesion can be represented as

$$(\sigma_1 - \sigma_2)^2 + (\sigma_2 - \sigma_3)^2 + (\sigma_3 - \sigma_1)^2 = 2(\sigma_C - \sigma_m)^2 \tag{2.12}$$

It is noticeable from this equation that if we keep increasing σ_m along the σ_m axis in the principal stress space, the critical stress for partcle/matrix decohesion σ_C becomes lower with the von Mises stress $\overline{\sigma}$ balanced. As $\overline{\sigma}$ is proportional to the radial distance from σ_m axis in principal stress space, equation (2.12) is represented by a conical surface as shown in Figure 2.2 with the apex located at the point $\sigma_m = \sigma_C$. When the stress state (*i.e.* the position vector in principal stress space) reaches this cylindrical yield surface,

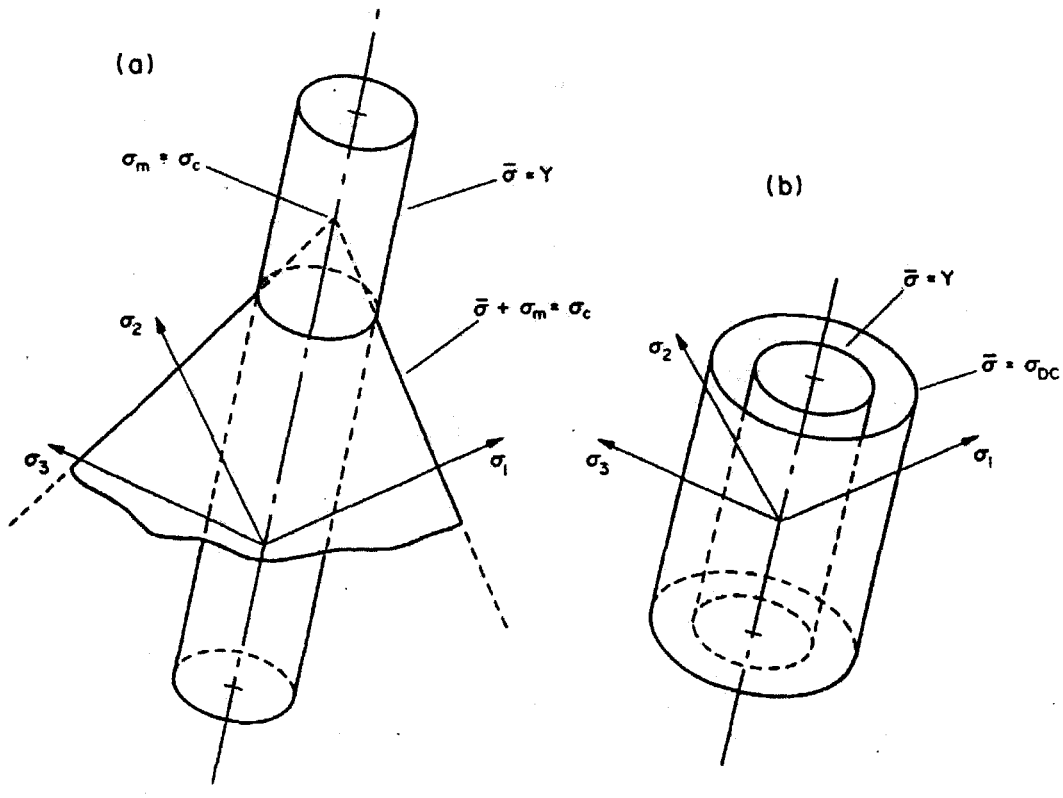

Figure 2.2: The initial yield surface in principal stress space (a) the conical surface for void nucleation by decohesion (equation 2.12) (a) and (b) Proposed cylindrical surface representing the critical shear stress condition for particle damage at low values of mean-normal stress. (equation 2.13)(Thomason, 1990)

materials start flowing.

The region outside of the yield surface does not have any physical meaning, since stress cannot be higher than the flow stress. If now we substitute $\sigma_m = \sigma_C - Y$ into equation (2.12) then $\overline{\sigma}$ is equal to $\sqrt{2Y}$, where the von Mises yield surface is located. This means that the conical surface for decohesion intersects the initial yield surface at $\sigma_m < \sigma_C - Y$. This implies, as mentioned previously, that void nucleation can occur even if the applied effective stress is very small. When $\sigma_m < \sigma_C - Y$, it is understood from the figure that the expansion of the loading surface is needed by work-hardening to increase the maximum stress at the matrix/particle interface so that stress state can reach the conical surface. It is also clear from the figure that at low values of mean normal stress σ_m , it is much more difficult to initiate void nucleation by decohesion since the conical surface is too far from the initial yield surface. Work-hardening rate must be very high to achieve decohesion. In this case an alternative criterion on the deviatoric stress for particle damage can be satisfied, having the form of

$$\overline{\sigma} = \sigma_{DC} \tag{2.13}$$

where σ_{DC} is a critical deviatoric stress for particle damage. This critical deviatoric stress must be estimated for each particle type by experiments.

An example of quantitative illustration of the calculated loci for 1045 steel in uniaxial tension, where Y=302 MPa and σ_c=1200 MPa. The calculated loci based on critical-stress dislocation model (equation (2.6)) and critical-strain continuum model (equations (2.10) and (2.12)) are plotted with the experimental results, as shown in Figure 2.3. These results show very good agreement with both the critical-strain model and critical-stress model. This is

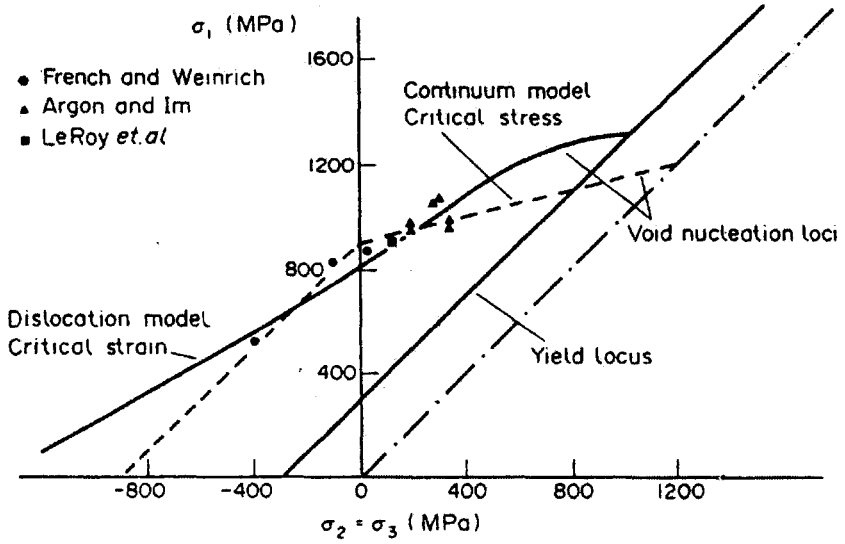

Figure 2.3: Illustration of the calculated loci for void nucleation. The loci for dislocation model (critical-strain based) and continuum model (critical-stress based) results are plotted for comparison as well as the various experimental results (Le Roy et al., 1981)

only possible when the particle size is around 0.5 μm, where the upper bound of dislocation model and the lower bound of continuum model are almost coinciding.

Analytical modeling and its comparison with the experiments have been discussed so far but it is also worth mentioning about utilization of numerical simulation for void nucleation. Finite element modeling (FEM) for void nucleation by decohesion was pioneered by Needleman and his colleagues (Needleman and Tvergaard, 1987; Nutt and Needleman, 1987).

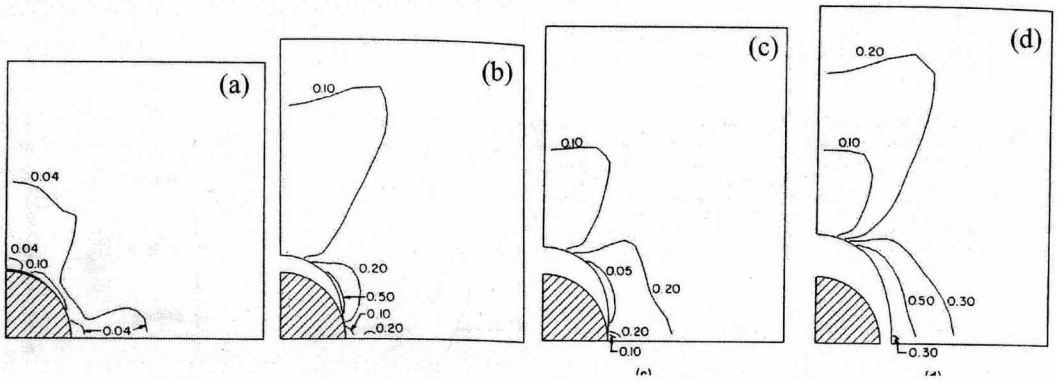

Figure 2.4: Contours of constant plastic strain,(a) Applied strain $\varepsilon = 0.04$ (b) $\varepsilon = 0.121$ (c) $\varepsilon = 0.169$ (d) $\varepsilon = 0.24.$, calculated by FEM. (Needleman and Tvergaard, 1987)

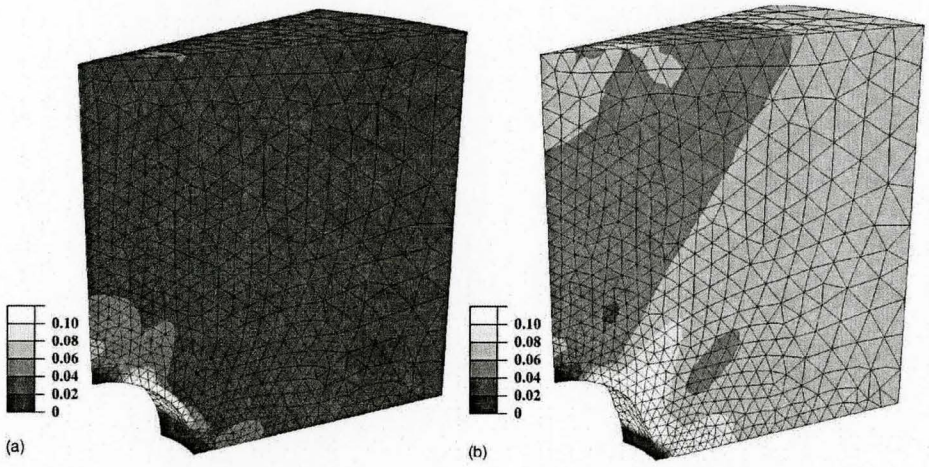

Figure 2.5: Contour plots of the accumulated plastic strain in the matrix around the particle (a) before the void nucleation (b) after the nucleation (Segurado and LLorca, 2004)

An example of FEM calculations for a 2D axisymmetric model is shown in Figure 2.4. It is well depicted that void nucleation has already occurred near the axisymmetric axis with $\varepsilon = 0.04$. It is also noted that maximum strain concentration occurs around 45° from the tensile axis while the bonding remains intact. Segurado and LLorca (2004) further developed Needleman's work to the three dimensional axisymmetric problem considering a cylindrical cell, in which a particle is located at its center. In this work only 1/24 of the cylinder cell is considered from the symmetry, as shown in Figure 2.5. The plastic strain is confined to the thinner layer around the particle before decohesion occurs. Once void nucleation is complete, which is defined as perfect decohesion in his work, the plastic strain suddenly spreads through the cylinder cell.

2.1.2 Void growth and ductile fracture

Experimental aspects

Once a void has been nucleated, either by decohesion or failure of a second-phase particle, voids start growing. Observation of the void growth has been mainly carried out by metallographic techniques (Puttick, 1959; Cox and Low, 1974). The results visualize how the voids grow and allow us to study qualitatively the effect of plastic strain and stress state during void growth. However, this technique does not provide information on three dimensional distributions of voids. Density measurement has also been used to study void growth since void growth involves a change in volume as well, yet this technique does not provide any information of the dimension, distribution or shape of voids either. These difficulties are essentially because voids inside the material are invisible during the deformation. One of the possible ways to observe them is X-ray computed tomography, which was pioneered by several researchers at INSA de Lyon (Buffière et al., 1999; Babout et al., 2001). Currently, this technique seems to be one of the most sophisticated and powerful methods to visualize the internal void growth behavior.

Void growth modeling in terms of principal void diameter

In the initial stage of void growth (*i.e.* right after void nucleation), it is adequate to assume there is no interaction in terms of stress and strain between voids that are nucleated apart from each other. It is therefore possible to consider a model for the early stage of void growth in terms of a single void in an infinite plastic solid.

This treatment was commenced by McClintock who proposed one of the

simplest models for void growth and ductile fracture (McClintock, 1968a,b). He considered a cylindrical element containing a cylindrical void. The diameter of the element, R, and the mean spacing between voids, l, are similar initially. He developed a model for void growth in various types of materials (Tresca, Mises and viscous materials) for circular holes, and extended the models so that the elliptical holes are treatable. He found from these analyses that the increment of void growth is exponentially proportional to applied strain. Another feature of this model is that strain-hardening exponent n is taken into account. It is assumed in this model that ductile fracture occurs when the void length increases to half of the mean spacing l.

The derived form of fracture strain for the case of elliptical holes, ε_f , is given by

$$\varepsilon_f = \frac{(1-n)\ln(l_b^0/2b_0)}{\sinh[(1-n)(\sigma_a+\sigma_b)/(2\overline{\sigma}/\sqrt{3})]} \tag{2.14}$$

where σ_a and σ_b are the principal stress components along major (a direction) and minor (b direction) diameter of elliptical holes, l_b^0 is the initial intervoid spacing along b axis, b_0 the initial size of a void along b axis. The drawback of this model is that it tends to overestimate the fracture strains observed in experiments, mainly because interactions between holes were neglected. The treatment of this interaction will be discussed in the next section.

Rice and Tracey (1969) developed the most successful and versatile model for void growth. As the initial state, they considered a spherical void of radius R, in a remote uniform strain-rate field ε_{ij} and remote stress field $\sigma_{ij} = S_{ij} + \sigma_m\delta_{ij}$. This strain-rate field is characterized by the Lode variable for strain-rate (Hill, 1950), which is given by

$$\nu = -\frac{3\dot{\varepsilon}_2}{\dot{\varepsilon}_1 - \dot{\varepsilon}_3} \tag{2.15}$$

If $\nu = 1$ the flow fields are in uniaxial tension, and if $\nu = 0$ pure shear, and if $\nu = -1$ biaxial tension. They applied a variational principle for the formulation on a rigid and incompressible plastic material containing a void (or voids) for the approximate flow field. The constants of the approximated velocity field were obtained in such a way that the strain energy rate is minimized. They also succeeded in modeling the effect of work hardening concerning isotropic linear-hardening material. The proposed form for void growth rate is

$$\dot{R}_i = \left((1+E)\dot{\varepsilon}_k + \left(\frac{2}{3}\,\dot{\varepsilon}_j\,\dot{\varepsilon}_j\right) D \right) \tag{2.16}$$

where $(i, j) = 1, 2, 3$, $(1 + E) = 5/3$ for linear hardening materials, and low values of the mean normal stress with non-hardening materials,$(1 + E) = 2$ for high values of the mean stress with non-hardening materials.

$D = \frac{3}{4}\frac{\sigma_m}{Y}$ for linear hardening materials,

and

$D = 0.558 \sinh \frac{\sigma_m}{Y} + 0.008\nu \cosh\left(\frac{3}{2}\frac{\sigma_m}{Y}\right)$ for non-hardening materials. Note that E here does not stand for Young's modulus but a different constant to represent how sensitive the void growth is to the strain-rate. D is also another constant which represents how sensitive the dilation of voids is. Thus, it can be said that the first term of equation (2.16) is responsible for the shape change of voids and the second term is responsible for the dilation of voids. The total strain can be given by integrating equation (2.16),

$$R_1 = \left(A + \frac{(3+\nu)}{2\sqrt{\nu^2+3}} B \right) R_0 \tag{2.17a}$$

$$R_2 = \left(A - \frac{\nu}{\sqrt{\nu^2+3}} B \right) R_0 \tag{2.17b}$$

$$R_3 = \left(A + \frac{(\nu-3)}{2\sqrt{\nu^2+3}} B \right) R_0 \tag{2.17c}$$

where

$$A = \exp\left(\frac{2\sqrt{\nu^2+2}}{3+\nu} D\varepsilon_1 \right)$$

$$B = \left(\frac{1+E}{D} \right)(A-1)$$

and ε_1 is the far field plastic strain. This set of equations essentially means that the total amount of void growth by plastic strain is exponentially proportional to the plastic strain and the stress triaxiality. The equation (2.17) was evaluated for various mean normal stress values and the Lode variables. An example of void growth modeling using this model is as shown in Figure 2.6. While minor radii decrease with plastic strain at a lower stress triaxiality σ_m/Y, they turned into increasing tendency at a higher value of σ_m/Y. This is consistent with the fact that volumetric change is dominated by the mean normal stress component. This figure also well depicts the fact that work-hardening effect tends to slow down the void growth behavior, since the strain concentration around voids become smaller. Le Roy et al. (1981) used this model to fit their experimental results of various steels and showed a good agreement.

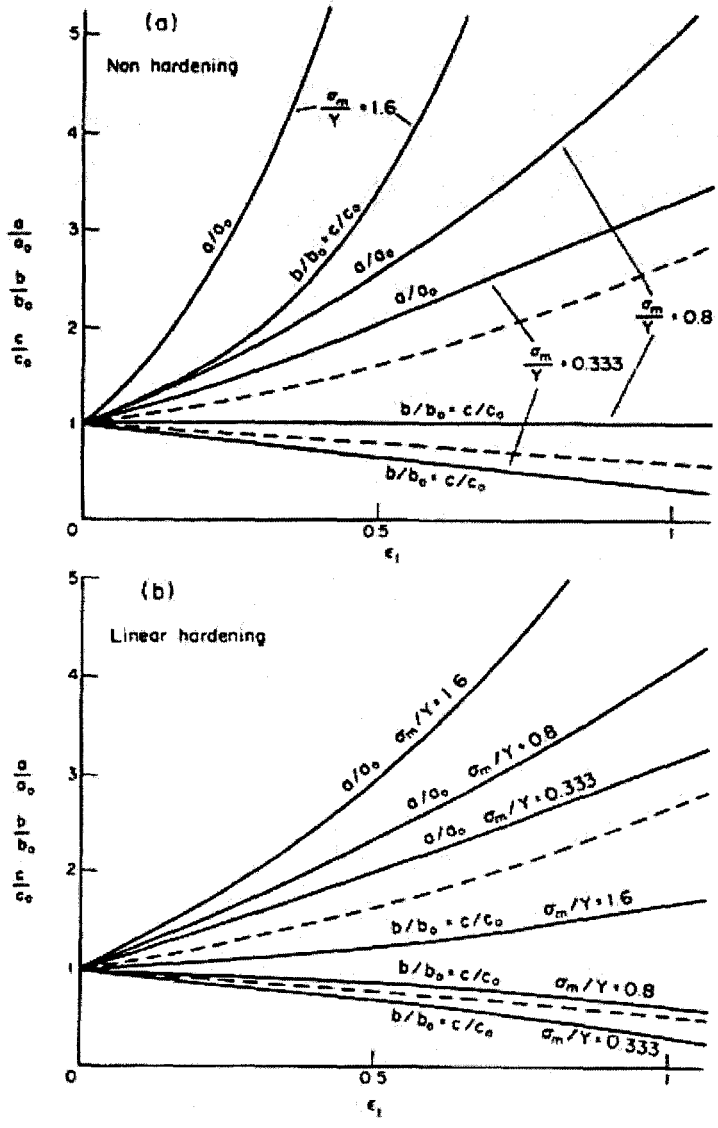

Figure 2.6: The effect of increasing plastic strain on the principal radii (a, b, c) of an initially spherical void ($a_0 = b_0 = c_0$) in uniaxial ($=+1$) tension at various stress triaxiality examined by the integrated form of the Rice and Tracey model. (a) Non hardening and (b) linear hardening materials. The dotted lines show the change in void dimension that would occur without any amplification (Thomason, 1990)

Effective stress of a porous solid

When a material contains voids internally, it is considered that the mechanical response of the voided material is less stiff than a void-free material. Berg (1970) and Gurson (1977) proposed an analytical form of the effective stress of a porous solid on the basis of the plastic potential theory and the normality rule of incompressible solids, assuming the existence of imaginary microvoids from the beginning. This model is based on the following assumption;

- Ductile fracture process is regarded as a result of weak dilational-yield surface. (This term is explained later)
- Imaginary spherical microvoids are distributed homogeneously from the beginning.
- The primary mechanism of fracture is not internal necking but localized shear band formation.

In this case the yield criterion of porous media is necessarily determined not only by the second deviatoric stress invariants J_2 (i.e. the Mises stress) but also by the other stress invariants I_1, I_2, I_3. The Mises yield surface in principal stress space might, as a result, be truncated. Such a truncated yield surface is called the weak-dilational yield surface (Thomason, 1990). This will be discussed in the following section in detail. A strong-dilational yield surface is formed when stress triaxiality suddenly increases. For example, internal necking causes high stress triaxiality at the center of ligament accompanied by the formation of a strong-dilational surface that intersects with initial yield surface. This aspect will also be mentioned later in detail.

Gurson (1977) developed the mathematical expression for the truncation of the yield surface of a porous media given by the form

$$\phi = \frac{3}{2}\frac{\overline{\sigma}^2_{porous}}{Y_n^2} + 2V_f \cosh\left(\frac{3}{2}\frac{\sigma_m}{Y_n}\right) - \left(1 + V_f^2\right) = 0 \tag{2.18}$$

or

$$\overline{\sigma}_{porous} = \sqrt{\frac{2}{3}\left(\left(1 + (V_f)^2\right) - 2V_f \cosh\left(\frac{3}{2}\frac{\sigma_m}{Y_n}\right)\right) Y_n^2} \tag{2.19}$$

where $\overline{\sigma}_{porous}$ is the effective stress of the porous media, Y_n the yield stress of the intervoid matrix, V_f the volume fraction of voids. It is noted that if we substitute $V_f = 0$ into the expression above, we obtain the simple von Mises criterion. The estimated form of the weak-dilational-plastic yield surfaces from the Gurson model is shown in Figure 2.7. From this figure, it is understood that the increase in void volume fraction V_f , i.e. the dilatation of the porous solid, results in the more truncated form of the yield surfaces. The comparison with experiment as well as the Thomason model showed that this model tends to overestimate the plastic strain for ductile fracture.

Ductile fracture criteria based on the Gurson model are given either by critical void volume fraction as proposed in the work of Tvergaard (1981), or by introducing shear instability (Rudnicki and Rice, 1975; Yamamoto, 1978). The biggest objection to the Gurson model is that this model has a poor physical basis, and thus usually ends up with seriously overestimating the fracture strains captured in experiments. This is due to the assumption that internal necking or any intervoid interaction is neglected from the primary fracture mechanism, which tends to overestimate the ductile fracture strain.

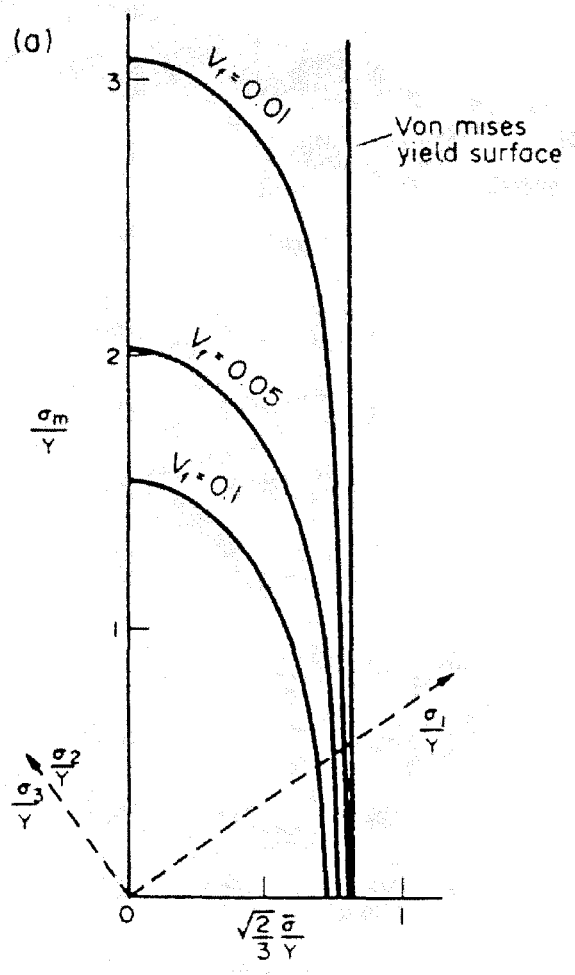

Figure 2.7: Truncated yield surfaces from the Gurson model for various volume fractions (Thomason, 1990).

Tvergaard (1981) attempted to modify the Gurson model by introducing new tuning parameters q_1, q_2. The parameters q_1 and q_2 amplify the influences of the void volume fraction and the stress triaxiality, respectively. The modified form is thus given by

$$\phi = \frac{3}{2}\frac{\overline{\sigma}^2_{porous}}{Y_n^2} + 2\left(q_1 V_f\right)\cosh\left(\frac{3}{2}\frac{q_2\sigma_m}{Y_n}\right) - \left(1 + \left(q_1 V_f\right)^2\right) = 0 \tag{2.20}$$

or

$$\overline{\sigma}_{porous} = \sqrt{\frac{2}{3}\left(\left(1 + \left(q_1 V_f\right)^2\right) - 2q_1 V_f \cosh\left(\frac{3q_2}{2}\frac{\sigma_m}{Y_n}\right)\right) Y_n^2} \tag{2.21}$$

Tvergaard proposed a failure model associated with the above yield function, assuming the critical volume fraction for coalescence is $V_{fc} = 0.15$ for the 2D case and $V_{fc} = 0.25$ for the 3D case. The former value was deduced from the works of Brown and Embury (1973) and Brown and Stobbs (1976), and the latter is from the classical FEM work by Andersson (1977). This model tells that the Gurson model is only applicable for volume fraction of voids below V_{fc} and is modified when $V_f = V_{fc}$ through the function V_f^* represented by

$$V_f^* = \begin{cases} V_f & (V_f < V_{fc}) \\ V_{fc} + K\left(V_f - V_{fc}\right) & (V_f \geq V_{fc}) \end{cases} \tag{2.22}$$

where K is a constant often called the acceleration factor. However, these treatments are only phenomenological. The discrepancy between the experimental results and the Gurson model should be explained by micromechanical parameters such as work hardening rate, the void/inclusion volume fraction, intervoid spacing, and the shape of inclusions.

Consequently, modeling ductile fracture necessarily becomes very complicated. However, while it would be extremely difficult to take into account all the factors in analytical modeling, the recent improvement in computational resources has boosted the activity of ductile fracture study using FEM. Predictions for the acceleration factor for equation (2.22) based on a detailed micromechanics were done in the FE cell calculations performed by Benzerga (2002).

Gologanu et al. (1993, 2001a) extended the Gurson model to take into account the varying values of aspect ratios during the void growth for axisymmetric ellipsoidal voids. The effective stress of a porous material containing non-spherical voids is given by,

$$(\Sigma_{eq} + \eta\Sigma_h)^2 = \sqrt{\frac{Y_n^2}{C}\left((g+1)^2 + q_w^2(g+V_f*)^2 - 2q_w(g+1)(g-V_f*)\cosh\left(\frac{\kappa\Sigma_h}{Y_n}\right)\right)} \tag{2.23}$$

where Σ_{eq}, Σ_h are the effective and hydrostatic stress at the level of porous media, Y_n is the initial yield strength of the ligament, g, C, q_w and κ are constants related to the shape of voids. This model excels in that the parameters used in it are all composed from physically meaningful quantities although the model clearly became more complicated.

2.1.3 Void coalescence and ductile fracture

The nucleated voids at particles will grow until they coalesce with each other. It is easily understood that coalescence events of microvoids are stochastic and can occur anywhere at anytime in materials. The other problem is that the void coalescence strain is so close to fracture strain that we cannot distinguish these two events clearly, even though we try to do so in a tensile test. Since these problems make it difficult to study void coalescence experimentally, there is little experimental evidence that captures void coalescence in a quantitative manner.

Figure 2.8 shows some examples of experimental evidence of void coalescence. From these results, Garrison and Moody (1987) proposed to classify void coalescence into two types; internal necking and void sheeting (See also Figure 1.1). The first type of void coalescence is widely seen when only one type of particles exists. In this case, once the voids nucleation has occurred at particles, the voids simply grow until internal necking takes place.

On the other hand, the second type of void coalescence, which is called void sheeting, tends to be seen when a material has two (or more) different classes of particles. In other words, the former tends to be observed in weaker and more ductile materials (fewer inclusions) while the latter is frequently seen in stronger and less ductile materials (more inclusions, precipitates and strengthening particles etc.). It is also said that void sheeting tends to happen when the metallic matrix has a low work hardening exponent. What happens in this case is that the first population of voids nucleates at a certain type of particles, followed by void growth. Further deformation then results in the nucleation of a secondary population of voids at the different type of particles where the

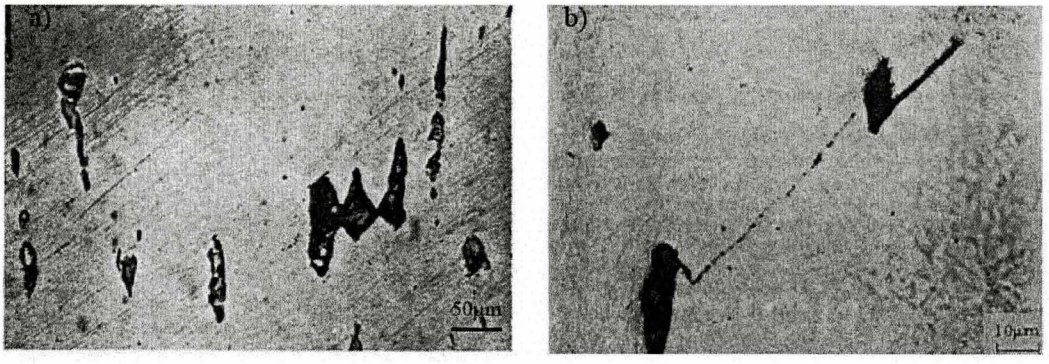

Figure 2.8: Experimental evidence of void coalescence by optical micrograph. a) internal necking in 99.9% copper (Puttick, 1959) b) void sheeting in tempered 4340 steel. (Cox and Low, 1974)

primary void nucleation did not occur. It is thought that the particles must be quite small, dispersed finely and bonded strongly to the matrix in order for void sheeting to occur. Although void sheeting is quite important since the void coalescence is accelerated by this mechanism, there is little research on it.

While experimental results are sparse, various models for void coalescence have been proposed. The major difference from the ductile fracture models based on void growth, which was mentioned in the last section, is that the following models aggressively consider the intervoid interaction. Among the models presented in the last section, for example, the McClintock model assumes fracture based on the concept of simple void impingement; yet the model does not take into account the inter-void interaction. This type of treatment is clearly not adequate and actually results in a serious overestimation of ductility.

Brown and Embury (1973) proposed a geometrical criterion, stipulating that void coalescence occurs when the void length is equal to intervoid spacing.

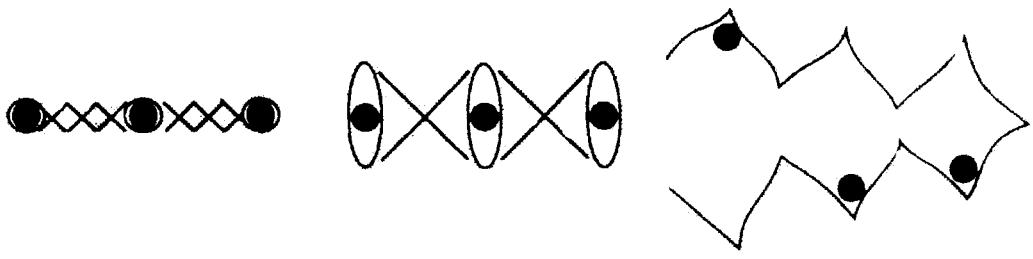

Figure 2.9: Schematic illustration of Brown and Embury model. (a) Right after void nucleation by particle decohesion. The constraint effect for localization is still high enough. (b) Intervoid spacing is equal to void length. The constraint is lost and slip lines can be drawn. (c) Spontaneous localization (i.e. internal necking) occurs (Brown and Embury, 1973). A very detailed derivation for Equation (2.24) can be found in Martin (1980).

The criterion may be summarized as the following; slip planes are developed between voids and, as a result, the constraint for deformation localization is lost as soon as the geometrical criterion above is satisfied.

This is equivalent to the neck geometry parameter $N = 1$ in Thomason's 2D model, which will be discussed later. The Brown and Embury model assumes that further plastic flow after the coalescence is confined in one plane, and thus the geometrical condition based on the removal of plastic constraint gives a strict lower bound of the fracture strain. Assuming the increase of strain during the coalescence is negligible, they derived the following form of fracture strain,

$$\varepsilon_f = \ln\left(\sqrt{\frac{\pi}{6f}} - \sqrt{\frac{2}{3}} + \varepsilon_n\right) \tag{2.24}$$

where ε_n is the strain to initiate void nucleation. Despite its simplicity it is

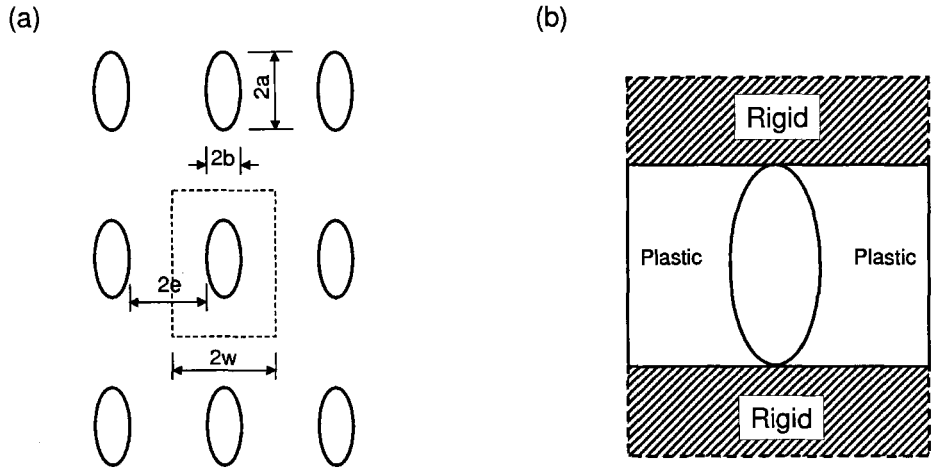

Figure 2.10: (a) Two dimensional plane strain model of hole array. Dotted rectangle represents a unit cell. (b)The virtual mode of internal necking. (Thomason, 1990)

known that this model shows good agreement with some experiments. This work was later improved by Le Roy, who took into account the effect of stress triaxiality on fracture (Le Roy et al., 1981). Another important fact is that the fracture strain ε_f becomes zero if we substitute $f = 15.9\%$. It follows that no void growth is needed in order for voids to coalesce when the initial void volume fraction is larger than 15.9%. This value has been employed as a critical volume fraction for void coalescence in the modeling work by Tvergaard and Needleman, as explained in the last section.

Prior to the Brown and Embury model, Thomason (1968) proposed a limit-load failure model, and extended it to a three-dimensional model in his later work. Among a series of his models, the first one was the ductile fracture model on the basis of internal necking, assuming a two-dimensional plane strain model as shown in Figure 2.10. The incipient limit-load condition for

internal necking can be represented in terms of the critical value of σ_n, which is the mean value of required stress to initiate internal necking in the rigid/plastic intervoid matrix whose local shear yield stress k_n. The values of σ_n for various neck geometry parameter N, which is defined as $N = a/e = a/(w - b)$, can be estimated by assuming the virtual mode[1] of internal necking as shown in Figure 2.10 (b). Although the situation in this figure does not represent the real mode of the deformation, if hypothetically the deformation were localized as illustrated, the plastic flow would have been much more *constrained* so that the required stress to maintain the plastic flow would be much higher. When voids are small and apart from each other (i.e. N is small), the magnitude of the constraint is very high and the deformation localization or internal necking is therefore prevented. This situation can be mathematically expressed as

$$\sigma_n A_n > \sigma_1 \tag{2.25}$$

where A_n is the areal fraction of the ligament in the two dimensional model and it is approximately given by

$$A_n \simeq N = (a/e) \tag{2.26}$$

In other words, this inequality is the stable condition for ductile flow. The further increase of plastic strain in the direction of σ_1 leads to the elongation of voids, resulting in a decrease in constraint effect. Thus σ_n keeps decreasing until it is equal to applied stress σ_1 . The resultant condition for microvoid coalescence by plastic limit load failure is given by

[1]This term will be explained later with Figure 2.13

$$\sigma_n A_n = \sigma_1 \tag{2.27}$$

Assuming that the far field yield shear stress k and local yield shear stress in the ligament k_n are the same, which is adequate for small volume fraction, the equation (2.38) can be normalized by $2k$. The rewritten form of the 2D plane strain Thomason model becomes

$$\frac{\sigma_n A_n}{2k} = \frac{\sigma_1}{2k} = \frac{1}{2} + \frac{\sigma_m}{2k} \tag{2.28}$$

It is important to note here that the average required stress for internal necking σ_n, or the plastic constraint factor $\sigma_n/2k_n$ for virtual mode of internal necking, is not a constant but a variable which is strongly dependent on the neck geometry parameter N. Also, note that these values can be estimated by a proper set of experiments as performed by Klassen et al. (1992a,b, 1993). In their work, they joined a pair of cylindrical steel blocks by silver or nickel braze so that the thin interlayer is highly constrained by steel blocks. By changing the thickness-to-diameter ratio, we can estimate the plastic constraint factor for "internal necking" experimentally. One may be confused with this concept because the intervoid ligaments in real materials are not constrained at all when voids are small and far apart. This weird terminology "virtual mode" has to used because the plastic constraint factor *for internal necking* cannot be estimated in the "real mode" but in the "virtual model" as illustrated in Figures 2.10(b) 2.13(b). When the inequality (2.25) is satisfied, the deformation is NOT localized yet, and thus the internal necking is not the real mode but virtual mode so that the internal necking is prevented. However, once the equation (2.27) is met the internal necking becomes the real mode and then

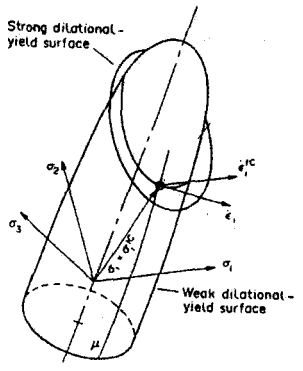

Figure 2.11: Strong dilational surface intersecting the weak dilational yield surface (which is originally Mises yield surface) (Thomason, 1990).

the internal necking can initiate. This is the physical meaning of the plastic constraint factor for virtual mode of internal necking meant by Thomason.

Of course, it is also possible to analyze the values of σ_n by a simple stress analysis following the concept illustrated in Figure 2.10(b). Thomason estimated these values of σ_n for void geometry parameter N by using the upper bound method, demonstrating that the plastic constraint factor decreases with the increase of N. The other feature of this model is that stress triaxiality is taken into account, which is quite important for a ductile fracture model. This is an advantage of this model compared to the Brown and Embury model which is essentially the same as the Thomason model when the neck geometry parameter $N = 1$ although the Brown and Embury model does not take into account the stress triaxiality.

To overcome this problem, Thomason (1981) introduced the concept of strong dilational yield surface which is expressed by the following equation

(see Figure 2.11).

$$\left(\sigma_1^{1c} - \sigma_1\right) \dot{\varepsilon}_1^{1c} > 0 \tag{2.29}$$

where σ_1 is the current maximum principal stress on the weak-dilational yield surface, and σ_1^{1c} is the required stress for internal necking estimated from the current geometry (which is used to draw the strong dilational-plastic yield surface), and $\dot{\varepsilon}_1^{1c}$ is the strain associated with $\sigma_1 = \sigma_1^{1c}$. It is easily understood from the equation (2.29) that the strong-dilational yield surface intersects with the weak-dilational surface perpendicularly to the σ_1 axis. This modified model shows that the limit load failure occurs whenever σ_1 coincides with σ_1^{1c}. This can be achieved either by the expansion of the initial yield surface (i.e. strain hardening) or the translation of the strong-dilational yield surface by the introduction of internal necking.

A series of these Thomason's models are developed using a two-dimensional plane strain assumption. We now turn to a three dimensional model . The two dimensional-model cannot be applied to the three-dimensional problem as it is because there is a disparity between 2-D and 3-D situations in terms of the initial geometry ratios c_0/w_0 and area fraction A_n, for a given volume fraction. This is explained with the assistance of the Figure 2.12. Assuming a unit cell as shown in this figure, a void volume fraction in the 2D problem is $V_f = \frac{\pi}{4}\left(c_0/w_0\right)^2$ and the void area fraction is $A_f = c_0/w_0$. The corresponding expression in the three-dimensional model is given by $V_f = \frac{\pi}{6}\left(c_0/w_0\right)^3$ and $A_f = \frac{\pi}{4}\left(c_0/w_0\right)^2$. It follows that, for a given geometry ratio c_0/w_0 , the values of V_f and A_f between 2D and 3D models are different as mentioned above. It is therefore necessary to develop appropriate expressions for the current net area-fraction of intervoid matrix A_n, which is expressed in the form $A_n = 1 - A_f$.

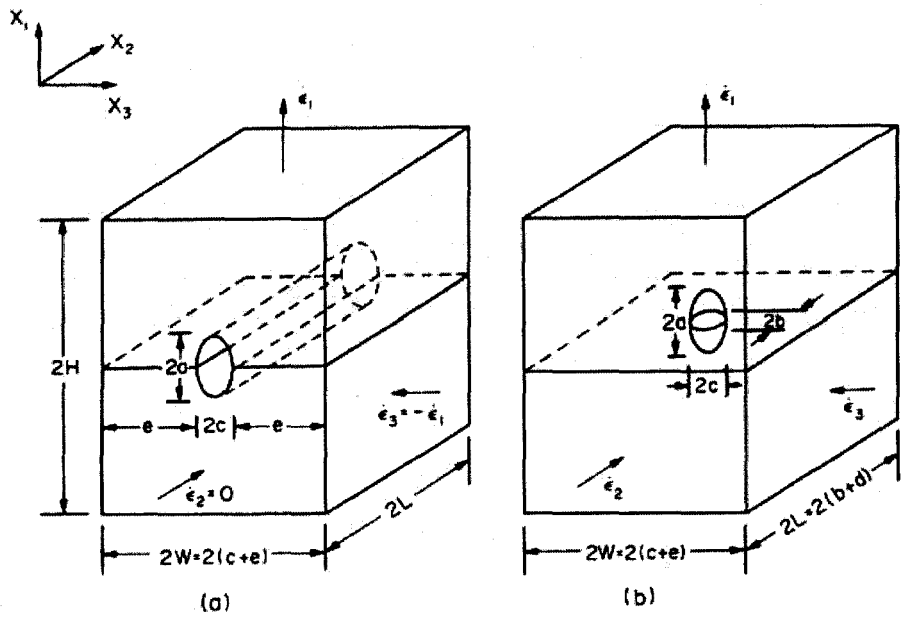

Figure 2.12: The unit cells of similar (X_1, X_3) planar geometry for (a) two-dimensional models with prismatic elliptical voids and (b) three-dimensional models with ellipsoidal voids. (Thomason, 1990)

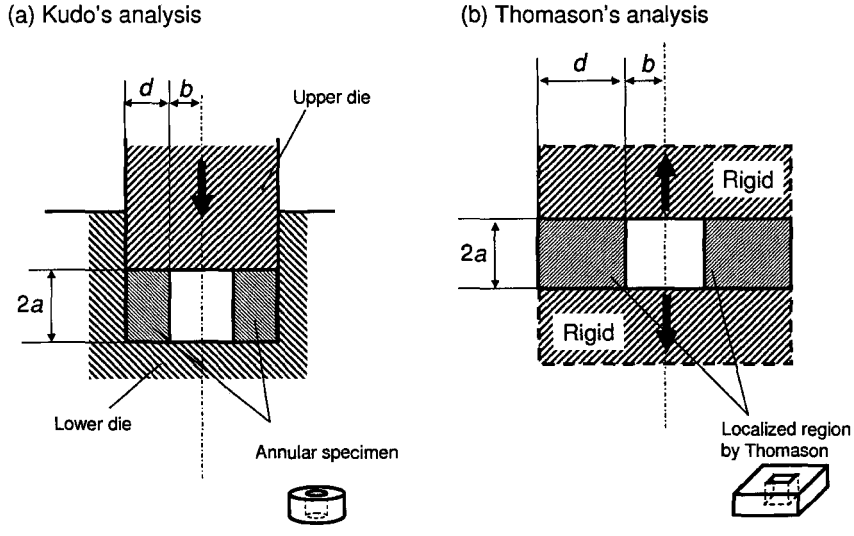

Figure 2.13: The schematically illustrated concepts of (a) Compression of an annular specimen in rigid dies (Kudo, 1960) (b) Virtual mode of internal necking. (Thomason, 1985)

The expressions for the area fraction for two-dimensional and three-dimensional problems are given by

$$A_n|_{2D} = 1 - \sqrt{\frac{4V_f}{\pi}}\left(\frac{c}{c_0}\right)\exp(\varepsilon_1) \tag{2.30}$$

$$A_n|_{3D} = 1 - \left(\frac{3\sqrt{\pi}V_f}{4}\right)^{2/3}\left(\frac{b}{b_0}\right)\left(\frac{c}{c_0}\right)\exp(\varepsilon_1) \tag{2.31}$$

The critical condition for void coalescence is given by

$$\sigma_1^{1c} = \sigma_n A_n = \sigma_1 \tag{2.32}$$

or, by normalizing the both hand sides with the macroscopic yield shear strength k we obtain

$$\frac{\sigma_1^{1c}}{2k} = \frac{\sigma_n A_n}{2k} = \frac{\sigma_1}{2k} \tag{2.33}$$

It is known that there is a relationship between the macroscopic yield shear strength k and the microscopic yield shear strength of the intervoid ligament k_n in the form of

$$k = (1 - V_f)k_n \tag{2.34}$$

Assuming the kinematically admissible velocity field as illustrated in Figure 2.14(c) and (d), Thomason (1985) estimated the constraint factor $\sigma_n/2k_n$ for two-dimensional plane strain problems by the upper bound method, finding the approximate form of

$$\frac{\sigma_1^{1c}}{2k_n} = \frac{0.3}{N} + 0.6 \tag{2.35}$$

where N in this case is the neck geometry parameter which has the form

$$N = \frac{a}{c}\left(\frac{1 - A_n}{A_n}\right) \tag{2.36}$$

and the constraint factor σ_n/k_n for the three-dimensional form

$$\frac{\sigma_n}{Y_n} = \frac{0.1}{(a/d)^2} + \frac{1.2}{\left(\frac{b}{b+d}\right)^{1/2}} \tag{2.37}$$

This fitting equation was adopted from the work by Kudo (1960). Kudo's work originally dealt with compression of an annular specimen within a die by upper bound analyses. The required stress to start plastic deformation of the annular specimen is dependent on the ratio between the thickness a to the difference between the outer and inner radii of the annulus (i.e. d in Figure 2.13). The smaller value of the ratio a/d, the higher value of the plastic constraint factor. Thomason perceived that the compression of an annular specimen is essentially the same problem as void coalescence, and he simply made a reversal of the velocity field to provide a good fitting equation for the plastic constraint factor for internal necking.

Combining the expressions of the constraint factors (equations 2.35 to 2.37), the expressions of the area fraction (equation 2.36) and equation (2.34) into equation 2.35, we obtain the ductile fracture criterion by limit-load for the 2D case represented by

$$\left(\frac{0.3}{N} + 0.6\right)(1 - V_f)^{-1} = \frac{1}{2} + \frac{\sigma_m}{2k} \tag{2.38}$$

Similarly for the 3D case,

$$\left(\frac{0.1}{(a/d)^2}+\frac{1.2}{\left(\frac{b}{b+d}\right)^{1/2}}\right)\frac{1}{(1-V_f)}\left(1-\left(\frac{3\sqrt{\pi}V_f}{4}\right)^{2/3}\left(\frac{b}{b_0}\right)^2\right)\exp(\varepsilon_1) = \frac{\sigma_m}{Y}+\frac{3+\nu}{3\sqrt{\nu^2+3}} \tag{2.39}$$

The limitation of this model is that it does not account for either strain-hardening effect or the array geometry of holes other than rectangular.

Pardoen and Hutchinson (2000) extended the Thomason model to take into account the effect of strain-hardening in their FE based modeling work. The constant values of 0.1 and 1.2 on the left hand side of the equation (2.39) are replaced by two parameters of α and β that incorporate a dependence of the onset of localization on the strain hardening exponent n. They determined the dependence of α and β on n, fitting these parameters to their numerical results for localization. They found that the parameter β is a constant being 1.24 and α has the following polynomial form

$$\alpha(n) = 0.1 + 0.217n + 4.83n^2 \tag{2.40}$$

Using these α and β the plastic constraint factor is modified as below.

$$\frac{\sigma_n}{\overline{\sigma}} = \frac{\alpha}{(a/d)^2}+\frac{\beta}{\left(\frac{b}{b+d}\right)^{1/2}} \tag{2.41}$$

Thus the condition for void coalescence in a work hardening material is

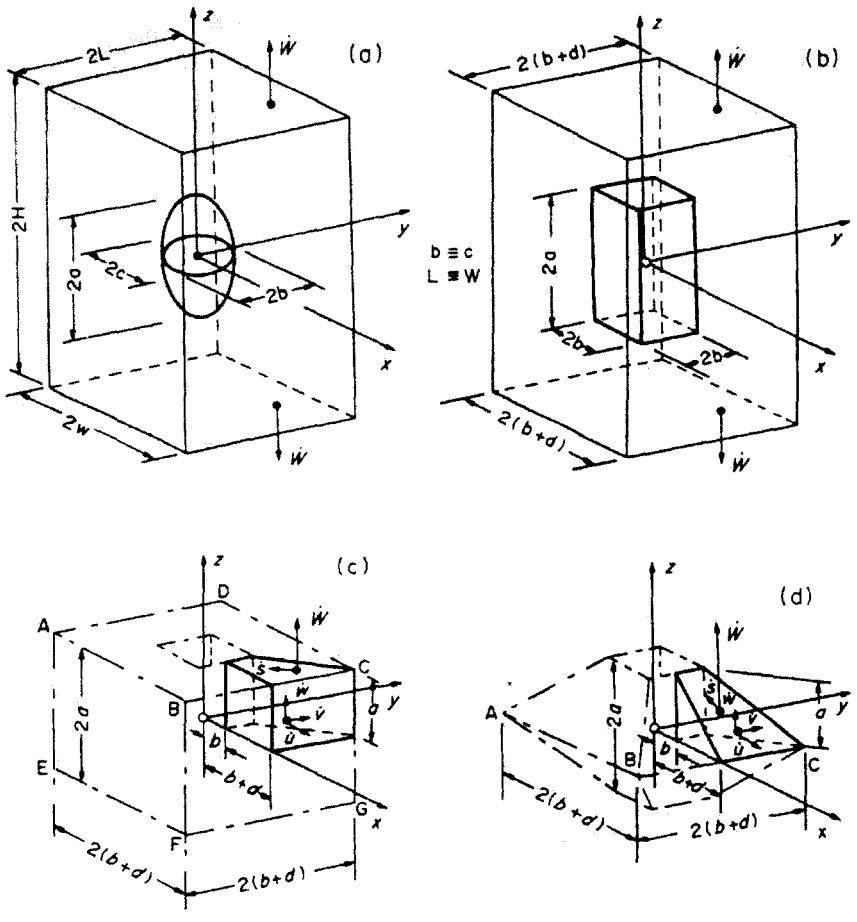

Figure 2.14: The unit cell with (a) an ellipsoidal void and (b) the equivalent square-prismatic void; also showing (c) the parallel (d) and the triangular velocity fields for the intervoid matrix in *virtual* mode. (After Thomason (1985))

$$\left(\frac{\alpha}{(a/d)^2}+\frac{\beta}{\left(\frac{b}{b+d}\right)^{1/2}}\right)\frac{1}{(1-V_f)}\left(1-\left(\frac{3\sqrt{\pi}V_f}{4}\right)^{2/3}\left(\frac{b}{b_0}\right)^2\right)\exp(\varepsilon_1) = \frac{\sigma_m}{\overline{\sigma}}+\frac{3+\nu}{3\sqrt{\nu^2+3}} \tag{2.42}$$

Note that uniaxial yield stress Y in the Thomason model was replaced by equivalent stress $\overline{\sigma}$ to account for work hardening.

Benzerga (2002) developed a micromechanical model by adjusting Thomason's model to fit the numerical results at low stress triaxiality when the void shape at coalescence is flat. He also numerically estimated the acceleration factor for a critical porosity model which was mentioned in the last section where Tvergaard's fracture model was discussed.

It is worth emphasizing here that work hardening exponent n and work hardening rate θ are two different things. Work hardening rate (WHR) θ represents the instantaneous work hardening behavior, which is represented by the following form;

$$\theta = \frac{d\sigma}{d\varepsilon} \tag{2.43}$$

The work hardening exponent represents the behavior over a range of strain. If we assume a simple power hardening behavior $\sigma = K\varepsilon^n$, the work hardening exponent n is given by

$$n = \frac{\varepsilon}{\sigma}\frac{d\sigma}{d\varepsilon} \tag{2.44}$$

or

$$n = \frac{d\ln\sigma}{d\ln\varepsilon} \tag{2.45}$$

Although the choice of n value or WHR to build a void coalescence model that accounts for work hardening is arbitrary, this difference has to be kept in mind when using these void coalescence models that take into account the effect of work hardening.

Gammage et al. (2004) proposed a model for the coalescence of penny shaped cracks in metal matrix composites based on the Brown and Embury model. The model is similar to the Considère type criterion for incipient macroscopic necking. According to this model the void coalescence occurs when the far field WHR θ is equal to the stress acting on the ligament between the voids separated by the distance λ , *i.e.*

$$\theta = \sigma_a \left(1 + \alpha\sqrt{\frac{a}{\lambda}}\right) \tag{2.46}$$

where a is the average particle diameter, σ_a the far-field applied stress. The drawback of this model is that it assumes that the far field work hardening rate is equal to that in the intervoid matrix. However, this model showed good agreement with the experiments carried out on metal matrix composites, in which penny-shape voids were nucleated by particle fracture.

The coalescence models mentioned in this section are summarized in Table 2.2. It is worth emphasizing here that these models are not designed to predict the simple linkage process but the onset of strain localization within the ligament.

Table 2.2: Coalescence models suggested by several researchers.

Authors	Criteria	Limitations
Brown and Embury (1973)	Void length = spacing	For horizontal void array No triaxiality considered No material property
Le Roy et al. (1981)	Brown and Embury model with stress triaxiality	For horizontal void array No material properties
Thomason (1990)	Limit load failure	No microscopic shear localization Non hardening material assumed
Pardoen and Hutchinson (2000)	Limit load failure with strain hardening	No microscopic shear localization
Benzerga (2002)	Limit load failure adjusted for low triaxiality	No microscopic shear localization
Gammage et al. (2001)	Stress equals to global WHR	Local WHR = Global WHR

2.1.4 Empirical Methods of Estimating Ductility

In the literature there are many other models that can predict ductility, yet many of them do not have realistic physical background in their formulation. They are typically dependent on inadequate assumptions and/or many adjustable parameters that have no physical meaning.

One of the most successful models in this category is that of Oyane (1972). This model supposes that ductile fracture occurs at a critical volumetric-dilational strain (ε_v =6 %), with the assumption that ductile fracture process is entirely controlled by dilatational strain as

$$d\varepsilon_V = \frac{d\bar{\varepsilon}}{(\rho/\rho_0)V_f^2}\left(\frac{\sigma_m}{\bar{\sigma}} + A_0\right) \tag{2.47}$$

where $d\varepsilon_V$ is the volumetric strain increment, $d\bar{\varepsilon}$ the equivalent strain increment, ρ and ρ_0 are the density of the material at the current and the initial states, respectively, and A_0 is a material constant. By integrating this equation, we obtain

$$\int_0^{\bar{\varepsilon}} \left(\frac{\sigma_m}{A_0\bar{\sigma}} + 1\right) d\bar{\varepsilon} = B_0 \tag{2.48}$$

Provided that the material constants A_0 and B_0 can be determined by experiments, the predicted fracture effective strain complies with the experimental results with reasonable accuracy. This model gives excellent prediction provided that material constants are known, and thus there is no problem in using it from an industrial viewpoint.

However, as previous sections showed, we know that this concept is wrong because ductile fracture usually develops after significant amount of "deformation" (i.e. shape change), and then undergoes the transition into a more "dilational" process. For example, in a pure torsion test, it is considered that there is no volumetric dilatation thus this model basically predicts the infinite fracture strain, yet the material under pure torsion test certainly fractures into two parts. Although the effective strain at fracture in these pure torsion tests can be used as the material constants (A_0 and B_0), it should be possible to develop more physically-realistic models.

This is why the current thesis places a emphasis not on these empirical models, but on the void coalescence models explained in the previous sections such as those by Thomason and by Pardoen and Hutchinson.

2.1.5 Further Development of Ductile Fracture Models

Microscopic Shear Coalescence

Most of the void coalescence models mentioned so far assume a periodic cubic void array; yet the configuration of voids in real materials are quite random. One can notice that when a pair of voids are configured in such a way that the normal direction of the intervoid plane is misaligned with the tensile axis by a certain amount of angle, θ, the microscopic shear localization can happen in the intervoid ligament. Care must be taken that this is different than macroscopic shear banding but happens only locally. It is important to clarify the effect of this angle θ on the onset of void coalescence. To the best knowledge of the author, there is no attempt to model the microscopic shear localization in literature, except for the work by Scheyvaerts (2008) and her co-workers. They

consider a spherical/spheroidal void array as illustrated by Figure 2.15 (a). Although this analysis was performed using a three dimensional FE model, the deformation along the thickness direction is prohibited. The predicted coalescence strains with different shear angles are present in Figure 2.15 (b), demonstrating the decrease in coalescence strain due to the shear. To account for more realistic situations, the void configuration has to be discussed three dimensionally instead of a simple in-plane (or 2D) configuration, which is extremely difficult yet.

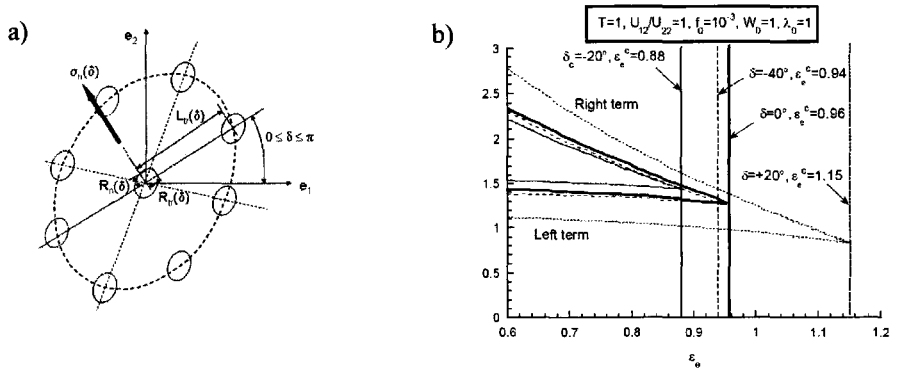

Figure 2.15: Effect of shear angle on the onset of void coalescence. (Scheyvaerts, 2008)

Void sheeting

As mentioned earlier, void sheeting is quite important as it accelerates the ductile fracture process, and the experimental data for this are not ample (except for Cox and Low (1974); Hancock and McKenzie (1976); Everett et al. (2001)). However, some attention has been paid to modeling this phenomena.(e.g. Fabregue and Pardoen (2008) and Faleskog and Shih (1997) using

FE modeling) Nevertheless, the influence of secondary void population on fracture is still an open problem.

2.2 Application of X-ray Tomography to the Study of Fracture

There are numerous ways to investigate ductile fracture. Among them, X-ray computed tomography is one of the most sophisticated due to the many advantages as summarized in the Table 2.3. In this section, the principle of the computed tomography and some examples of experimental works by X-ray tomography are presented.

2.2.1 Principle of Computed Tomography

X-ray tomography is a non-destructive technique which allows us to perform three-dimensional observations of an object. The terminology tomography is originated from a Greek word, $\tau o \mu o \varsigma$ (tomos = slice or cut), and thus this word is etymologically related to the words such as an atom (= cannot be cut anymore), microtomy (= small or precise cutting), anatomy (= cut into pieces) etc. The original concept of computed tomography was proposed by

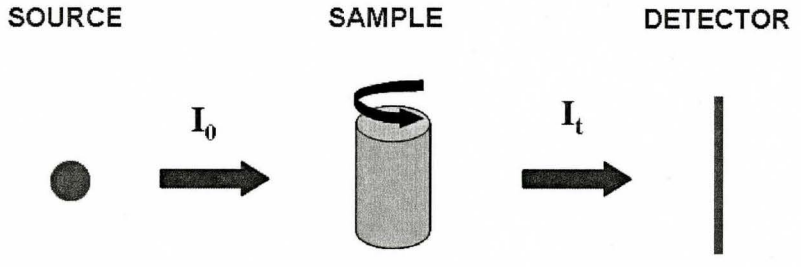

Figure 2.16: X-ray computed tomography

Table 2.3: Experimental techniques to study ductile fracture. (Weck, 2007)

Technique	Advantages	Disadvantages
Fractography	Easy	2D No sub-surface information No deformation history Destructive
Freeze Fractography	Easy Deformation history	Only for BCC metals No sub-surface information Destructive
Polishing	Easy Sub-surface information Deformation history	2D Polishing artefact Destructive
3D Fractography	3D	No sub-surface information Destructive
3D Freeze-Fractography	3D Deformation history	Only for BCC materials No sub-surface information Destructive
Serial sectioning	3D Full 3D reconstruction Can reveal microstructure	Time consuming Polishing artefact Destructive
X-ray tomography	3D Full 3D reconstruction High resolution Non destructive Can follow deformation in-situ	Availability
Ultrasound	3D	Averaged information
Densimetry	3D	Averaged information

an Austrian mathematician, Johan Radon(Radon, 1917). He proved that a three dimensional feature of an object can be reconstructed from a series of radiographs in 1917. Later, Godfrey Hounsfield (Hounsfield, 1972) successfully managed to reconstruct a tomogram based on 80×80 pixel^2 images and he was awarded 1979 Nobel Prize in Physiology or Medicine for the development of the computed tomography (CT) scanner. This prize was shared with Allan Cormack who also had developed some of the algorithms independently prior to Hounsfield (Cormack, 1963, 1964).

The principle of this technique is schematically illustrated in Figure 2.16. We illuminate an object by X-rays and record a projection by detecting the transmitted X-rays. The object is then rotated slightly and we record another projection. This process is iterated until the projections from all the angles are recorded over 180° rotation. A series of the collected images are subjected to the proper reconstruction algorithm so that a full 3D image is formed.

Reviews on reconstruction theories and algorithms can be found in several books (Morgan, 1983; Kak, 1988). In explaining the reconstruction theory, it is inevitable to use mathematical expressions. Although it is beyond the scope of this thesis to provide a full description of mathematics in the reconstruction theory, some important aspects of them are reviewed in the following.

Generally speaking, the internal structure of a metallic object (e.g. internal cracks, microvoids etc.) cannot be observed in a non destructive manner. The only possible thing we can do is to record a projection by X-rays, converting the 3D feature (= 3D distribution of X-ray attenuation coefficient) into a 2D projection. Note that X-rays can be replaced by any particle beams such as neutron beams and electron beams, as long as the image can be formed, but let us focus on X-rays here.

As mentioned earlier, the mathematical treatment between the projection and the original image (i.e. the 3D distribution of the X-ray attenuation coefficient within material) was initiated by Radon. What he proposed is that the projection is a result of the line integral of the density distribution along the X-ray path, and this integral is called a Radon Transform. In other words, obtaining a Radon transform and recording a projection in experiments are exactly the same thing.

In a real experiment, what we measure is the 2D projection of 3D features of an object, but the similar discussion can be made using a slice of 3D object (i.e. a 2D plane normal to the rotation axis) as illustrated in Figure 2.17. The projection of this slice is reduced to a 1D distribution (i.e. the distribution of P_θ along t direction) and this helps the mathematical formulation simpler. Indeed, this treatment does not deteriorate the discussion at all, because the original 3D feature can be reconstructed by stacking those 2D reconstructed images along the rotation axis. Thus we focus on the reconstruction principle of a 2D image from 1D projections hereafter.

Radon transform of the 2D object $f(x, y)$ is defined as

$$P_\theta(t) = \int_{(\theta,t)line} f(x, y)ds \tag{2.49}$$

and t is defined by

$$t = x\cos\theta + y\sin\theta \tag{2.50}$$

The function $P_\theta(t)$ is called Radon transform of the original 2D image $f(x, y)$, and θ the rotation angle. For a full reconstruction of this 2D image, the projections have to be recorded over the 180° rotation. However, these pro-

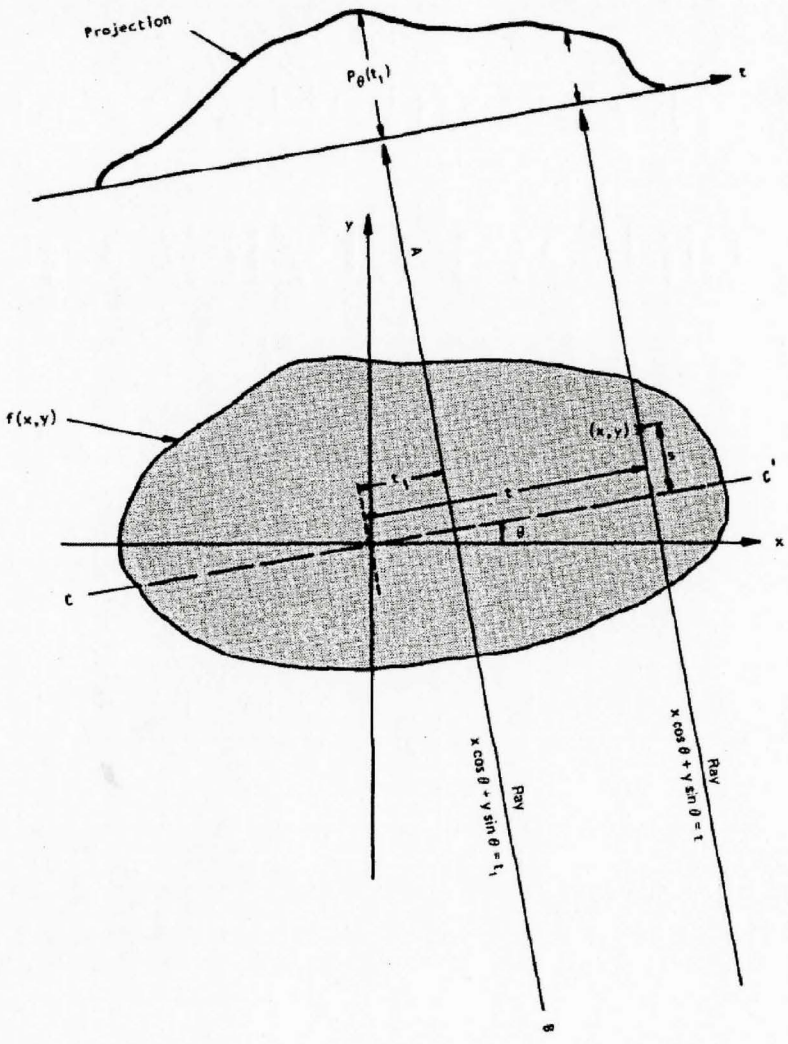

Figure 2.17: An object, $f(x, y)$, and its projection, $P_\theta(t_1)$, are shown for an angle of θ (Kak, 1984).

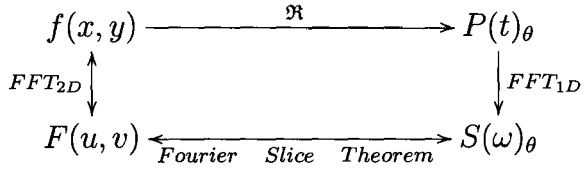

Figure 2.18: Schematically illustrated relationship between an object and its projection.

jections cannot be directly inverse-transformed to the original 2D image. The reconstruction process have to be performed through what is called the Fourier slice theorem as illustrated in Figure 2.18.

The Fourier slice theorem shows that the Fourier transform of a 1D parallel projection $P_\theta(t)$ of a 2D image $f(x,y)$ gives the slice of the Fourier transformed 2D image, $F(u,v)_\theta$ at an angle θ. If the projections from all the direction are known, the Fourier transform of the original 2D image can be obtained. Then, the only task remaining is to perform the inverse Fourier transform of $F(u,v)$. A series of these processes to obtain the original image is called back-projection or image reconstruction. In the real computation processes, the quantities are discrete, but the concept is the same.

The problem is that a blurred image is necessarily formed by reconstruction using this simple back projection method, as pointed out by Kuhl et al. (1973). The origin of this blurring is explained by Figure 2.19. During the simple back projection (i.e. no filtering), it was assumed that the original object has the same distribution in X-ray coefficient along the X-ray path. In the case of the figure, we have a point-like feature in a circular object. However, since the position of the point-like feature cannot be identified from the projection (it's referred to as 'signal' in the figure), we have to necessarily "assume" that the

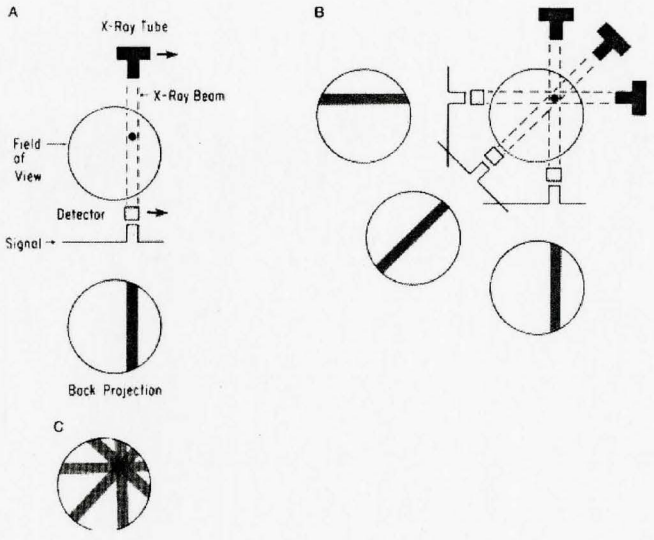

Figure 2.19: Simple back projection (Morgan, 1983)

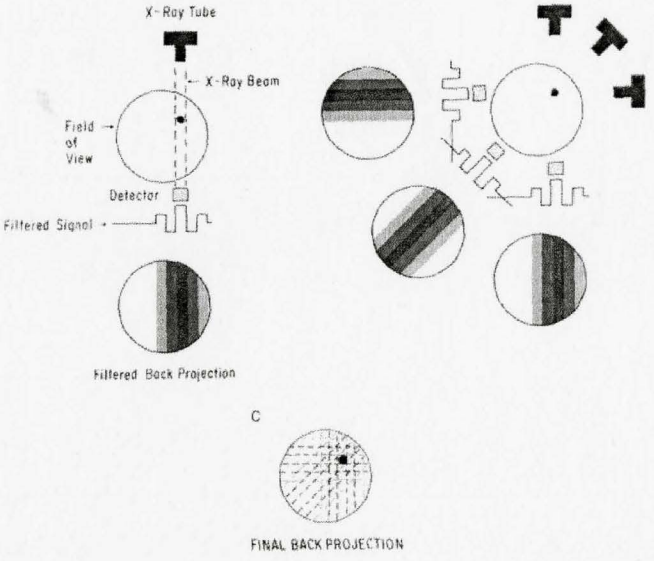

Figure 2.20: Filtered back projection (Morgan, 1983)

projection is obtained from a homogeneous banner-type feature instead of a point-like feature. Note that the contrast in the banner is much weaker than the on at the point feature. If this process is repeated over 180° rotation, the original feature can be reconstructed. The assumption that the original object has the same X-ray coefficient along the X-ray path also results in the noisy background, since the background that is originally supposed to be empty is smeared out coercively. As a result, the contrast of the point-like feature compared to the background becomes weaker relatively. This problem cannot be solved no matter how many projections are taken. Even if an infinite number of projections were recorded, the reconstructed image will be still blurred.

To remove this blurring, the filtered back projection method or the convolution back projection method have to be applied. Figure 2.20 illustrates how the filtered back projection method works. In this method, some filtering function is multiplied with the Fourier transform of the projection in the frequency space. This filtering function emphasizes the contrast of the boundaries, such that the blurring of the image is filtered out. The product of the filtering function and the Fourier transform of the projection is subject to the inverse Fast Fourier Transform (FFT) to reconstruct the original image, in a non-destructive manner. The convolution back projection method is a variant of this technique, in which the projection (radiographs) is convoluted with a filtering function and then back-projected. The difference between these two is whether the filtering function is applied in real space or in frequency (reciprocal) space.

2.2.2 Application of X-ray tomography to ductile fracture

Computed tomography was initially developed in the medical field and later utilized to study materials behavior. However, unlike the medical field, in which the object normally consists of soft materials such as the human body, material scientists are interested in hard metallic materials that are much more X-ray absorbing. Care must be taken to choose the proper source of X-ray so that it can penetrate the object and consequently an image can be formed on a detector. The intensity of a transmitted X-ray beam I_t is given by

$$I_t = I_0 e^{(-\mu t)} \tag{2.51}$$

where I_0 is the intensity of the incident beam, μ the attenuation coefficient dependent on the type of elements absorbing the X-rays, the density and the wavelength of the X-rays, and t the depth of material through which the X-rays can travel. The attenuation coefficient can be normalized by the density (this normalized quantity μ/ρ is called mass-attenuation coefficient) so that the above equation is rewritten as

$$I_t = I_0 e^{\left(-\frac{\mu}{\rho}\rho t\right)} \tag{2.52}$$

The attenuation coefficient is not a material property but mass-attenuation coefficient is.

Meanwhile, brilliance is also another important parameter which is defined as the number of photons emitted by the source in unit time in a unit solid angle, per unit surface of the source, and in a unit bandwidth of frequencies

around the given one (its unit is thus photons/s/mm^2/mrad^2/0.1%BW).

For relatively light materials such as aluminum or magnesium, a lab-based conventional X-ray machine can be used for imaging within a relatively short period, but it is much more time consuming for heavier materials such as steels or copper.

One solution for this problem is to employ a stronger and more brilliant X-ray source available at large scale synchrotron radiation facilities such as the European Synchrotron Radiation Facility (France) and SPring-8 (Japan). Figure 2.22 shows the difference between so-called the third generation synchrotron radiation facility and a conventional X-ray machine.

Synchrotrons are devices for the production of high intensity beams of lights at a variety of wavelengths. Synchrotron radiation is generated when the trajectory of an electrically charged particle (e.g. an electron) is bent by magnetic field.

In the case of the third generation synchrotron radiation facilities like ESRF or SPring-8, electrons are initially accelerated in a linear accelerator (linac) to 0.2 GeV approximately, then they are thrown into what is called the acceleration ring (or a booster synchrotron) for further acceleration. Once the electrons reach a certain kinematic energy ($\sim$ 6 GeV (ESRF) or 8 GeV (SPring-8)), the electrons are released into the storage ring. Within the storage ring, the pulsed electron beams are kept bending by a series of magnets, losing their kinematic energy. Note that these electrons are not a continuous wave but circulated in packets, and thus the generated X-rays are pulsed.

Depending on how electrons are bent, synchrotron radiation generation devices are classified into two categories namely, bending magnets and insertion devices. In the case of a bending magnet, the trajectory of electrons are bent

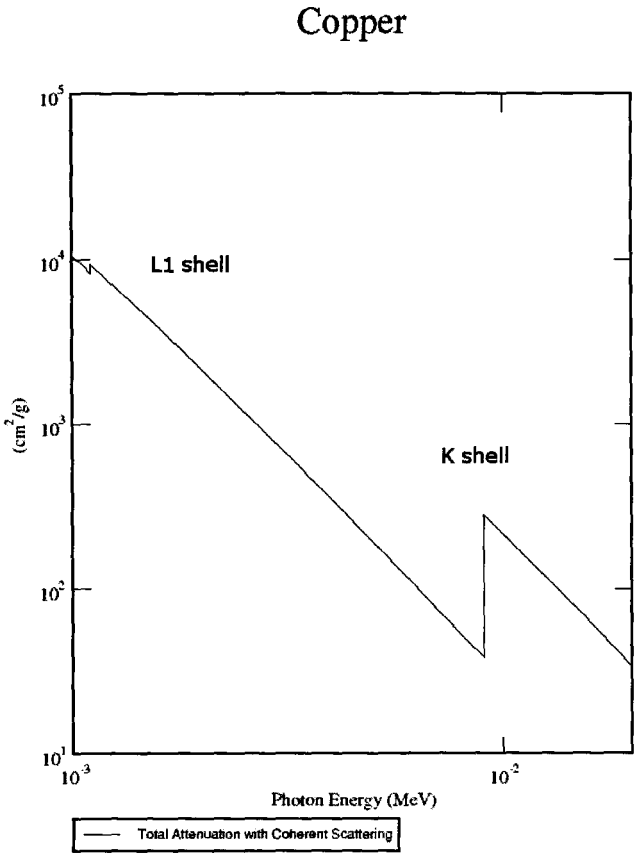

Figure 2.21: Copper attenuation as a function of X-ray energy. The curve was calculated by a free software XCOM developed by researchers from National Institute of Standard and Technology, U.S.A. (http://physics.nist.gov/PhysRefData/Xcom/Text/XCOM.html))

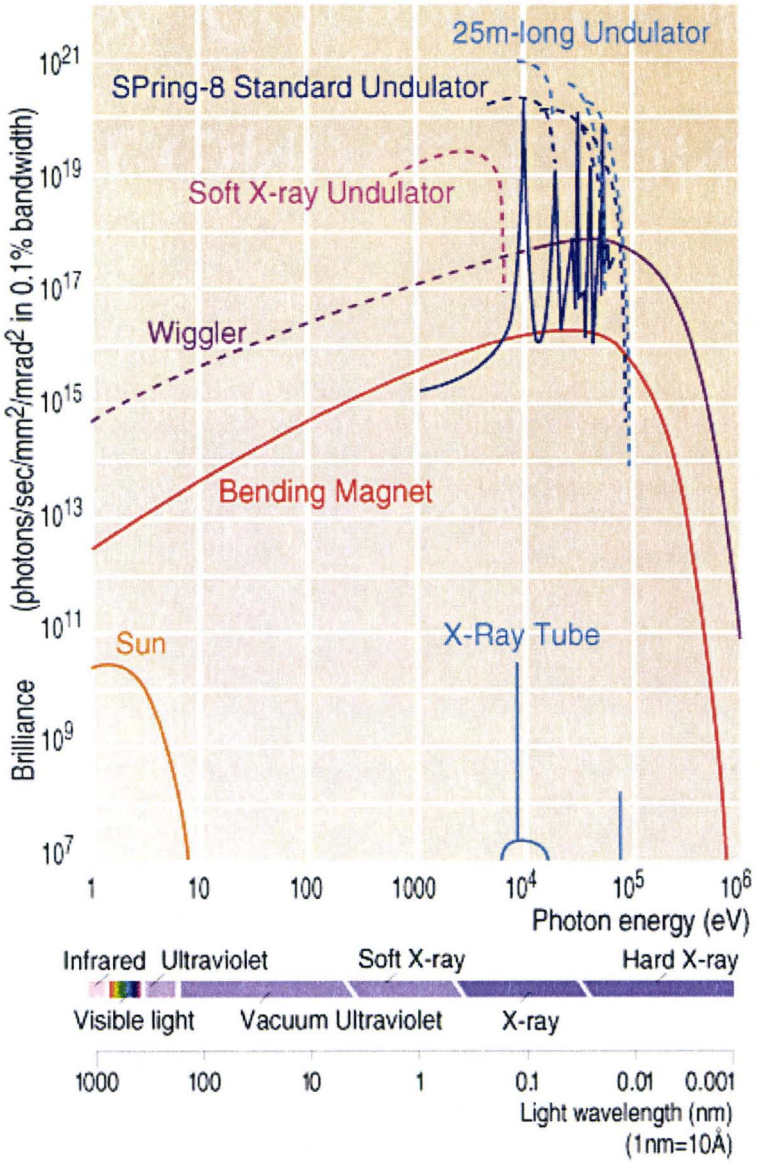

Figure 2.22: Spectral ranges available at SPring-8. (http://SPring-8.co.jp)

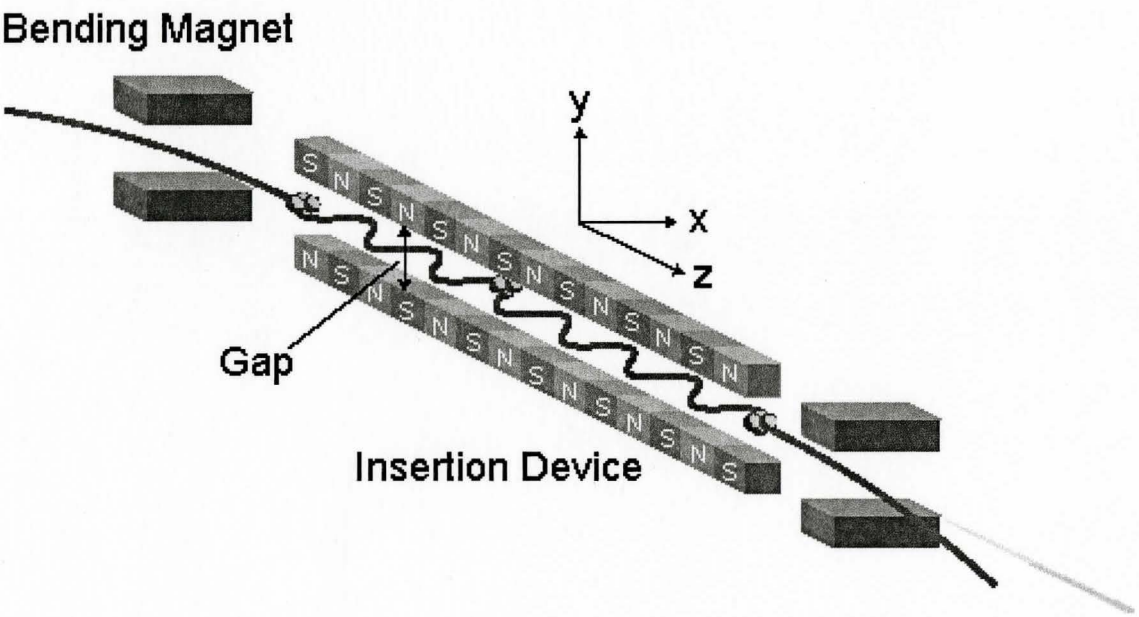

Figure 2.23: Insertion device "inserted" between two bending magnets. Reprinted from the website of SPring-8. (http://www.spring8.or.jp/en)

only once, and X-rays are generated along the tangential line. On the other hand, an insertion device consists of a series of bending magnets that are linearly arranged. This insertion device can generate X-rays along its arranging direction since electrons are bent alternatively several times as illustrated in Figure 2.23. The insertion devices have to be located between two bending magnets. In this way, electrons can keep flying within the storage ring, generating X-rays also at the other beamlines. Insertion devices can be further classified into a wiggler and an undulator. A wiggler typically generates very white X-rays, while an undulator generates semi-monochromatic ones. The gap between an upper series of magnets and the lower series of magnets are also different; the undulator has wider gap than the wiggler's. The structure and the way they work are however the same.

Such a large scale synchrotron radiation facility was employed in the field

of materials science during the 1990s as soon as the facilities became available (ESRF and SPring-8 opened in 1994 and 1997, respectively). Application to fracture study was pioneered by Buffière et al. (1999) who used this technique to study the damage evolution in a metal matrix composite. This experiment proved that the number of broken particles inside a material is higher than that on the surface. This clearly tells the importance of 3D observations. Babout et al. (2001) also studied void nucleation by X-ray tomography. The other application of 3D observation was shown by Martin et al. (2000). They estimated the void volume fraction from the cross section of 3D reconstructed image, and compared this value with the one quantified from 3D reconstructed images itself. A significant difference was seen between the two values, which implies that the void volume fraction estimated from the cross section (which corresponds to metallographic technique for example) is not plausible. This result warns us that 2D observation may not result in a correct conclusion.

Chapter 3

Previous Work at McMaster University

It was shown in the last chapter that ductile fracture involves progressive processes of nucleation, growth and coalescence of voids. However, void nucleation and coalescence have a very stochastic nature (i.e. they can happen anywhere at anytime), and thus it seems almost impossible to analyze the void growth behavior and the transition into the coalescence stage in commercial engineering materials. One of the best approaches to tackle this problem is to create a class of model materials that contain an artificial void array from the beginning. This chapter presents the fabrication process for those model materials and the characterization method that was developed in the Ph. D. thesis work of A. Weck (Weck, 2007). The current study is largely based on this work.

3.1 Previous work at McMaster University

3.1.1 Motivation

Although various predictive models on ductile fracture had been proposed in the literature, ductile fracture still remains difficult to predict precisely. This is attributed to a lack of experimental validation for void coalescence. Such difficulties are summarized as below.

- The fracture strain and coalescence strain are so close that it is difficult to distinguish the two of them clearly.
- Voids inside the real materials are invisible, and 2D experiments are not representative.
- Both the nucleation and the coalescence of voids are so stochastic that we can not predict where they will occur.

Weck and Wilkinson (Weck, 2007) therefore devised a new methodology to study the void growth and coalescence of an artificial void array embedded in a metallic matrix (Weck and Wilkinson, 2008; Weck et al., 2008b). To do this

- A class of model materials was made so that the stochastic nature of void nucleation and coalescence can be avoided.
- In situ mechanical testing associated with SEM and X-ray computed tomography was employed to observe the behavior of voids.

3.1.2 Model Material Fabrication

The fabrication method of model materials in this work is illustrated in Figure 3.1. Two types of model materials were fabricated; 2D model materials and

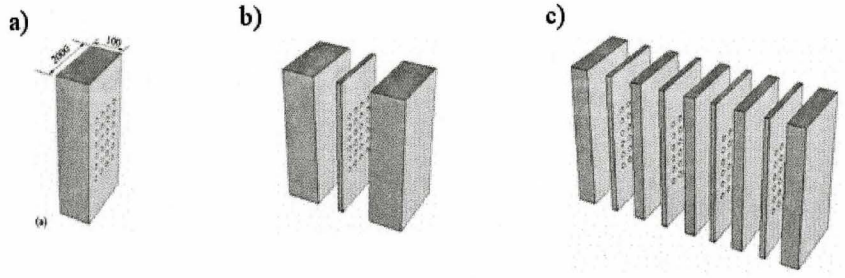

Figure 3.1: Fabrication of model materials. (a) 2D model materials for in situ SEM (b) single layer 3D (c) multi layered 3D model material

single-layer 3D materials. The 2D model materials were made of AA5052 and Glidcop[1] while the 3D model materials were made of pure copper and Glidcop. The reason why copper-based materials were chosen for 3D model materials is due to its convenience in the diffusion bonding process. It was also found that pure titanium is easy to bond but an HCP material such as titanium is not ideal for this study due to its mechanical anisotropy. Generally speaking, each crystallographic grain in a metallic material has three shear and three tensile components of the strain tensor, but only five components are independent since plastic deformation must satisfy the constant-volume law. To satisfy the compatibility of displacement, at least five independent slip systems are required according to the Mises-Taylor criterion (von Mises, 1928; Taylor, 1938). However, HCP materials have only two independent slip systems whereby the condition is not satisfied. Choosing titanium as a model material was avoided since the situation mentioned above makes the

[1]Glidcop is a pure copper matrix composite reinforced by Al_2O_3 nanoparticles. Al-25 contains 0.5 wt% of Al_2O_3.

interpretation of results rather difficult.[2] In contrast, FCC materials such as copper, which have 12 slip systems, satisfy this condition and its fracture behavior is not nearly as anisotropic.

The hole machining was performed by an ultra short-pulsed laser machining system with XYZ motorized stage which allowed us to machine holes at arbitrary positions. The laser machining system mentioned above can machine a hole array with great accuracy (0.3 μm) within one sheet[3], and thus as-drilled sheets can be used directly for 2D model materials (3.1(a)). However, some ingenuity is required to align those holes perfectly in three dimensional space after diffusion bonding. In the case of Weck's work, the sheets were all bound at one side (like the pages of a book) before the holes were machined. The holes were machined based on the xy coordinates from the corner of the rectangular sheet, by turning over the "pages." In this way, the holes along the stacking direction were almost perfectly aligned.

3.1.3 Selected outcomes from the work of Weck et al.

This methodology successfully paved a way to produce a new class of model materials containing a void array embedded in a metal matrix. The combination of this class of model materials with in-situ X-ray tomography during tensile tests succeeded in visualizing the void growth and coalescence behaviors. With the assistance of the commercial visualization software, quantitative analysis of the void growth and coalescence were also performed. The experimental results were compared with the values predicted by models, and

[2]In parallel with the current thesis project, a similar project dealing with pure magnesium is under progress by M. Nemcko (Nemcko, 2010).

[3]The accuracy of the coordinates of the center of a hole from the origin (normally a corner of the rectangular sheet) has this value.

provided a means to assess the void coalescence models. One highlight of a series of works performed by Weck et al. can be observed by comparing Figures 3.2 and 3.3 which are the results from in-situ SEM and X-ray tomography during tensile deformation, respectively.

The results from the 2D experiments which were performed for materials with open holes were in a good agreement with the classical Brown and Embury model (Brown and Embury, 1973), while the 3D experiment using X-ray tomography did not agree with the Brown and Embury model but agreed instead with the Thomason model. This fact clearly indicates that the void coalescence behavior in a 3D matrix cannot be tested by 2D experiments or the models based on a 2D concept. Furthermore, it is remarkable that this work gave a quantitative correlation with one of the new-generation FE-based void coalescence models by Pardoen and Hutchinson (2000). In principle, Weck's method can be also used to provide the quantitative assessment for models developed by Gologanu et al. (1993, 2001b), which extended the Gurson model in such a way that the effect of the aspect ratio of spheroidal microvoids on the effective stress of a porous solid can be taken into account. This can be done by laser-machining the array that consists of elliptical holes instead of cylindrical holes. Furthermore, it is also possible to create much more complicated void array such as clustered voids, bi-modal void population (i.e. two different classes in void size) and so on.

3.1.4 Critical problems remaining from Weck's method

The attempt to produce multi-layered 3D materials was also made by Weck et al., but it did not completely succeed. This was attributed to the fabrication method. Binding the stack of sheets prior to laser drilling made it impossible to polish the surfaces properly, leaving an oxide layer that prevented diffusion bonding. Thus, the results presented by their work are limited to the 3D materials with a single-layer array embedded. While, samples with multi-layer void arrays were made, they suffered from delaminations of the bonded samples during the tensile tests. Another drawback of the previous work is that they were not able to capture the onset of void coalescence but only the final void linkage, because of the limited number of tomographic scans per experiment. *Void coalescence is different than void linkage.* Most of the existing models of void coalescence are indeed designed to predict the onset of void coalescence. This point will be elaborated in more detail at the beginning of Chapter 5.

The purpose of the thesis was to overcome these difficulties by;

- Improving the fabrication process to avoid inter-layer delamination so that fully 3-D samples can be tested.

- Improving the innovative methodology so as to fully capture the coalescence process.

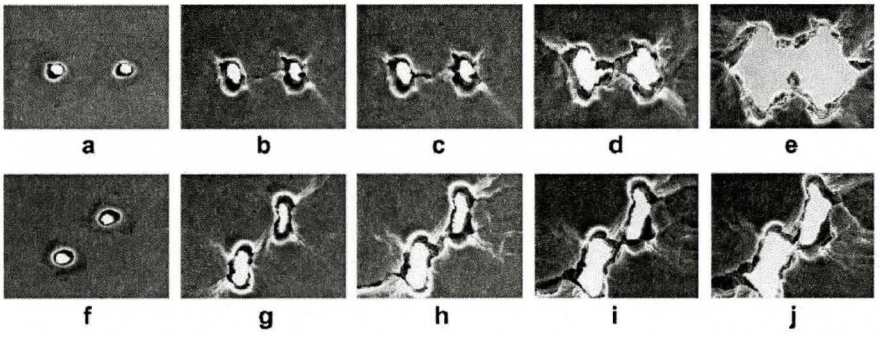

Figure 3.2: The 2D analysis by SEM performed by Weck.

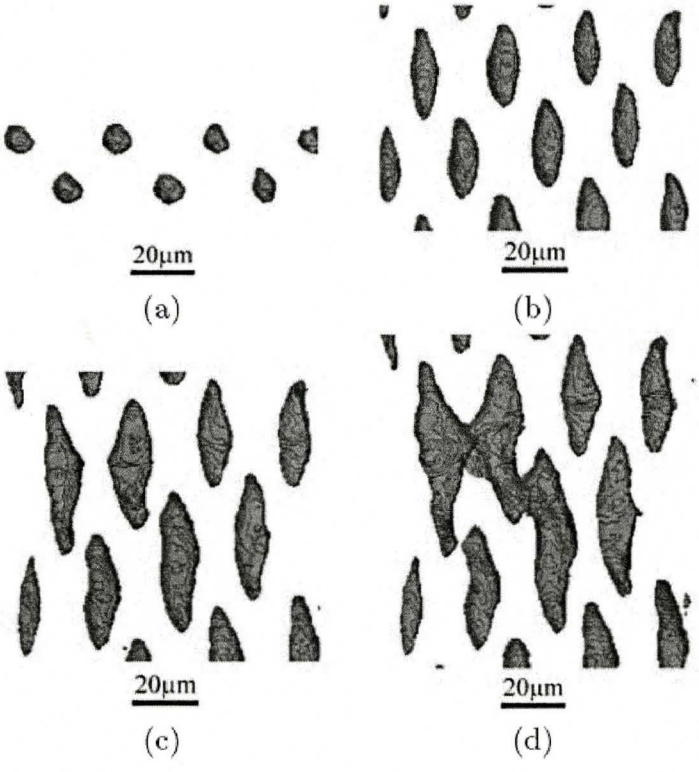

Figure 3.3: The 3D analysis by X-ray tomography by Weck. (a) $\varepsilon = 0$ (b) $\varepsilon = 0.5$ (c) $\varepsilon = 0.77$ (d) $\varepsilon = 1.01$

Chapter 4

Experimental Methods

4.1 Sample preparation in the current project

4.1.1 Difference from the approach by Weck

In the current thesis project, a similar methodology to what Weck proposed is employed. The starting materials used in the current project are pure copper (99.9999wt%), Glidcop (AL-25) [1] and cartridge brass (C26000, Cu:Zn=7:3, commercial purity). The main objective is to capture the void coalescence behavior in model materials with multi-layered void arrays without delamination. In the Weck method, as mentioned in section 3.1.2, the stack of sheets were bound at one side like the pages of a book such that the holes are almost perfectly aligned along the stacking direction. However, this method made it extremely difficult to polish the surfaces to be bonded, resulting in the inter-layer delaminations after the tensile tests.

An alternative approach was developed here. As-received metallic sheets

[1] Glidcop is a pure copper matrix composite reinforced by Al_2O_3 nanoparticles. Al-25 contains 0.5 wt% of Al_2O_3.

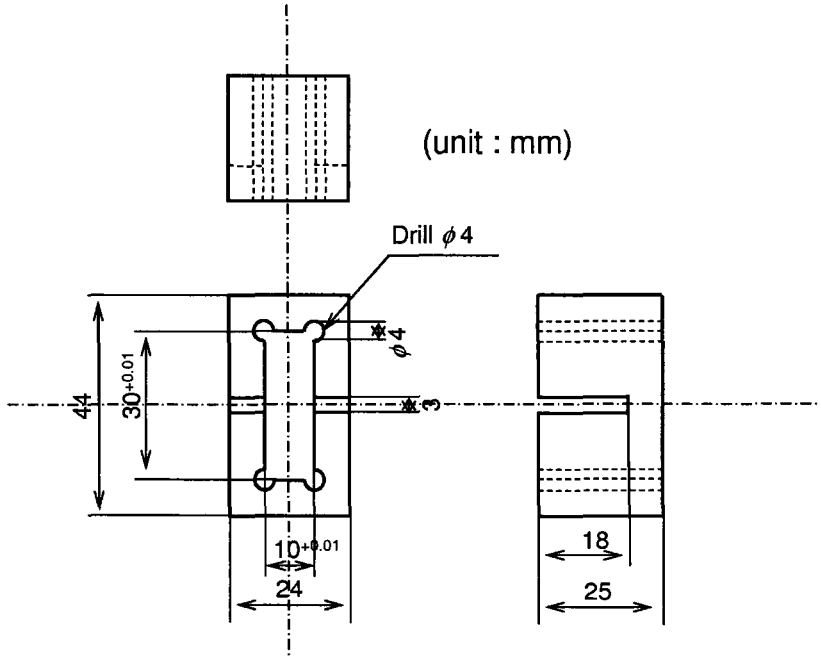

Figure 4.1: The drawing of the Inconel mold employed in the current thesis project.

were first cut into a rectangular shape ($10^{+0.01}$ mm x $30^{+0.01}$ mm = W x L in Figure 4.1) with the best possible precision. An array of holes can be laser-machined with respect to the corners of these rectangular sheets, that play the role of the origin for the XY coordinate. A mold with a square hollow was made. This hollow has the same dimension as the rectangular sheets, i.e. $10_{-0.01}$ mm $\times$ $30_{-0.01}$ mm = $W' \times L'$ in Figure 4.1, and a series of metallic sheets were stacked within this mold. The stack was sandwiched between two Inconel push rods to apply pressure ($\sim$ 3 MPa) and then diffusion bonded at desired temperatures (Figure 4.2). The surfaces of the Inconel pushrods were coated with a boron nitride spray prior to the diffusion bonding, in order to diffusion bonding between the model materials and the pushrods. In this

way, although the hole alignment along the stacking direction is less precise compared to the Weck method, we can expect better bonding at the inter-layer boundaries. However, we can still expect the alignment as precise as the machining processes of the rectangular pieces and the Inconel molds.

Let us consider an example that we diffusion bond two layers, and each sheet has two holes, as shown in Figure 4.3. We already know that the accuracy of the hole drilling coordinates (x_1, y_1) and (x_2, y_2) are as precise as 0.3 μm. Now, the perfect alignment is obtained when the dimensions of the rectangular piece (W' and L') and the Inconel molds (W and L) are exactly the same. The expected accuracy of the alignment is approximately as precise as the machining (i.e. $\sim \pm 0.01$ mm). The quality of the hole alignment in the individual model materials will be discussed with the visualized tomograms in Chapter 5.

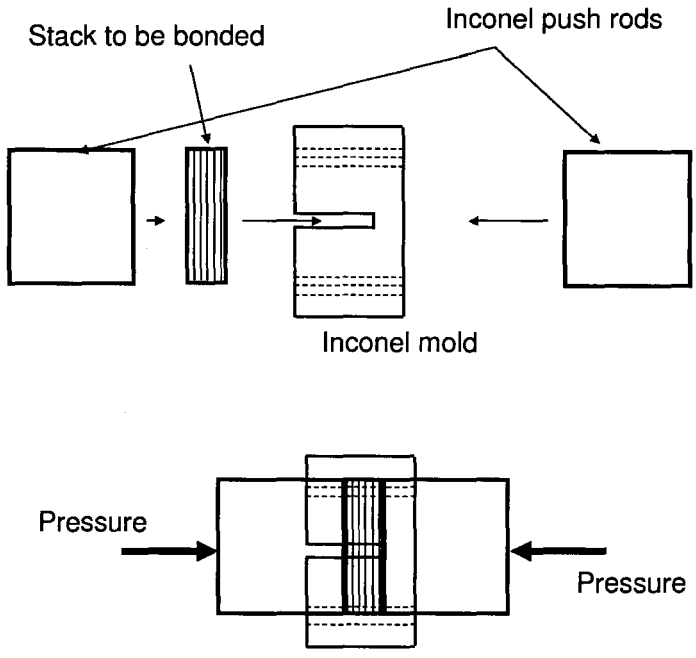

Figure 4.2: Assembling of the pushrod, the stack of drilled/undrilled sheets and the mold.

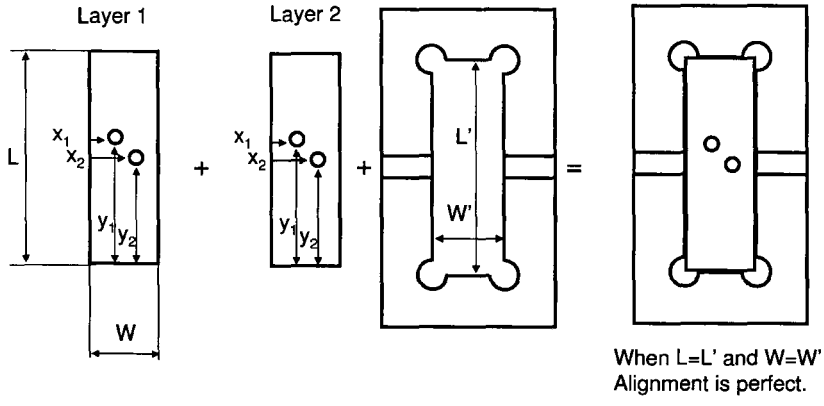

Figure 4.3: The mechanism of hole alignment by the current method.

4.1.2 Laser drilling set-up

The hole drilling was performed by a combination of commercially available laser systems as shown in Figure 4.4, which schematically depicts how a pulsed laser for machining is generated. The Ti:sapphire laser (*Tsunami* ®) has a very short pulse but its energy is still too low for machining. To amplify the energy of the laser, it undergoes the following three steps: pulse stretching, regenerative amplification and pulse compression. The initial laser from Tsunami first has to be stretched to minimize the damage to the regenerating pumping system (*Milenia V* ®) before it is sent to the regenerative amplifier. Then the laser using with a stretched pulse length ($\sim$ 200 ps) is amplified to 500 μJ (1 kHz in laser repetition rate, 500 mW in power) at the regenerative amplifier (*Merlin* ®). The laser medium of the Merlin is the same Ti:sapphire as the Tsunami but the pump for this is made from Nd:YLF crystal. The amplified beam is finally compressed to decrease its pulse length to the range between 150 fs to 35 ps. During these three steps, the wavelength of the laser keeps the same value of 800 nm.

The amplified short pulsed laser is then sent to the machining system shown in Figure 4.5. The machining was performed inside a vacuum chamber to minimize the contamination by debris and X-ray hazard. The spot size of the laser, which is the most important in hole drilling, is controlled by the magnification of the lens system and the amount of defocusing. The more detailed description about this laser set-up can be found in the theses by Hsu (2007) and Weck (2007).

The vacuum chamber is installed on a XYZ precise motion stage (0.3 μm in accuracy). This stage allows machining of holes at any location for a given XY

coordinate. The motion along Z axis is also motorized but it is not as precise as XY motions since the Z coordinate is based on the focal point, which has to be determined by literally looking at the optical image on a video monitor by eyes.

The laser machining parameters employed in this thesis project is summarized in Table 4.1.

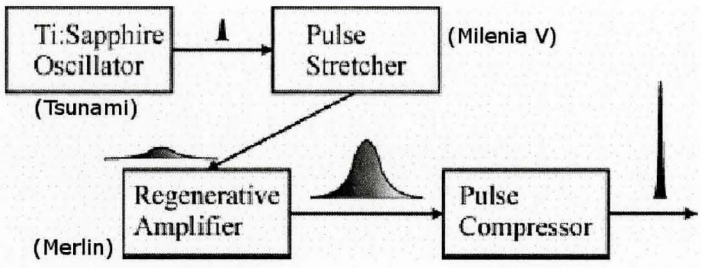

Figure 4.4: The generation mechanism of a short pulsed laser. (Hsu, 2007)

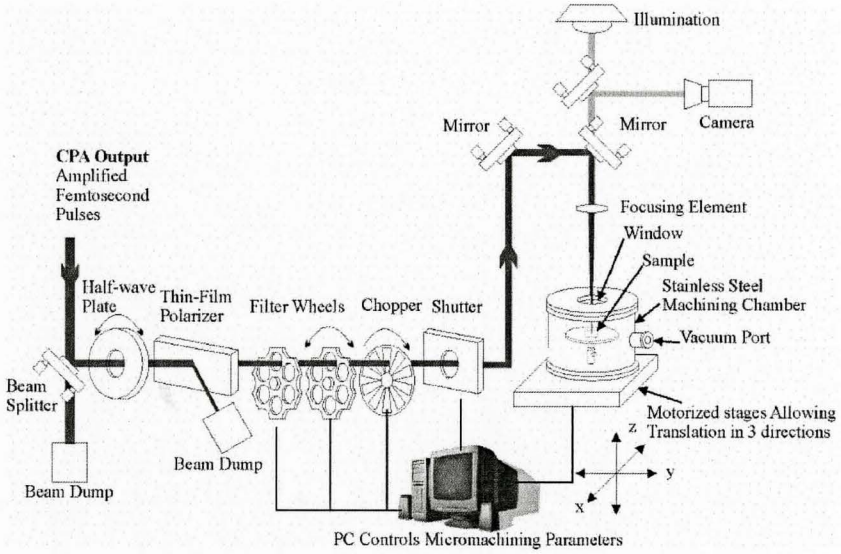

Figure 4.5: Laser machining set-up. (Hsu, 2007)

Table 4.1: The laser machining parameters employed in the current work.

Laser energy	10 mJ
Number of Pulse	5000
Pulse length	5 ps

4.1.3 Possible factors that cause the offset of the alignment: Drawback of the machining system

In principle, the void arrays of model materials were designed to have a certain distance to the nearest neighboring void. In the case of the model materials in Chapter 5, for example, the distance to the nearest neighboring void is designed to be 0.141 mm. However, as illustrated in Figure 4.6, if some offset of void alignment exists, the actual inter-void distance after diffusion-bonding always ends up with a smaller value.

The biggest source for the offset originates from the offset of the origin itself for the xy machining coordinates, simply due to some crude aspects of the current laser machining system. In the current method, the origin for the xy machining coordinates is located at the bottom-left corner of the 10 mm $\times$ 30 mm rectangular sheets. The machining of all the holes are performed based on this origin. Before a set of laser machining was performed, this origin was set by looking at an optical image on a monitor that is recorded from a camera, as illustrated in Figure 4.5. If the image on the monitor is clear, the square corner of the rectangular sheet can be easily found and thus the quality of the machining is also good.

However, as mentioned in the last section, also as shown in Figure 4.5, there are three optical parts that can deteriorate the quality of the image on the monitor: the window of the vacuum chamber, the filter (installed in front of the camera), a sheet of slide glass (installed underneath the window of the vacuum chamber).

Among the three, only the first one, the window of the chamber, is shown in Figure 4.5. The second one, the optical filter, is installed in order to prevent the

camera from the damage due to the extraordinary strong light that generates at the sample surface during the laser machining. The third one, the slide glass, is installed to avoid the debris accumulating on the expensive window of the vacuum chamber. These three parts are inevitable in terms of safety concerns, but unfortunately they deteriorate the quality of the optical image recorded by the camera, and consequently they deteriorate the quality of the machining as well. Without updating the laser machining system, a certain amount of the offset cannot be avoided. The actual amount of offset in the model materials are discussed individually using the 3D reconstructed image in later chapters.

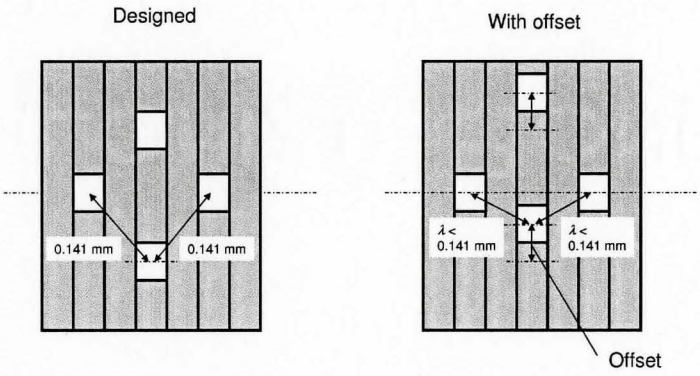

Figure 4.6: How the off-set influences the actual inter-void distance in a model material.

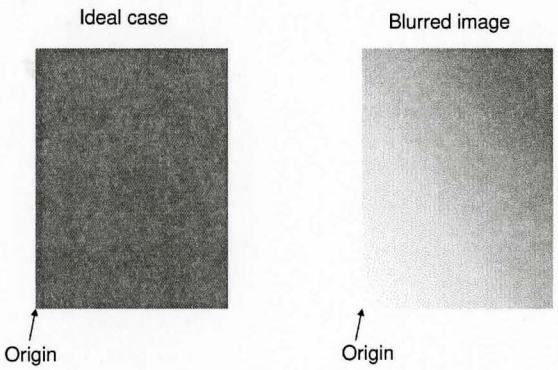

Figure 4.7: The biggest source of the offset by the image blurring. If the image on a display at the laser machining system is blurred, the origin cannot be determined uniquely.

4.1.4 Diffusion bonding treatment

Laser drilled sheets and hole-free sheets were mechanically polished by SiC abrasive papers (grit 1200 $\sim$ 4000) and diamond paste (1 and 3 μm). Sulfuric acid solution (H_2SO_4:Water=8:2) was used for chemical rinsing after the polishing.

Soon after this[2], a stack of hole-free and drilled metallic sheets was put into an Inconel mold (Figure 4.1) and then diffusion-bonded by Instron Model DSW Dead Weight Load Creep/Stress Rupture Testing System. (Figure 4.8). This machine allows us to apply about 3 MPa static pressure on the laminated stack in the current set-up (i.e. a rectangular piece of 10 mm x 30 mm) with 160 lb weight. The samples installed in a mold were set inside the chamber in which the argon with 3% hydrogen (Ar+3%H) gas was circulated to maintain the reduction atmosphere. A typical heating rate is 400 $\sim$ 450°C per hour. Since the maximum temperature of the machine is 930 °C, pure copper and Glidcop were diffusion bonded isothermally at the temperature for 45 minutes. The diffusion bonding temperature for brass was determined to be 860 °C which is just below the solidus line at Cu-30wt%Zn in the Cu-Zn binary phase diagram. The isothermal period for this case was also 45 minutes. The isothermal period of the heating profile was followed by furnace cooling which usually takes one night.

4.1.5 Materials characterization

Optical microscopy and transmission electron microscopy (TEM) were performed to characterize the as-diffusion-bonded materials. Prior to the met-

[2]Ideally, the last step of polishing and installing the samples into the creep machine should be done in the same day.

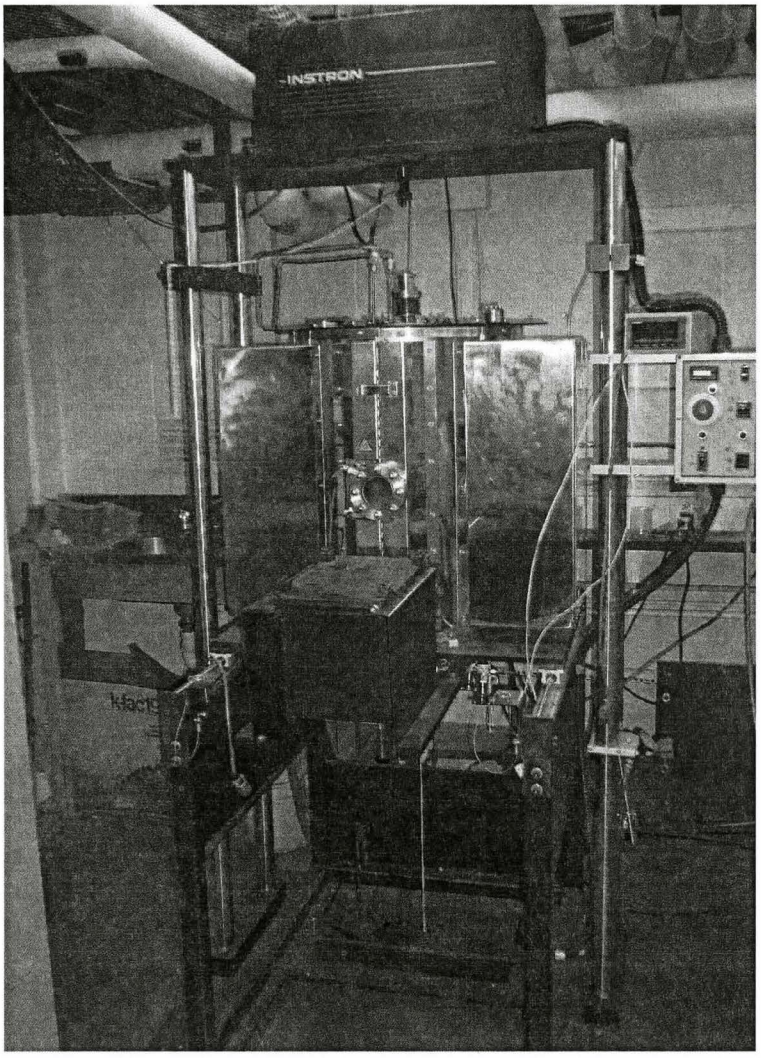

Figure 4.8: Instron Model DSW Dead Weight Load Creep/Stress Rupture Testing System

allography, the specimens were mechanically polished by SiC abrasive paper (grit 800 $\sim$ 4000), diamond paste (1 and 3 μm) and colloidal silica (0.05 μm) and then etched by appropriate etchants for individual materials. Fractography was also performed for hole-free materials as well as diffusion-bonded model materials tested at the synchrotron radiation facilities by making use of scanning electron microscopy (SEM).

4.2 Digital Image Correlation

Tensile testing coupled with the digital image correlation technique was also performed to obtain the constitutive behaviors of hole-free diffusion bonded materials as well as annealed bulk materials. The full description of the principle behind this technique is mathematically complicated and lengthy, yet a brief review is given here.

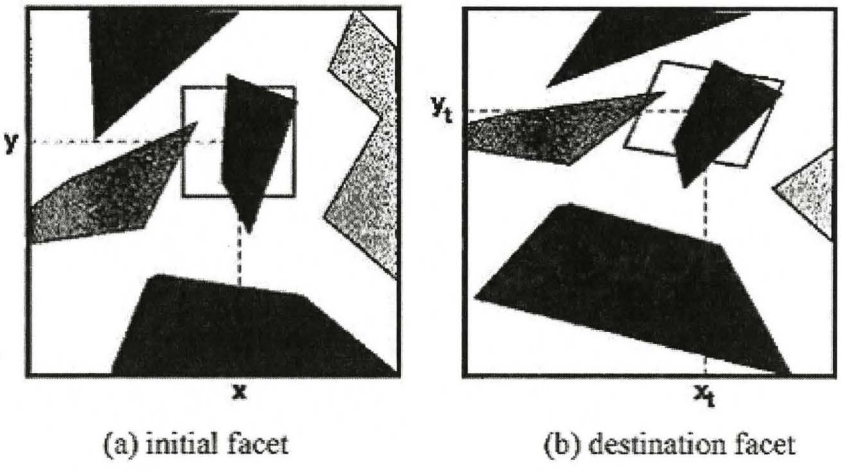

Figure 4.9: The principle of the digital image correlation technique showing images before and after deformation. (Aramis, 2001)

Let us consider deforming a 2D image as illustrated in Figure 4.9, which generally involves the information of the grayscale at each pixel with each position identified by xy coordinates. In the case of this figure, matrix is virtually white, and several polygons with darker colors are embedded. If some homogeneous tensile deformation takes place in the image, strain will be homogenous within the picture so that the polygons will get elongated along the tensile direction. On the other hand, if the deformation is inhomogeneous, these polygons will deform in accordance with the local strain. The digital

image correlation technique enables us to estimate such local strains for each small subimage called a "facet" that makes up the total image. The local strain for a facet is estimated simply by the distortion of the facet. Given the local strains for all these facets, the strain mapping is obtained for a whole image.

Note that each increment of the deformation must be moderately small, since two images before and after deformation have to be *correlated.* We can not obtain a strain mapping from two completely different pictures (e.g. a picture of a dog and a picture of a cat) because there is no correlation between the two. In the digital correlation technique, the correlation between the two pictures is quantitatively estimated. This value is referred to as the correlation factor, r, which is defined by

$$r = \frac{\sum_{i,j=1}^{n} A(x_i, y_j) \sum_{i,j=1}^{n} B(x'_i, y'_j)}{\sqrt{\sum_{i,j=1}^{n} A(x_i, y_j)^2 \sum_{i,j=1}^{n} B(x'_i, y'_j)^2}} \qquad (0 < r < 1) \qquad (4.1)$$

If the value of r is smaller than a threshold value, the local strain computation is terminated.

In the current thesis project, the commercial digital image correlation system ARAMIS ®was employed to characterize the constitutive behavior of diffusion bonded hole-free materials. To provide a good contrast for the hole-free diffusion bonded tensile specimens, black ink was sprayed on their surface. This random speckle pattern formed by the black ink is used for strain mapping. The detail of this technique can be found in Aramis (2001).

Table 4.2: Etching procedures for each material.

Sample	Etchant	Time
Copper and Glidcop	20 ml NH_4OH + 38 ml water + 2 ml H_2O_2.	1 minute
Brass	12.5 g $FeCl_3$ + 10 ml HCl + 50 ml H_2O	10 seconds

4.2.1 Characterization result of hole-free materials

Prior to the results of in-situ tomography experiments during tensile deformation, it is useful for us to know the differences both in the microstructure and the mechanical properties between the following three: the bulk materials, the diffusion bonded model materials and the hole-free diffusion bonded materials. The differences between pure copper, Glidcop and brass are also of interest. This section presents the microstructural cross sectional views of diffusion bonded materials made of the three different materials. Furthermore, the stress-strain curves and the fractographs for both the diffusion bonded and the bulky materials made of the three materials will be exhibited. The etching procedures for the metallography are summarized in Table 4.2

Pure Copper

The cross sectional micrograph by optical microscopy of the diffusion bonded materials is shown in Figure 4.10. Due to the high purity of the material and the high bonding temperature, the grain size observed was found to be comparable with the material thickness (i.e. several mm). It is seen that the grain boundaries and annealed twins are running across the inter-layer boundaries, which suggests the good quality of bonding. A tensile test coupled with ARAMIS strain mapping system were performed, and the SEM fractograph

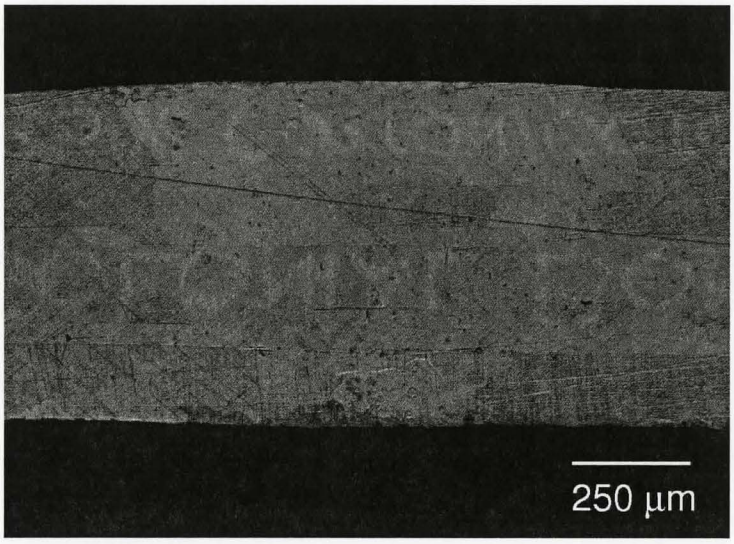

Figure 4.10: The cross sectional view of the diffusion bonded hole-free pure Cu material by optical microscopy.

of the fractured sample and the obtained local stress-strain curve by ARAMIS are shown in Figures 4.11 and 4.13 , respectively. A snap shot of the strain map right before the complete fracture is shown in Figure 4.12. The local strain data was captured from the region near the fracture surface. These SEM and the optical micrograph suggest quite good bonding except for a minor delamination seen in the SEM fractograph. This stress-strain curve will be later used as an input for the FE simulations.

Glidcop

The cross sectional view of the diffusion bonded material was observed by optical microscopy, and the dispersed Al_2O_3 nano particles in Glidcop samples were observed by TEM (Figure 4.14). The TEM foil was prepared by ion milling. Within the range of the observation, the size of Al_2O_3 were about 5$\sim$20 nm. The grain size was much smaller than that of pure copper materials,

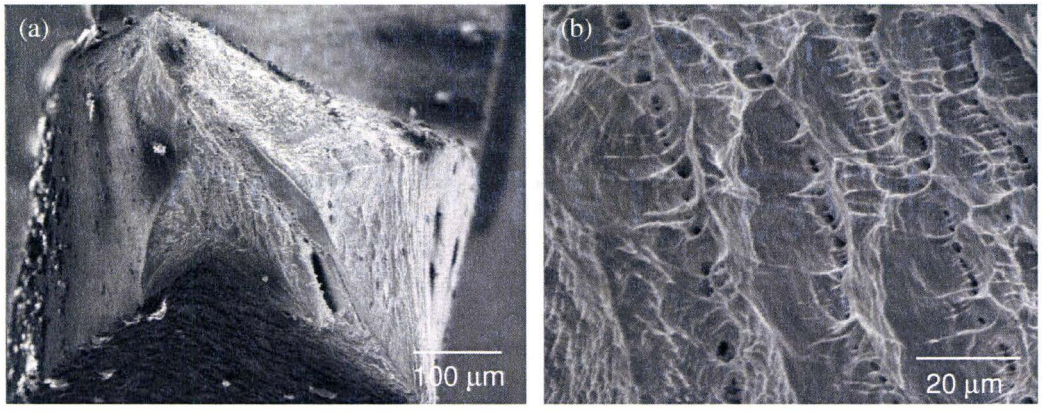

Figure 4.11: The fractograph of the diffusion bonded hole-free pure Cu material. (a) the entire image (b) a close-up.

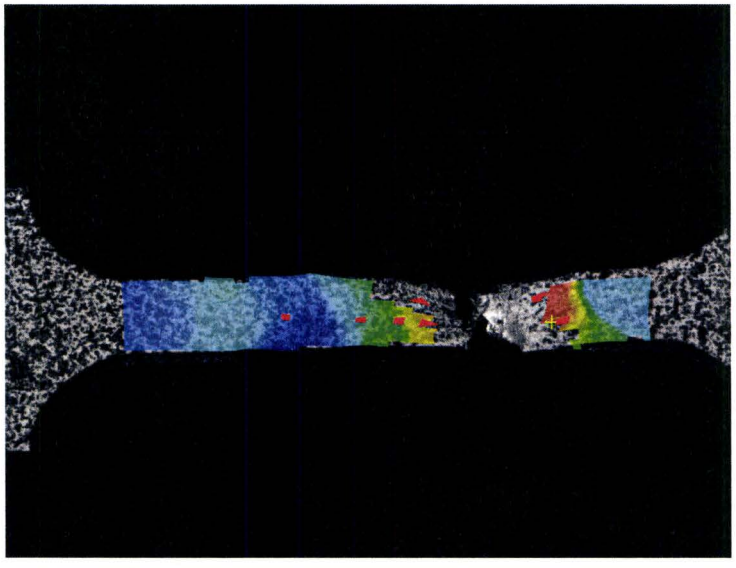

Figure 4.12: A typical strain mapping image of the diffusion bonded hole-free pure Cu material by ARAMIS system. Image is in color in the electronical file.

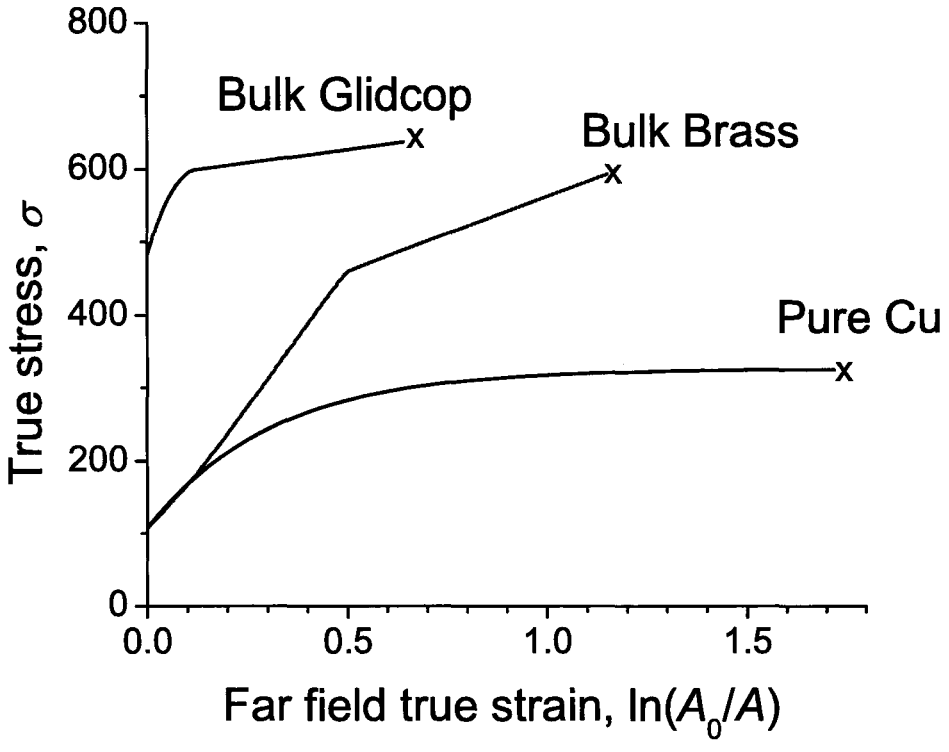

Figure 4.13: The true stress-true strain curves for the diffusion bonded hole-free pure Cu material, bulk glidcop and bulk brass material. The curve for pure Cu is from ARAMIS, and the others are simply from the read out of the tensile machine (Instron 5555).

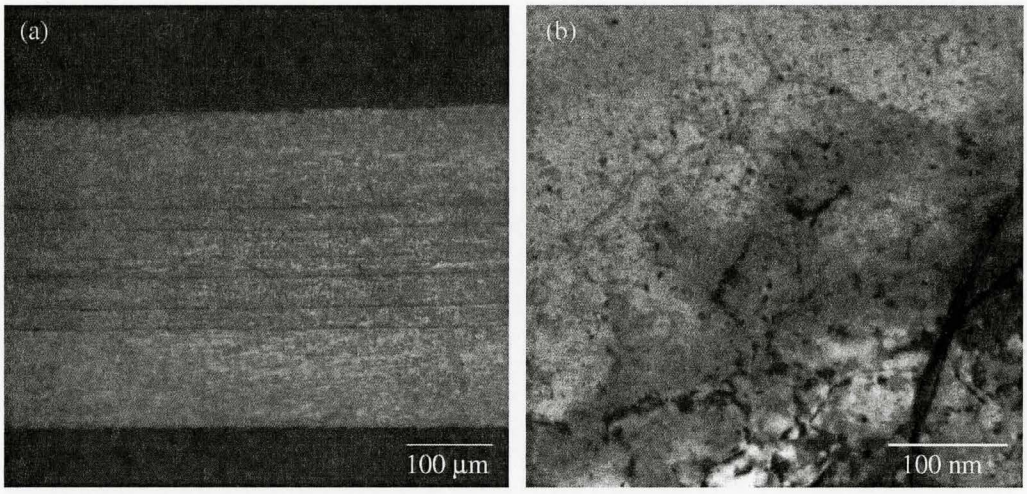

Figure 4.14: The microstructure of the diffusion bonded Glidcop material. (a)The optical micrograph. (b) TEM bright field image showing a dislocation bowing at Al_2O_3 particles.

probably due to the Zener drag effect of the particles during the recrystallization process (Hunphreys and Hatherly, 1995). A tensile test of a bulk Glidcop material after annealing at 930°C for 45 minutes (i.e. the same as the diffusion bonding) was performed, and its result is shown with the result of the diffusion bonded pure copper. Although the work hardening behavior seems very similar to the copper, the initial yield strength was about 500 MPa, which is 5 times as high as that of the pure copper. The fractograph is shown in Figure 4.15. A slew of equiaxed dimples (i.e. voids) nucleated from the Al_2O_3 particles in some region while the elongated dimples by the intervention of macroscopic shear were also observed. As observed both in the fractographs and in the stress-strain curves, the fracture strain of the Glidcop sample was significantly smaller than the pure copper.

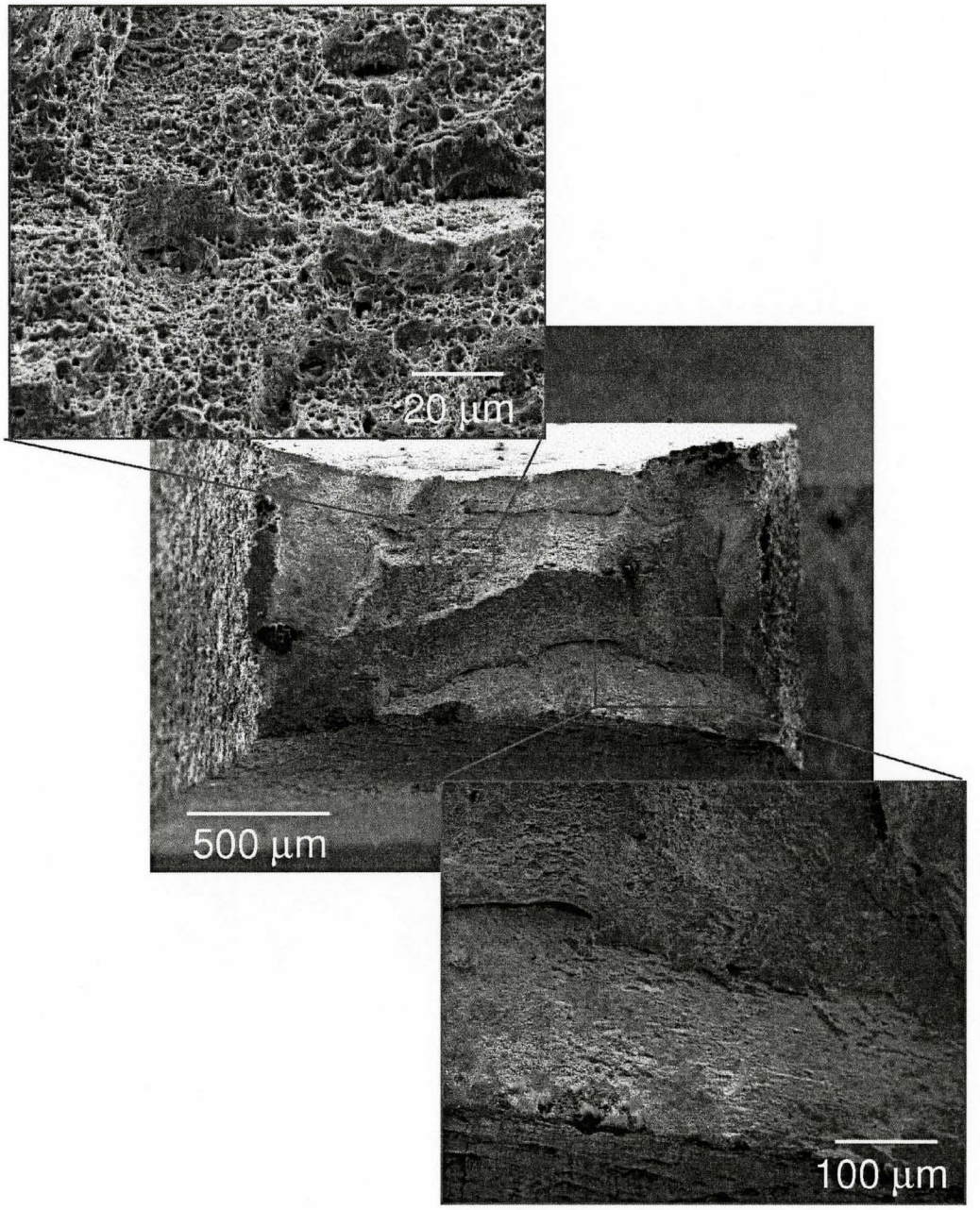

Figure 4.15: The fractographs of the bulk Glidcop sample.

Brass

The bulk brass material after annealing at 860 °C for 45 minutes was also characterized. Figure 4.16 (a) shows the surface morphology of the bulk brass tensile sample, and (b) is the microstructure of the sample. The cross section of the diffusion bonded material is shown in Figure 4.17. The grain size was about the order of the thickness of the sample (i.e. a few mm). The heterogeneous deformation observed in Figure 4.16(a) is considered to be due to these coarse grains. Although the yield strength is about the same as the value in pure copper, the work hardening (especially the slope) is remarkable compared to copper and Glidcop samples probably because of its low stacking fault energy (SFE, SFE_{Cu}=78 mJ/m^2, SFE_{brass}=14 mJ/m^2 (Murr, 1975)) and the deformation twins that might have been introduced during the deformation. The point at which necking initiates and the fracture point was linearly interpolated and thus the curve is kinking when the engineering stress hits the maximum. The fracture strain was smaller than that of pure copper but much larger than that of Glidcop. Dimples that were originated from impurities were observed (Figure 4.18), but the number of those is small compared with the Glidcop sample (Figure 4.15).

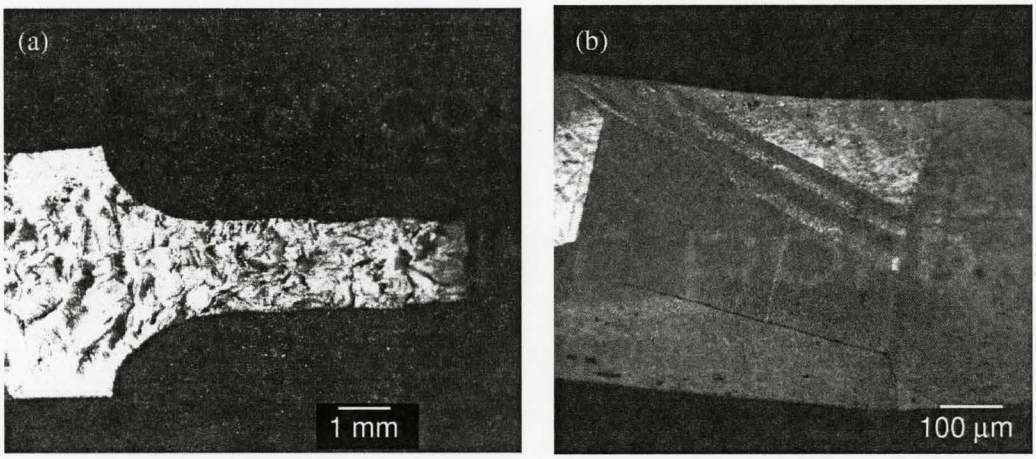

Figure 4.16: (a)The surface morphology of a brass tensile specimen. (b)The cross sectional view of the bulk brass sample by optical microscopy.

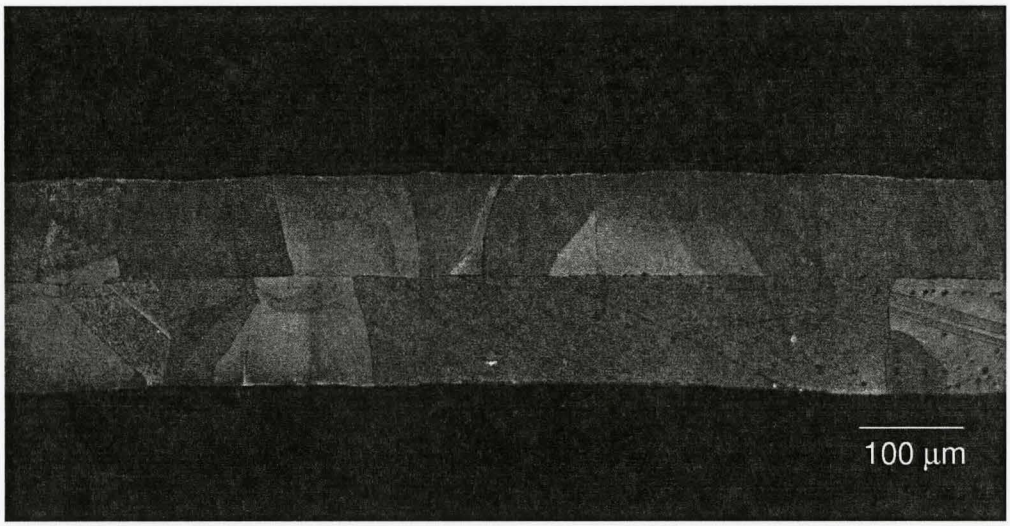

Figure 4.17: The cross section of the brass diffusion bonded material.

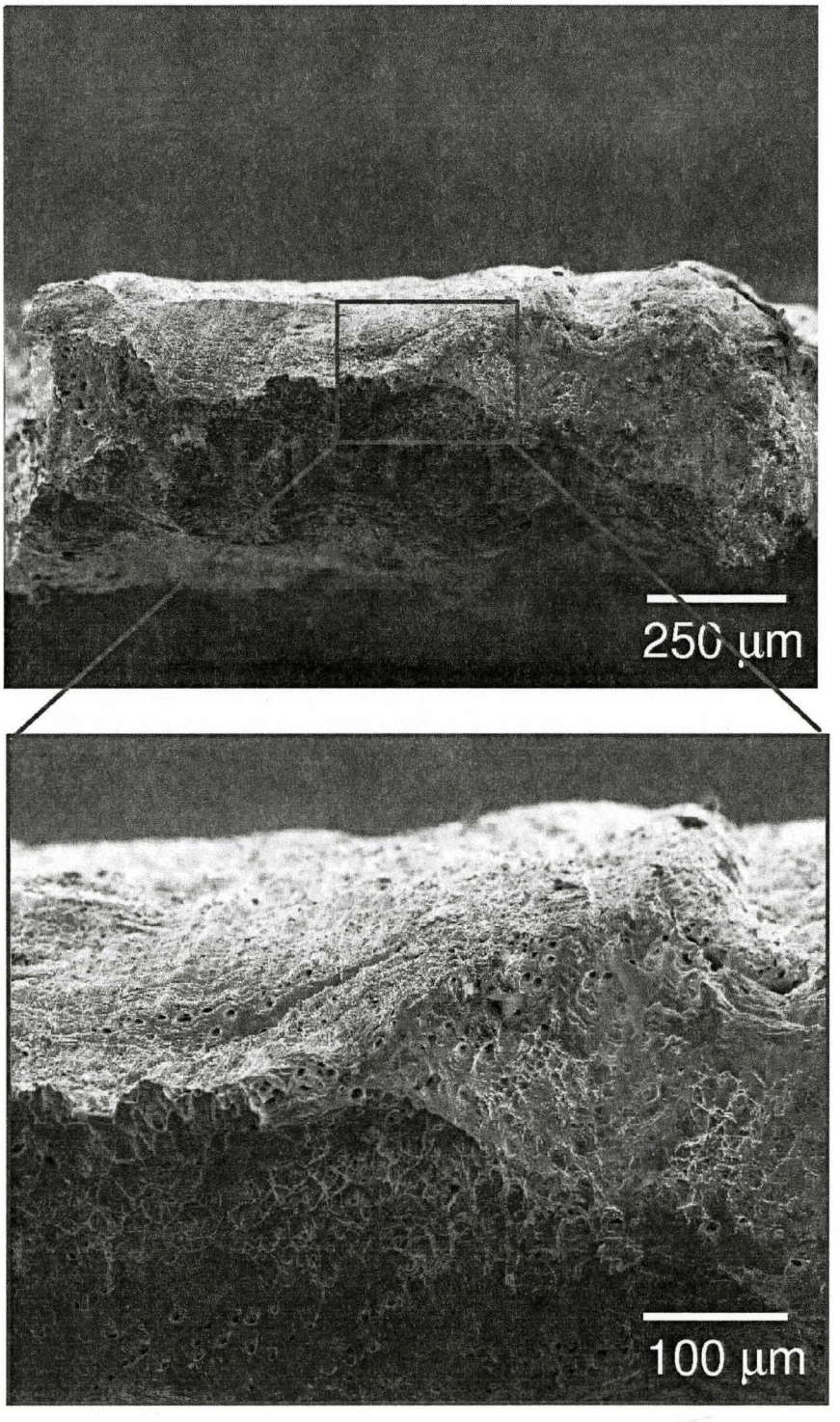

Figure 4.18: The fractographs of the bulk brass sample.

4.3 Experimental set-ups at synchrotron radiation facilities

The model materials fabricated via the method explained in the previous sections are subjected to in-situ X-ray computed tomography coupled with tensile deformation at the beamlines of ESRF or SPring-8. In the current thesis project, two beamlines were adopted namely, ESRF ID15 and SPring-8 BL20XU. This section presents the set-ups of these beamlines in detail.

4.3.1 ESRF ID15

"ID" of ID15 is an abbreviation for "Insertion Device", so that we can easily know that the X-rays at this beamline are generated by an insertion device. The beamline set-up for in-situ tensile testing is illustrated in Figure 4.19. This white X-ray beamline provides the strongest and the most brilliant light in the world, and thus it is adequate for the tomography experiments of copper. The combination of this brilliant strong beamline with the CCD camera called DALSTAR 1M60 in binning mode significantly reduces the readout time. A typical tomographic scan, which takes 20 $\sim$ 30 minutes at ESRF ID19 or SPring-8 BL20XU, takes only 3 minutes at this beamline. The readout time of DALSTAR 1M60 is 9 ms (i.e. 110 frames/s) in binning mode and 17 ms (60 frams/s) in normal model. This fast readout time is achieved in such a way that the camera is equipped with 2 CCDs for every single pixel of 1024 x 1024, which allows an exposure process for a new image to begin while an old image is being read. The pixel size of the CCD is 14 μm, yet the image pixel size can go down to 1.59 μm through 9x optics as shown in Figure 4.20.

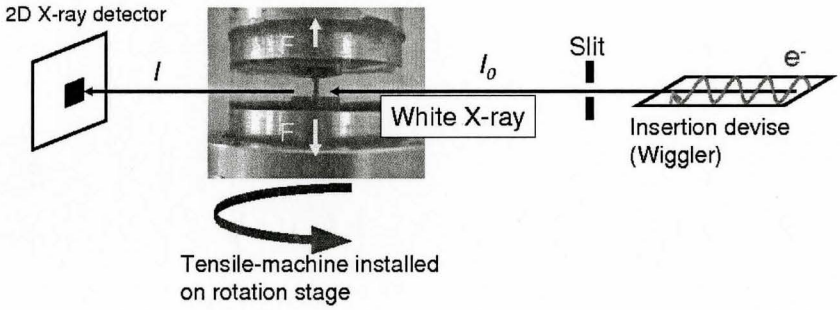

Figure 4.19: The set-up of ID15 at ESRF

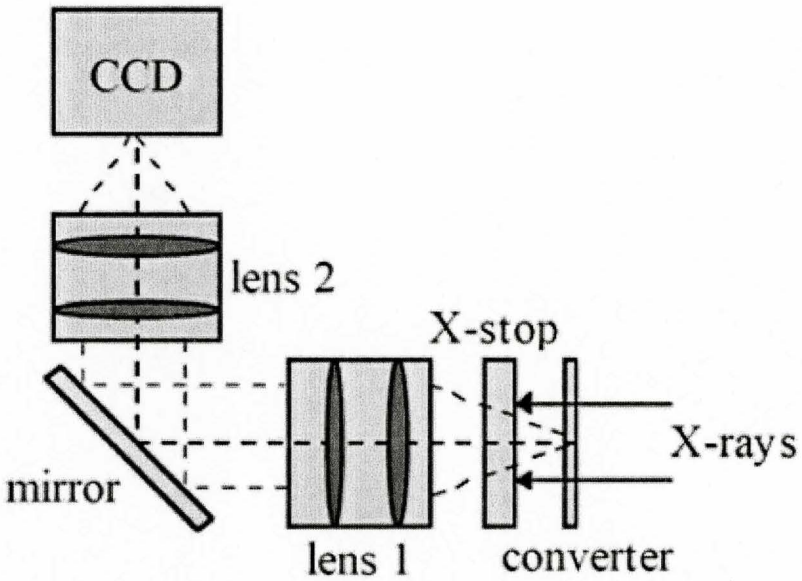

Figure 4.20: A typical set-up for synchrotron radiation detector. (Cloetens, 1999) The converted visible light are magnified and change the pixel size to 1.59 μm.

4.3.2 SPring-8 BL20XU

BL20XU is an abbreviation for "Beam Line 20 with X-ray Undulator" according to the website of SPring-8. This beamline provides a highly coherent monochromatic X-ray from an undulator with excellent brilliance at the energy range or 7.62 $\sim$ 113 keV, and thus it allows tomography experiments at a very good spatial resolution ($\sim$ 1 μm). The monochromator consists of double Si (111) or (511) crystals. The former covers the relatively lower energy range while the latter covers the higher one. This beamline has two hutches in which the first hutch is located at 80 m from the source, and the second hutch is located at 245 m. The experiments for the current thesis work was performed at the second hutch, which is in another building outside the storage ring building. The problem is that most of photons are lost at the monochromator such that the brilliance (or flux if we assume a parallel beam) becomes quite low. This deteriorates the contrast of radiography especially for the materials with a higher atomic number Z such as copper based materials. This problem however can be compensated for by reducing the sample thickness. For the current case, the thickness of diffusion bonded model materials was set to 200 μm. It would be extremely difficult to perform tomography for copper based materials that are much thicker than this value. The pixel size of the high resolution X-ray camera can be controlled by the optical system, ranging from 0.3 μm $\sim$ 2 μm. Since the theoretical spatial resolution is considered to be worse than the wavelength of the light from the fluorescence screen (i.e. green light $\lambda \sim$ 800 nm), the pixel size was set to be 0.48 μm for the best compromise between the largest field of view and the smallest pixel size. The beam energy was set to 37 keV with Si (111) monochromator that

yields the best compromise between the highest flux and the highest energy. The sample-detector distance was 55 mm. The gap between upper poles and lower poles of the undulator was 10.15 mm.

4.4 Tomographic Reconstruction and Visualization

The image reconstruction and the 3D visualization (also called *image rendering*) are two different things. The data we obtain after the tomographic scanning is just a series of radiographs. The 3D tomograms are reconstructed through the algorithms explained in section 2.2. The image reconstruction codes (typically written in MATLAB, C++ or FORTRAN) were provided at each beamline. The information contained in these reconstructed data only tells us which pixel has what value of grayscale ranging from 0 to 255. The process to obtain this type of data from a series of radiographs is called *reconstruction.* Visualization is another process to visualize the more graphical 3D volume from the reconstructed data. Then, a certain region with a certain values of grayscale is "labeled" as an arbitrary material (e.g. matrix, void, inclusion, exterior, etc.). These visualization processes are performed by a commercial software Avizo ®. This software enabled users to render the 3D volume based on the labeling information.

4.5 Finite Element Modeling

Finite element modeling was performed to address some of the questions that arose from the analysis of experiments. The problems tackled are specified

in the appropriate sections, yet the computation environment is summarized here. The finite element modeling in this thesis project was performed by the general purpose finite element software ABAQUS. It is worth emphasizing that this thesis does NOT rely on the element deletion technique or nonlocal damage approach employed by Weck et al. (2007b). In absence of secondary void population, the intervoid matrix is considered to follow the simple J_2 plasticity. The hardware used for the simulations consisted of a PC with two CPUs of Intel ®Core i7 with quad cores (i.e. 8 processors in total) and 11.9 GB RAM.

Chapter 5

Onset of Void Coalescence

5.1 Coalescence vs. Linkage

In this chapter, the experimental data for the onset of void coalescence studied by X-ray tomography is presented, focusing on the results of the smooth specimens made of pure copper tested at ESRF ID15. It is worth emphasizing that the coalescence process is defined here as being distinguished from simple linkage. *Coalescence and Linkage are two different phenomena.* Let us consider a pair of voids as illustrated in Figure 5.1. As the tensile deformation is applied along the vertical direction, the two voids would start growing along the tensile direction, while the voids would shrink laterally, as suggested by the Rice and Tracey model. However, it is inevitable that lateral void shrinkage is terminated at some point of the deformation, followed by the lateral expansion of the voids. Without this, voids would never get linked to each other. In this chapter, therefore, we shall define void coalescence as the process that occurs from the onset of lateral void expansion to the point of the void linkage. This is quite important in comparing the experimental results on void coalescence

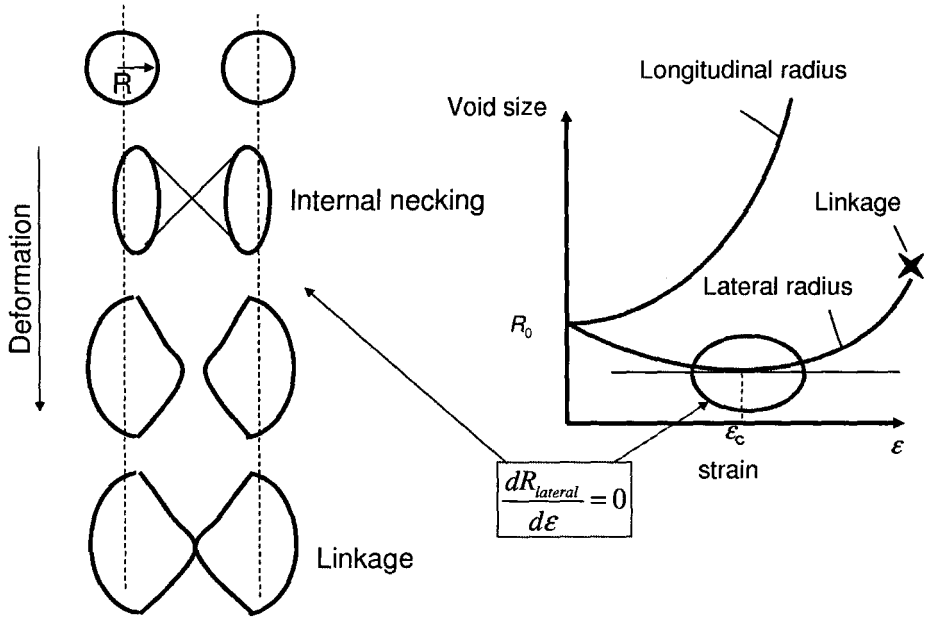

Figure 5.1: Schematic illustration of void coalescence occurring in a void pair by tensile deformation. Voids shrink laterally in the beginning of the deformation, but they have to start expanding to get linked.

with the existing models, since the models are usually designed to predict the onset of coalescence instead of linkage. As we will see however, the experimental determination of the onset of coalescence is rather more difficult than the observation of linkage events.

5.2 Samples discussed in this chapter

Attention is paid to the two model materials with the void array shown in Figure 5.2, referred to as the FCC 1 and the FCC 2 materials, respectively. The both have a FCC type void array but the "crystallographic" orientations with respect to the tensile axis are different. If we use the Miller index to represent the orientation of void array for the sake of convenience, the FCC 1 material

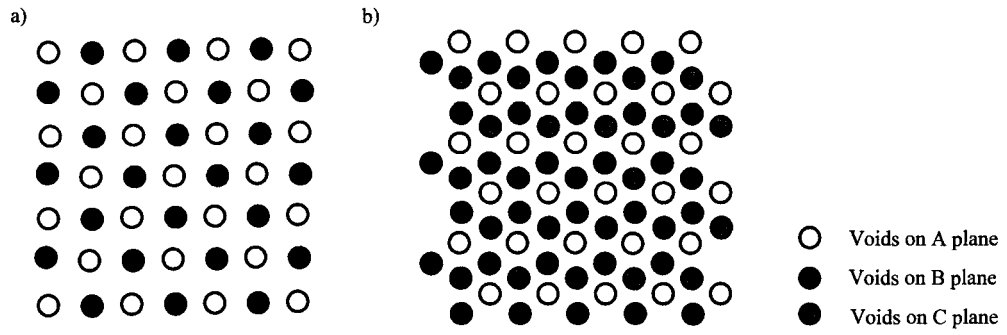

Figure 5.2: Schematic illustrations of the three dimensional void array in (a)FCC 1 (b)FCC 2. The tensile loading is applied vertically.

Table 5.1: The features on each model material.

Model materials	Stacking order	Remarks
FCC 1	ABABA	FCC type hole array Tensile axis $\parallel < 001 >_{array}$ Maximum shear plane $\parallel \{110\}_{array}$
FCC 2	ABCBA	FCC type hole array Tensile axis $\parallel < 112 >_{array}$ Inter-layer boundary $\parallel \{111\}_{array}$

contains the void array in such a way that the $(111)_{array}$ plane is parallel to the maximum shear plane (i.e. 45° from the principal stress directions), while the FCC 2 material contains the array with inter-layer boundaries parallel to the $(111)_{array}$ plane and $< 112 >_{array}$ is parallel to the tensile axis. The detailed information is summarized in Table 5.1. A hole-free diffusion bonded material is also prepared to see the difference in mechanical behavior from that the model materials with holes.

5.3 Experimental procedures

The diffusion bonded samples described in the last section were first machined to a typical dog-bone tensile specimen. The gauge length was 11 mm, the cross sectional area is a rectangular shape of 1 mm $\times$ 1 mm. This is the maximum acceptable thickness to record an image by radiography, which is determined due to the X-ray absorption issue of copper (section 2.2). Any smaller size would make it difficult to handle the samples. The machined tensile samples were then subjected to in-situ tensile testing coupled with the X-ray computed tomography at ESRF ID15. The tensile tests were carried out at room temperature in air. The crosshead speed was set to 5.0×10^{-6} ms^{-1} at the beginning of the deformation, and then decreased to 2.0×10^{-6} ms^{-1} once the slope of the load-displacement curve started saturating, so as to capture the necking process in detail. At this beamline, white X-rays with high energy and high flux are available so that we can obtain good mass-thickness contrast for materials with high absorption coefficients and relatively large sample dimensions. During tensile testing, continuous tomography was also performed. In continuous tomography, tomographic scans are performed continuously while the sample is being pulled non-stop in tension. In doing continuous tomography, some technique to accelerate the read out time is required. In ordinary slow tomographic scanning at ID15, the total time required for a single scan is about 3 minutes. In order to perform continuous tomography, however, the total time for scanning has to be reduced further. In the current case, the number of radiographs was reduced to 500 and each radiograph taken was binned (i.e. a group of 2 x 2 pixels = 4 pixels is re-sized to a single pixel). The total time required for each scan by this technique was approximately 20

seconds. Continuous tomography is able to capture the moment just where the first void coalescence occurs as well as the microstructure before and after void coalescence. Continuous tomography was typically started as soon as the load monitored approached the maximum (i.e. when macroscopic necking initiates). Once the continuous tomography started, the crosshead speed was kept constant at 1.0×10^{-7} ms^{-1}, and the true strain rate $\dot{\varepsilon}$ is estimated as 2.31×10^{-4} s^{-1}. The tomograms for this data set were reconstructed based on a series of radiographs using the supercomputer NICE at ESRF. The visualization was performed with a commercial software Avizo ®.

5.4 Constitutive behavior

The true stress-strain curves for the model materials are plotted in Figure 5.3. True stress and true strain were estimated from the following equations.

$$\sigma = \frac{F}{A} \tag{5.1}$$

$$\varepsilon = \ln\left(\frac{A_0}{A}\right) \tag{5.2}$$

where F is the applied load, A_0 the initial cross-sectional area of the ligament, A the current cross-sectional area which can be directly measured from the tomograms by the visualization software. Since the measured data of cross-sectional area is sporadic due to the limited number of the measured values of current cross-sectional area, the data points were interpolated by the Voce's

Table 5.2: The parameters for the Voce fitting

	C_1	C_2	C_3
Hole free Cu	286.8	181.3	3.53
FCC 1	326.2	218.5	3.23
FCC 2	255.8	156.5	4.80

law which is defined as

$$\sigma = C_1 - C_2 \exp(-C_3\varepsilon) \tag{5.3}$$

and its derivative is

$$\frac{d\sigma}{d\varepsilon} = C_2 C_3 \exp(-C_3\varepsilon) \tag{5.4}$$

where C_1, C_2 and C_3 are the arbitrary fitting parameters. The consequent fitting parameters C_1, C_2 and C_3 for the current model materials and the hole-free diffusion bonded material are summarized in the Table 5.2.

The derivatives of the fitting curves $\frac{d\sigma}{d\varepsilon}$ are also plotted in order to estimate the necking strains ε_n, based on so-called the Considère criterion (i.e. the intersections of the true stress-true strain curve and its derivative), which is given by

$$\frac{d\sigma}{d\varepsilon} = \sigma \tag{5.5}$$

The necking strains will be later used in fitting the results of principal radii with the Rice and Tracey model. The failure strain is represented by x in Figure 5.3. The failure strains in this case were estimated by a free software Image J from the cross-sectional area of SEM fractography as shown in Figure 5.4 instead of using tomograms because the failure strain estimated from the tomogram would be the strain at the tip of chisel points that could be infinite.

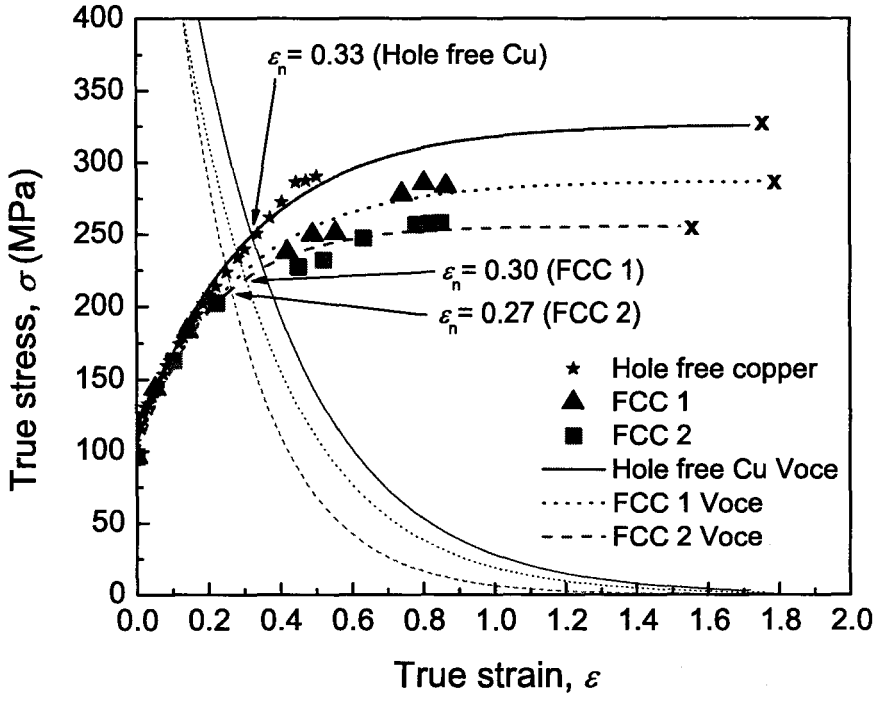

Figure 5.3: True stress-true strain curves(thicker lines)for the model materials. The evolution of their derivatives are also plotted (thinner lines).

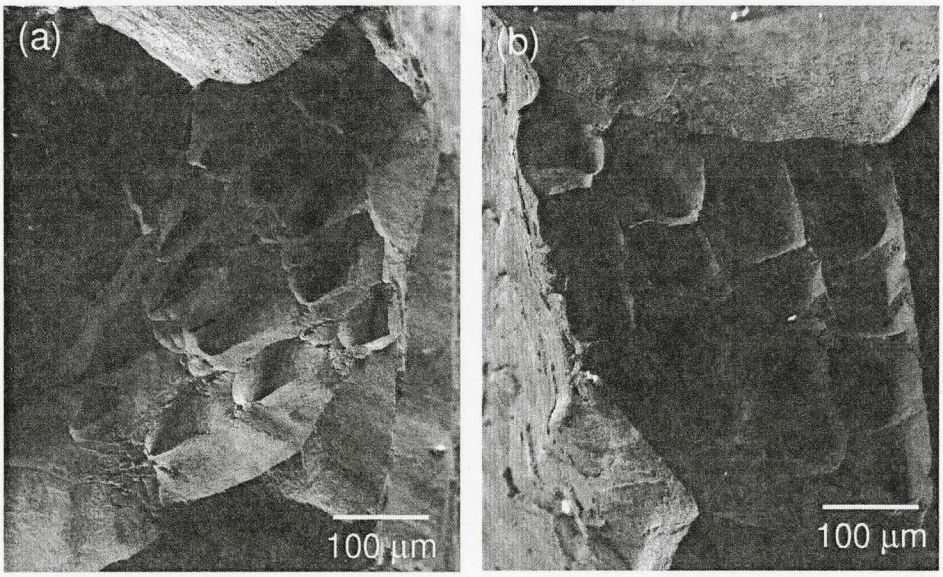

Figure 5.4: SEM fractographs for the model materials.(a)FCC 1(b)FCC 2

5.5 Reconstructed images

5.5.1 Assessment of the spatial resolution

The spatial resolution of the current X-ray tomography setup was estimated from a slice of the reconstructed image in the following way. As shown in Figure 5.5 (b), the line profile of the grayscale was obtained using the software Image J along the distance that encompasses the matrix/void interface, and then the grayscale was fitted with a sigmoidal function. The derivative of the fitted curve shows a peak at the matrix/void interface and its full width at half maxima (FWHM) is considered as the spatial resolution. The measurement was performed 7 times and the arithmetic mean was taken as the result after the highest and the lowest value were removed, yielding the spatial resolution as 5.39 μm.

As shown in Figure 5.5(a), the initial shape of each hole (which appears dark in the figure) is a tapered cylinder. This tapered shape results from the laser drilling process with the wider end being the entrance of the laser beam..

5.5.2 Assessment of the hole alignment

As discussed in section 4.1.3, the offset of the hole alignment influences the initial intervoid distance. Figure 5.6 and 5.7 shows the reconstructed images of the FCC 1 and the FCC 2 materials being compared with the ideal array. In the figures, red circles in the close-up picture represent the ideal positions of the holes in the first layer. In order to have an ideal FCC type structure, the voids at the second layer have to be lined up as illustrated in Figures 5.6 (b) and 5.7 (b). The second layer of void arrays are quite close to the ideal

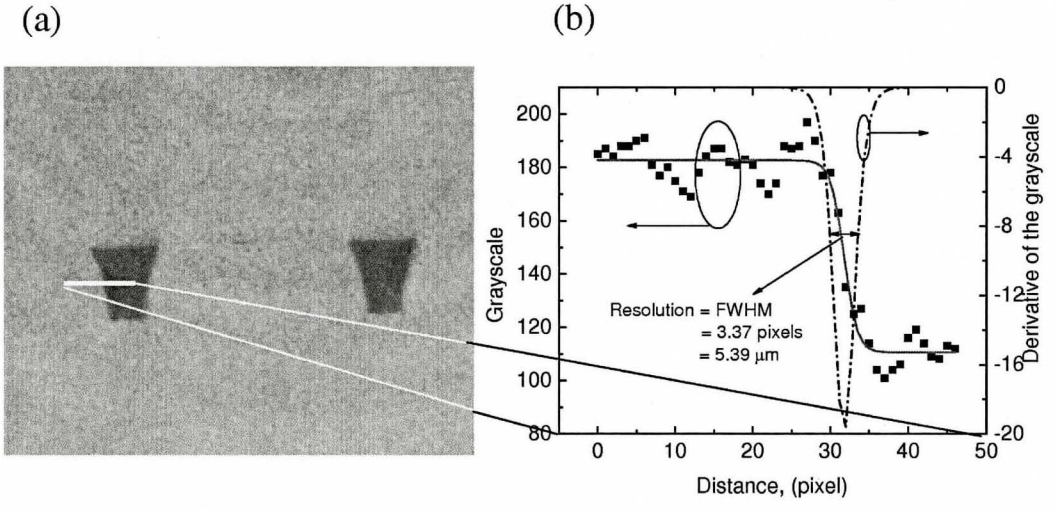

Figure 5.5: The procedure to estimate the spatial resolution of the tomography. (a) The reconstructed image of the cross-sectional view (voids represented by the darker contrast) (b) and the line profile of the grayscale (square dots) along the distance (pixels). The gray scale is fitted with a sigmoidal curve (solid line) and the spatial resolution is estimated from the FWHM of the derivative (dashed line). The pixel size here is 1.6 μm $\times$ 1.6 μm.

positions, yet the alignment is not perfect. Thus, it is expected that the initial intervoid distance of the first void pair that would link up would be smaller than the designed value of 0.141 mm. This will be quantitatively measured and will be used for the analyses in later sections.

5.5.3 Void growth and coalescence behavior

The visualized images of the tomograms containing different void arrays are presented in Figures 5.8 and 5.9. In these tomograms, some transparency is numerically applied to the matrix to make the internal voids visible. The growth and the coalescence of voids are well captured in each set of tomograms. One challenge in interpreting these tomograms is the formation of the free surface and the fracture surface. As soon as the voids contact the free surface, they are considered by the software to be as free surface instead of internal voids. It therefore appears that the voids suddenly disappeared (e.g. see Figure 5.9(d)), but in fact this is not really the case. Beyond the necking strain, the deformation is not homogeneous such that only the voids at the central part tend to elongate longitudinally. The surface also indicates a significant localization is occurring. In the model materials presented here, the fractography in Figure 5.4 and the tomograms here suggest that the failure is due to an internal necking process. Figure 5.9(c) clearly shows the void linkage within the region with the minimum cross-sectional area, and the resultant lateral morphology of the fracture surface by internal necking is well captured in Figure 5.9(d).

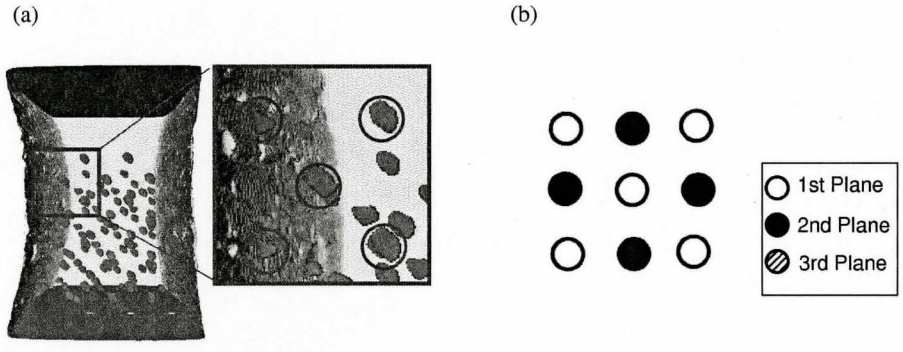

Figure 5.6: (a)3D visualization of the FCC 1 model material at the initial state and (b)the ideal positions of voids. The circles in the close-up pictures are representing the positions of the holes in the first layer.

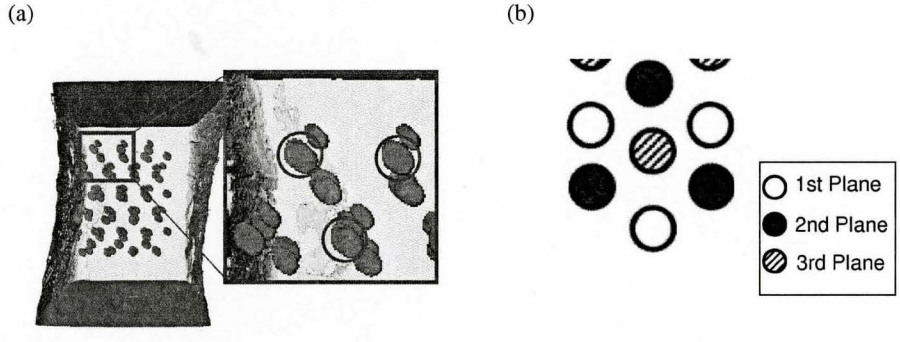

Figure 5.7: 3D visualization of the FCC 2 model material at the initial state and (b)the ideal positions of voids. The circles in the close-up pictures are representing the positions of the holes in the first layer.

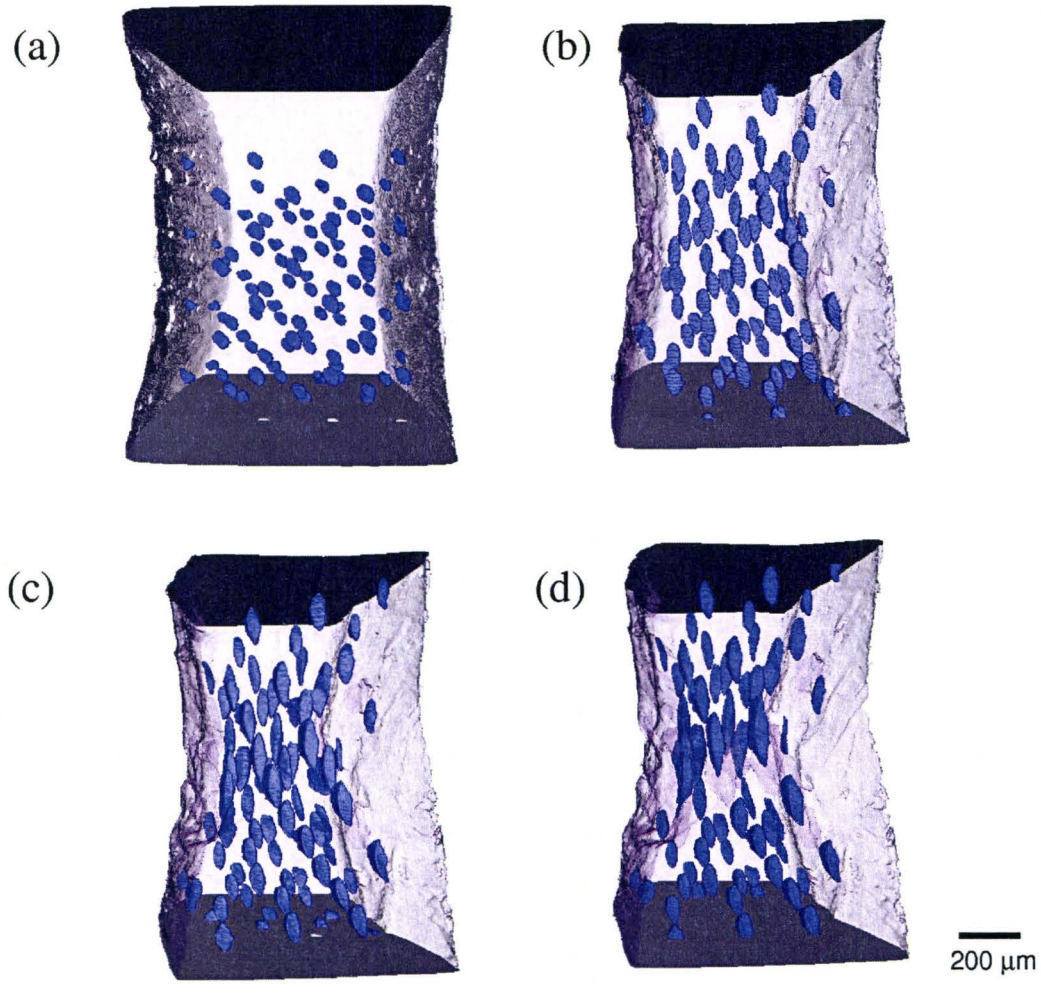

Figure 5.8: 3D visualization of the growing/linking voids in the FCC 1 material. (a) $\varepsilon = 0$ (b) $\varepsilon = 0.44$ (c) $\varepsilon = 0.88$(d) $\varepsilon = 1.20$.

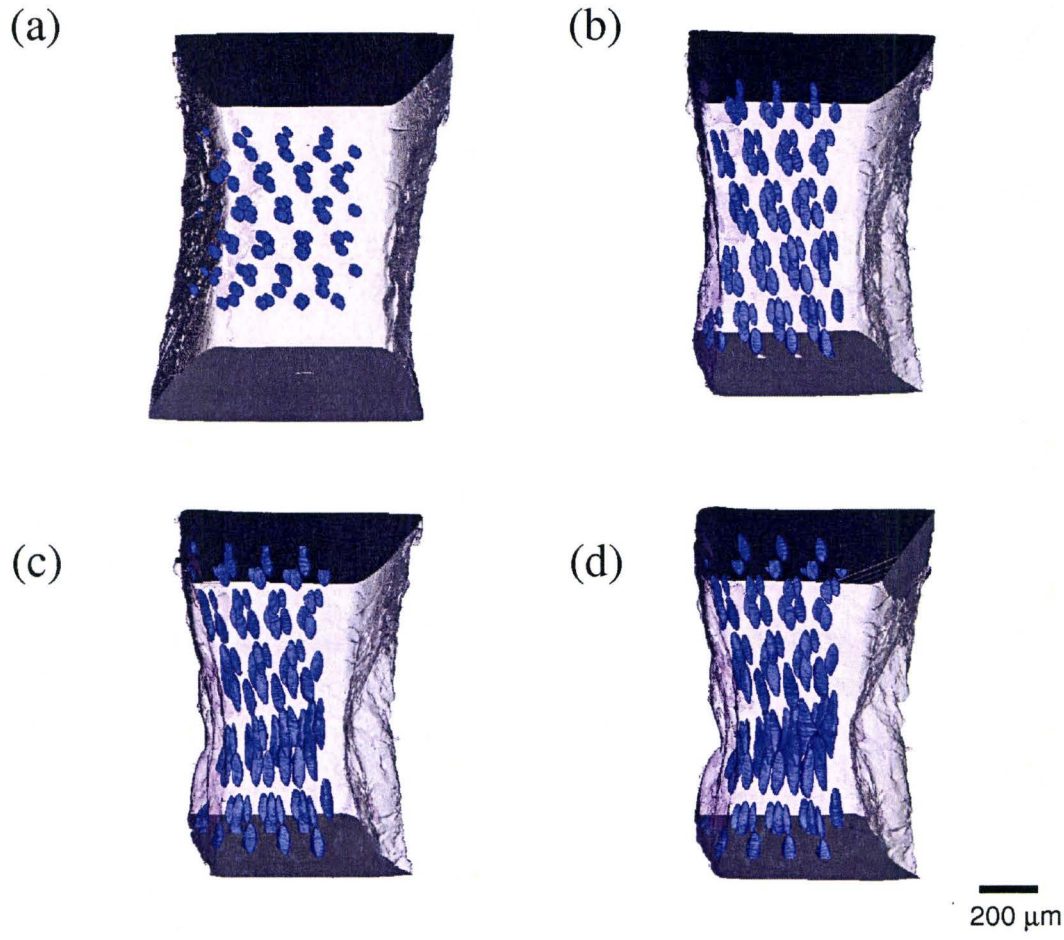

Figure 5.9: 3D visualization of the growing/linking voids in the FCC 2 material. (a) $\varepsilon = 0$ (b) $\varepsilon = 0.52$ (c) $\varepsilon = 0.81$(d) $\varepsilon = 1.01$.

5.6 Quantitative analysis of onset of void coalescence

5.6.1 Collective behaviors of void growth and coalescence

As soon as necking starts, the strain distribution within the model materials in tension becomes non-uniform. This results in a variation of the void size within the sample. By measuring the principal diameters of these voids, one can see the tendency of the growth of the voids both laterally and longitudinally. Attention should be paid to the evolution of the lateral growth as mentioned in section 5.1, because the onset of the lateral growth is an indication of the onset of the void coalescence. In Figure 5.10, the measured values of lateral principal local strain, which is defined by the lateral void growth as $\ln(b/b_0)$ and $\ln(c/c_0)$, are plotted as functions of the major axis local strain $\ln(a/a_0)$. The definition of the direction of the principal radii a, b and c is also shown in Figure 5.10. The lines in this figure represent the well-known Rice and Tracey void growth model as shown in equation (2.17).

Although there is significant scatter, the results for the materials FCC 1 and FCC 2 show that the voids initially shrink laterally, showing some agreement with the Rice and Tracey model, and then started expanding. This tendency can be seen more clearly in the void growth along b axis shown in Figure 5.10(b), which is parallel to the laser drilling direction. This is mainly due to the result that the inter-void distance becomes shorter than the values designed because of the poor hole alignment, as discussed in section 5.5.2. In the result of the FCC 2, it can be seen that the local strain along the b axis

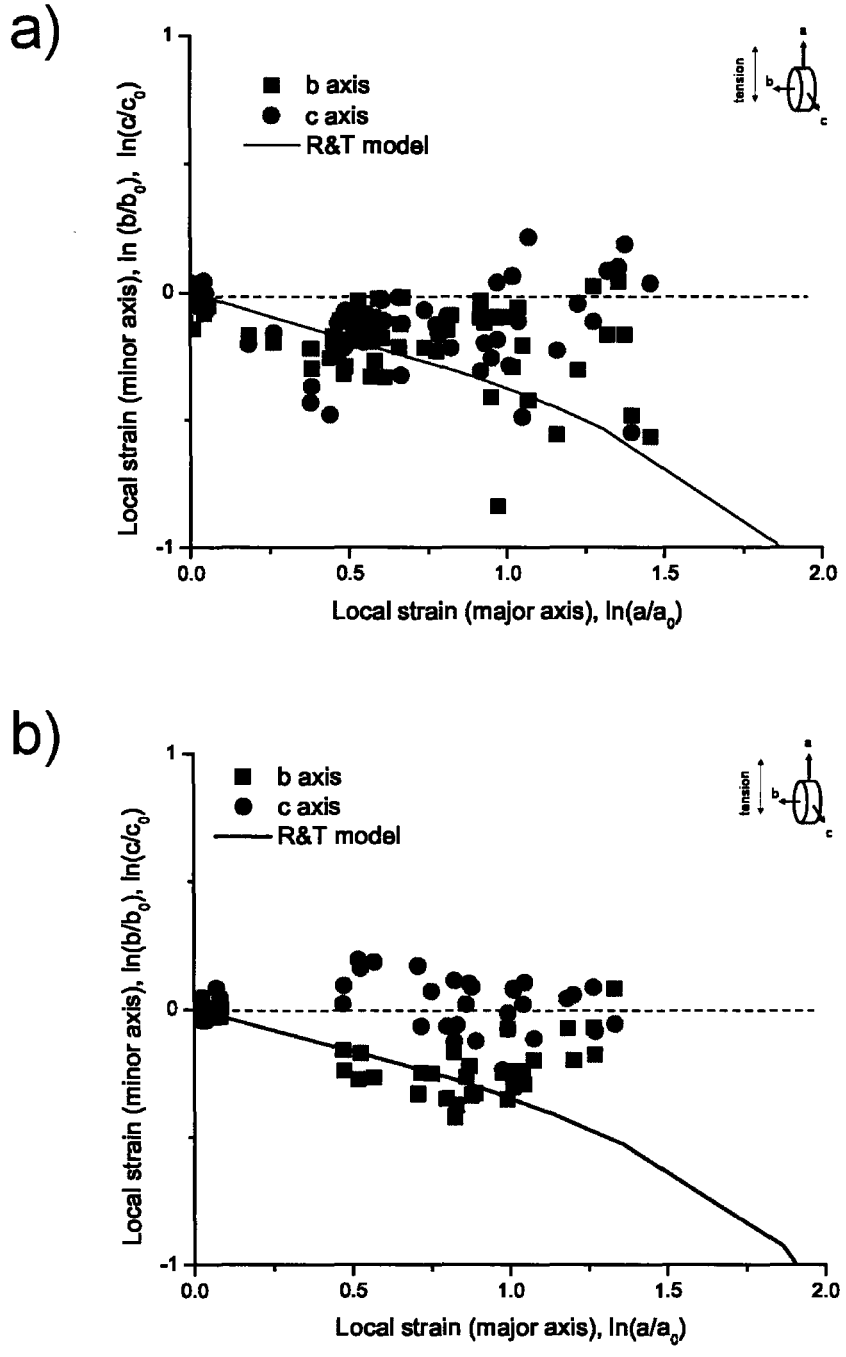

Figure 5.10: Collective void growth behaviors in FCC 1 and FCC 2 model materials.

deviates from the Rice and Tracey model around the longitudinal local strain of 1.0 approximately. Since the Rice and Tracey model is valid until the onset of void coalescence, the value of true strain at the onset of coalescence can be estimated from the values of local strain at around 0.8 for the FCC 2 material.

5.6.2 Void growth and coalescence of the first void pair to link

The previous section revealed collective information on the void growth and coalescence in the model materials. In contrast, this section pays special attentions to the first pair of the voids to exhibit linkage. By virtue of the in situ continuous tomography, it is possible to identify the first pair of the voids to link and observe the behavior of the voids as shown in Figures 5.11 and 5.12. 100% transparency is numerically applied to the matrix to visualize the voids (painted blue). The evolution of the shape and the size of the void as well as their interaction leading to the linkage are well captured. The final linkage occurs evidently through internal necking.

Both the materials show that coalescence and linkage occur along the thickness direction that corresponds to the b-axis. Examining Figure 5.11(e) and 5.12 (e) carefully, one notices that the localized deformation in the FCC 1 is suppressed until the later stage of the macroscopic deformation, while localization and linkage in the FCC 2 clearly starts at a much earlier stage of the macroscopic deformation. This will be quantitatively discussed later.

The measurement of the principal void diameters as well as the intervoid distance $2e$ was carried out using the visualization software Avizo. The volume of the two voids was also extracted from the tomograms using the software, which essentially counts the number of voxels that had been labeled as voids. The obtained values of the principal diameters, the intervoid distance and the volume are plotted as functions of the far field plastic strain in Figures 5.13(a) and 5.14(a). In Figures 5.13(a) and 5.14, natural logarithmic strains (i.e. instantaneous true strain just like true strain of tensile testing) calculated

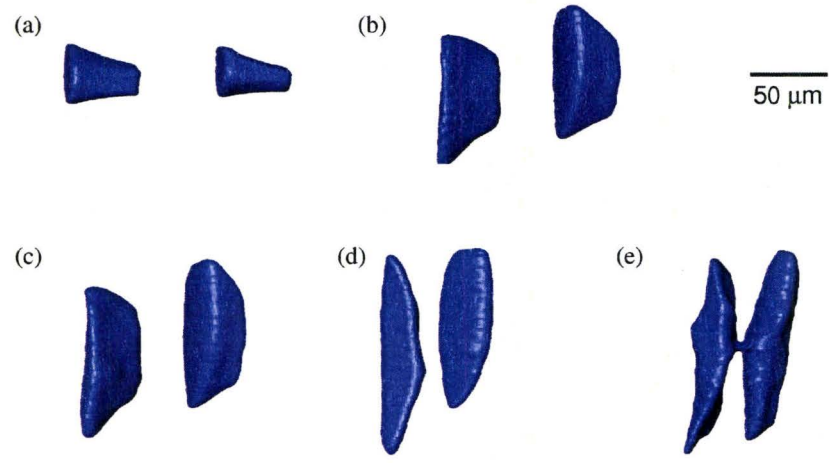

Figure 5.11: The growth and coalescence behavior of the first void pair to link in the FCC 1 model materials. (a) $\varepsilon = 0$ (b) $\varepsilon = 0.44$ (c) $\varepsilon = 0.51$(d) $\varepsilon = 0.61$(e) $\varepsilon = 0.96$

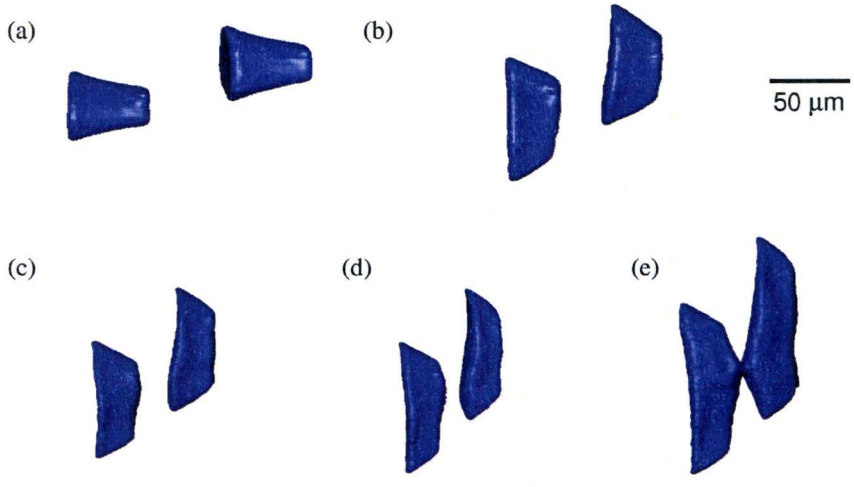

Figure 5.12: The growth and coalescence behavior of the first void pair to link in the FCC 2 model materials.(a) $\varepsilon = 0$ (b) $\varepsilon = 0.44$ (c) $\varepsilon = 0.52$(d) $\varepsilon = 0.64$(e) $\varepsilon = 0.78$

from the measured principal diameters are plotted instead of simple absolute values of radii. The scales of horizontal axes of each graph were made uniform for the comparison. In Figures 5.13(b) and 5.14(b), the absolute values of the two voids and the volumetric strain,

$$\varepsilon_V = \frac{\Delta V}{V}, \tag{5.6}$$

was set as the secondary axis (the right side of the graph), and the normalized distance which is defined by e/e_0 was set for Figures 5.13(c) and 5.14(c).

As expected intuitively, the two voids in each model material grow longitudinally showing reasonable agreement with the Rice and Tracey model while the voids shrink laterally in the beginning but then start increasing as the far field strain increases, deviating from the Rice and Tracey model. There is small difference in void growth behaviors in b-axis and c-axis, which might be due to local plastic anisotropy (i.e. crystallographic orientations). The minimum lateral void dimension was used to define the onset of void coalescence, according to the definition proposed by Koplik and Needleman (1988) which states that the void coalescence is the void enlargement after the transition of the deformation to uniaxial straining. Several authors (Benzerga, 2002; Pardoen, 2006) pointed out that further deformation results in the lateral growth of the voids until the voids link together. In other words, the void volume should increase when the void coalescence in the strict sense occurs. This is nicely illustrated by comparing Figures 5.13(a) and 5.13(b), or Figures 5.14(a) and 5.14(b) where it is clear that when the principal diameters along the b and the c axes start deviating from the Rice and Tracey model around

$\varepsilon_{coalescence} = 0.76$, in the case of the FCC 1 material. This is considered as the onset of void coalescence, which is clearly different from the linkage strain $\varepsilon_{linkage} = 0.96$, which is the point at which the intervoid distance becomes zero (Figure 5.13(c)). Similarly, $\varepsilon_{linkage} = 0.52$ and $\varepsilon_{coalescence} = 0.85$ are obtained for the FCC 2 material from Figure 5.14(a). The volume of the two voids accordingly increases whereas the intervoid distance decreases all the way to the void linkage. The prediction of the volumetric growth by the Rice and Tracey model seems unsuccessful in both the model materials within the range of the observation.

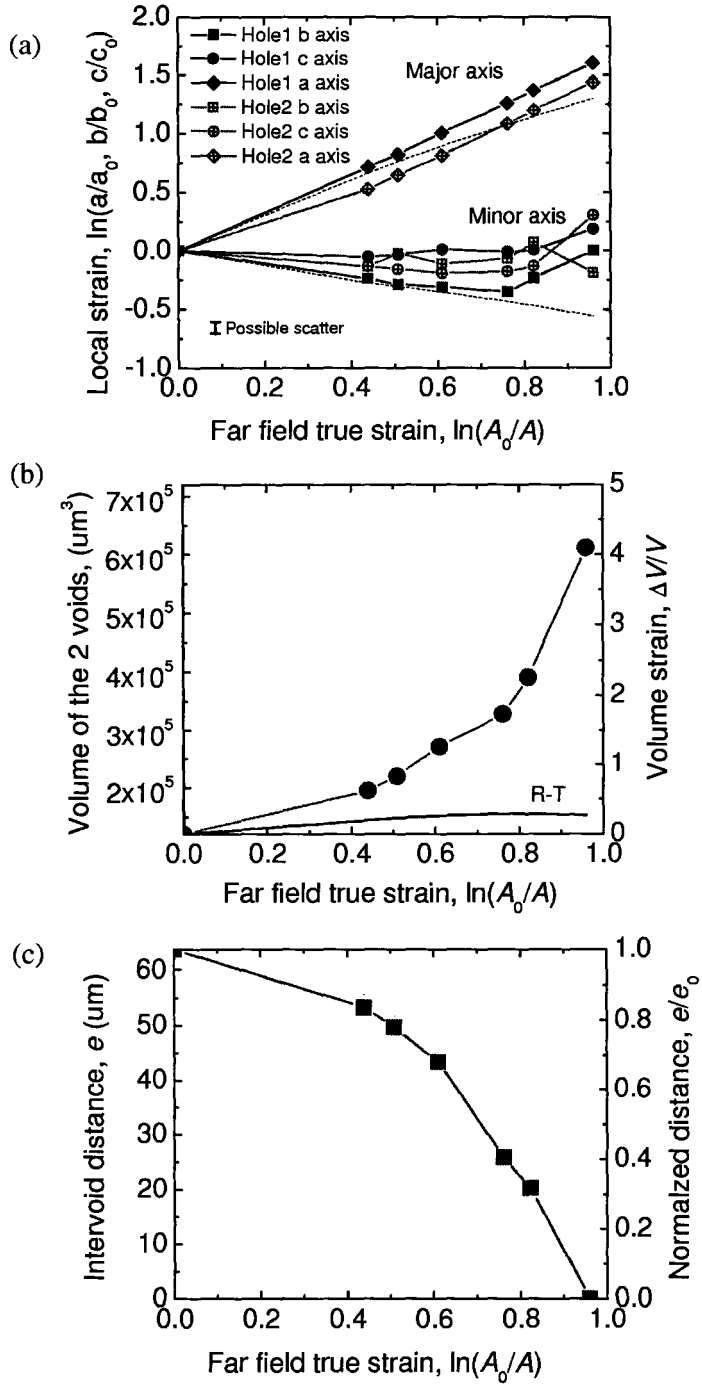

Figure 5.13: Various parameters representing void growth behavior plotted as a function of the far field plastic strain in the FCC 1 material. (a) Evolution of the local strain. (b) Evolution of the void volume. (c) Evolution of the intervoid distance.

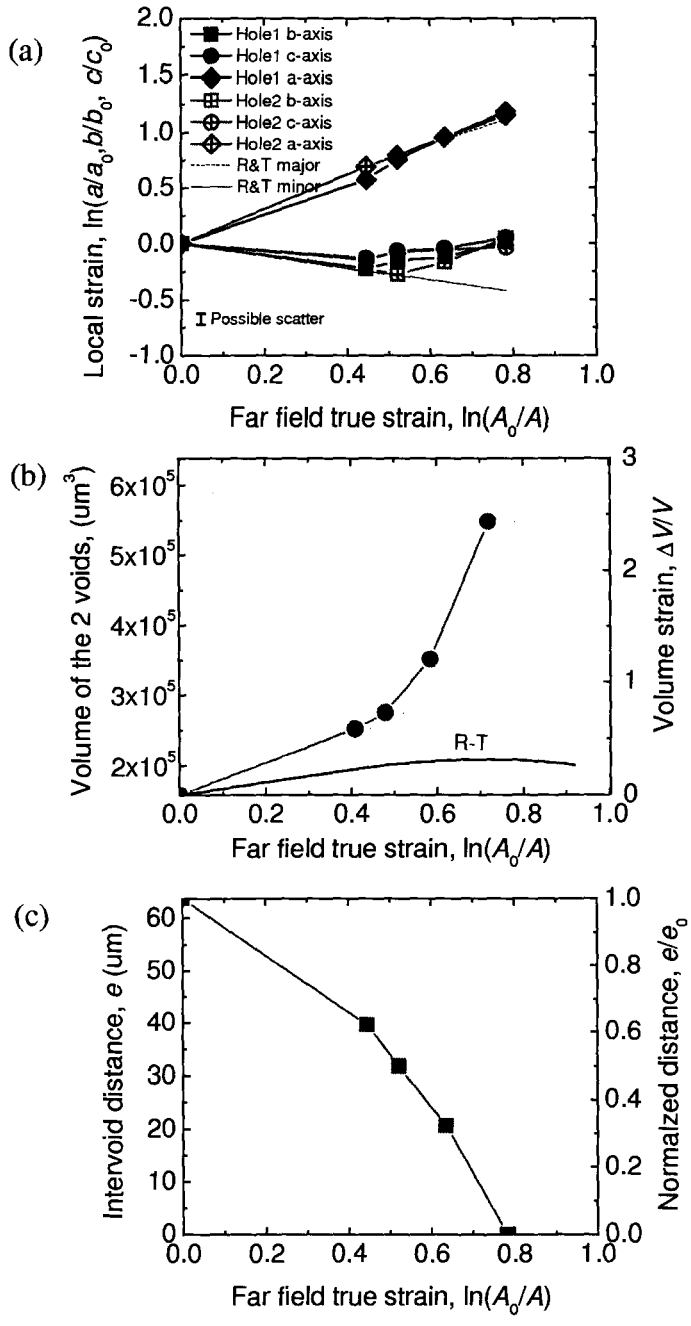

Figure 5.14: Various parameters representing void growth behavior plotted as a function of the far field plastic strain in the FCC 2 material. (a) Evolution of the local strain. (b) Evolution of the void volume. (c) Evolution of the intervoid distance.

5.6.3 Post-linkage stage

Once void coalescence starts leading to linkage at the first void pair, this void pair keeps linking with the neighboring voids and eventually forms a fracture surface. Although there is not much that we can investigate quantitatively, this set of experiments reveals the morphologies and linking-up processes of the voids pictorially as shown in Figures 5.15 to 5.18. Close examination of Figures 5.15(a) and 5.16(a), which present the exterior of the model materials, reveals the coarse surface steps due to the macroscopic shear banding that develops by the time the multiple voids have linked up.

From a comparison between Figures 5.17 and 5.18, one can infer why the FCC 1 model material was slightly more ductile than the FCC 2 material. In the FCC 1 model material, the linked voids merged with the free surface so that the further void linkage was prevented, and the subsequent fracture process proceeded in a relatively stable manner. In the FCC 2 model material, however, the linked voids did not merge with the free surface until a later stage of the fracture process, as seen in Figure 5.18. Furthermore, as confirmed in last section, the first void linkage was faster in the FCC 2 material due to the local shear coalescence. It is thought that this shear coalescence also contributed to the acceleration of the fracture process.

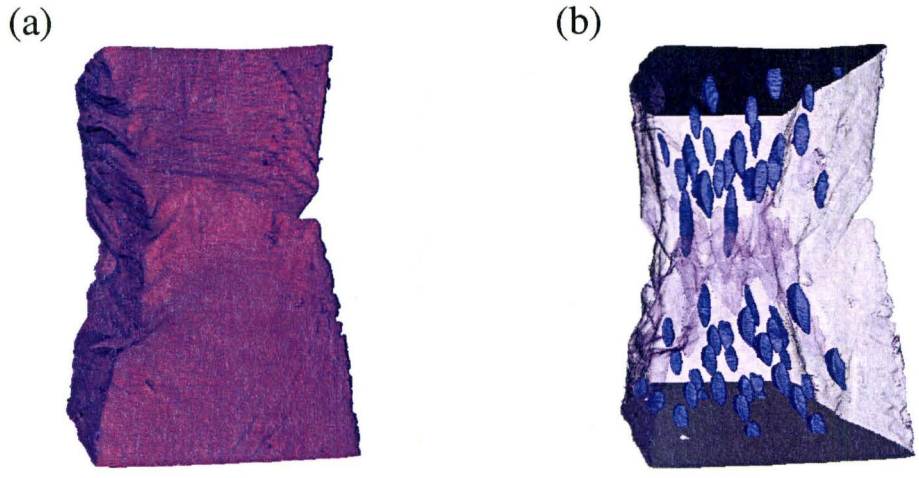

Figure 5.15: (a) The exterior of the FCC 1 material after multiple void linkage and (b) its internal structure. $\varepsilon = 1.02$. Only the voids embedded are painted blue. The linked voids have already merged with the free surface and thus they are not painted in this figure.

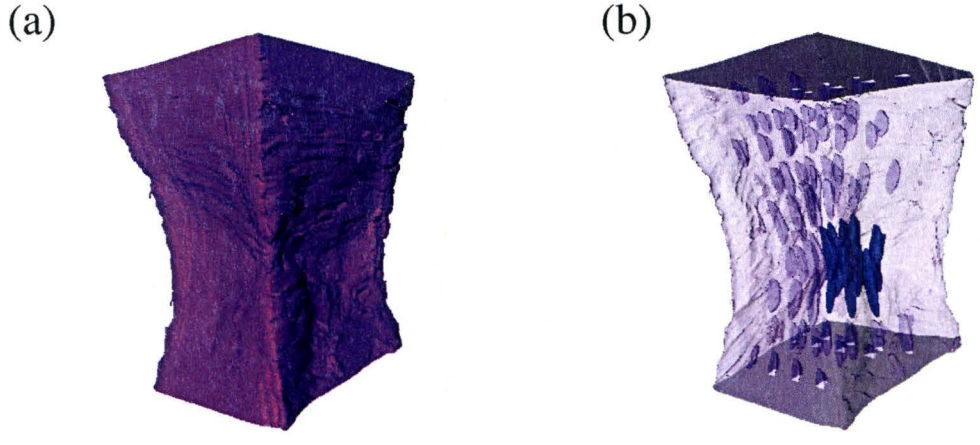

Figure 5.16: (a) The surface morphology and (b) the internal structure of the FCC 2 model material.$\varepsilon = 1.20$. The voids linked are painted blue and the other isolated voids and the matrix are numerically made transparent.

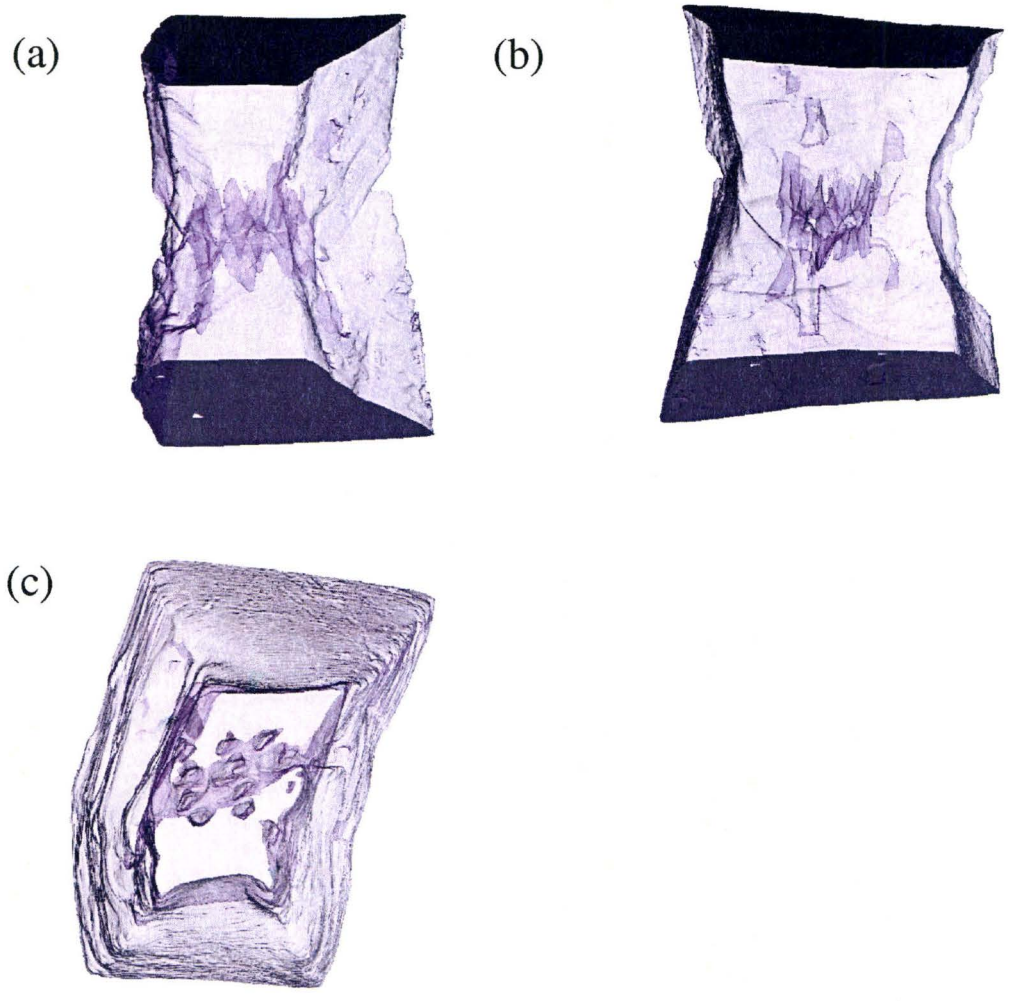

Figure 5.17: The voids after multiple linkage in the FCC 1 material. $\varepsilon = 1.02$. The embedded voids that haven't linked are all made numerically invisible. The views from (a) the b-axis direction. (b) the c-axis direction (c) the a-axis direction.

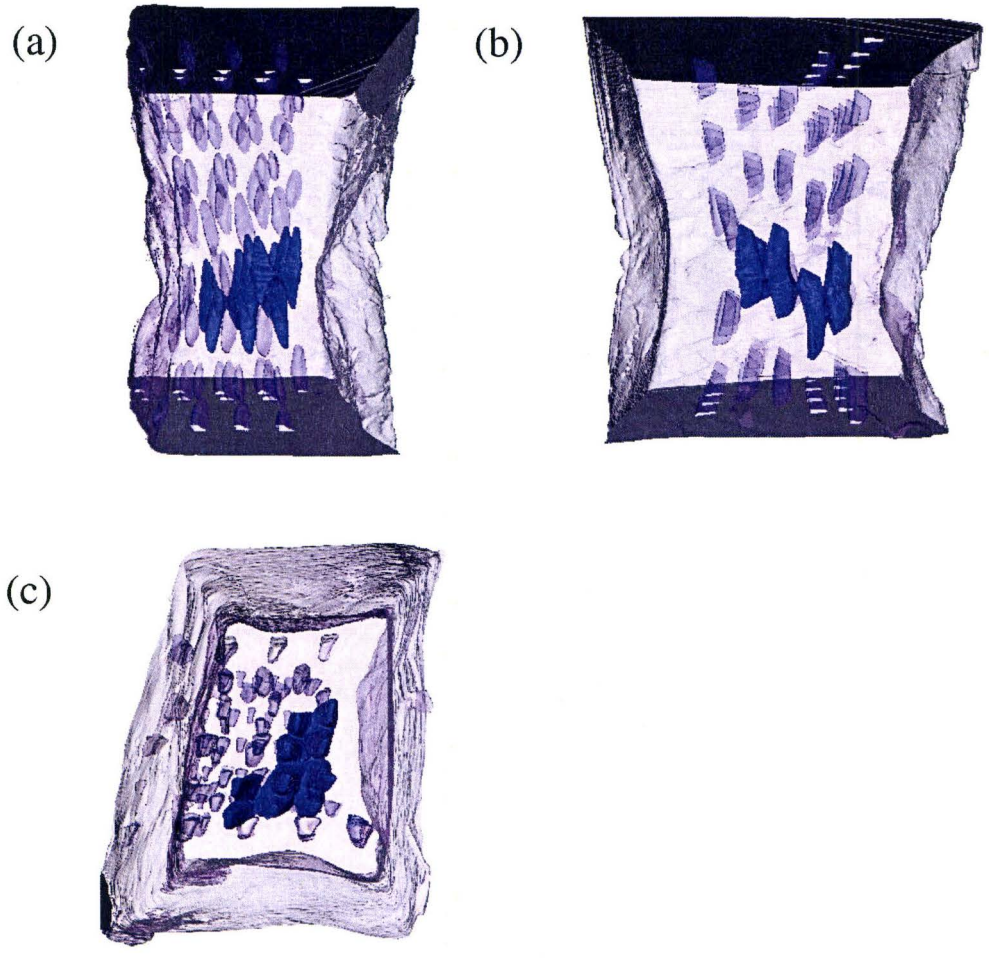

Figure 5.18: The voids after multiple linkage in the FCC 2 material. $\varepsilon = 1.20$. The views from (a) the b-axis direction. (b) the c-axis direction (c) the a-axis direction.

5.7 Discussion

5.7.1 Comparison with the Brown and Embury models

From the experimental results, the strains at the onset of void coalescence were extracted. These values are now compared with various void coalescence models.

First the results were compared with the classical Brown and Embury model. This model states that void coalescence occurs when the longitudinal void length is equal to the intervoid distance so that slip lines can be drawn along 45° with respect to tensile direction. The coalescence strain by this model can be estimated by plotting the longitudinal void length and intervoid distance versus far field true strain as shown in Figure 5.19.

The intersection of the two curves gives the coalescence strain of the Brown and Embury model. Table 5.3 summarizes the results of the comparisons. It is noted that the Brown and Embury model seriously underestimates the void coalescence strain.

Generally speaking, a higher local stress emerges around voids due to the external force that is applied to an object containing voids. Even if the local stress is much larger than the yield stress, deformation localization (i.e. internal necking) in the ligament cannot be initiated because the localization is constrained by the intact matrix. Considering an array of open cylindrical holes, this effect is considerably large in plane strain while there is no constraint in plane stress. In the the current case, in which a spherical/spheroidal void is embedded in a metal matrix, the constraint effect is higher than having an open-hole in a metal matrix. Therefore, this model is implicitly valid for 2-D case only, and the coalescence strain predicted from this model necessarily

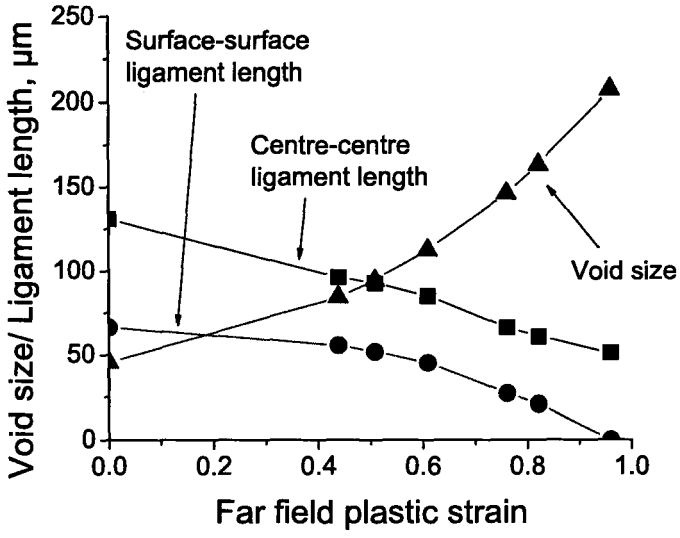

(a) FCC 1

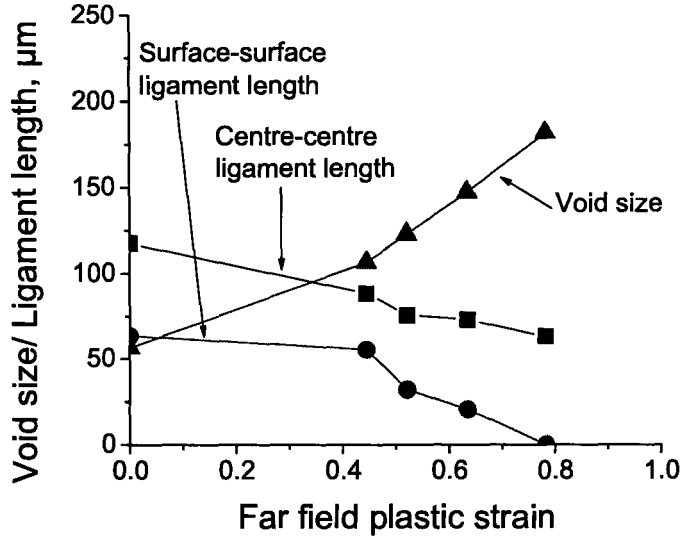

(b) FCC 2

Figure 5.19: The evolution of the void length and the ligament length as a function of far-field plastic strain in each model material.

Table 5.3: Comparisons of the experimental results of void coalescence and linkage strains with the various values predicted from the models.

		FCC 1	FCC 2
Experiments	Coalescence	0.76	0.52
	Linkage	0.96	0.85
Models	Brown and Embury	0.18	0.05
	Difference (%)	-79.5	-90.4
	Thomason	0.90	0.76
	Difference (%)	2.2	46.2
	Pardoen and Hutchinson	0.95	0.83
	Difference (%)	7.9	59.6

underestimates the experimental result due to the above reasons. Weck and Wilkinson (2008) also confirmed that this model shows excellent agreement with model materials containing an array of open-holes (i.e. 2-D) for which plastic constraint effect is much smaller, but the comparison with the model materials containing an internal single-layer void array showed a poor agreement. It seems quite conclusive that this model is only valid for the 2-D case but not for 3-D.

5.7.2 Comparison with the Thomason model and the Pardoen and Hutchinson models

A void coalescence model which treats a three dimensional periodic array of voids was proposed by Thomason. As discussed in the previous section, the local principal stress values within the intervoid matrix is much higher than the macroscopic stress due to the plastic constraint. The required stress to initiate a virtual [1] mode of internal necking must also have a much higher

[1]The required stress to initiate internal necking does not exist in a real material in tension. This is only the *virtual* value if hypothetical internal necking intervenes for the current void geometry.

value which can be estimated using the upper bound method, by assuming a perfect plastic (non-hardening) intervoid matrix sandwiched between rigid matrix regions. Before internal necking can take place, the following inequality is thus satisfied.

$$\sigma_n A_f > \sigma_1 \tag{5.7}$$

where, σ_n is the average value of the required principal stress to initiate the virtual mode of internal necking within a ligament, A_f the net area fraction of the ligament, σ_1 the macroscopic applied uniaxial stress. The ratio σ_n to uniaxial yield stress Y, called the plastic constraint factor. σ_n/Y decreases with the increase of the far field true strain as the microvoid keep opening. When the left hand side (LHS) of the inequality (5.7) is equal to the right hand side (RHS), void coalescence can finally initiate.[2] Using the upper bound method, Thomason estimated an expression for σ_n and related it to the geometric parameters as shown in equation (2.39). This equation can be simplified for the case of uniaxial tension by substituting $\nu = 1$, such that,

$$\left(\frac{0.1}{(a/e)^2} + \frac{1.2}{\left(\frac{b}{b+e}\right)^{1/2}}\right) \frac{1}{(1-V_f)} \left(1 - \left(\frac{3\sqrt{\pi}V_f}{4}\right)^{2/3} \left(\frac{b}{b_0}\right)^2\right) \exp(\varepsilon_1) = \frac{\sigma_m}{Y} + \frac{2}{3} \tag{5.8}$$

Since the Thomason model assumes an initially cubic unit cell containing a spherical void, the following relationship is used between the void volume fraction V_f and the intervoid distance $2e$.

[2]The virtual mode becomes the real mode.

$$e = a_0 \left(\sqrt[3]{\frac{\pi}{6V_f}} \exp\left(-\frac{1}{2}\varepsilon_1\right) - \frac{b}{b_0} \right) \tag{5.9}$$

Thus, the intervoid distance $2e$ and the volume fraction V_f vary with the increase of the far-field true strain. Pardoen and Hutchinson (2000) modified the Thomason model, equation (5.8), to include the effect of the work hardening, which has the form of

$$\left(\frac{\alpha(n)}{(a/e)^2} + \frac{\beta(n)}{\left(\frac{b}{b+e}\right)^{1/2}} \right) \frac{1}{(1-V_f)} \left(1 - \left(\frac{3\sqrt{\pi}V_f}{4} \right)^{2/3} \left(\frac{b}{b_0} \right)^2 \right) \exp(\varepsilon_1) = \frac{\sigma_m}{\bar{\sigma}} + \frac{2}{3} \tag{5.10}$$

where $\alpha(n)$ and $\beta(n)$ can be found in equation (2.40) in Chapter 2.

In comparing the experimental results with the Thomason model, there are two problems that need to be addressed:

- The first is the geometry of the void array in the model materials. The current model materials containing FCC arrays were fabricated such that the distance between the closest neighboring voids becomes 0.141 mm. Since the Thomason model and the Pardoen and Hutchinson essentially assume cubic arrays of voids, a direct comparison cannot be made.

- The second is the initial intervoid distance in the model materials. Due to the hole alignment issue (see section 5.5.1), the intervoid distance between the first pair of voids to link is also closer than the designed value of 0.141 mm.

These two problems were avoided as below. Direct measurements from Figures 5.11 and 5.12 were able to determine that the initial intervoid distances

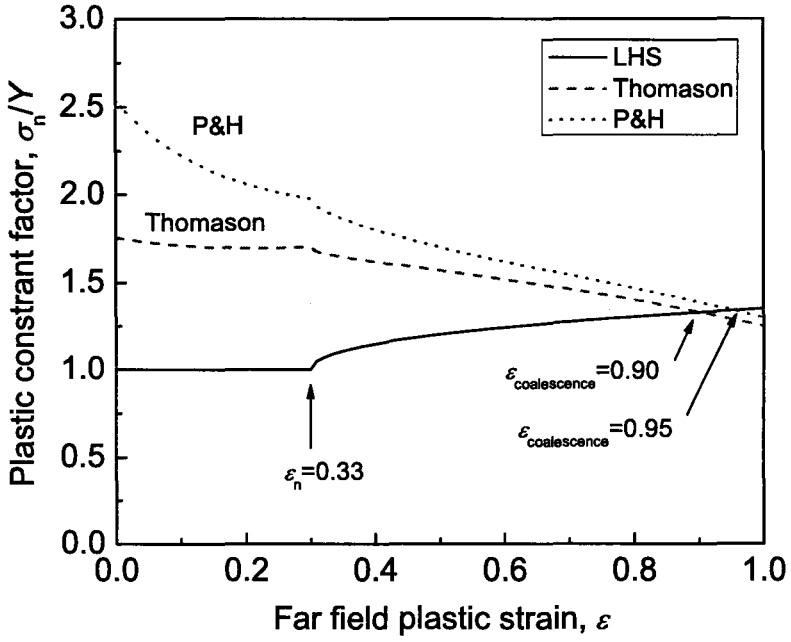

Figure 5.20: A typical tendency of plastic constraint factor predicted by the Thomason model and the Pardoen and Hutchinson model for the FCC 1 material using the value of $V_f = 4.4\%$.

$2e_0$ are 0.063 mm for the both materials. Substituting this value into equation (5.9), one obtains the value of the effective local void volume fraction of 4.4 %. Therefore, an imaginary cubic array with a volume fraction of 4.4 % (which is equivalent to $e_0 = 0.032$ mm and $a_0 = b_0 = c_0 = 0.025$ mm) is considered for the modeling. By doing this, the comparison between the experimental coalescence strain and the Thomason model is summarized in Table 5.3. A typical tendency of plastic constraint factor over the deformation is estimated as shown in Figure 5.20.

Note that the comparison was made between the models and the result from the two-void analysis. Comparison with the collective coalescence strain

(Figure 5.10) is not performed since the far field true strain to substitute in the Thomason model becomes obscure (i.e. minimum cross-sectional area is not uniquely determined). It can be noticed that the Thomason model gives a very good estimation of the coalescence strain in the FCC 1 material, with the underestimation of 2.2 %. However, the model seriously overestimates the FCC 2 material by 46.2 %.

It is extremely difficult to tell whether the Thomason model gives an upper bound solution or lower bound solution of coalescence strain. On one hand, since the Thomason model assumes non-hardening materials, it is possible that a real material with a moderate strain-hardening exponent exhibits a higher value of coalescence strain (i.e. lower bound for a model). On the other hand, the Thomason model may predict higher coalescence strains (i.e. upper bound) when compared to experiments, because the values of the plastic constraint factor for the virtual mode of internal necking as estimated from the upper bound method gives an rigorous upper bound of the coalescence strain. The competition between these two effects can "shift" the predicted strain either higher or lower. Furthermore, the Thomason model assumes a perfect 3-D cubic void array which is different from the current model materials, and thus it is not too surprising that the coalescence strain is different from the model.

However, close examination of Figure 5.11(e) for the FCC 1 material indicates that the alignment of the pair of voids and the failure path is quite horizontal (i.e. normal to the tensile axis), while it is seen that the pair of voids in Figure 5.12(e) for the FCC 2 material involves internal necking as well as microscopic shear localization (clock-wise) which accelerates the coalescence. It seems clear that such a difference in localization mechanisms resulted in the different coalescence strain.

A similar tendency is seen in the case of the Pardoen and Hutchinson model. Since this model is able to include the effect of work-hardening exponent, the predicted coalescence strains are supposed to be higher compared to the non-hardening case, and this can be actually observed in Table 3. The Pardoen and Hutchinson model revealed an overestimated coalescence strain by 5 %, which is slightly larger compared to the Thomason model. This overestimation is consistent with the nature of the model that accounts for the contribution by work hardening. The difference between the two models however is modest in comparison with the experimental accuracy of the experiments. As would be expected, the comparison with FCC 2 is actually worse, but this is attributed to the effect of the shear localization. In fact, these experimental observations clearly suggest that the existing models become indeed inadequate as soon as shear localization intervenes.

5.7.3 Critical Porosity

Although the concept of critical porosity proposed by Needleman and Tvergaard (1984) is overly simplified, it is still a rather attractive way to model void coalescence. In their original work, they proposed two different values of critical porosities at coalescence. The first is the porosity of 15.9% which is estimated based on the Brown and Embury model, and the second is 25% estimated from the classical FE modeling work performed by Andersson (1977). In the current experiment the local critical porosity at the onset of void coalescence can also be estimated. The volume of the first void pair at linkage is known from tomograms (directly measured from the number of voxels that are labeled as voids), and the values of void size (a, b, c) and intervoid spacing

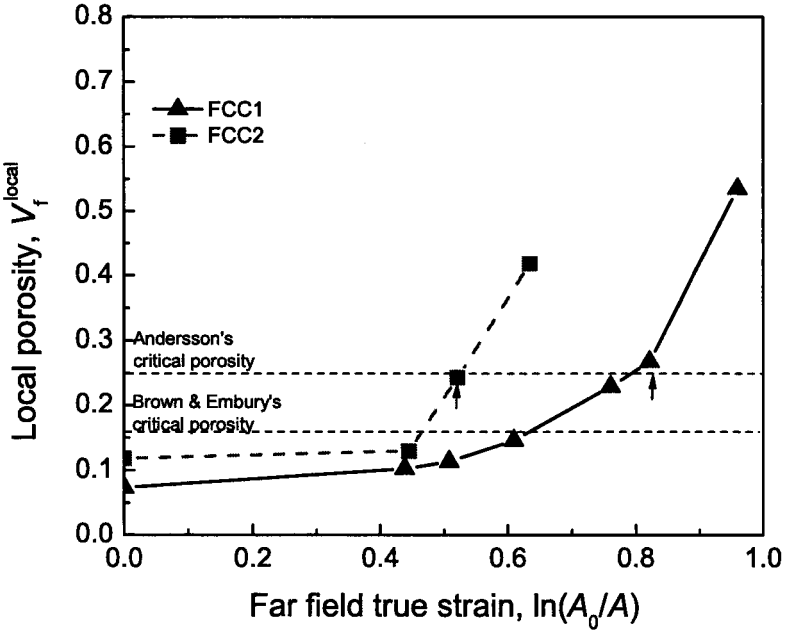

Figure 5.21: Evolution of local porosity with the deformation. Blue arrows indicate the onset of void coalescence estimated from Figures 5.13(a) and 5.14(a).

e at the coalescence are also known. Just as in the last section, an imaginary cubic unit cell containing a void is considered to estimate the local porosity, V_f^{local} , which is defined as

$$V_f^{local} = \frac{V^{1void}}{V^{cell}} = \frac{V^{1void}}{(a+e)(b+e)(c+e)} \tag{5.11}$$

where V^{1void} is the volume of one single void, V_{cell} is the volume of the unit cell, and its evolution with the plastic deformation is plotted in Figure 5.21. The arrows in the figure indicate the onset of void coalescence captured from Figures 5.13(a) and 5.14(a).

The local porosity at the onset of void coalescence seems to be in a remark-

ably good agreement with the value proposed by Andersson, yet the Brown and Embury model is not successful due to the same reason discussed in section 5.7.1. The local porosity at the onset of coalescence cannot be estimated either from the Thomason model or the Pardoen and Hutchinson model because a constant void volume fraction (i.e. initial volume fraction) was assumed estimate the intervoid distance e by Equation (5.9). This approach excels in fact that a coalescence strain for a given void volume fraction can be predicted with performing neither experiments nor FE simulations. It is also possible to use the updating values of e and V_f measured from experiments, but this approach becomes semi-experimental. The comparisons between the experimental data with the predicted coalescence strains by the semi-experimental approach is given in Appendix A.

Nevertheless, we have to keep in mind that such concept of critical porosity is not adequate if the initial local porosity is significantly different.

A remaining question is how to treat the intervention of the microscopic shear instability and void sheeting process. Once these happen, the ductility of material significantly degrades, and then none of the existing models are able to predict void coalescence properly. Generally speaking, shear instability is known to intervene when the work hardening rate saturates significantly. The growth of local porosity is also terminated when shear instability intervenes. This will be later demonstrated in Chapter 7, section 7.6.

5.8 FE simulation

5.8.1 Effect of void shape

As seen in tomograms, the shape of the voids in the model materials is not spherical but rather like a tapered cylinder. Since the most of the models assume a simple spherical (or spheroidal) void, the question arises as to the validity of the comparison made in this work. Simple FE models as illustrated in Figure 5.22 containing arrays of voids with different shapes can help to answer this question.

To simplify the problem, models containing only 12 voids comprising FCC arrays are considered here. The problem is that the mechanical response by this type of FE models is expected to be stronger than the experimental results because there are fewer voids in the FE models than in the model materials tested experimentally. To compensate for this difference, we assign the mechanical property of pure copper measured by ARAMIS technique to the intervoid ligament region located in the central part of the FE model, while the mechanical property measured in the experiment of the porous model material (which is weaker than pure copper as shown in Figure 5.3) is assigned to the surrounding matrix, as illustrated in Figure 5.23. Typical mesh geometries before and after some deformation in the FE models containing voids with different shapes are shown in Figures 5.25~5.27. The color contours represented in those figures are the effective plastic strains. Especially in the later stage of plastic deformation, the distribution of the effective stress exhibit almost no asymmetry around the tensile axis. In fact, the analysis of the lateral void growth behavior estimated by local strain $\ln(r/r_0)$ clarified that there is virtually no effect of the void shape on void growth behaviors as presented in

Figures 5.28 and 5.29.

Another question is which part of the diameter should be measured to quantify the void growth. In the case of spherical voids and cylinder, the diameter and the height should be measured of course. However, in the case of the tapered cylindrical void, there remains some ambiguity in choosing which type of diameter should be measured, as illustrated in Figure 5.30 (b). In the current experiments, the biggest values were measured for the sake of simplicity. The FE simulation result shown in Figure 5.30 (a) clearly shows that no matter which type of diameters we pick, the void growth behavior ends up with a similar parallel tendency in the local strains plotted as functions of far field plastic strain $\ln(A_0/A)$.

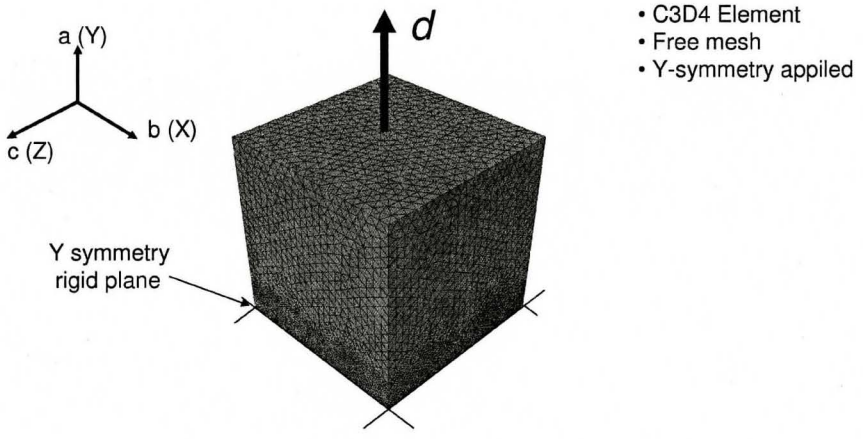

Figure 5.22: The FE model considered in the current simulations showing a typical mesh geometry.

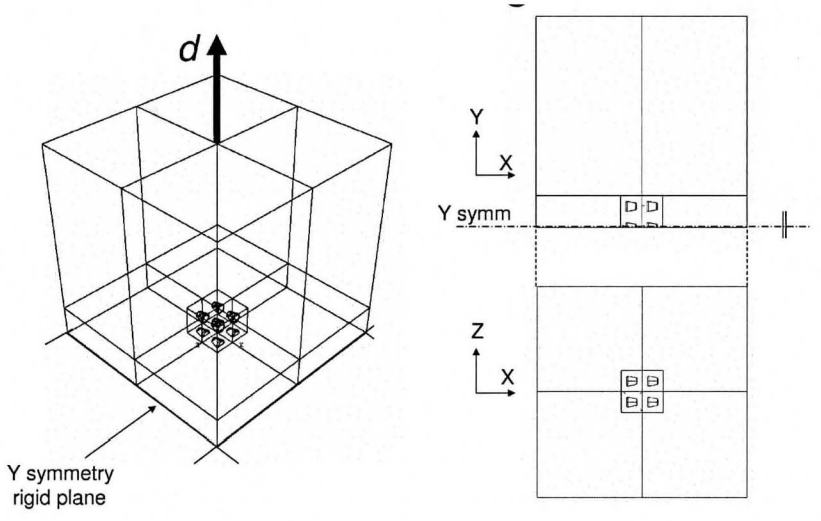

Figure 5.23: The FE model considered in the current simulations showing the void array.

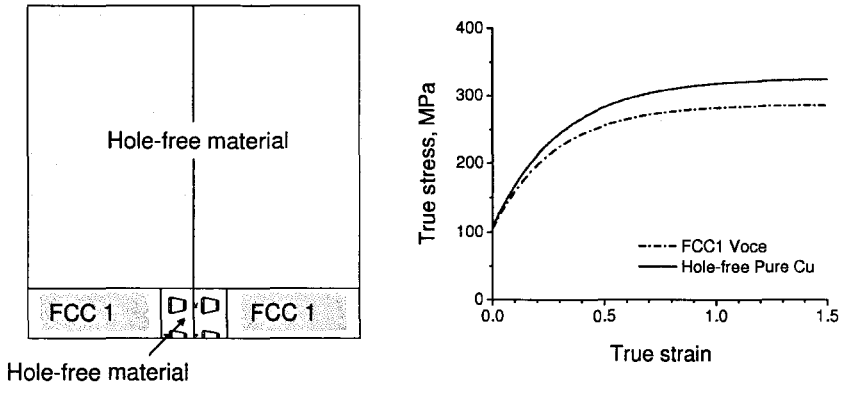

Figure 5.24: Mean field approximation to adjust the mechanical response.

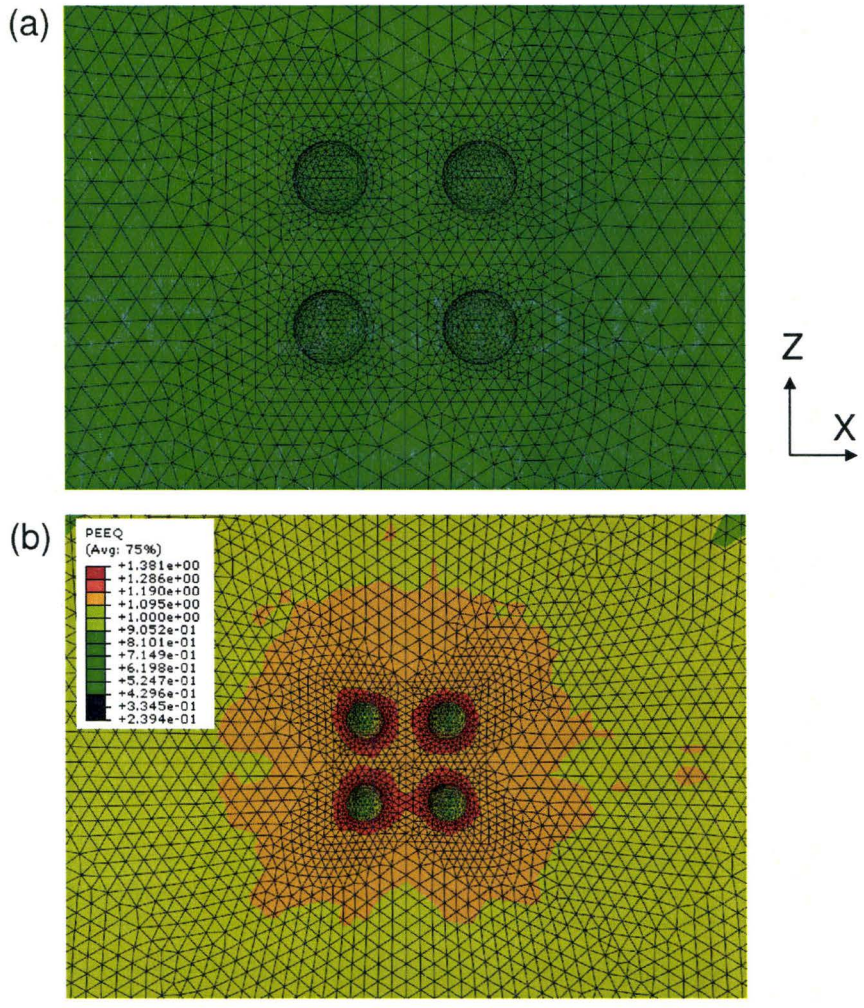

Figure 5.25: The FE mesh for the analysis of spherical voids. (a) Before deformation (b) After deformation

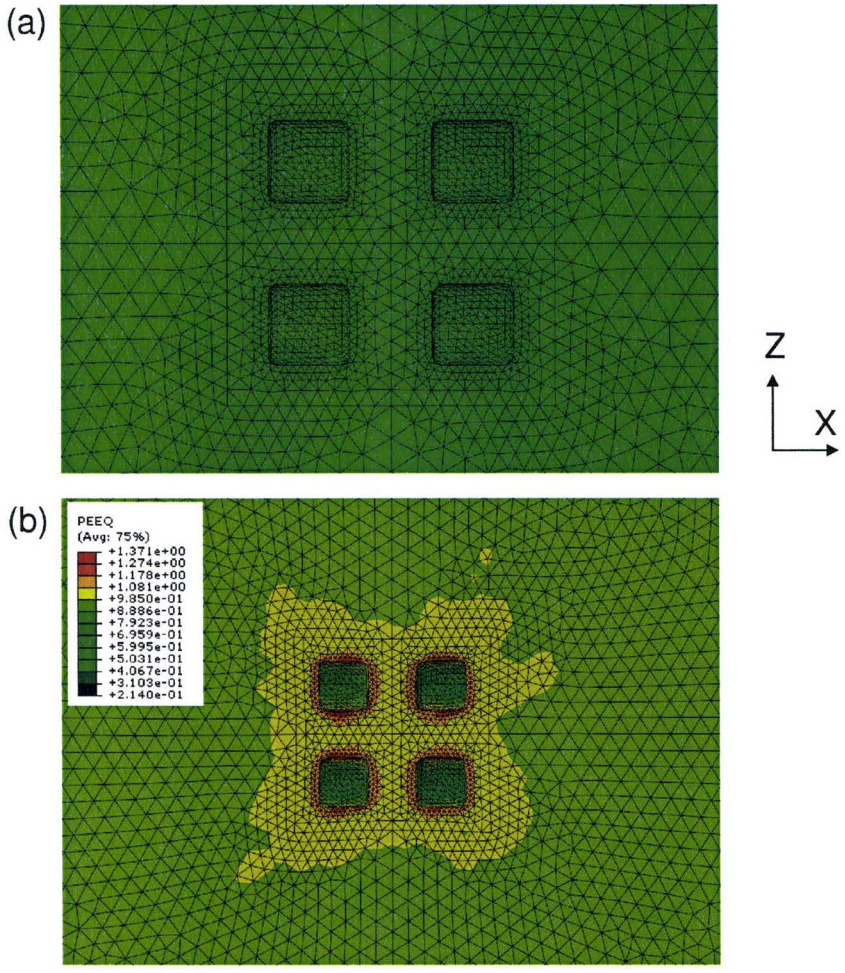

Figure 5.26: The FE mesh for the analysis of cylindrical voids. a) Before deformation (b) After deformation

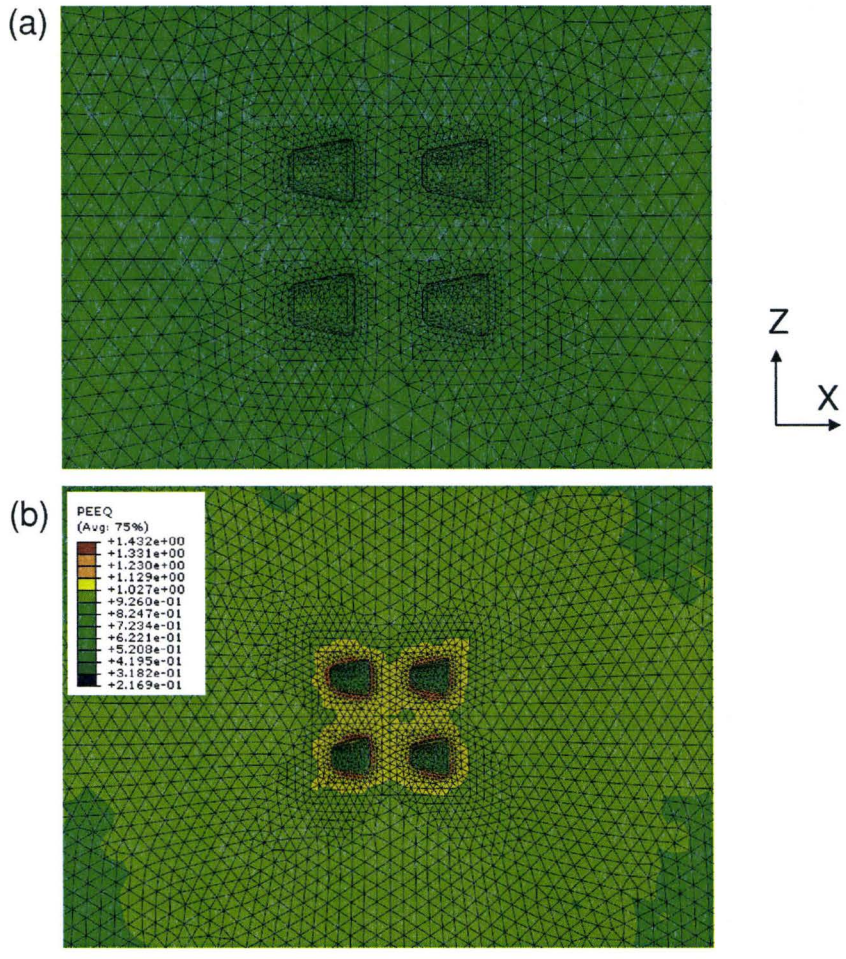

Figure 5.27: The FE mesh for the analysis of tapered cylindrical voids. a) Before deformation (b) After deformation

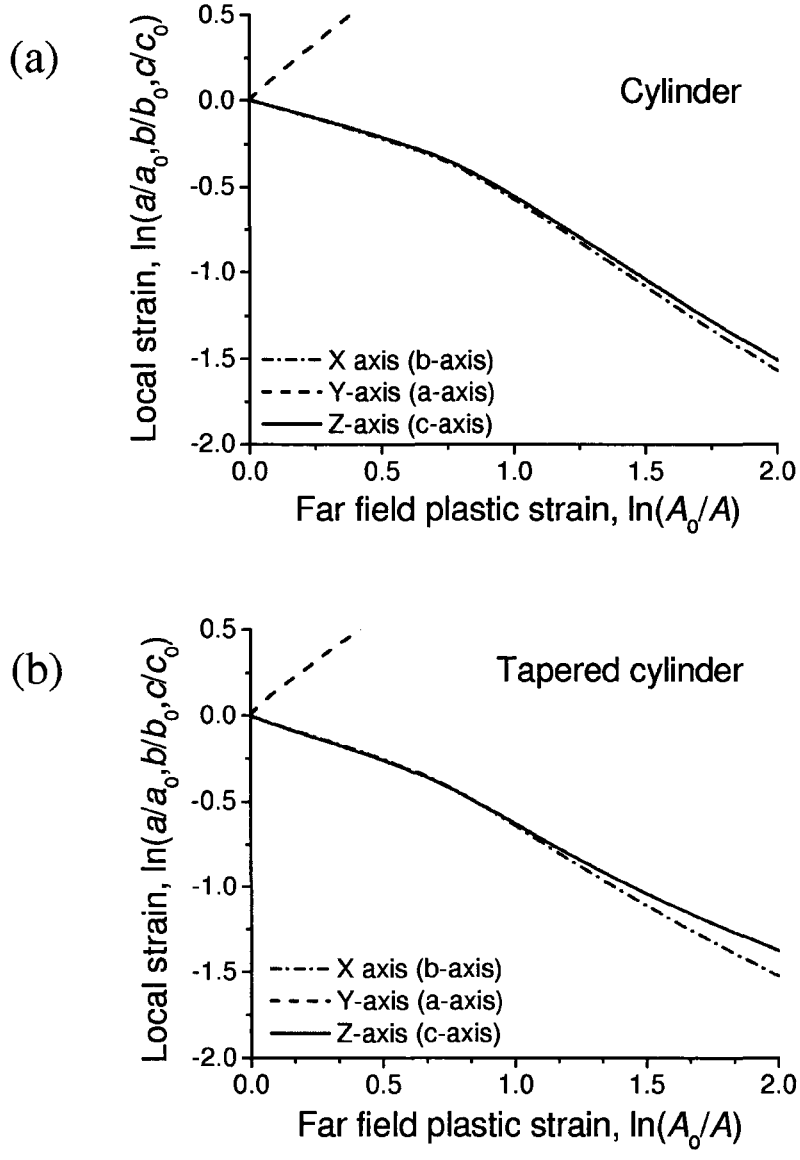

Figure 5.28: The influence of the void shape on the void growth beahviors.

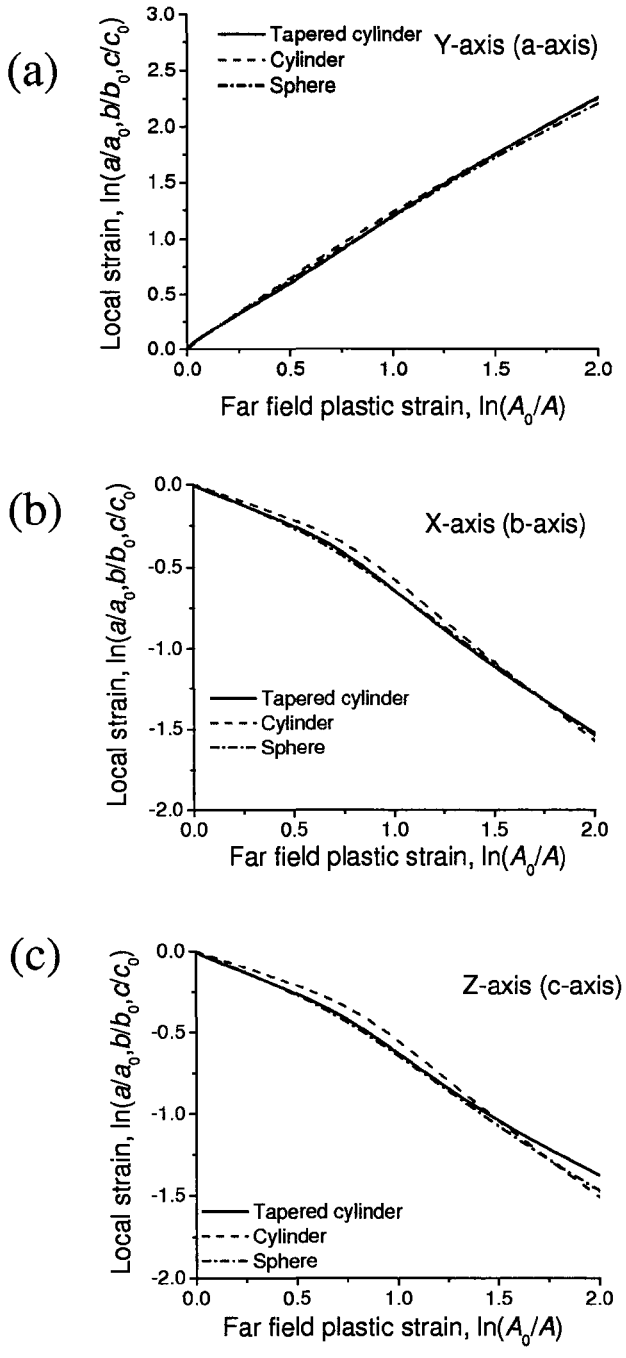

Figure 5.29: The asymmetric void growth behavior due to the effect of the void shape. The data plotted are identical to the Figure 5.28. (a) Y-axis (Tensile axis) (b) X-axis (c) Z-axis.

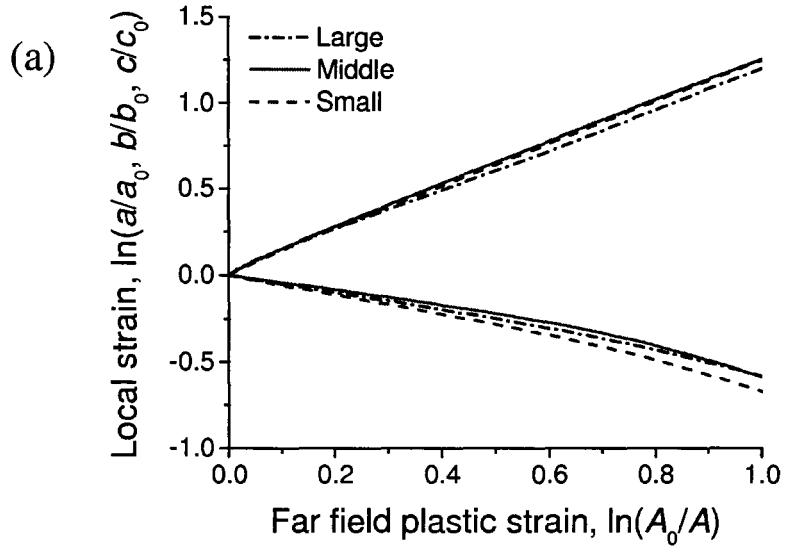

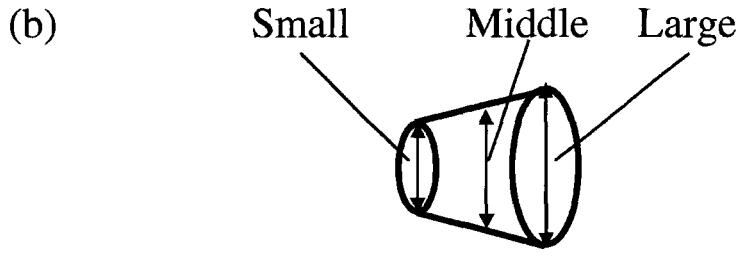

Figure 5.30: The difference in void growth behavior at the positions of measurement. Large represents the largest possible void diameter as illustrated in (b).

5.8.2 Effect of shear coalescence

2D plane strain

When the void array is off the horizontal axis as in the situation of the first coalesced void pair in the FCC 2 material, we have shown that the existing models cannot provide a good prediction because of the microscopic shear coalescence. However, this is only a qualitative explanation.

In fact, it is extremely difficult to estimate the 3D plastic constraint factor for internal necking once shear coalescence intervenes, as pointed out by Scheyvaerts (2008).

Surprisingly, there is no work in literature that has attempted to extend the 2D plane strain Thomason model to account for shear. One similar approach can be seen in the experimental work by Bannister and Ashby (1991) (Figure 5.31). In their work, lead was sandwiched between glass sheets and a pair of very sharp and deep notches were cut so that the plastic flow within the minimum cross sectional area becomes constrained. The maximum possible plastic constraint factor emerged by very sharp notch is estimated about 6, both by experiments and theories (See also (Ashby et al., 1989; Evans and McMeeking, 1986; Sigl et al., 1988)). By changing the relative positions of the pair of notches, the shear angle can be controlled. The constraint factor can be experimentally measured from the true stress divided by the initial yield strength. However, the intervoid distance (i.e. distance between cracks/notches) changes with the change of initial shear angle. In extending the 2D Thomason model, the intervoid distance has to remain the same.

Doing a similar set of experiments like this is tedious, yet 2D plane strain FE simulations can be performed quite easily. In order to do so, the 2D Thoma-

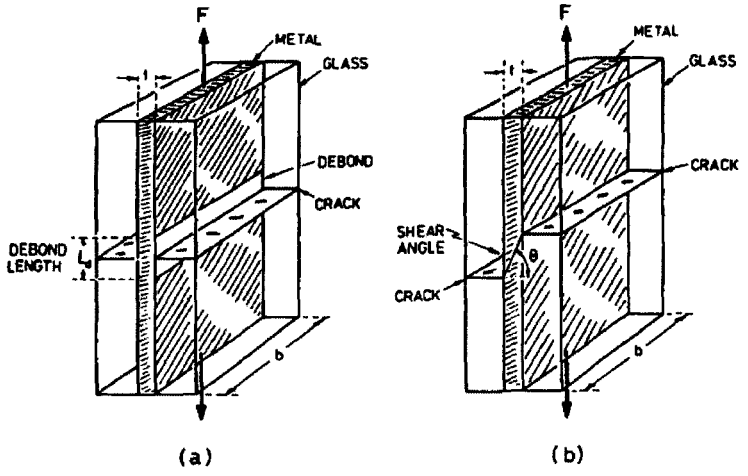

Figure 5.31: Experiments performed by Bannister and Ashby (1991). A pair of sharp notches constrains the plastic flow of the minimum cross sectional area.

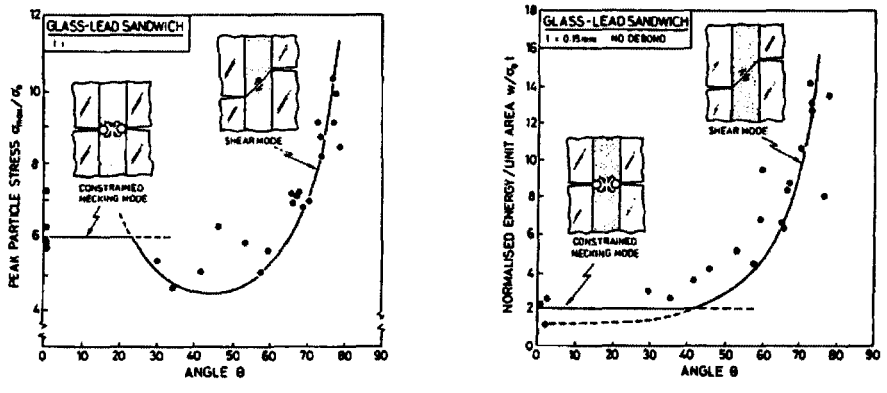

Figure 5.32: Influence of the shear angle on the plastic constraint factor. (Bannister and Ashby, 1991)

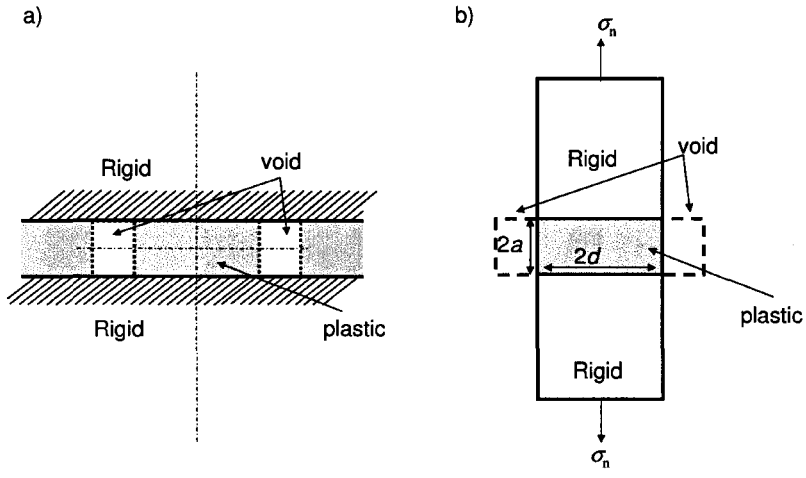

Figure 5.33: The 2D plane strain FE model to reproduce the 2D Thomason model. Element type: CPE4R

son model, which is originally based on the classical upper bound method, was first reproduced by FE calculations. As illustrated in Figure 5.33, the model consists of a non hardening plastic region sandwiched between rigid blocks. A typical mesh geometry is shown in Figure 5.34. By changing the value of a/d, the plastic constraint factor for internal necking can be estimated by measuring the peak engineering stress σ_n divided by the Tresca effective stress $2k$. The result is shown in Figure 5.35 (a). The current FE results show good agreement with the original 2D Thomason model. Similar work can be done using the constitutive behavior of hole free pure copper in Figure 5.3. The result is shown in Figure 5.35. Although work hardening significantly increases the plastic constraint factor especially for smaller values of a/d, the trend line will be very similar to the original Thomason model.

The next step is to study how the plastic constraint factor changes when the initial void configuration inclines. The FE model used is schematically

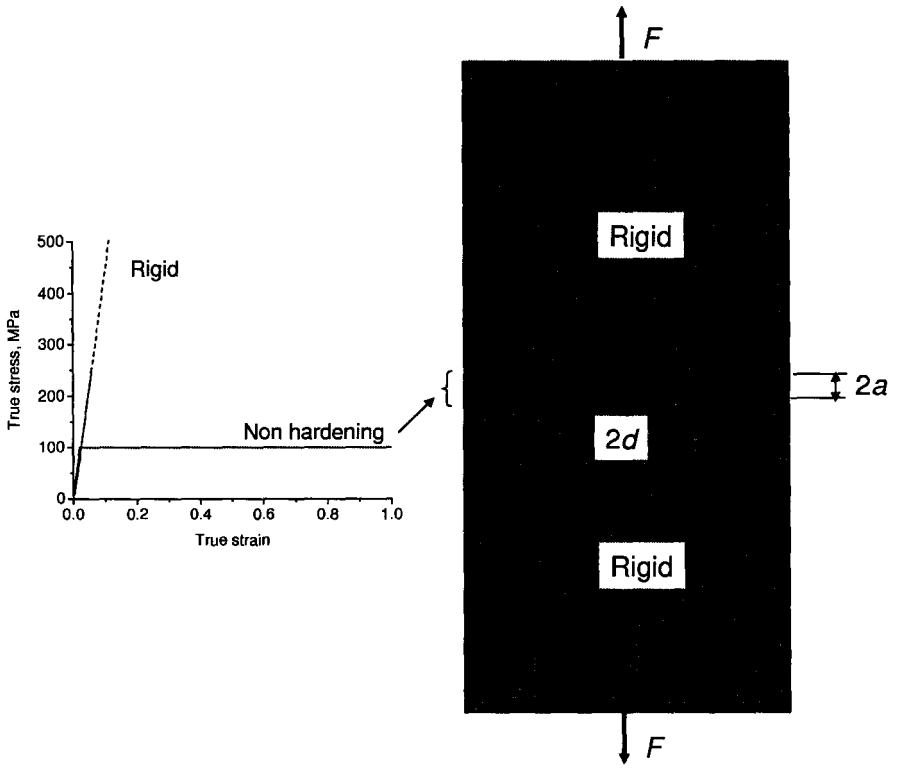

Figure 5.34: A typical finite element mesh for 2D plane strain FE simulation and the corresponding constitutive behaviors assigned for each region.

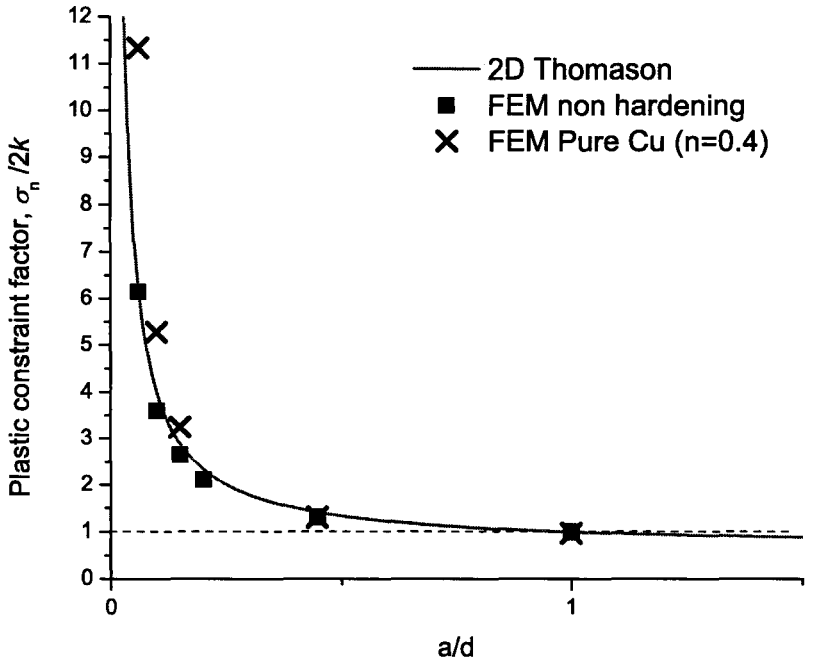

Figure 5.35: The plastic constraint factor estimated by the current FE calculation. The fitting curve is the original 2D plane strain Thomason model. (Equation (2.38))

illustrated in Figure 5.36, and the effect of the angle on the plastic constraint factor is seen in Figure 5.37. The plastic constraint factor significantly decreases with the shear angle θ to unity above 22.5 °.

The model by Bannister and Ashby can anyhow account for the result shown in 5.37. Note that this model is only valid when plane strain and cylindrical holes can be assumed. If the shear strength of the shear plane is k, then the axial stress required to shear is

$$\sigma = \frac{k}{\sin\theta\cos\theta} \tag{5.12}$$

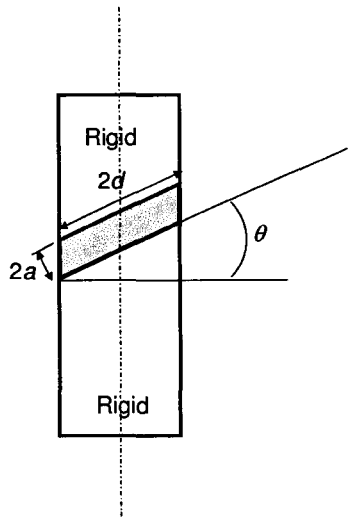

Figure 5.36: The 2D plane strain FE model to estimate the effect of the shear angle θ. Non hardening material was assumed.

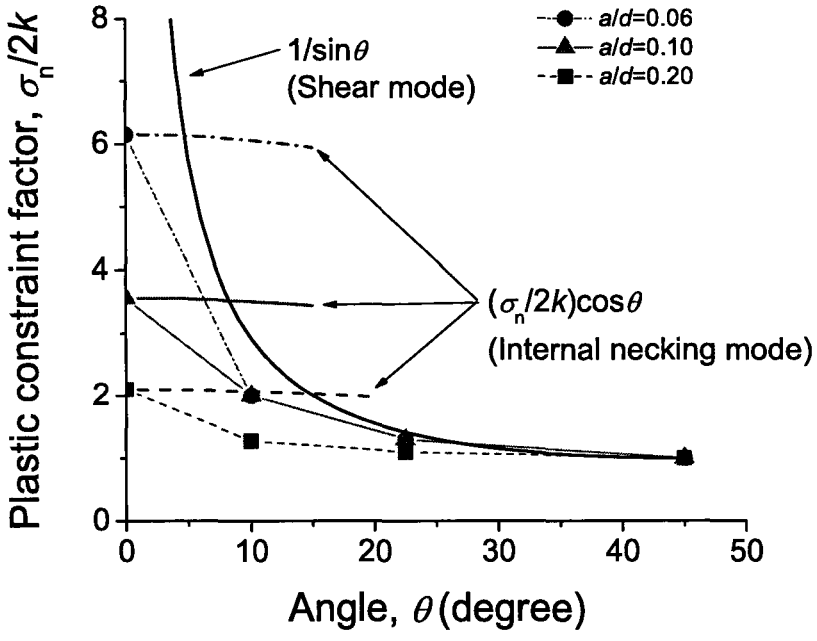

Figure 5.37: The plastic constraint factor plotted as a function of the shear angle θ.

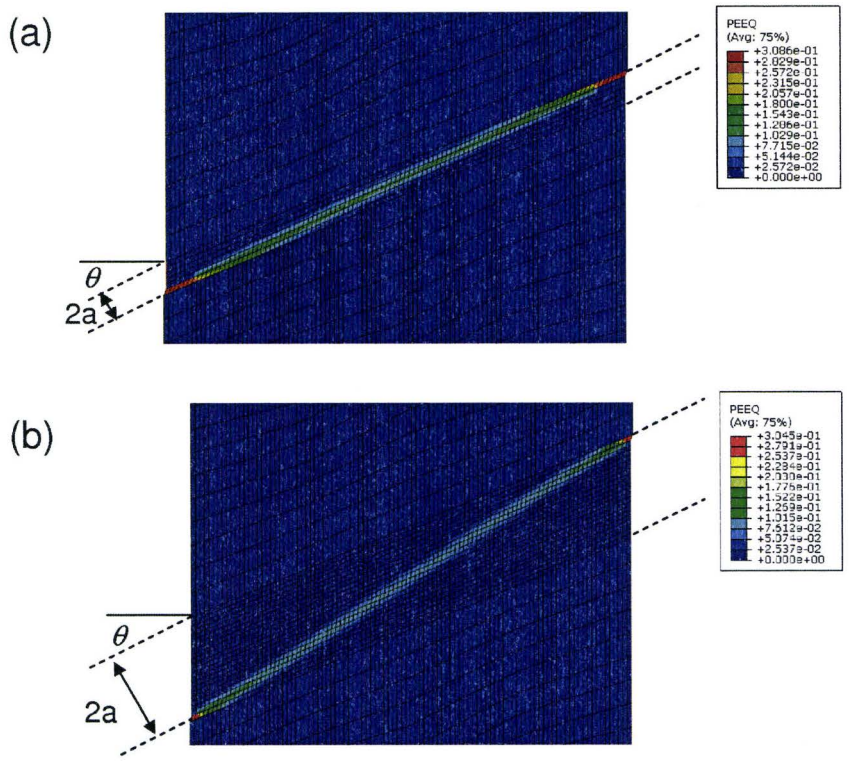

Figure 5.38: The distribution of local plastic effective strain within the plastic part. The shear angle θ is 22.5 ° (a) $a/d = 0.06$ (b) $a/d = 0.2$

This equation can be rewritten as

$$\frac{\sigma}{2k} = \frac{1}{2\cos\theta\sin\theta} \tag{5.13}$$

In the original version of this model, the ligament area increases by a factor of $1/\cos\theta$ when the shear angle changes. However, we assumed that the ligament area does not change over even if the shear angle changes (i.e. a/d remains constant over the rotation). To compensate for this difference, a modified version of the Bannister and Ashby model leads to the following form.

$$\frac{\sigma}{2k} = \frac{1}{2\sin\theta} \tag{5.14}$$

The original equation is plotted in Figure 5.37 along with the FE simulation result. Also a simple projection of the plastic constraint factor onto the direction normal to the shear plane ($\sigma_n/2k$) is plotted, which is labeled as "internal necking mode" in the figure. Among these two, whichever is lower is compared with the right hand side of the 2D Thomason model, in order to judge whether the deformation localization (either internal necking or shear coalescence) is in *virtual mode* or not. For example, the constrained necking mode is easier for the lower value of θ, since the required axial stress for necking mode is smaller, while it is contrary for the higher value of θ.

This model shows a relatively good agreement with the case of $a/d = 0.06$, but it was not successful to fit the plastic constraint factor for the cases with lower values of a/d.

The reason for this discrepancy can be seen in Figure 5.38 which demonstrates the distribution of the effective plastic strain within the ligament that

is inclined by 22.5 °. The model by Bannister and Ashby implicitly assumes that the deformation within the ligament is homogeneous such that the angle of the maximum shear is the same as θ. This is actually a quite good assumption when a/d is sufficiently small, as in the case of their experiment of a lead sheet surrounded by cracked glass. However, if a/d becomes larger, this assumption becomes invalid since the plastic deformation is not as homogeneous within the ligament, but the deformation is localized into a strip which is much thinner than the value of $2a$, as shown in Figure 5.38(b). This effective angle of the thin strip, θ_{eff} is not 22.5 °, but more close to 45 °. This explains why the evolution of the plastic constraint factor for a/d is lower than the Banister and Ashby model.

This observation suggests a more generalized version of the 2D Thomason model that can account for shear coalescence, by quantifying the influence of the effective angle on the plastic constraint factor for internal necking. As illustrated in Figure 5.39, the effective shear angle θ_{eff} is always a sum of the original shear angle θ and the angle formed in a plastic region by a diagonal line ϕ, which means

$$\theta_{eff} = \theta + \phi \tag{5.15}$$

where the angle ϕ is simply given by $\tan^{-1}(a/d)$. Therefore, equation (5.14) can now be rewritten as the following form.

$$\frac{\sigma}{2k} = \frac{1}{2\sin\theta_{eff}} = \left[2\sin\left\{\theta + \tan^{-1}\left(\frac{a}{d}\right)\right\}\right]^{-1} \tag{5.16}$$

This equation, plotted in Figure 5.40, shows excellent agreement with the values of the plastic constraint factor estimated by the current FE simulations.

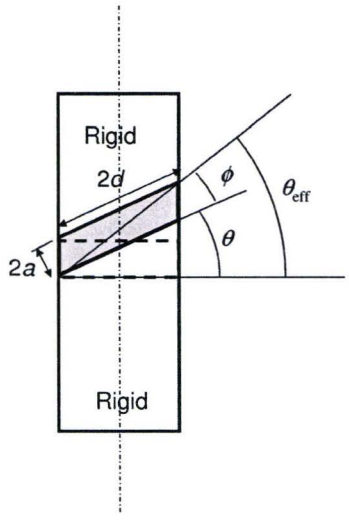

Figure 5.39: The schematically illustrated relation between the nominal shear angle θ and the effective shear angle θ_{eff}.

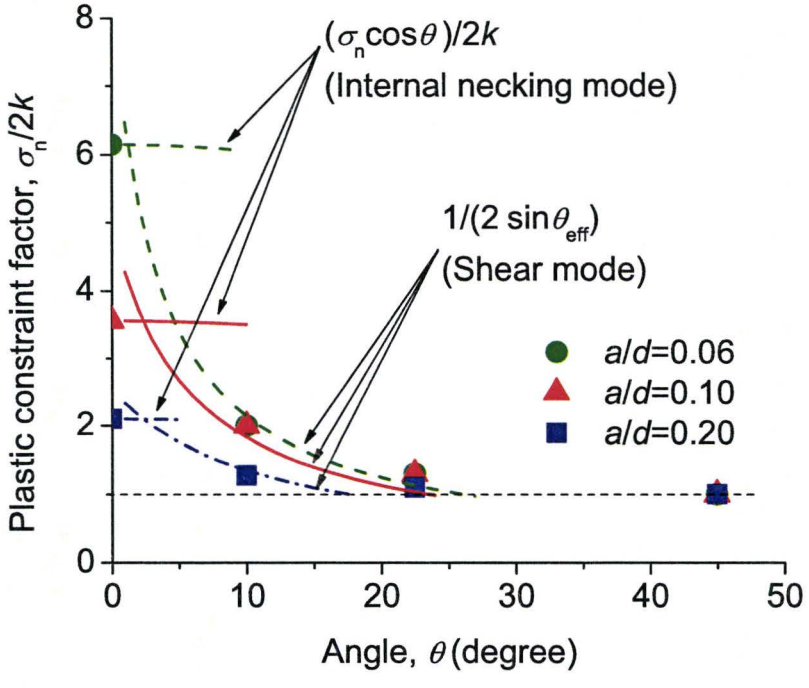

Figure 5.40: The plastic constraint factors plotted as functions of the nominal shear angle θ. The fitting curves are eq. (5.16).

General 3D situation

One would like to extend this analysis to build up a model that can account for the shear coalescence in a void array that has a general 3D arrangement, in order to explain the overestimation of the coalescence strain of the FCC 2 model material by the Thomason model and the Pardoen and Hutchinson model. However, this is a very difficult problem.

In fact, there are still several things that have to be done in the 2D calculations to fully account for shear coalescence. Some aspects of the problem can be illustrated by Figure 5.41. The 2D FE simulation performed in last section is a simple unit cell calculation, assuming a simple situation as illustrated in Figure 5.41(a). The remaining question is whether the unit cell FE simulation is valid or not for an isolated void pair as shown in Figure 5.41(b). The situation can be much more complicated as the same unit cell may be embedded in horizontal void rows like Figure 5.41(c). Furthermore, the neighboring voids may be very different in size as shown in Figure 5.41(d).

Clearly, it could be complicated even in a 2D situation to deal with a general void array. A 3D void coalescence model with a general void arrangement has even more variables to consider. Therefore, development of this kind of model was not attempted in the current thesis.

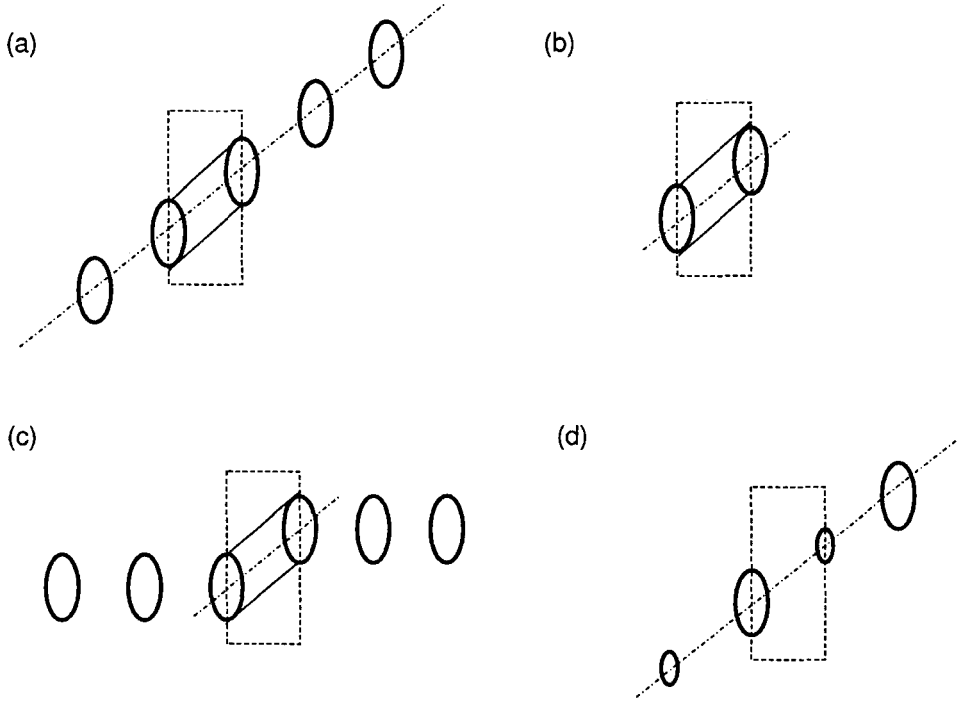

Figure 5.41: (a) A unit cell considered in a void row (b) A unit cell of an isolated pair of voids.

5.9 Chapter Summary

- The void growth and void coalescence in the FCC 1 and the FCC 2 model materials were well visualized by means of X-ray computed tomography. The measurement of principal diameters was performed to evaluate the void growth behavior in a quantitative manner. The void growth behavior was in good agreement with the Rice and Tracey model in the beginning of the plastic deformation until the lateral void diameters (i.e. b-axis and c-axis) start increasing when the onset of void coalescence intervenes.

- The onset of void coalescence for both the model materials were measured, and compared with the existing void coalescence models. The Brown and Embury model failed to predict the void coalescence due to its lack of constraint. The Thomason model and the Pardoen and Hutchinson model successfully predicted the void coalescence in the FCC 1 model material in which the first void pair to link was aligned normal to the tensile axis. However, none of the models was successful in predicting the onset of void coalescence in the FCC 2 model material, in which the void configuration was slightly offset. This is due to the fact that the shear coalescence intervened leading to premature coalescence.

- FE simulations show that there is no significant anisotropy in void growth behavior of a tapered cylindrical void. In fact, the growth in spherical, cylindrical and tapered-cylindrical voids were found to be almost identical.

- The plastic constraint factor for internal necking in 2D plane strain was

estimated by FE simulation. The plastic constraint factor significantly decreased when the configuration of neighboring voids is inclined from the horizontal arrangement. This provides a rational basis for understanding the effect of local shear instability on void coalescence.

Chapter 6

Effect of Stress State

In this chapter, the data on the influences of the stress state on void growth and coalescence are presented. As discussed in Chapter 2, higher stress triaxiality induces significant expansion of voids, which is known to accelerate fracture.

There are several ways to change the stress state during plastic deformation. The first involves multi-axial tests such as bi-axial tensile tests, which might be intuitively the most understandable. The second is to deform material in a fluid, the pressure of which is adjustable. The last one, which was employed in the current experimental approach, is to cut a set of notches. These notches have to be deep enough, otherwise the material at the minimum cross section is not constrained.

6.1 Samples and Experimental Procedures

Three model materials were fabricated based on the technique proposed by Weck et al. (2007a). One of them consists of a 5-layered void array, the 3D "crystallographic" array is supposed to be essentially the same as the

FCC 2 material in the last chapter. The other two involve a single layer of voids; one with a hexagonal array and the other with a random array of voids embedded in pure copper matrix. The experimental set-ups are exactly same as the last chapter. In fact, this set of experiments and the experiments described in the last chapter were performed at ESRF ID15 during the same period. The major difference from the last chapter is that the tensile specimens discussed here have a pair of round notches as illustrated in Figure 6.1. This notch geometry was determined from the limitations by the experimental set-up. To demonstrate the influence of the stress state on the void growth and coalescence in model materials, sharper and deeper notches is desired. There are however many limitations to produce a model material with very sharp and deep notches:

- The first is the sample thickness. Due to X-ray absorption (see section 5.3), the thickness at the view of interest (i.e. where a void array is located) cannot be larger than 1 mm.

- The grip part of the tensile sample has to be small enough to fit in the tensile rig provided by INSA de Lyon. 2 mm is about the maximum.

- The drilled hole size is determined by the pixel size of the tomography set-up (1.6 μm at ID15). The hole size should be 20$\sim$30 times larger than the pixel size to obtain a good image. To have a nearly spherical void after diffusion bonding, the sheet thickness must be the same as the diameter of the hole. In the current experiments, the nominal hole diameter was set to 50 μm.

- Before deformation, one would like to have holes moderately distant from

each other. The designed intervoid distance was set to 141 μm in the current experiments.

- a/R has to be as small as possible to maximize the stress triaxiality, as proposed by the Bridgman equation (Bridgman, 1952).

The notch geometry for the current set of experiments was determined to satisfy all the conditions here.

The sample nomenclature used in this chapter is shown in Table 6.1. The multi-layer material, the FCC 2 Notched material was subjected in a continuous tomography. The other two were tested by an ordinary (non continuous) tomography technique, which is the same technique employed in the previous work (Weck et al., 2008b).

6.2 FE simulation procedure

6.2.1 Preliminaries

A pair of notches causes two issues in interpreting the results obtained from the set of experiments. The first is that the magnitude of the plastic constraint due to the notches is not clear. The principal stresses within sheet materials that undergo localized necking (i.e. necking develops along only one direction) is given by the following equations (Bridgman, 1952).

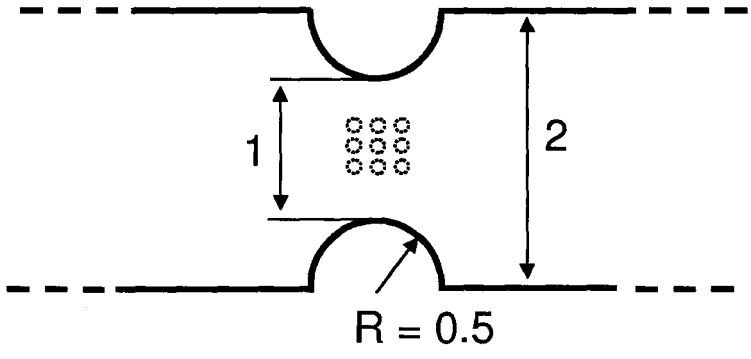

Figure 6.1: Schematic illustration of the tensile specimen with a pair of round notches. Dimensions are provided in mm. Thickness = 1 mm. $a/R = 1$. Note that the void array is embedded in material. Note that the cross sectional shape is rectangular.

Table 6.1: Nomenclature for the samples used in chapter 6.

Sample name	Number of layer embedded	Type of array
FCC 2 notched	5	FCC 2 type
Hexagonal	1	Hexagonal type
Random	1	Random type

$$\sigma_1 = Y \ln \left[1 + \frac{a}{2R} \left(1 - \frac{x^2}{a^2} \right) \right] \tag{6.1a}$$

$$\sigma_2 = Y \left\{ \frac{1}{2} + \ln \left[1 + \frac{a}{2R} \left(1 - \frac{x^2}{a^2} \right) \right] \right\} \tag{6.1b}$$

$$\sigma_3 = Y \left\{ 1 + \ln \left[1 + \frac{a}{2R} \left(1 - \frac{x^2}{a^2} \right) \right] \right\} \tag{6.1c}$$

Estimated value of σ_1/Y for the current material's geometry (i.e. $a/2R$=0.5) from this set of equations is 1.69. However, this equation is valid only in the beginning of the deformation. Once the plastic deformation proceeds, the initial round notch blunts out, and the triaxiality and the constraint effect will be significantly decreased. Furthermore, thickness reduction (i.e. along c-axis) due to necking occurred (See the tomograms in the later sections). Therefore, it would be inadequate to simply use the above Bridgman equation for the localized necking.

The second issue is that the void growth behavior becomes anisotropic, because the pair of notches enhances the lateral stress only along the c-axis. It is expected that the void growth behaviors along b-axis and c-axis would be different due to the effect of notches. Although the Rice and Tracey model can predict the isotropic void growth behavior for a given value of the stress triaxiality, the anisotropic growth cannot be modeled properly.

To solve these problems, simple FE simulations were done. These FE simulations can predict the principal stress-strain curves and the void growth behaviors that would be considerably different from the case of the smooth specimens.

6.2.2 Detailed FE simulation procedure

The FE simulations were carried out by using ABAQUS. Detailed information of the computation environment was given in section 4.5. Three FE models are considered here as shown in Figures 6.2-6.4. The first is the hole-free model, which is utilized to check the magnitude of the constraint as well as the stress triaxiality within a notched sample. The second model contains 8 voids that are aligned in a single row, which is comparable with the experimental result of the Hexagonal and the Random model materials that contain a single-layer void array. By applying the Y-symmetry and Z-symmetry to the model, only 1/4 of the array is modeled and thus only 4 voids appear in Figure 6.3. Although the influence of the void shape on void growth was determined to be negligible in the last chapter (See Figure 5.28), the shape of the voids in this FE models was set as the tapered cylinder instead of a simple sphere, to represent the situation in the experiments performed. The third model contains 12 voids that consists of two cubic arrays as illustrated in Figure 6.4, the situation of which approximately represents the FCC 2 Notch model material. Strictly speaking, FCC type void array, instead of simple cubic arrays, should be simulated for a more direct comparison. However, the treatment of the symmetry (of the void array and the stress distribution due to the notch geometry) becomes extremely difficult for the non-cubic 3D void configuration. To avoid this complexity, only the computation on cubic arrays composed of 12 voids was performed. The constitutive behavior for diffusion bonded hole free Cu measured by the digital image correlation technique (from Figure 5.3) was used in this FE simulation. The element type, meshing procedure and the number of elements that were used for individual simulations are presented

in Figures 6.2~6.4. The results of the simulations will be presented along with the experimental results in later sections, which help us to interpret the results.

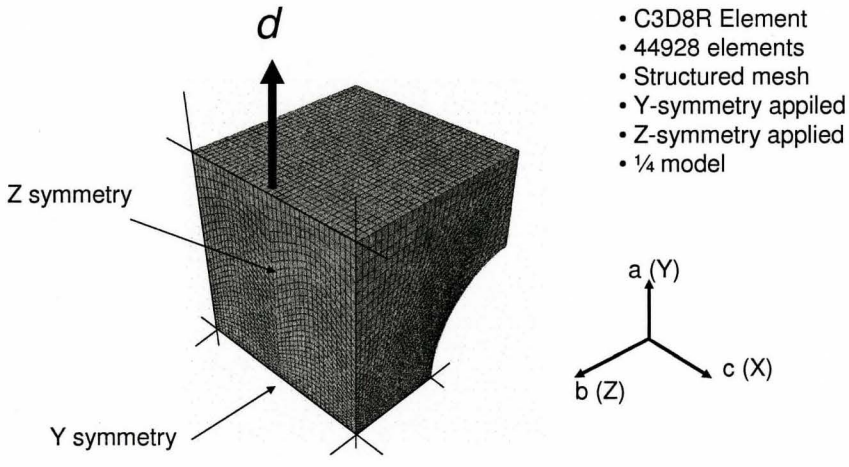

Figure 6.2: FE modeling set-up for the round notched hole-free sample.

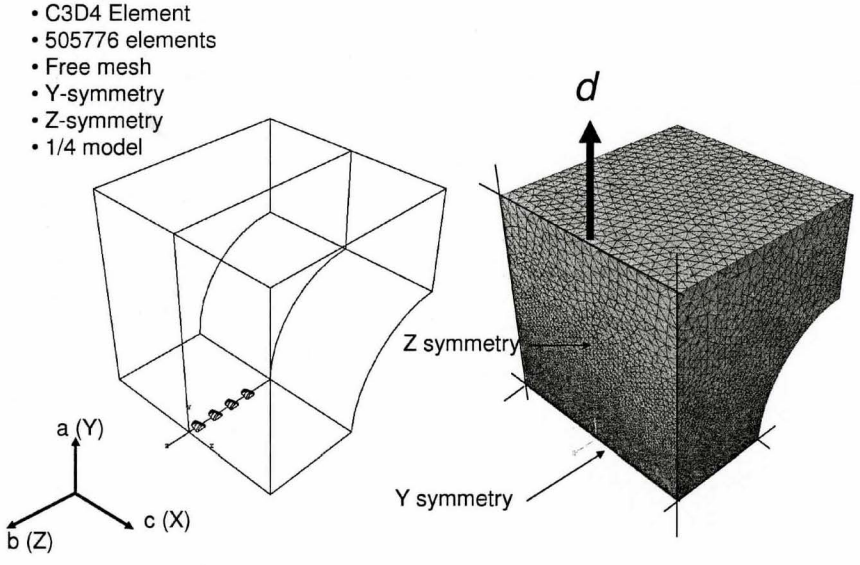

Figure 6.3: FE modeling set-up for the round notched sample containing single layer void array.

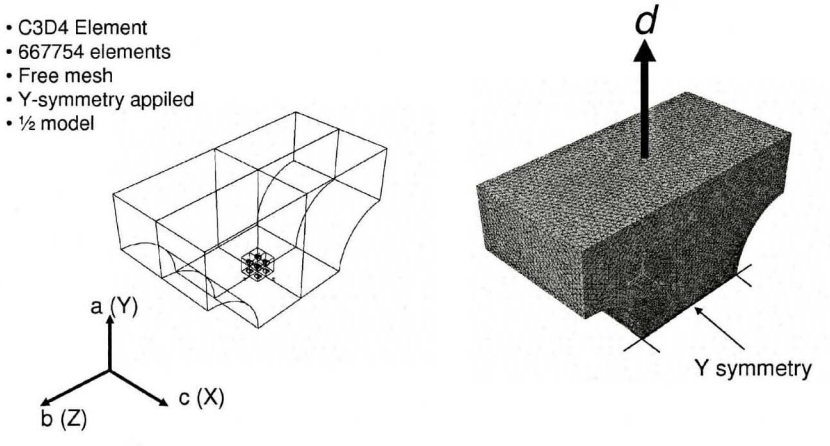

Figure 6.4: FE modeling set-up for the round notched sample containing multi layer void array.

6.3 Stress-strain curves

The experimentally measured maximum principal stress-true strain curves are plotted in Figure 6.5 for the three model materials. The true stress-true strain curve for the smooth FCC 1 material from Figure 5.3 and the stress-strain curve estimated by the FE simulation for the hole-free material are also plotted for comparison. The axial principal stresses for the notched model materials are significantly higher than that of the smooth FCC 1 material because of the high constraint effect by the round notches, and the experimental results for the Hexagonal model material is in good agreement with the FE simulation. The difference between the FE simulation for the hole-free material and the experimental results are due to the existing voids. The FCC 2 Notch model material shows the larger damage effects simply because the material contains more voids in number, while the Hexagonal and the Random model materials exhibit less damage especially in the beginning of the deformation. Although the Hexagonal model material shows slightly higher values of the principal stress than the FEM result, this may be due to the minor experimental variation such as surface hardening by sample machining, or the finer grain size which might be slightly different for individual samples. At any rate, it appears that the Hexagonal material suffered from the least damage during the deformation. Nevertheless, the principal stress for the Hexagonal material does start deviating from the FEM result at a strain of about 1, which is considered to be affected by the void growth and linkage processes. This will be confirmed from the results of the tomograms in the later sections.

6.4 SEM fractography

The fracture surfaces of the model materials were observed by SEM, and the results are shown in Figure 6.6. No significant delamination is observed in any model material. As in the case of the last chapter, clear ridge lines are formed around voids, which is a clear evidence of internal necking. No secondary void populations were observed at the tip of the ridge lines. The population of the smaller voids seen in the fractographs are considered to be originated from the inter-layer boundaries. The fracture strains for individual materials are estimated by the Image J software as 1.74, 1.62 and 2.6 for the FCC 2 Notch material, the Hexagonal material and the Random material, respectively.

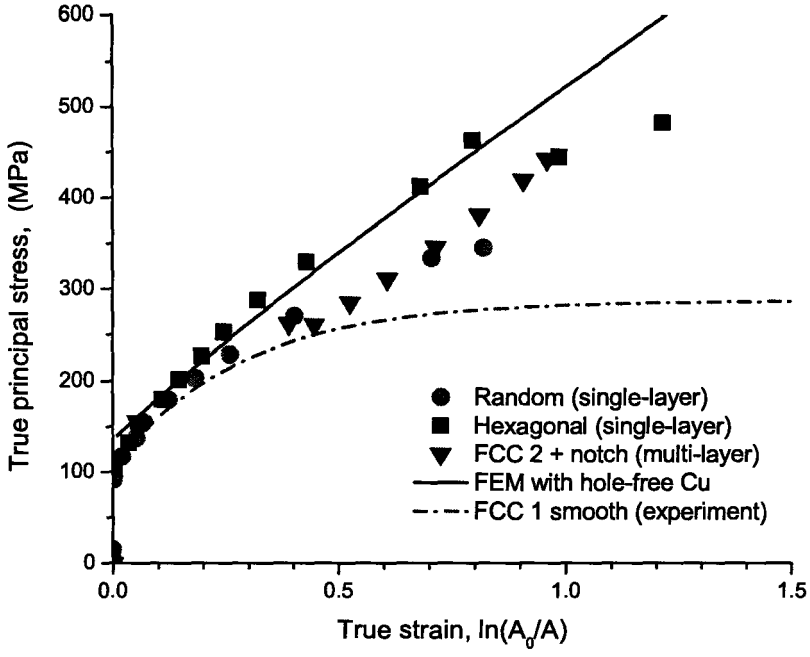

Figure 6.5: True principal stress-true strain curves for the model material with a pair of round notches. The result from FE simulation for the notched hole-free materials as well as the true stress-true strain curves from the experiment (Figure 5.3 are also plotted together.)

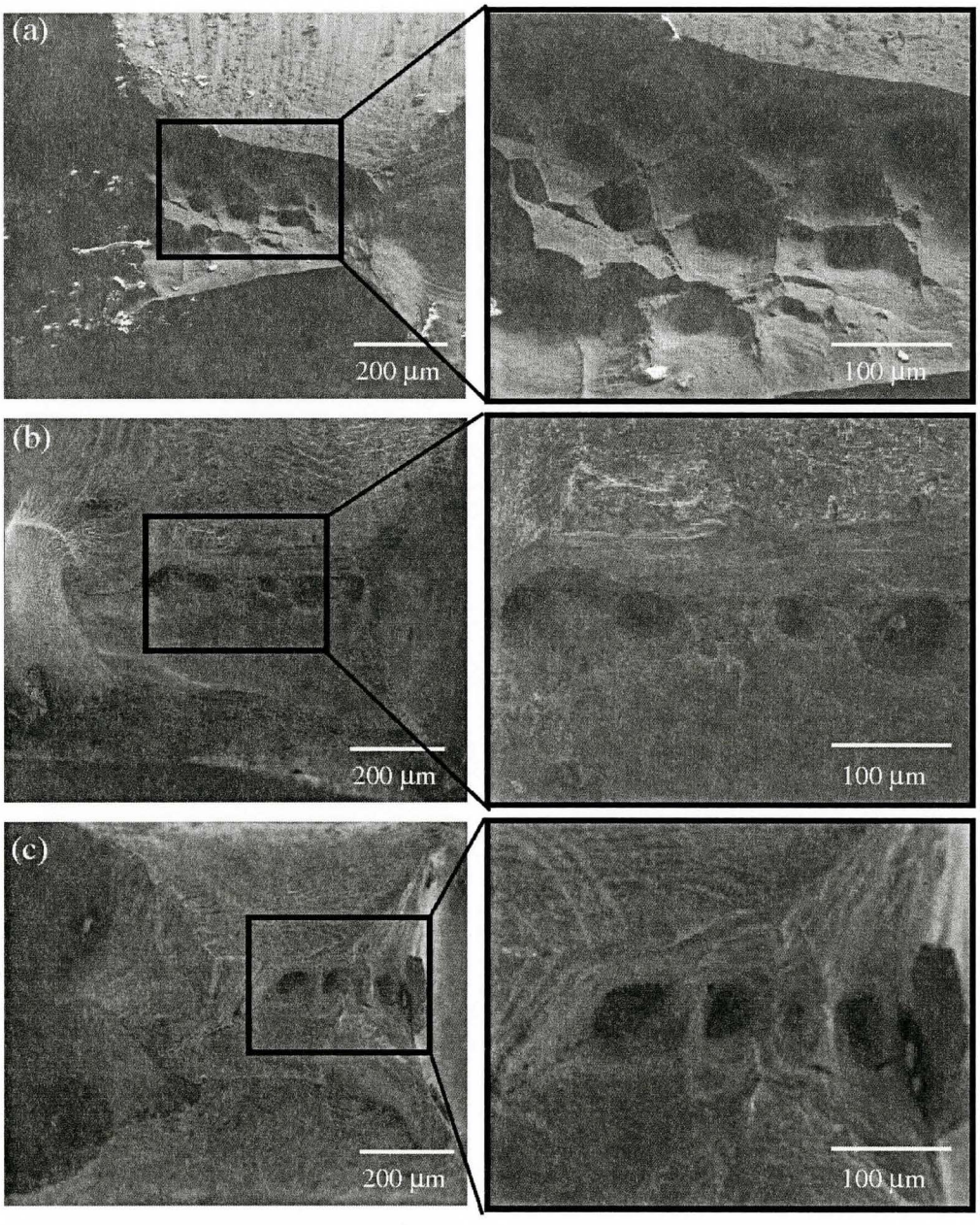

Figure 6.6: SEM fractograpphs for all the model materials in this chapter.(a)The FCC 2 Notch material (b) The Hexagonal material (c) The Random matrial The fracture strains ε_f for individual materials are 1.74, 1.62 and 2.6 respectively.

6.5 Tomography results from the materials containing a single-layer void array

6.5.1 Reconstructed images

The visualized tomograms for the single-layer model materials (Hexagonal, Random) are shown in Figure 6.7 and Figure 6.8. It may appear that the notch geometry does not match with the schematic illustration in Figure 6.1. This is simply because the field of view of the camera used for the radiography was not large enough to capture the entire neck geometry, yet the field of view is still large enough to capture the entire growth processes of voids that link up within the minimum cross sectional area. The void arrays were originally designed to be located at the middle of the tensile specimens, but they ended up with slightly deviated positions due to the quality of the hole alignment, as discussed in section 4.1.3.

For identification of the voids, let us assign the numbers for the individual voids that lead to the linkage as illustrated in Figures 6.9 and 6.10. The local strain due to the void growth ($\ln(a/a_0)$, $\ln(b/b_0)$, $\ln(c/c_0)$) for the individual voids will be plotted and discussed in the later sections.

In the Hexagonal model material, it is clearly demonstrated that the void linkage initiated between the void #1 and #2. The merged void first gets linked with the free surface of the right side in the figure, forming a dendrite-like cylindrical hole with one end being embedded in the matrix (Figure 6.7 (d)). The cylinder then started linking with the neighboring void one by one (Figure 6.7 (e)), by a form of crack propagation, leading to fracture by the intervention of macroscopic shear between the cylinder and the free surface at

the other side (Figure 6.7 (f)).

A similar linking process was also seen in the Random model material. The void #1 linked with the free surface first, then linking up with the neighboring voids sequentially as the numbers assigned. From the tomogram, no macroscopic shear was observed unlike the case in the Hexagonal material (Figure 6.7 (f) and 6.8(f)).

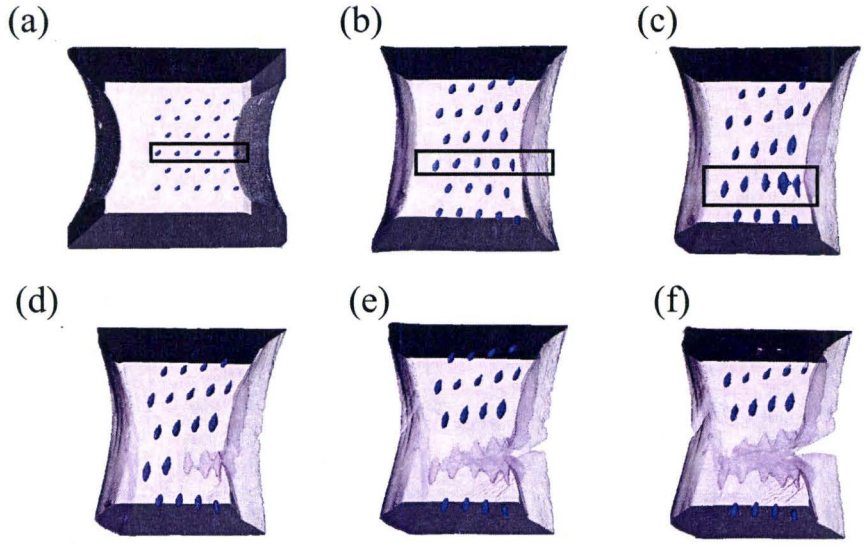

Figure 6.7: The reconstructed images for the hexagonal material. (a) $\varepsilon = 0$ (b)$\varepsilon = 0.43$ (c) $\varepsilon = 0.68$ (d) $\varepsilon = 0.80$ (e) $\varepsilon = 1.21$ (f) $\varepsilon = 1.62$*. (The star symbol * represents that the value was captured from SEM fractography.)

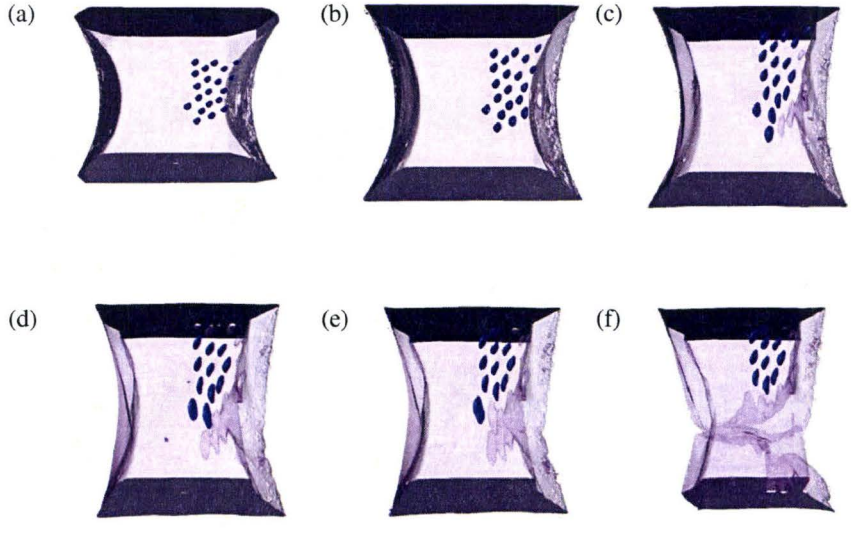

Figure 6.8: the reconstructed images for the random material. (a) $\varepsilon = 0$ (b) $\varepsilon = 0.12$ (c) $\varepsilon = 0.4$ (d) $\varepsilon = 0.71$ (e) $\varepsilon = 0.87$ (f) $\varepsilon = 2.6$*.(The star symbol * represents that the value was captured from SEM fractography.)

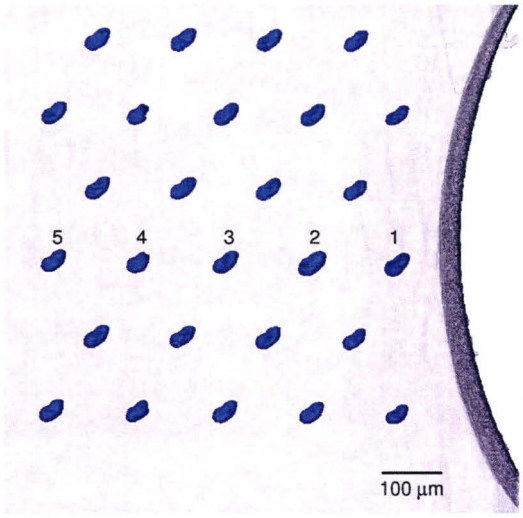

Figure 6.9: The close-up of the void array in the Hexagonal model material and the void identification number.

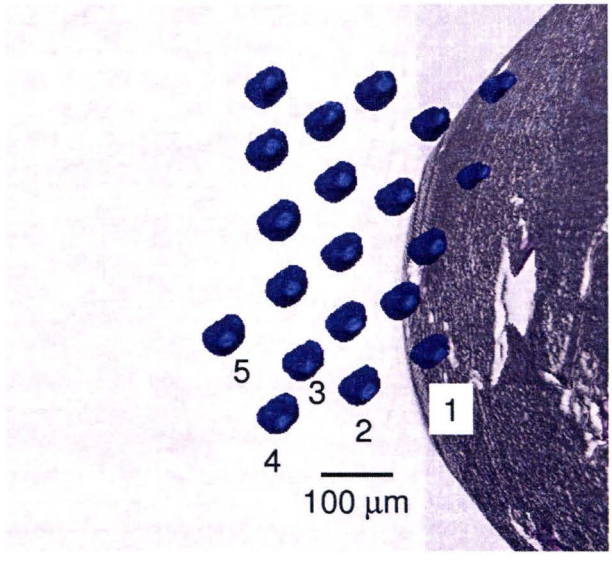

Figure 6.10: The close-up of the void array in the Random model material and the void identification number.

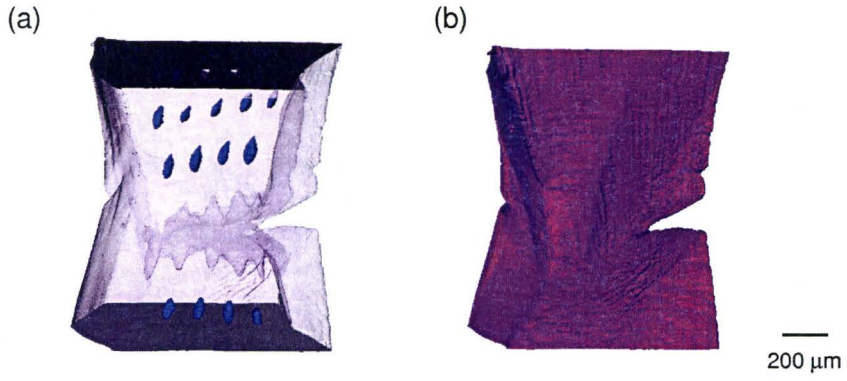

Figure 6.11: The morphology of the deformed Hexagonal model material. (a) the internal void array (b) the exterior.

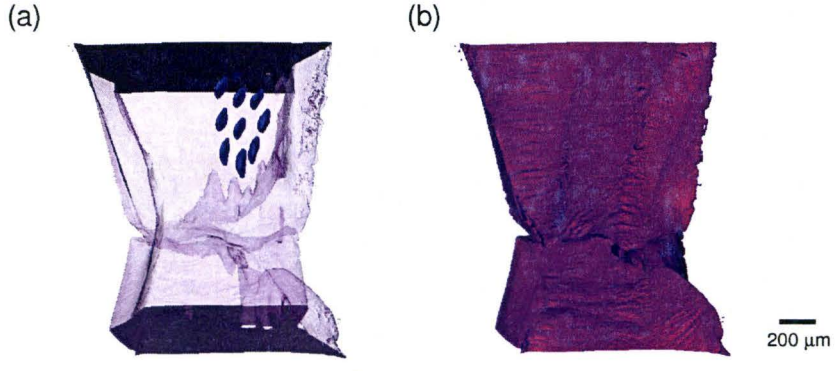

Figure 6.12: The morphology of the deformed Random model material. (a) the internal void array (b) the exterior.

6.5.2 Analysis of void growth: Experiment

The void growth behavior was quantified in terms of the local strain due to the void growth ($\ln(a/a_0)$, $\ln(b/b_0)$, $\ln(c/c_0)$) as in the last chapter. Although the first pair of the voids that leads to linkage was analyzed in the last chapter, all 5 of voids that were numbered in the last section were analyzed by measuring the evolution of principal radii during the deformation. The experimental results of the local strain, estimated from the principal radii measurements, are shown in Figures 6.13 and 6.14. A general observation is that the void growth along c-axis was larger than that along the b-axis, which was observed in both of the two model materials.

When the value of the stress triaxiality is higher than 1.15[1], the definition for the onset of void coalescence is difficult to be applied(See section 5.1). Thus, the strains for void linkage were captured in this chapter instead.

In Figure 6.13 the longitudinal principal radii (a-axis) showed a monotonous increase with the plastic deformation as expected. The principal radii of the void #1 along b-axis showed a significant decrease (i.e. shrinkage) but the other four voids did not shrink as much as the void #1. The lateral void growth of the hole #1 along b-axis exhibited the minimum extremum at a strain of 0.2 and then linkage with the void #2 is completed at 0.68.

On the other hand, the void linkage in Figure 6.14 was faster since the void array were significantly shifted from the central region, which results in the lower value of the stress triaxiality and the higher magnitude of strain concentration around notches. This will be later confirmed by a FE simulation

[1]According to the Rice and Tracey (1969) model, when the stress triaxiality $\sigma_m/Y <$ 1.15, the minor diameter decreases with the plastic strain. However, when $\sigma_m/Y \backsimeq 1.15$, the minor diameter increases with the deformation from the beginning.

(Figures 6.16). As a result, the principal radii of the void #1 in the Random material increase at the early stage of the deformation and led to the linkage at the strain of 0.4. Once the first linkage takes place, the stress/strain concentration around the merged voids (or the cylinder) generates the higher lateral stress (along c-axis) and this makes the principal radii along c-axis increase. The local strain associated with the growth in the principal radius of the void along c-axis showed a monotonic decrease with the deformation.

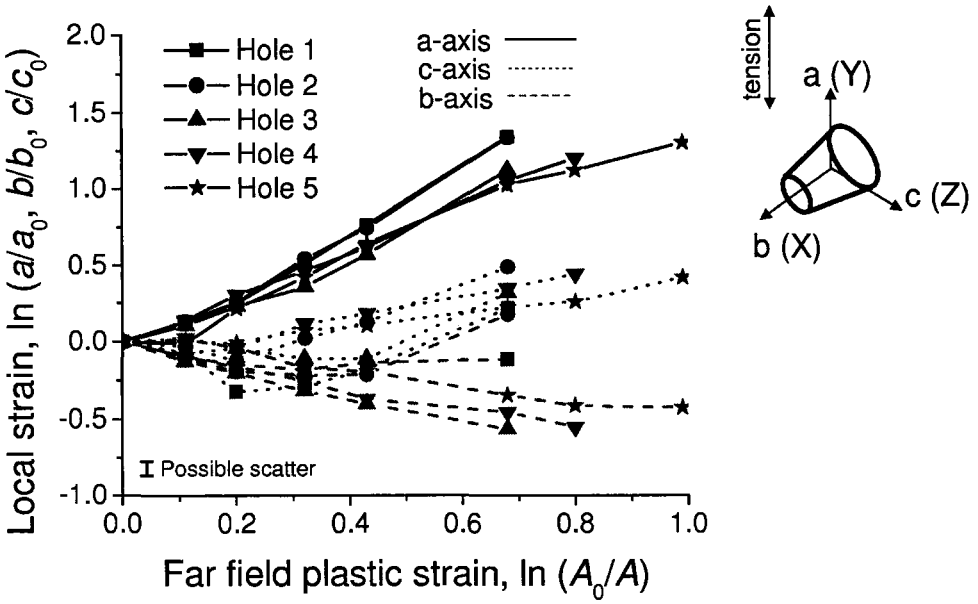

(a) The growth behaviors of the 5 voids.

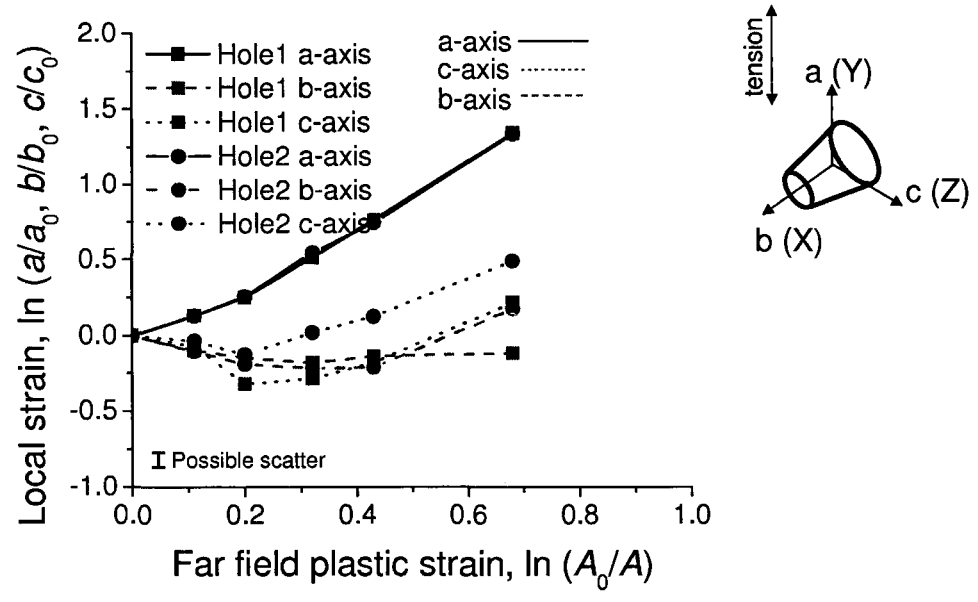

(b) The growth behaviors of the 2 voids that are first to link.

Figure 6.13: The experimentally captured evolution of the local strain due to the void growth plotted with the far-field plastic strain in the Hexagonal model material.

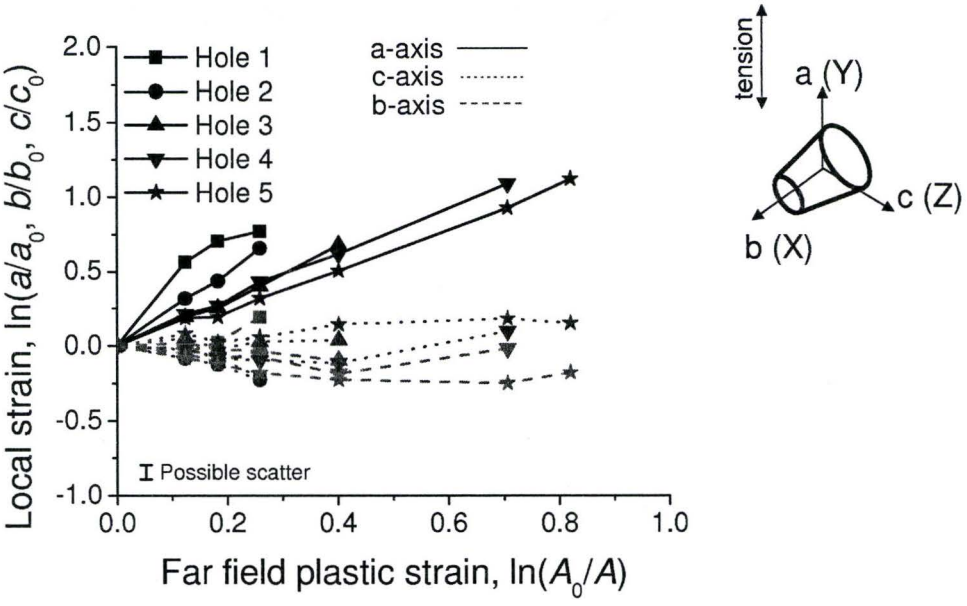

(a) The growth behaviors of the 5 voids.

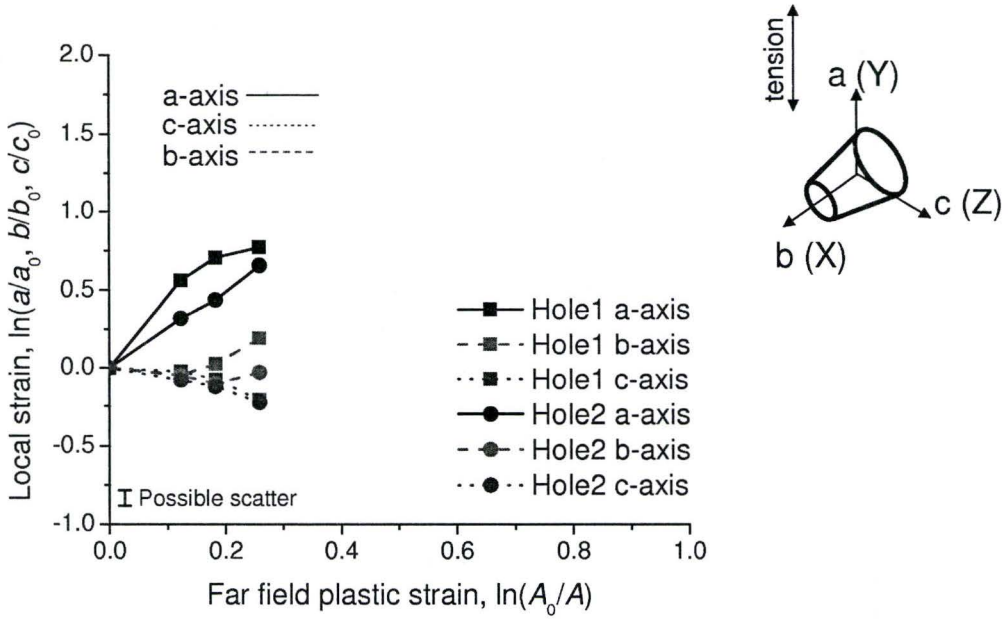

(b) The growth behaviors of the 2 voids that are first to link.

Figure 6.14: The experimentally captured evolution of the local strain due to the void growth plotted with the far-field plastic strain in the Random model material.

6.5.3 Analysis of void growth: FE simulation

This section presents the simulation result from the FE model shown in Figure 6.4. The distribution of principal strain parallel to the tensile axis (PE22) within the cross section is presented in Figure 6.15. This figure indicates that the magnitude of strain concentration near notch surfaces is much larger than that within the central region.

Figure 6.16 shows the void growth behavior for all the 4 voids, and the hole number was assigned as illustrated in the inset of Figure 6.16. To prevent confusing these with the hole numbers (#1, #2, #3, #4, #5) in the experiments (last section), Roman numbers (#I, #II, #III, #IV) are used to represent the hole # in the FE simulation. Figure 6.16 clearly demonstrates that the voids shrink quickly along the b-axis while those are slow along c-axis due to the pair of notches. Another thing observed from Figure 6.16 is that the growth of the outermost void (i.e. $\ln(a/a_0)$ of the Hole #IV) undergoes the fastest evolution while that of the innermost void is the slowest. This conflicts with what we expect from the Bridgman equation. The Bridgman equation suggests that the stress triaxiality has a parabolic distribution with its maximum at the center of the material (i.e. a=0 in equation (6.1)), and thus the volumetric expansion of voids at the center should also be the largest. This contradiction is because the current notch geometry is not sharp or deep enough. To change the stress state, the artificial notches have to be sharp and deep in order for the Bridgman equation to be used, since the Bridgman equation was originally developed to analyze the stress state within the necked region of the material under localization process. However, as mentioned in section 6.1, this is the deepest and sharpest possible notch geometry due to

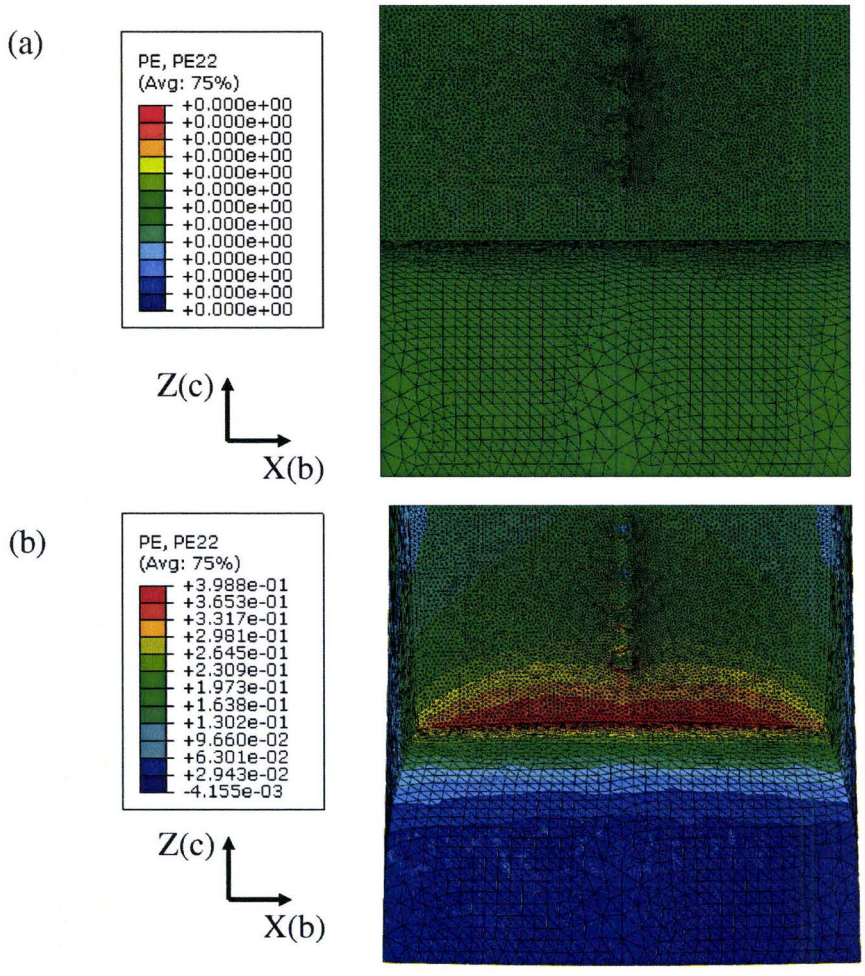

Figure 6.15: The distribution of the principal strain (PE22) of single-layer model material simulated by FE modeling (i.e. Figure 6.3). (a) Far field plastic strain $\varepsilon = 0$ (b) $\varepsilon = 0.22$.

the experimental limitation.

It appears that the contribution by the plastic strain concentration around the notches to the void growth is more significant than that by the stress triaxiality as shown in Figure 6.15, although this tendency becomes less explicit when voids are located near the center.

Figure 6.17 shows the void growth behavior of the hole # I along with the Rice and Tracey void growth model that was used in Chapter 5. This clearly demonstrates the anisotropic behavior of the lateral void growth. In fact, the void shrinkage along b-axis was found to be faster than that of the minor diameter predicted by the Rice and Tracey model.

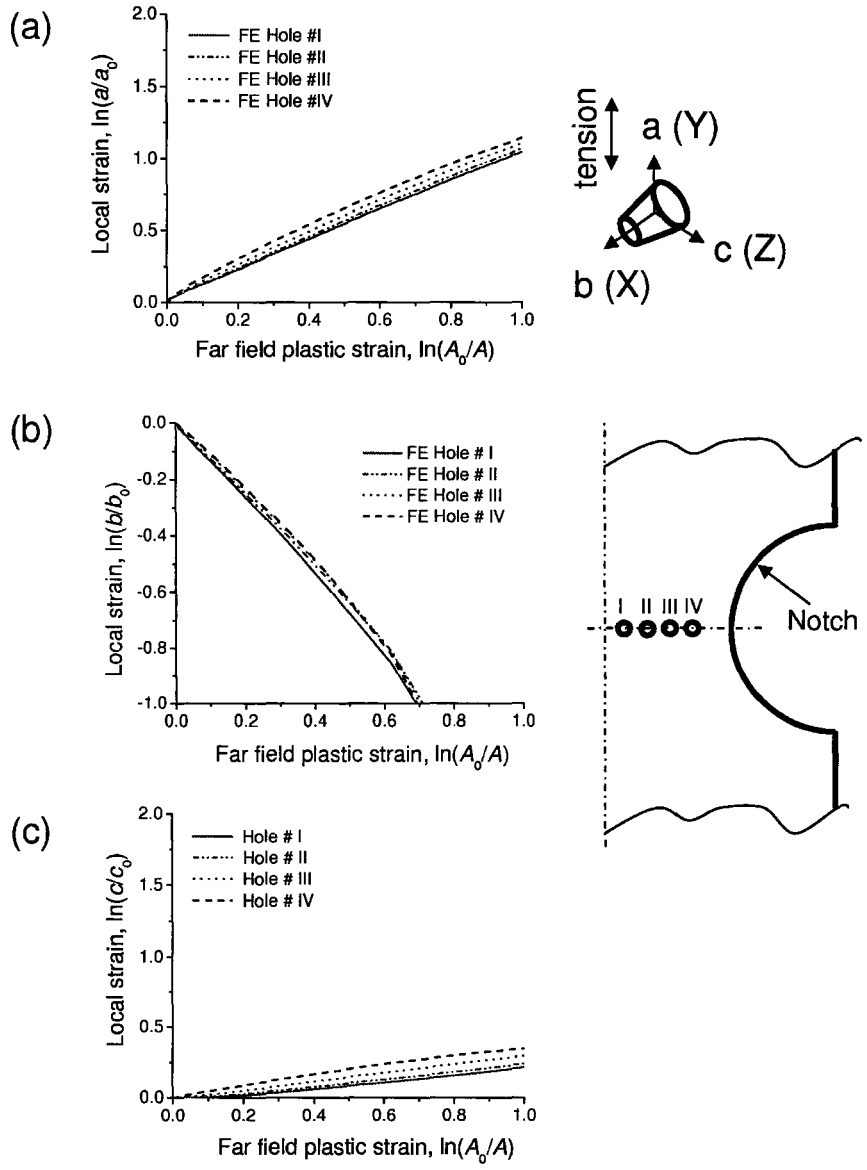

Figure 6.16: The simulation results on void growth behaviors of the 4 voids from the FE model shown in 6.4. (a) a-axis (b) b-axis (c) c-axis. The hole numbers are assigned as shown in the inset.

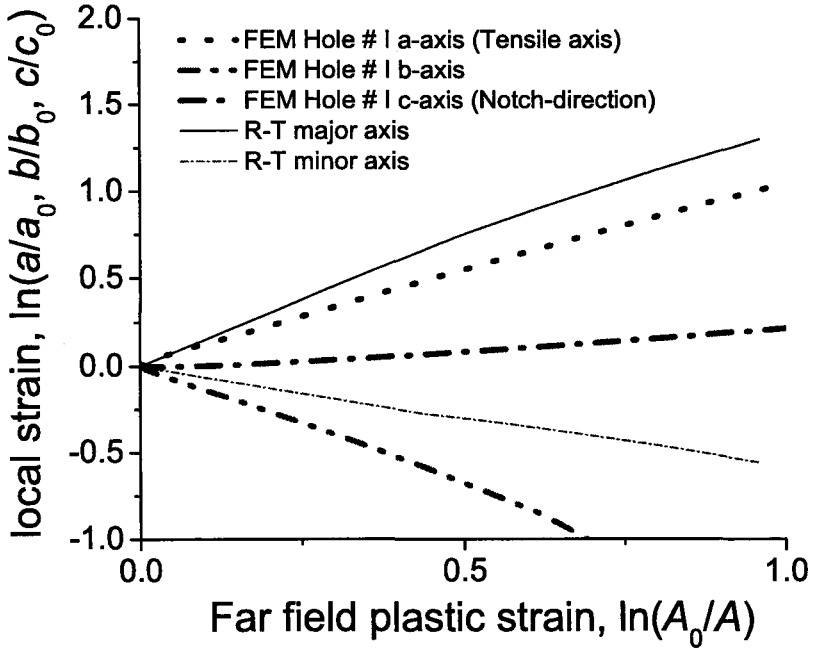

Figure 6.17: The void growth behaviors in a smooth specimen (modeled by the Rice and Tracey model) and a notched sample (by FEM).

6.5.4 Analysis of void growth: Experiments and FE simulations

It is useful to superimpose these simulation results onto the experimental results on void growth presented for comparison, as shown in Figures 6.18-6.19(a). To avoid unnecessary complexity in the figure, only the growth of two voids (the innermost #I and the outermost #IV) out of the 4 voids that appear in Figure 6.3 are plotted.

Most of the holes in Figures 6.18(a) and several in 6.19(a) show that the FE simulation results were in reasonable agreement with experimental results especially in the beginning of deformation. The most serious disagreement between the experiments and the FE simulation is seen in Figure 6.19(b), in which the experimentally captured void growth of hole #1 and #2 in the Random material. This deviation is probably attributed to the fact that the void array in the Random model material was quite shifted in such a way that the hole #1 ended up with a position that is very close to the notch surface. The distance between the notch surface and the hole surface is slightly closer than that is considered in the FE model. Compare Figures 6.10 with Figure 6.15, for example. It seems, however, that the growth behavior of voids that are moderately distant from the notch surface are in the range between the simulated growth behaviors of the innermost (Hole #I) and the outermost voids (Hole # IV).

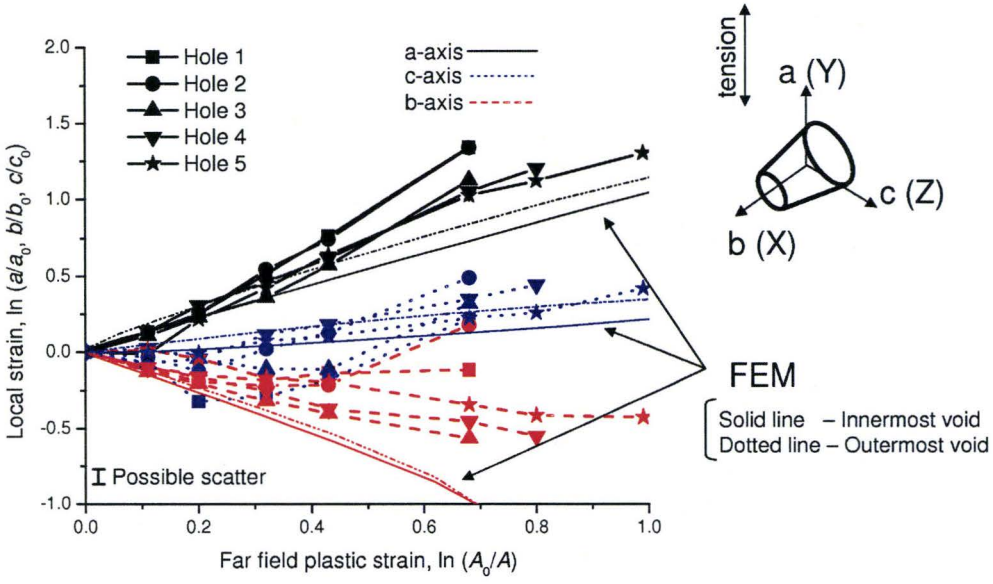

(a) The growth behaviors of the 5 voids.

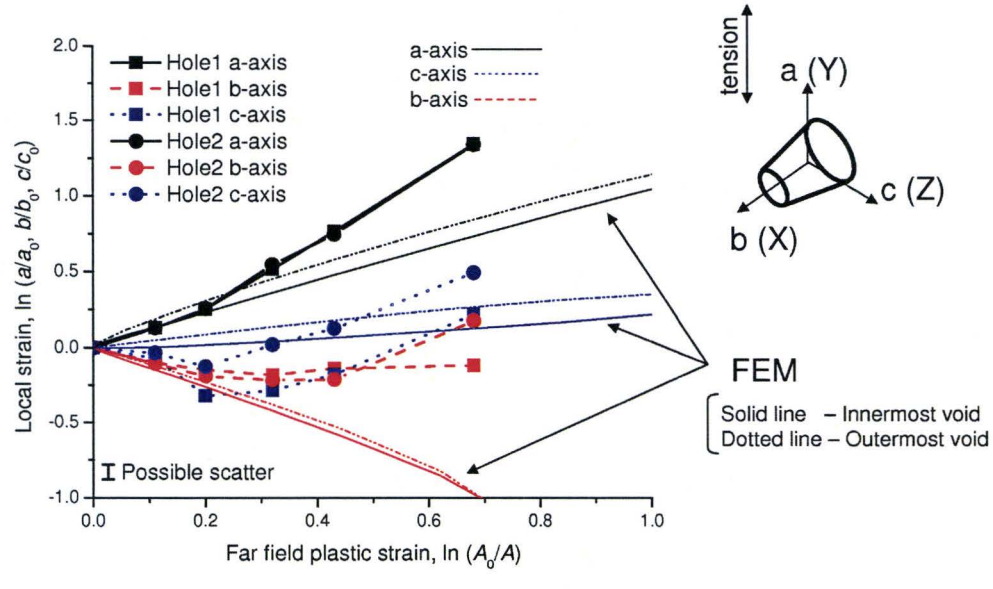

(b) The growth behaviors of the 2 voids that are first to link.

Figure 6.18: The comparison between the results of experimental and the FE simulations in terms of the void growth in the Hexagonal material material.

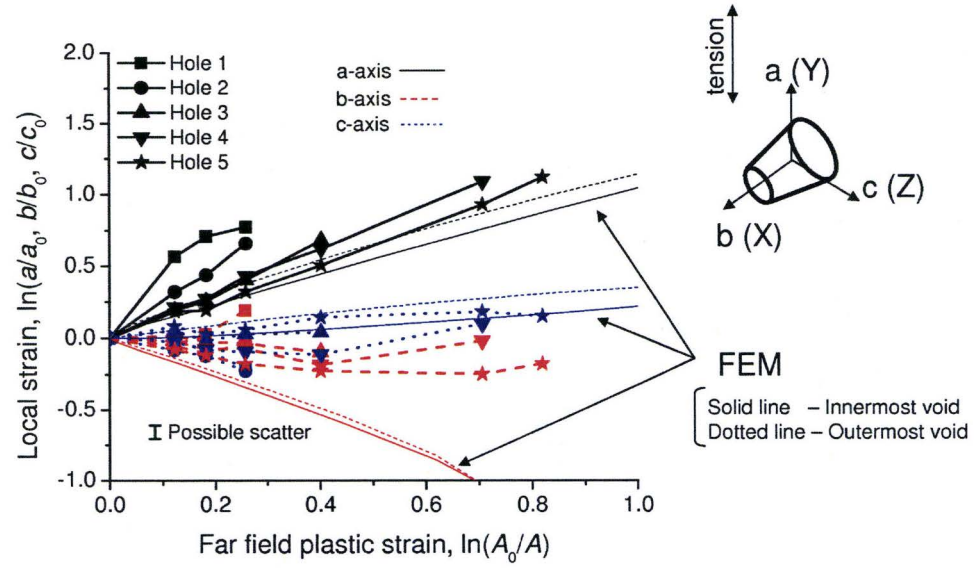

(a) The growth behaviors of the 5 voids.

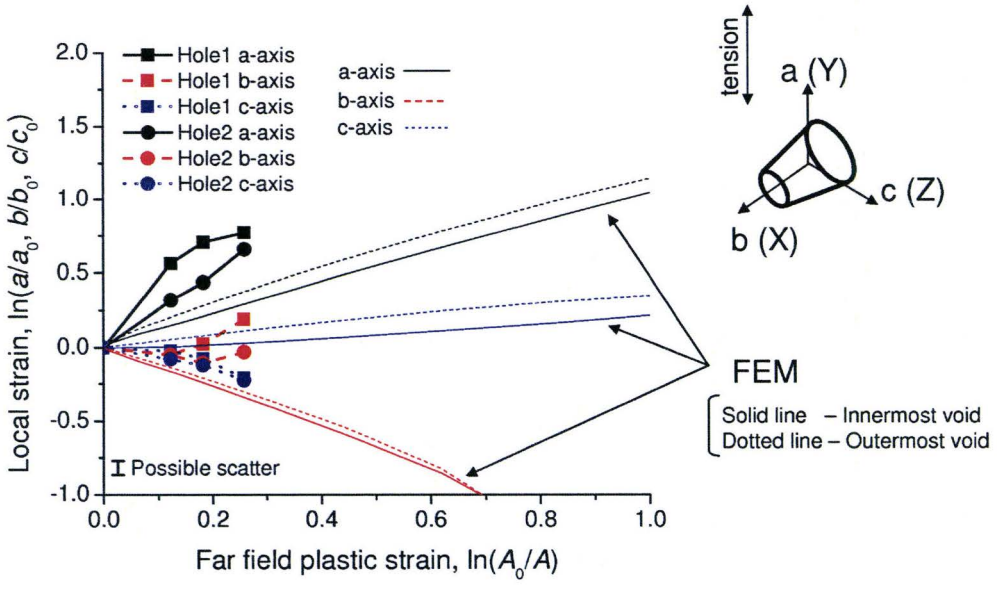

(b) The growth behaviors of the 2 voids that are first to link.

Figure 6.19: The comparison between the results of experimental and the FE simulations in terms of the void growth in the Random material.

6.6 Tomography results from the materials containing multi-layer void array

6.6.1 Reconstructed images

The visualized tomograms for the multi-layer materials (i.e. the FCC 2 Notch) are summarized in Figure 6.20. The void growth and linkage processes were successfully captured. A minor delamination can be seen in the tomograms. However, it is thought that this does not affect seriously the analysis of the first void pair which will be presented in the following section since the first void pair is fairly far from the delaminated region.

6.6.2 Analysis of the first void pair to link

In this section, the principal radii of the first void pair to link were measured as was performed in section 5.6.2. The void growth evolution of the void pair until the linkage event is presented in Figure 6.22. 100% transparency was applied to the metal matrix region numerically by the visualization software. Although it was expected that the linkage occurred along the direction of notches (i.e. c-axis), the void linkage actually would occur along the b-axis, as demonstrated in section 6.5.2. It should be noted that the initially asymmetric distribution of principal stresses due to the notches becomes more symmetric with deformation since this notch is significantly blunted out. Also, necking happened along the b-axis, which generates a significant lateral stress along b-axis. It can be confirmed that the necking developed along the b-axis from the tomograms (Figure 6.21).

The local strains estimated from the growth in principal radii of voids,

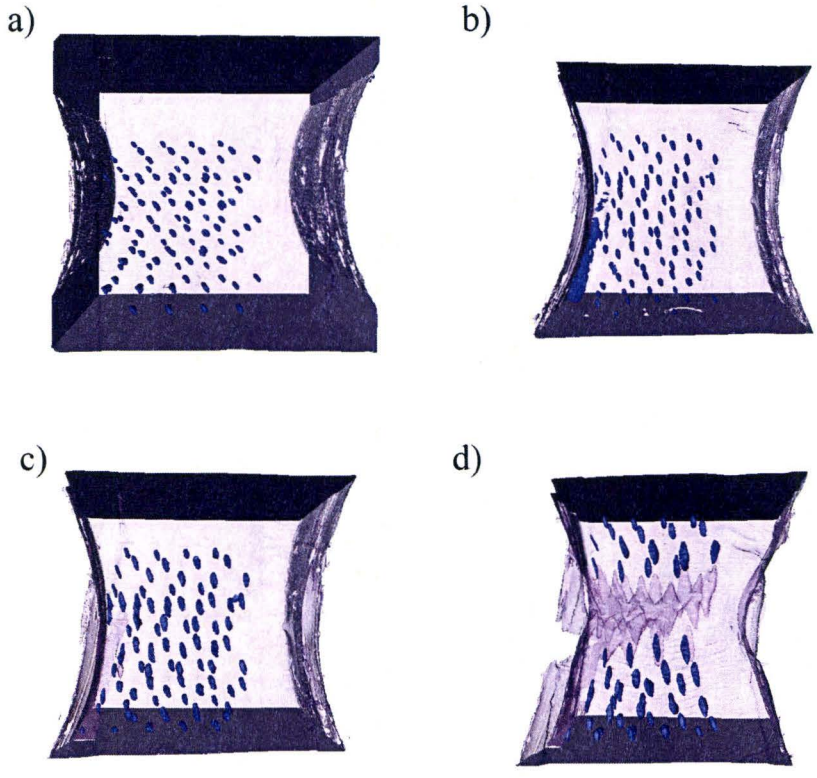

Figure 6.20: Reconstructed images for the FCC 2 Notch material. (a) $\varepsilon = 0$(b) $\varepsilon = 0.39$ (c) $\varepsilon = 0.45$ (d) $\varepsilon = 0.99$

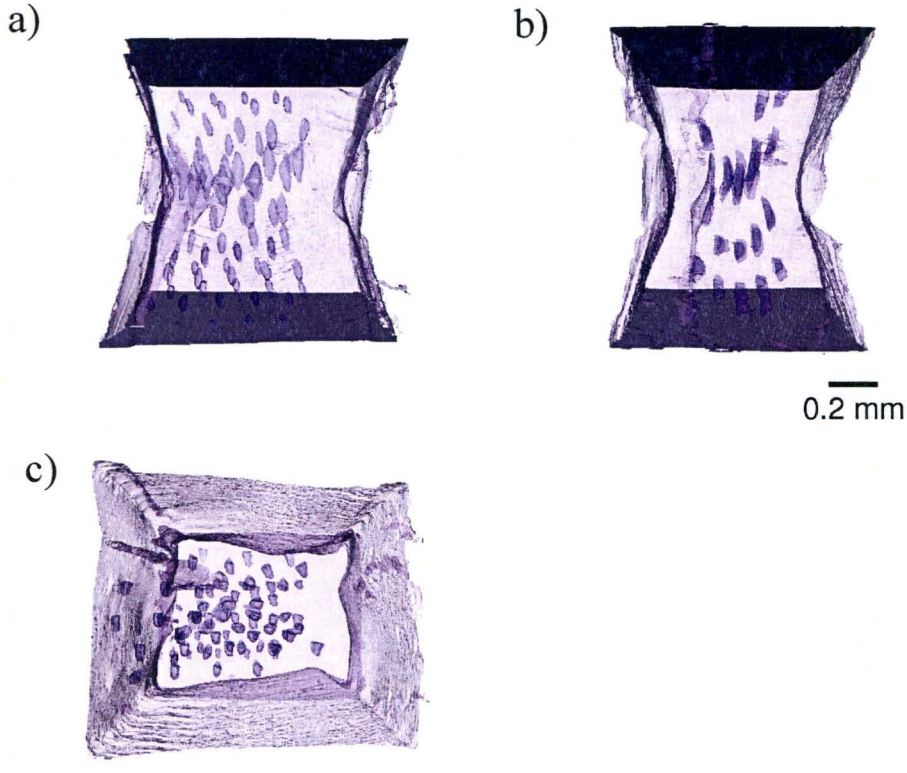

Figure 6.21: Reconstructed images from the three directions. $\varepsilon = 0.99$. Significant necking has already taken place along b-axis. (a) Frontview (b) Sideview (c) Endview.

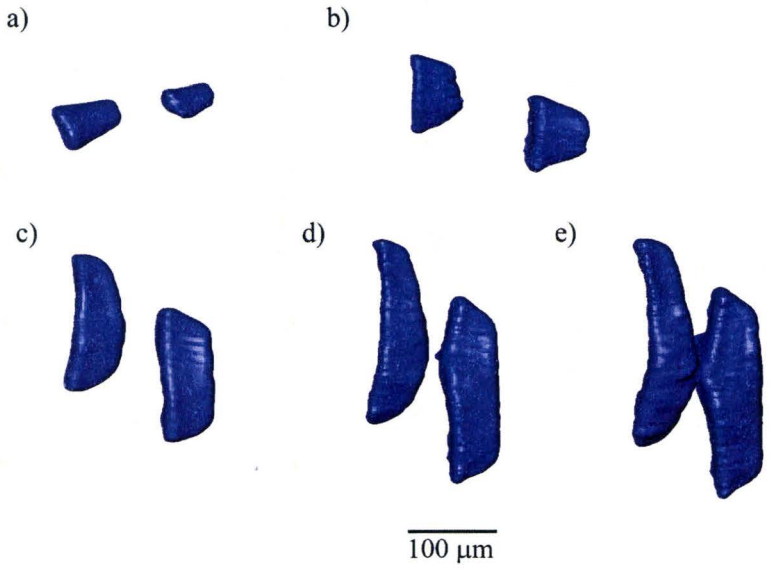

Figure 6.22: Reconstructed images for the FCC 2 notch material. (a) $\varepsilon = 0$ (b) $\varepsilon = 0.39$ (c) $\varepsilon = 0.45$ (d) $\varepsilon = 0.71$ (e) $\varepsilon = 0.99$.

the volumetric strain and the inter-void distance were measured as performed in section 5.6.2, and their evolutions as functions of far field plastic strain $\ln(A_0/A)$ are shown in Figure 6.23. Figure 6.23 (a) clearly shows that the void growth probably related to coalescence along c-axis was faster than that of the b-axis due to the existence of notches. Although the minimum extremum can be observed both in the b- and c-axes, it is difficult to conclude whether they are due to the high stress triaxiality or the onset of void coalescence.

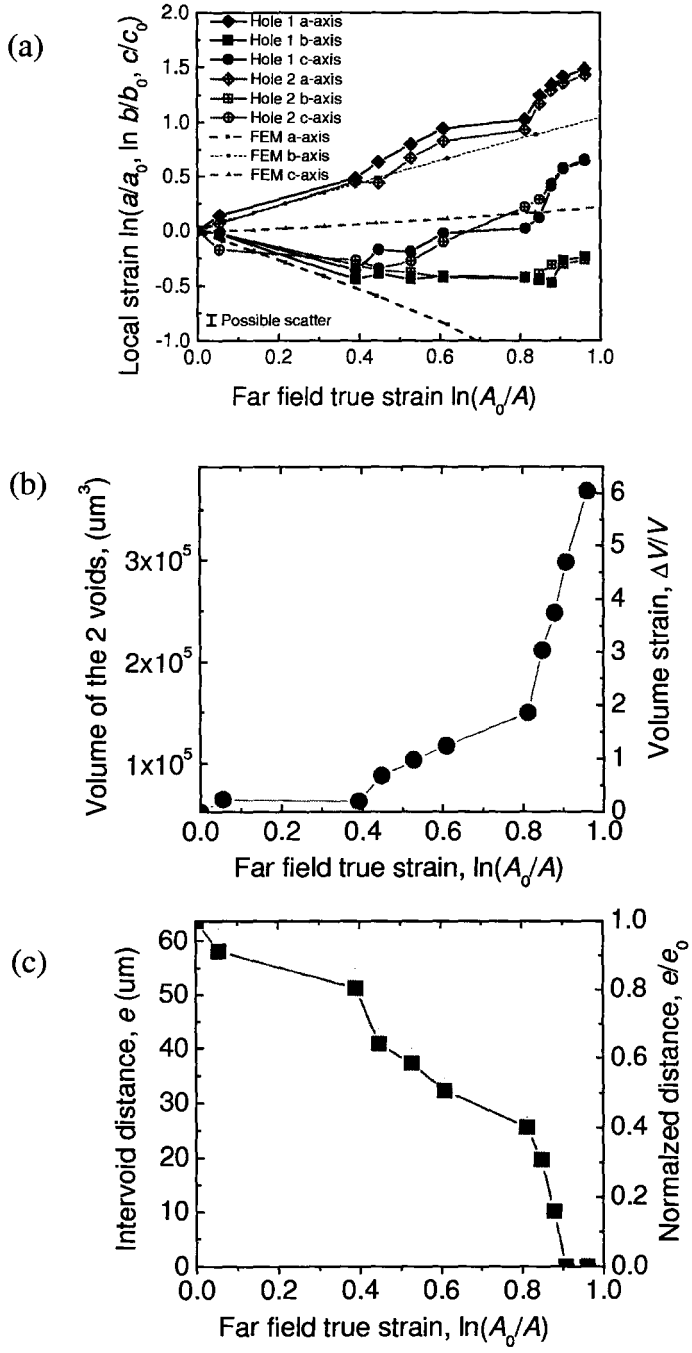

Figure 6.23: Various parameters representing the Void growth behavior for the FCC2 Notch sample plotted as a function of the far field plastic strain. (a)Local strain estimated from void growth (b) Evolution of the void volume. (c) Evolution of the intervoid distance.

6.7 Discussion

6.7.1 Influence of notches on void linkage strains

There is a remarkable influence of the notches on void growth behavior, as observed both in the experiments and the FE simulations. The next question is whether the notches actually influence the linkage or not. The experimentally captured void coalescence/linkage strains of each model material in this chapter are summarized in Table 6.2. Needless to say, void coalescence/linkage events are strongly influenced by the initial void volume fraction; the higher volume fraction, the earlier coalescence. In order to discuss the influence of the stress state changed by notches on void linkage, the model materials that have the same void volume fraction must be subjected to the comparison. Again, due to the hole alignment issue (see section 4.1.3), the initial void volume fractions of the model materials are not uniform (i.e. holes in some model materials are closer), as shown in Table 6.2. It appears that a good comparison can be made between the FCC 2 Notch model material and the FCC 1 and FCC 2 model materials, since all of these model material have similar values of the initial void volume fractions. However, the coalescence/linkage occurred along the *b*-axis direction which is perpendicular to the direction of notches in these model materials, and thus it is very difficult to draw any conclusion about the notch effect. Misalignment between layers means that voids are closer in the *b*-axis than the c-axis. This effect dominates over the *c*-axis notching. Thus, as a whole, the multi-layered model materials in the current experiments (both in chapter 5 and 6) ended up with void arrays in such a way that the linkage always happened along the *b*-axis direction.

A better comparison, however, can be made between the Random model

material and the Pure Cu 1 material that was extracted from the work by Weck et al. (2008b). The void volume fractions are similar, and the linkage direction are parallel to the direction of notches in both the model materials, except for the difference in the stress triaxiality value by existence or nonexistence of notches. This comparison reveals that the linkage in the Random model material ($\varepsilon_{linkage} = 0.40$) was earlier than that of the smooth model material in Weck's work ($\varepsilon_{linkage} = 1.01$). We suppose this difference to be purely contributed by the existence of notches.

The linkage strain in the Hexagonal model material also supports this idea. Since the initial void volume fraction in the Hexagonal model material is much smaller ($V_f^0 = 0.7$ %) than that of the Random model material ($V_f^0 = 4.69$ %), the linkage strain in the Hexagonal model material has to be much higher. As will be shown later, the Thomason model proposes the coalescence strain for the material containing voids with their volume fraction of $V_f^0 = 0.7$ % is 1.03, which seriously overestimates the experimentally captured linkage strain in the Hexagonal model material ($\varepsilon_{linkage} = 0.66$). Within the range of the current observation, it seems that the linkage strains in the notched specimen ($\sigma_m/Y = 0.47 \sim 0.55$) are smaller compared to the smooth specimens ($\sigma_m/Y = 0.33$).

6.7.2 Comparison with the Brown and Embury model

The experimentally captured void length and the intervoid distance were plotted to predict the void coalescence strain by the Brown and Embury model (Brown and Embury, 1973), as shown in Figure 6.24. The intersections of the void length and the intervoid ligament length in the figure provide the predicted coalescence strains. Here, two different definitions of the intervoid lig-

Experiments								
	# of layer	σ_m/Y	V_f^0	$V_f^{critical}$	$\varepsilon_{coalescence}$	$\varepsilon_{linkage}$	$\varepsilon_{fracture}$	Direction of linkage
Cu FCC 1	5	0.33	4.40%	26.70%	0.76	0.96	1.73	b-axis
Cu FCC 2	5	0.33	4.40%	24.30%	0.52	0.85	1.51	b-axis
Cu Hexagonal	1	0.47	0.70%	14.2% ~	N/A	0.68	1.62	c-axis
Cu Random	1	0.47	4.69%	3.57% ~ 60.7%	N/A	0.40	2.6	c-axis
Cu FCC Notch	1	0.55	5.15%	24.7% ~ 59.4%	N/A	0.99	1.74	b-axis
Pure Cu 1	1	0.33	0.90%	N/A	0.5~0.77	1.01	N/A	c-axis

Table 6.2: The experimentally captured coalescence/linkage strains for the notched model materials and the smooth samples (from Chapter 5).

ament length were adopted: the surface-to-surface intervoid distance and the center-to-center intervoid distance. The original Brown and Embury model does not stipulate which one is supposed to be used. Both methods however underestimated the void linkage. If we were able to capture the onset of void coalescence, the underestimation with respect to the onset of coalescence would be much larger. In the current situation, there are two significant contribution in this error. One is the fact that the Brown and Embury model does not take into account the 3D array as discussed in last chapter. The second is another drawback of this model, that is the superimposed hydrostatic stress cannot be modeled properly. Weck et al. (2008a) proposed that the Brown and Embury model with the use of the surface-to-surface intervoid distance instead of the center-to-center intervoid distance provides a better prediction for the notched composite specimens. In the current experiment, too, the surface-to-surface intervoid distance gives a better prediction compared to the center-to-center intervoid distance, but the underestimation is still significant due to the constraint of the surrounding matrix in the model materials.

6.7.3 Comparison with the Thomason model and the Pardoen and Hutchinson model

Unlike the last chapter, the Rice and Tracey model cannot be used as the input for the void coalescence modeling since the void growth behavior of the model materials in this chapter exhibits a significant planar anisotropy due to the pair of notches, which cannot be properly modeled by the Rice and Tracey model. Instead, the values of principal radii estimated by FEM were directly substituted to the individual void coalescence models namely, the Thomason

model and the Pardoen and Hutchinson model, respectively.

In using these models, the initial void volume fraction was estimated in the same manner as outlined in section 5.7, and the evolution of the plastic constraint factors for internal necking was obtained as shown in Figure 6.25. The significant influence of the work hardening exponent on the plastic constraint factor for internal necking, especially for the Hexagonal model material, is proposed by the Pardoen and Hutchinson model. However, as discussed in section 5.7, the difference in the coalescence strain between the two models is not as remarkable since the work hardening rate becomes significantly smaller by the time the coalescence happens. The right hand side (RHS) is also different from that in the last chapter, estimated from the FE simulation. Due to the existence of the notches, the plastic constraint factor is slightly higher than unity from the beginning of the deformation, and its evolution with the plastic deformation can be estimated as shown in the figure. The linkage strains that were captured in the experiments and the values predicted from these void coalescence models are summarized in Table 6.3.

The Thomason model predicts the linkage strain of the Random model material with a good accuracy (error of 10%), but it was not very successful to predict the void linkage in the other notched materials. The overestimation by the Pardoen and Hutchinson model overestimates linkage strain by a significant amount.

In the current set of experiments, the stress triaxiality varies at the position within the tensile samples (i.e. maximum at the center), and also it keeps changing over the deformation as the notch geometry changes. This makes it difficult to apply the Thomason model and the Pardoen and Hutchinson model directly to the current experiments. Moreover, the models predicts

onset of coalescence while the data is for linkage. It might therefore be unfair to conclude that those models do not adequately account for stress triaxiailty based on the current experiments. Nevertheless, it seems that one should be cautious in using these models for void coalescence/linkage events within the materials with notches.

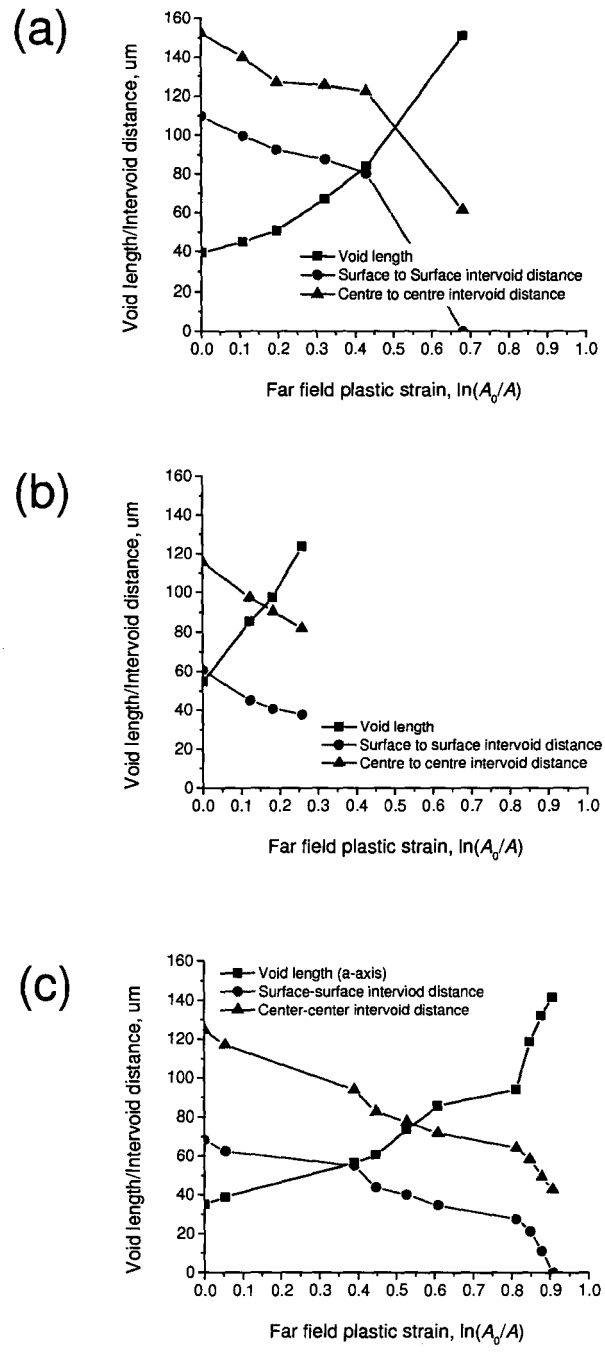

Figure 6.24: The void length and the intervoid distance between the first void pair to linke plotted as functions of the far field plastic strain. (a) Hexagonal (b) Random (c) FCC Notch

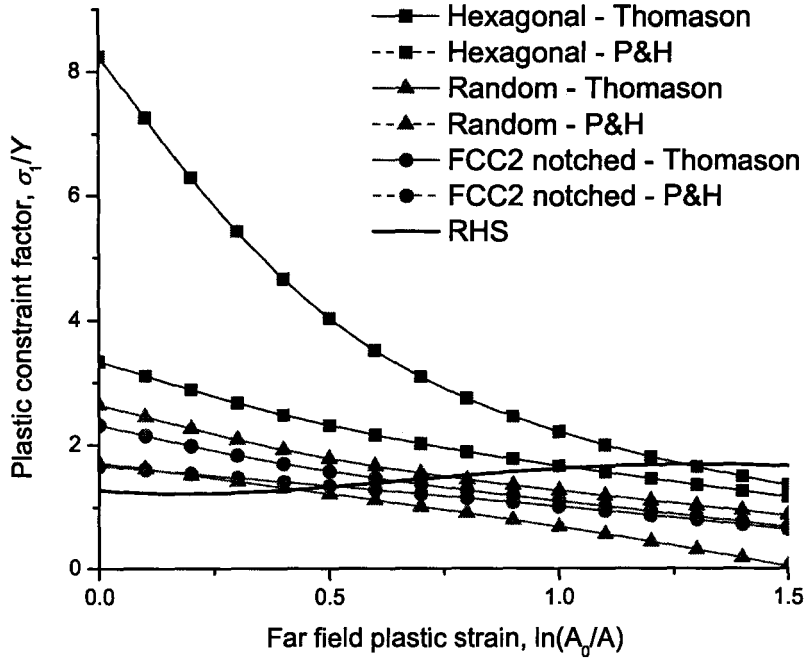

Figure 6.25: The evolutions of the plastic constraint factor for the internal necking by the Thomason model and the Pardoen and Hutchinson model.

Table 6.3: Comparisons of the experimental results of void coalescence and linkage strains with the various values predicted from the models.

		Hexagonal	Random	FCC Notch
	$V_f^0(\%)$	0.7	4.69	5.15
Experiments	Linkage	0.68	0.40	0.99
Models	Brown-Embury	0.51	0.16	0.54
	Difference (%)	-25.0	-60.0	-45.5
	Thomason	1.03	0.44	0.51
	Difference (%)	51.5	10.0	-48.5
	Pardoen-Hutchinson	1.29	0.76	0.66
	Difference (%)	89.7	90.0	-33.3

6.8 Chapter Summary

A series of model materials containing a pair of notches were fabricated and subjected to the *in situ* X-ray computed tomography under tension. The knowledge obtained in this chapter is summarized as below.

- Void growth and coalescence in model materials with a pair of notches were successfully visualized.
- Quantitative analyses on void growth were performed by measuring principal diameters of voids, showing a significant anisotropy. The void growth along the notch direction (c-axis) was much faster in comparison with that of b-axis.
- For single-layer model materials, it was found that not only the void growth but also the linkage strains are accelerated along the notches.
- The prediction of void coalescence/linkage in notched samples is difficult because of continuous change in notch geometry. Existing model are generally not able to accurately predict the strain to coalescence in these samples.

Chapter 7

Effect of void sheeting and work hardening

In this chapter, the results from the experiments performed at SPring-8 on the BL20XU beamline are presented. The materials used in this chapter consist of Glidcop and brass. Making use of Glidcop allows us to study the effect of the secondary void population nucleated at Al_2O_3 nanoparticles, and the experiments using brass will elucidate the influence of the difference in work hardening behavior on void growth and coalescence events, by comparing the results of pure copper. Since the continuous tomography technique explained in Chapter 5 is not available at this beamline, it becomes extremely difficult to capture the onset of void coalescence. Thus, we focus on capturing the linkage instead of the onset of coalescence.

Table 7.1: Nomenclature for the samples used in chapter 7.

Sample name	Number of layer embedded	Type of array
Glidcop Rectangular	1	Rectangular array
Glidcop Line	1	One line of voids located near the sample surface
Glidcop FCC	3	FCC type array
Brass Rectangular	3 (1)	Rectangular array

7.1 Materials and Experimental Procedures

Three model materials made of Glidcop and one model material made of brass were produced by the method as described in Chapter 3. The sample nomenclature is summarized in Table 7.1, which also provides the details of the void array for the individual model materials. As-diffusion-bonded sheets were cut into the shape as illustrated in Figure 7.1. The thickness and width were set to be 0.2 mm due to the limitation of the brilliance of the X-rays (See section 4.3.2). The *in situ* tomography scans coupled with tensile deformation were performed at room temperature in air, and the tensile specimens in tension were located 55 mm ahead of the detector. The cross-head speed was set to 0.0004 mm/sec (i.e. 4.0 x 10^{-6} ms^{-1}), which corresponds to a strain rate $\dot{\varepsilon}$ = 1.0 x 10^{-8} s^{-1}. The tensile deformation was occasionally paused for tomographic scans in such a way that typically 4$\sim$7 scans are performed for each model material. Since there is no supercomputer at SPring-8, the tomographic reconstructions were carried out by PC as described in section 4.5.

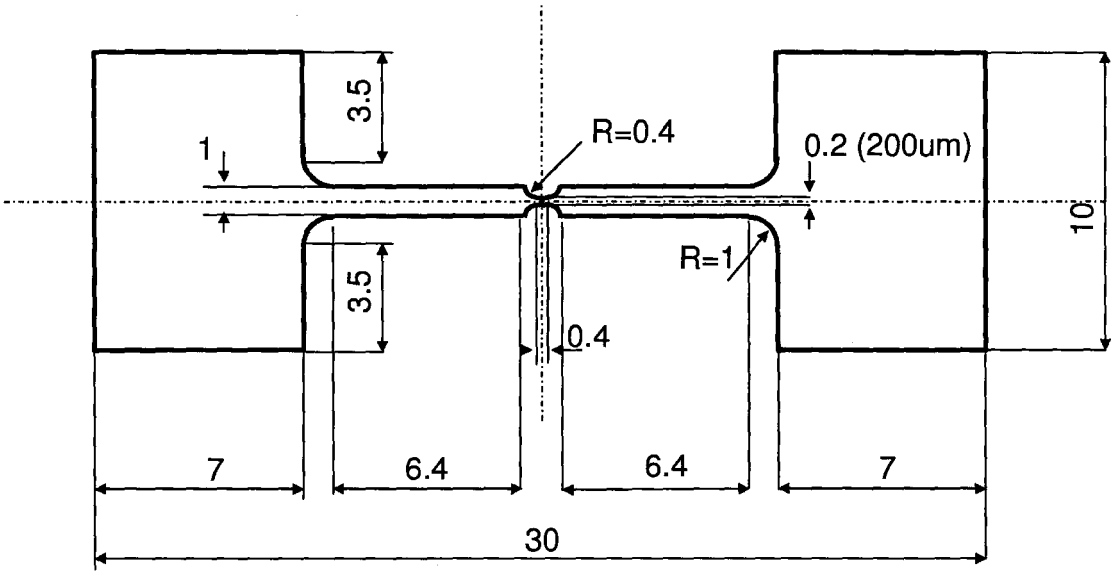

Figure 7.1: The schematic drawing of the tensile specimens tested at SPring-8 BL20XU. The thickness is 0.2 mm.

7.2 Stress-Strain curves

The true stress-true strain curves for the model materials are shown in Figure 7.2. As discussed in Chapter 5, the true stress plotted here is defined as the load measured divided by the current net area captured from the tomograms. Again, the number of the data are limited to the number of tomographic scans performed for each model material. Therefore, the Voce equation (Equation (5.5)) was used to interpolate the data points. The curve for the hole-free pure copper is also plotted as a guideline. The initial yield strength of the Glidcop model materials are about 4 times as high as that of the hole-free pure copper materials, mainly because of the dispersion-strengthening by Al_2O_3 particles. The work hardening of the Brass Rectangular material is remarkable even though its yield strength is comparable with that of pure copper. Figure 7.3 shows the derivatives $d\sigma/d\varepsilon$ (=WHR) plotted with thinner lines using the

Table 7.2: The parameters for the Voce fitting

	C_1	C_2	C_3
Glidcop Rectangular	456	122	6.97
Glidcop Line	681	283	1.48
Glidcop FCC	571	186	4.07
Brass Rectangular	255.8	156.5	4.8

same type of line (solid, broken, dotted for the brass, the Glidcop and pure Cu materials, respectively). The intersections of the flow stress and the WHR give the necking strains for each model materials.

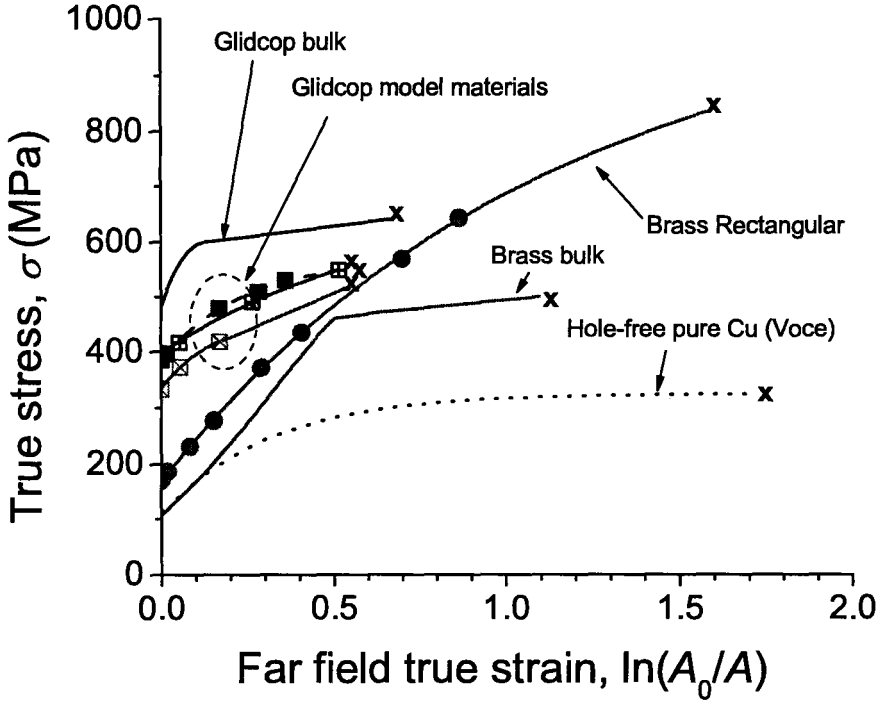

Figure 7.2: True stress - true strain curves for the various model materials. The result for pure Cu (Chapter 5) is also plotted for a reference.)

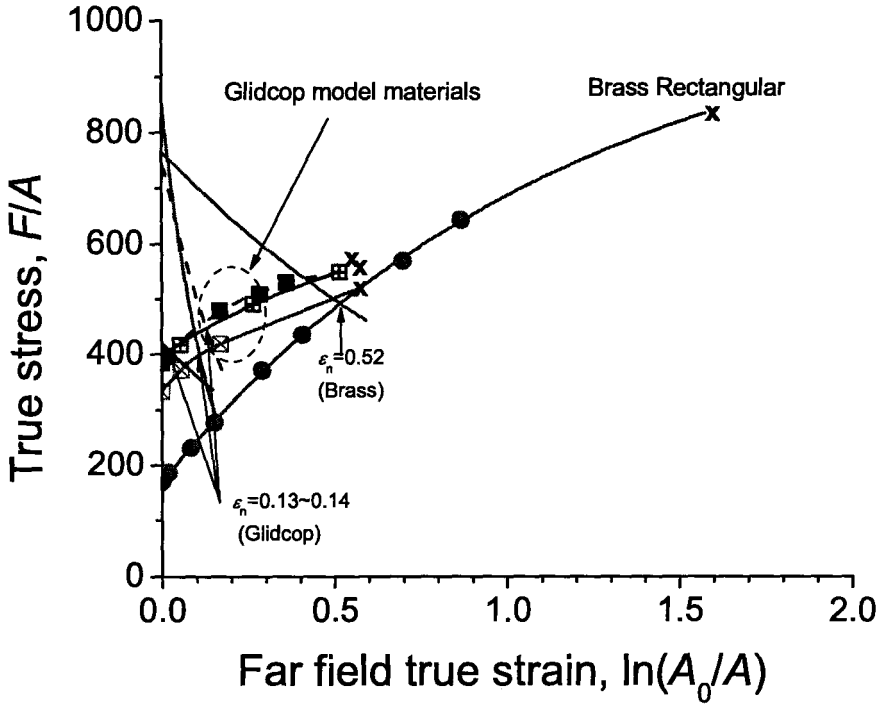

Figure 7.3: True stress - true strain curves for the various model materials with their derivatives $d\sigma/d\varepsilon$. the derivatives are plotted with thinner lines.

7.3 SEM Fractography

The fracture surfaces of the model materials were observed by SEM, as shown in Figures 7.4 and 7.5. Significant delamination was observed in the Glidcop Rectangular material (Figure 7.4 (a)) and the Glidcop FCC material (Figure 7.5 (a)), while the Glidcop Line material (Figure 7.4 (b)) and the Brass Rectangular material (Figure 7.5 (b)) ended up with nearly no delamination. The secondary population of voids nucleated from Al_2O_3 particles were observed at the intervoid ligament in Glidcop. Close examination of the intervoid ligaments in the Glidcop Rectangular material (Figure 7.4 (a)) and the Glidcop FCC material (Figure 7.5 (a)) revealed that some minor delamination first occurred and the void linkage took place by void sheeting. This will be later demonstrated by the results of tomography. In these materials, the dimples due to the secondary population of voids are in relatively equi-axed in shape, while the dimples in the ligament of the Glidcop Line material are indicating the fact that shear coalescence intervened. This is also later validated by tomography. The other part of the fracture surfaces in this material also exhibited a number of elongated dimples probably due to macroscopic shear that would have terminated the fracture process. The fracture surface of the Brass Rectangular material exhibited no secondary void populations except for the small voids originating at the inter-layer boundaries.

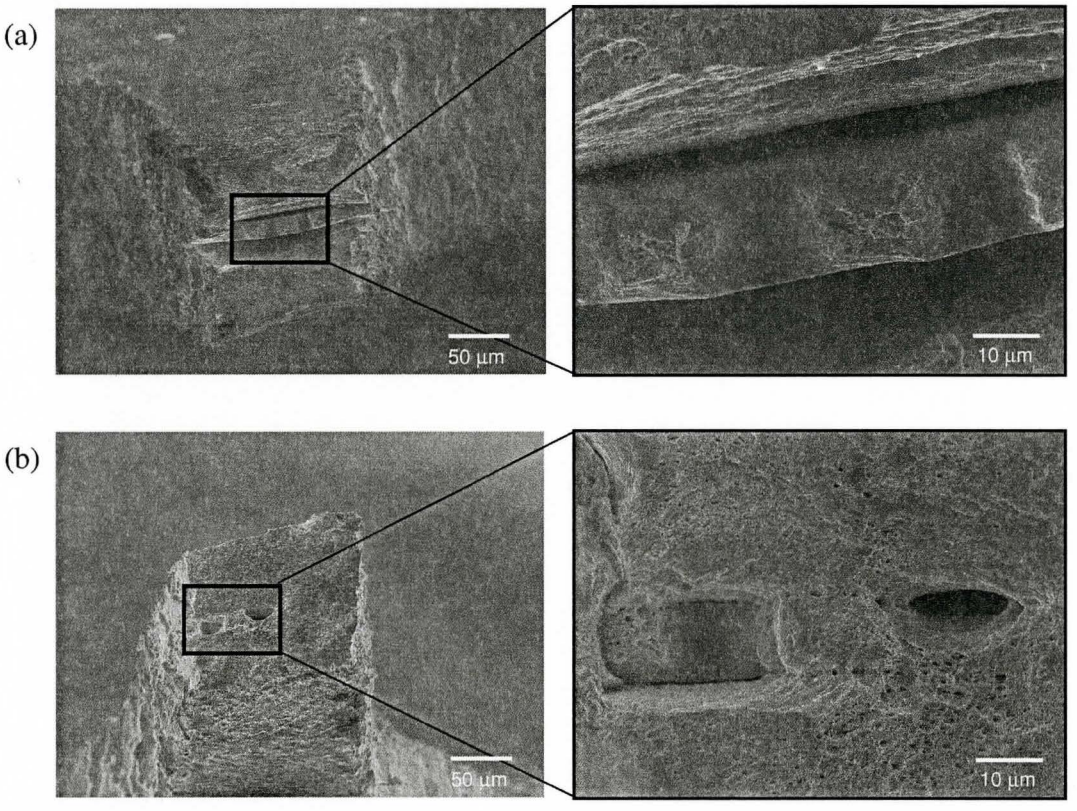

Figure 7.4: SEM fractograpps for all the model materials in this chapter.(a)The Glidcop Rectangular and (b) the Glidcop Line. The fracture strains ε_f for individual materials are 0.85, 0.55, respectively.)

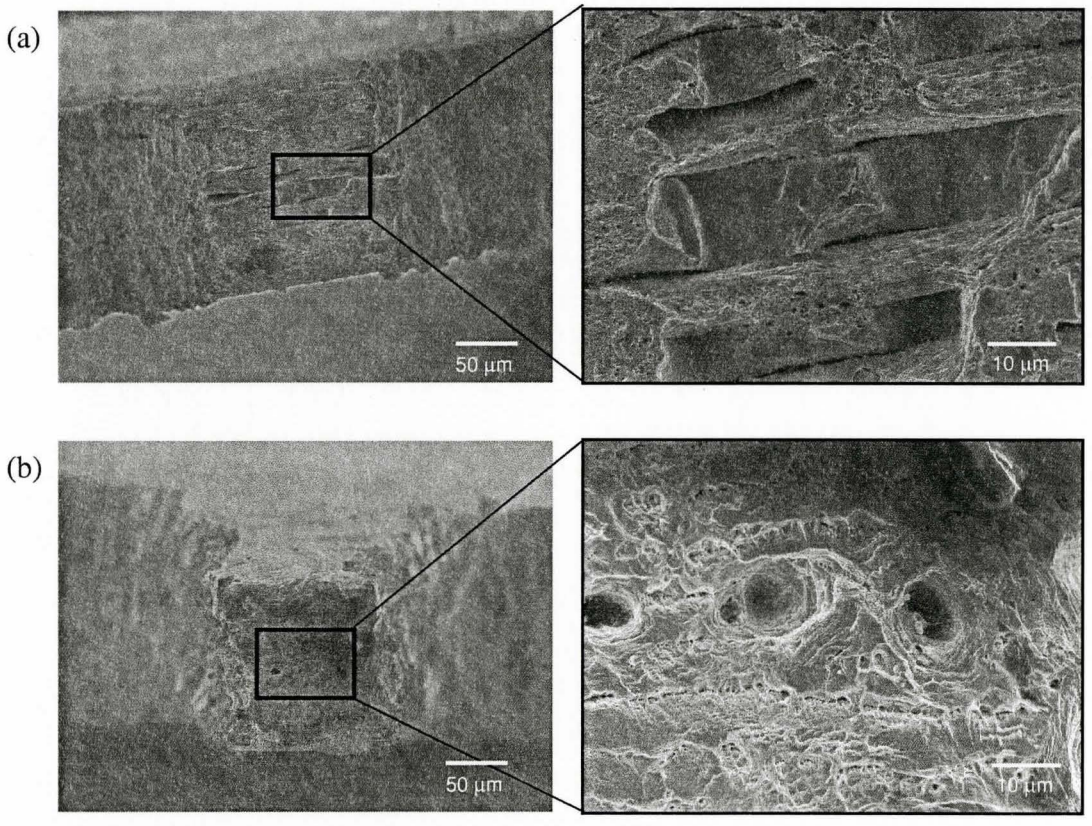

Figure 7.5: SEM fractographs for all the model materials in this chapter.(a) The Glidcop FCC and (b) The Brass Rectangular. The fracture strains ε_f for individual materials are 0.52 and 1.58 respectively.)

7.4 Tomography and Radiography

In this section, the results of tomography and radiography are presented altogether. The results for the Glidcop materials and the Brass materials are discussed separately.

7.4.1 Glidcop Model Materials

Figures 7.6(a) and 7.6(b) show a series of the projections[1] and reconstructed tomograms of the Glidcop Rectangular material. As shown in Figure 7.6(a), delamination took place at a quite early stage of the deformation. Figure 7.6(b), however, shows that the linkage by void sheeting also occurred almost simultaneously. The final fracture took place by the propagation of the delamination and the shear fracture of the central drilled layer.

Figures 7.7 and 7.8 show a series of the reconstructed tomograms and the projections of the Glidcop Line model material. Indeed, this model material was originally designed to have an rectangular array (5×3). The position of the void array was however significantly misaligned so that a half of the array was cut off when the tensile specimen was cut. As observed in Chapter 5 and 6, it is difficult to control the position of holes after diffusion bonding (i.e. b-axis). The sample preparation for a set of experiments at SPring-8 BL20XU is even more challenging since the limitation in terms of thickness is more severe (Remember $t = 0.2$ mm) compared with ID 15 ($t = 1$ mm). A roughly estimated misalignment from Figure 7.7 is about 60$\sim$70 μm. This misalignment may not so serious for the model materials for ID 15, but it is certainly serious in controlling the position of voids. Since the rectangular void

[1]A projection is the same thing as a radiograph except for the opposite contrast. (i.e. bright color means dense material in a projection.)

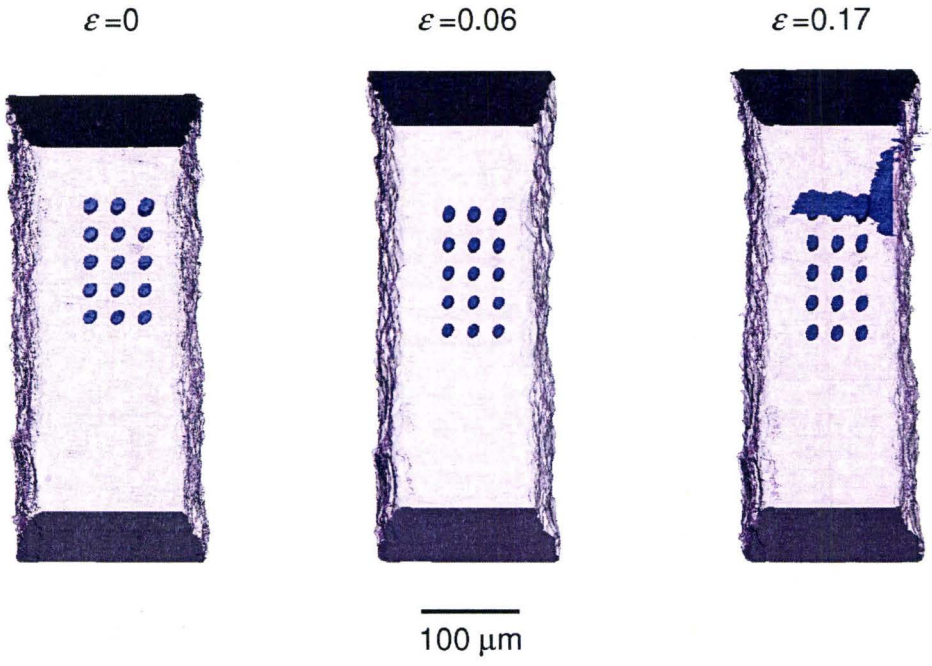

(a) Tomograms

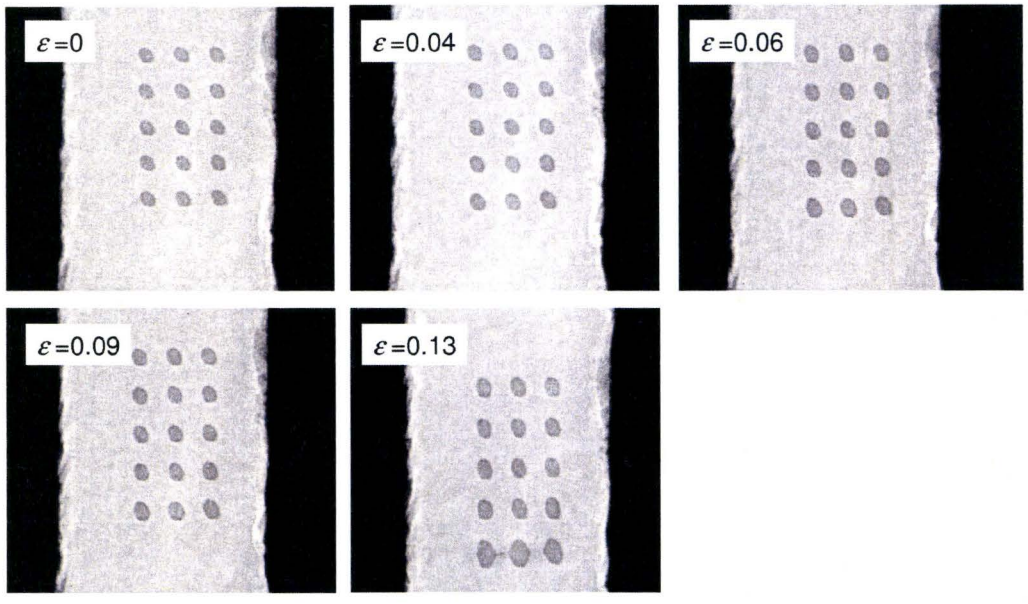

(b) Projections

Figure 7.6: Tomograms and Projections for the Glidcop Rectangular material.

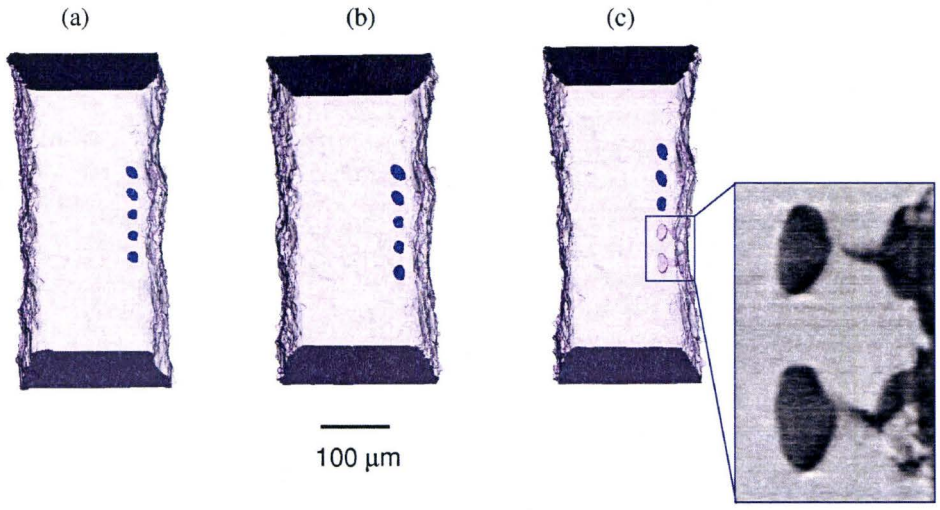

Figure 7.7: Tomograms for the Glidcop Line material.(a) $\varepsilon = 0$ (b) $\varepsilon = 0.05$ (c)$\varepsilon = 0.264$.

array ended up with an void array that aligned like a "line" that is parallel to the tensile axis.

The voids at the bottom of the "line" first connected with the free surface through the void sheet. Once the voids merged with the surface, the voids acted as a strain concentrator, growing themselves rapidly. However, since there is no neighboring void around, the final fracture took place by macroscopic shear, without introducing delamination as observed in the SEM fractograph.

Figure 7.9 shows the tomogram of the Glidcop FCC material, while Figure 7.10 presents the first void pair to link up captured from the Figure 7.9. The voids in the second layer from the near side ended up with a rather ugly shape (not spherical/spheroidal) probably due to the poor calibration of the laser path alignment. This also accelerated the void linkage process as illustrated

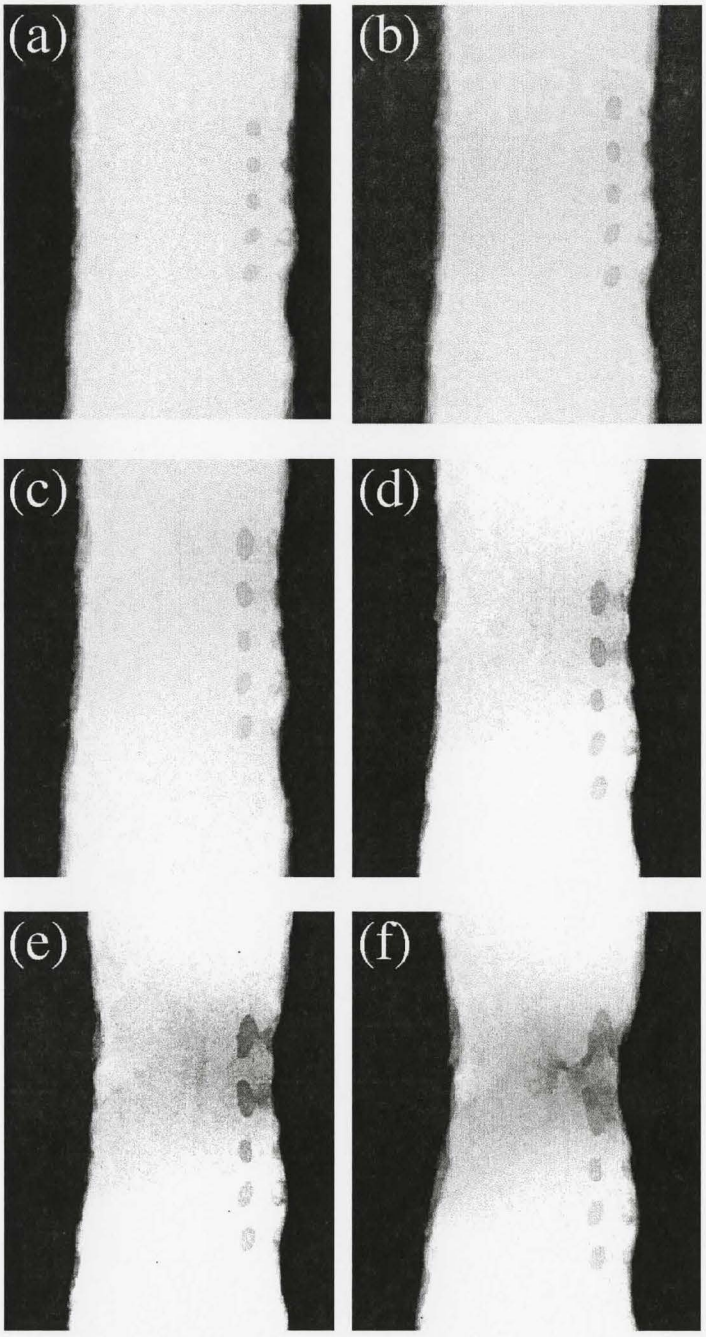

Figure 7.8: Projections for the Glidcop Line material. (a) $\varepsilon = 0$ (b) $\varepsilon = 0.183$ (c) $\varepsilon = 0.282$ (d) $\varepsilon = 0.300$ (e) $\varepsilon = 0.495$ (f) $\varepsilon = 0.687$.

in Figure 7.10 in such a way that the edge of the voids can link to each other. The projections (or radiographs) for this model material (i.e. multi-layer model materials) is not as useful as the case in the single-layer model materials, because more than two voids can be located in the X-ray path and this makes more difficult to interpret the void growth behavior recorded on projections. In this material, too, delamination occurred although it is not as significant as the case in the Glidcop Rectangular material.

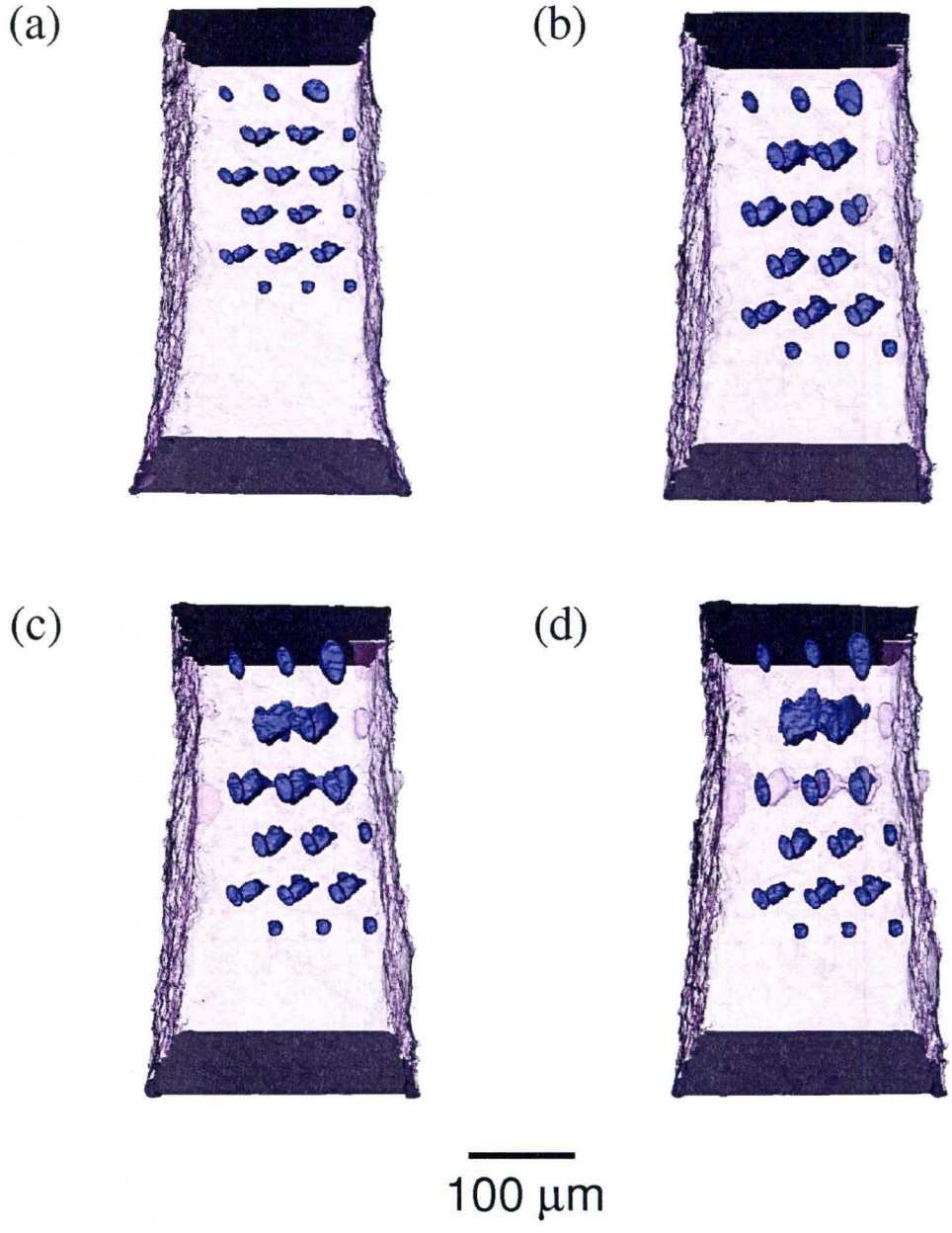

Figure 7.9: Tomograms for the Glidcop FCC material. (a) $\varepsilon = 0$ (b) $\varepsilon = 0.288$ (c) $\varepsilon = 0.290$ (d) $\varepsilon = 0.300$

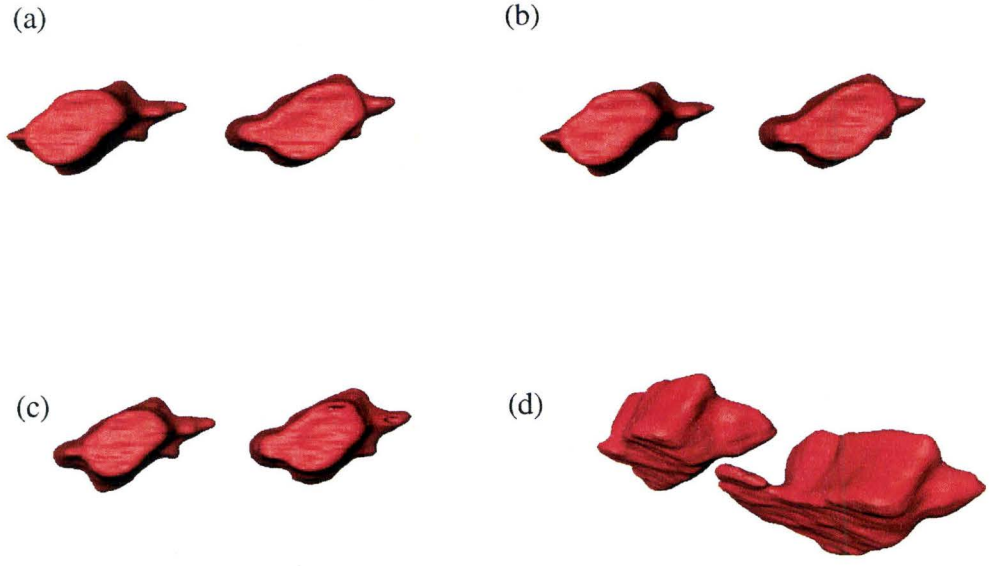

Figure 7.10: The analysis of the first pair of voids to get linked. (a) $\varepsilon = 0$ (b) $\varepsilon = 0.0001$ (c) $\varepsilon = 0.0142$ (d) $\varepsilon = 0.1683$

7.4.2 Brass Model Material

The tomograms and the projections of the Brass Rectangular materials are shown in Figures 7.11 and 7.12. The initial void diameter ($\sim$ 8 μm) after the diffusion bonding ended up with rather small values compared to the as-machined hole ($\sim$ 15 μm). The diffusion bonding temperature for brass should have been slightly high (below 850°C). At any rate, the bonding of the model materials was so excellent that no delamination took place until the final fracture. Although the void growth behavior was well captured, the tomogram that should have captured the linkage process could not be successfully reconstructed. This model material was originally designed to fabricate a three-layer cubic array, yet the inter-layer alignment of holes was not so perfect that only one single void layer affects the fracture process (i.e. no other void not located in the X-ray path like a single-layer model material). Thus, the projections can be used to visualize the void growth and linkage process, as shown in Figure 7.12. A series of the projections clearly indicate that the final fracture occurred by macroscopic shear fracture, yet the local shear coalescence between the central void and the void at the right hand side (Figure 7.13) has also clearly occurred.

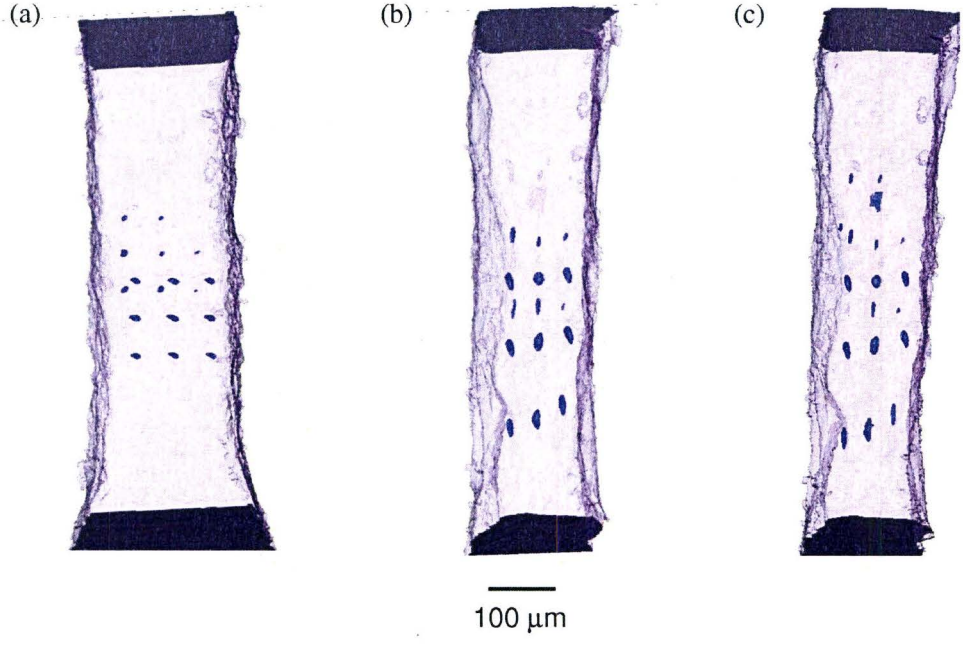

Figure 7.11: A series of the tomograms for the Brass Rectangular material during plastic deformation. (a) $\varepsilon = 0$ (b) $\varepsilon = 0.700$ (c) $\varepsilon = 0.867$.

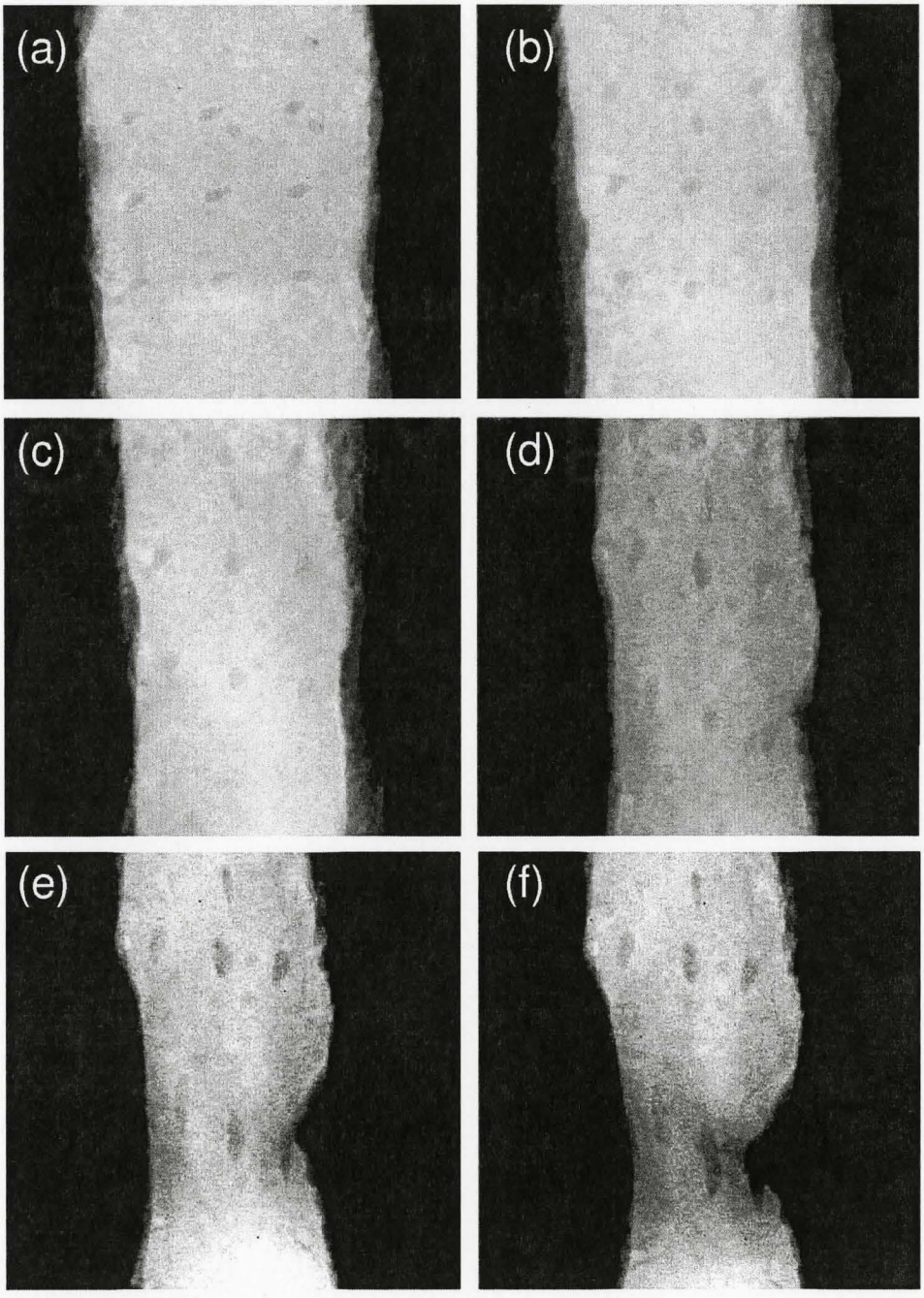

Figure 7.12: A series of the projections of the Brass Rectangular material during deformation. (a) $\varepsilon = 0$ (b) $\varepsilon = 0.27$ (c) $\varepsilon = 0.47$ (d) $\varepsilon = 0.85$ (e) $\varepsilon = 0.1.26$ (f) $\varepsilon = 1.58$.

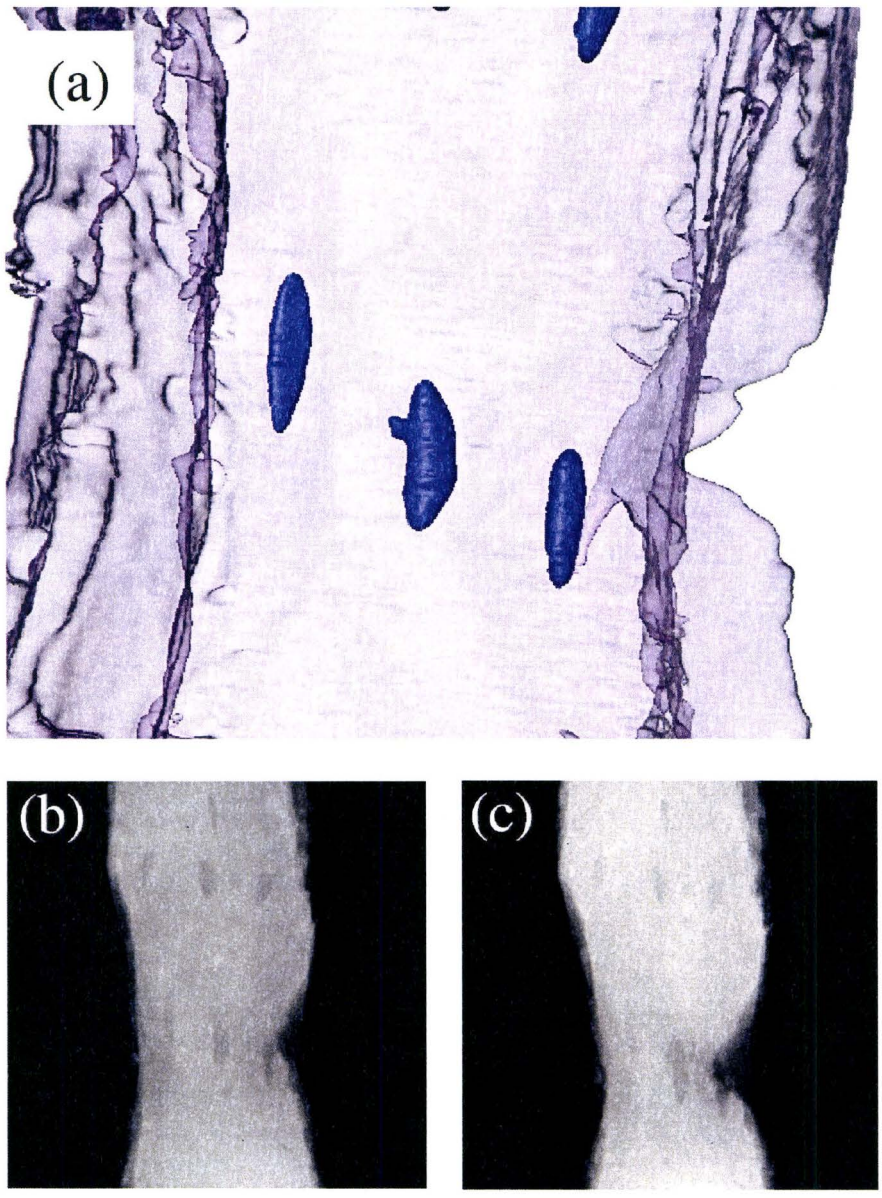

Figure 7.13: (a)Close-up of the Brass Rectangular material right before the linkage event. (b)The projection before the linkage.(c)The projection after the linkage.

7.5 Analysis of Void Growth and Linkage

Using the tomograms and the projections presented in the last section, the local strains due to the void growth were measured as summarized in Figures 7.14-7.17.

The result of the Glidcop Rectangular material, which was captured only from projections, is shown in Figure 7.14. Unlike the results obtained in the copper as shown in Figures 5.11 and 5.12, the lateral shrinkage (i.e. c-axis) was not observed. In fact, the voids appeared to grow laterally almost from the beginning of the plastic deformation. Another feature is that neither the longitudinal nor the lateral void growth show good agreement with the Rice and Tracey void growth model. It may be because the voids are too close to each other from the initial state so that the voids start to coalesce as soon as the plastic deformation commences. The other more unfortunate reason is that minor delamination did occur. the first linkage observed in the model material occurred when $\varepsilon = 0.13$.

Figure 7.15 shows the result of the Glidcop Line material, capturing the growth behavior of only the first single void that linked with the surface. The larger symbols in the figure represent the results obtained from tomograms, while the smaller symbols represent the values captured from the projections. Solid lines represent the Rice and Tracey model, which predicted the void growth behavior more successfully in comparison with the case for the Glidcop Rectangular material, at least along the a-axis and b-axis. The linkage strain of this model material was $\varepsilon = 0.49$.

The result for the Glidcop FCC material is shown in Figure 7.16. The data from the projections are not presented as explained previously. The

measurement was performed in terms of the diameters of "torso" by neglecting the "hands" originated by the poor calibration of the machining laser. The Rice and Tracey model predicted the lateral void growth behavior well, but it was not successful in predicting the longitudinal void growth. The actual linkage strain was $\varepsilon = 0.17$, where minor delamination was also observed in the same scan of tomography.

The results for the three voids in the Brass Rectangular material is presented in Figure 7.17. The results are in a good agreement with the Rice and Tracey model. A close examination of the growth of the holes #3 and #2 along c-axis shows a very shallow but surely a minimum extremum of the trajectory around $\varepsilon \sim 1.2$ probably due to the onset of void coalescence between the hole #3, the hole #2 and the free surface at the right. This tendency was not observed in the hole #1, and thus it is considered that the final macroscopic shear fracture took place right after the coalescence of the holes #2 and #3 but before the linked voids could coalesce with the hole #1. The first linkage occurred when $\varepsilon = 0.17$.

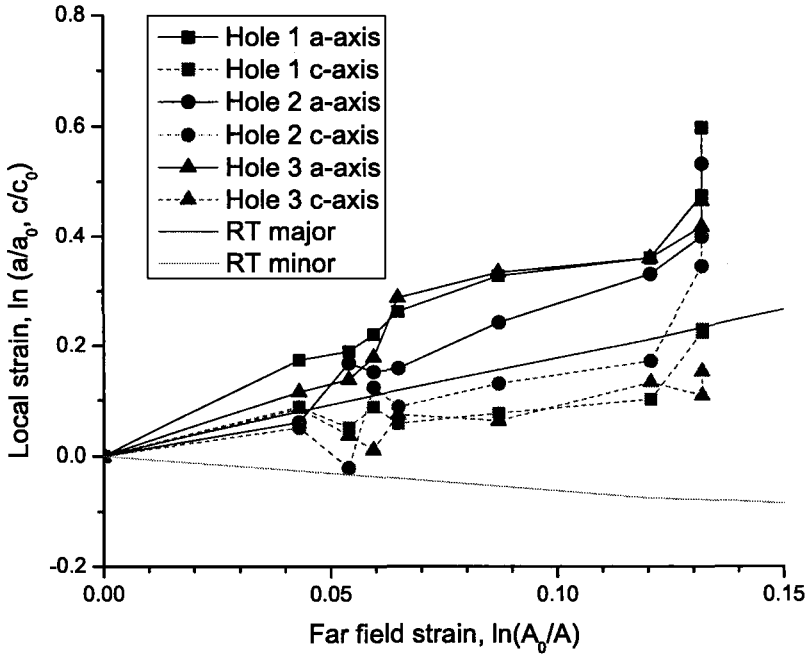

Figure 7.14: The local strain associated with the void growth behavior of the Glidcop Rectangular material.

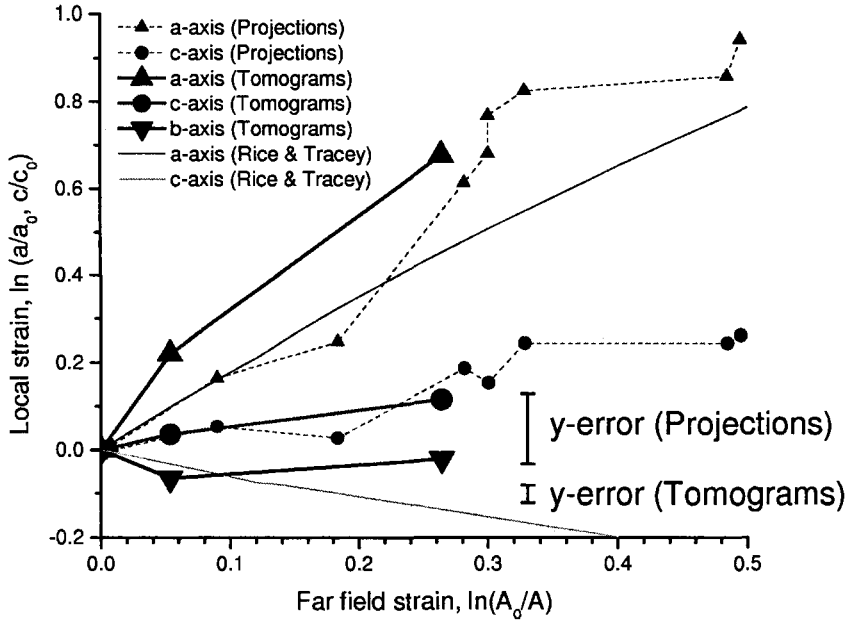

Figure 7.15: The local strain associated with the void growth behavior of the Glidcop Line material.

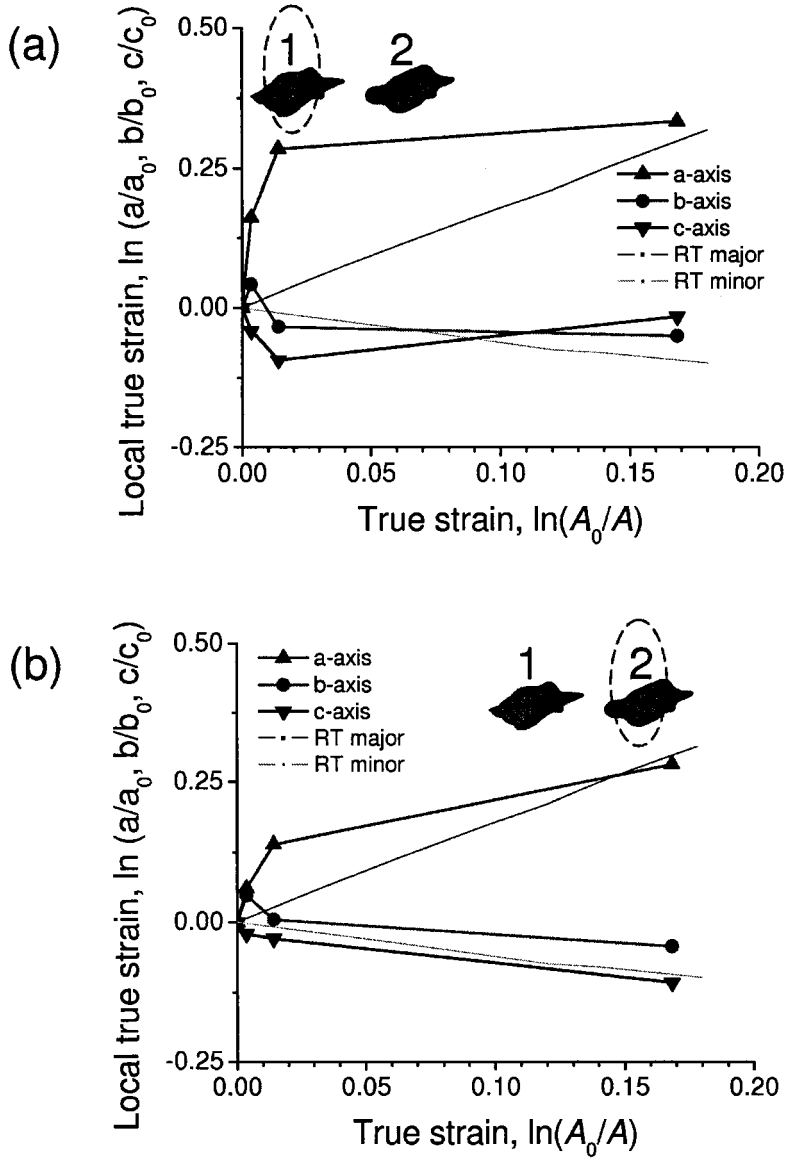

Figure 7.16: The void growth behavior of the Glidcop FCC material. (a) Hole #1 (b) Hole #2

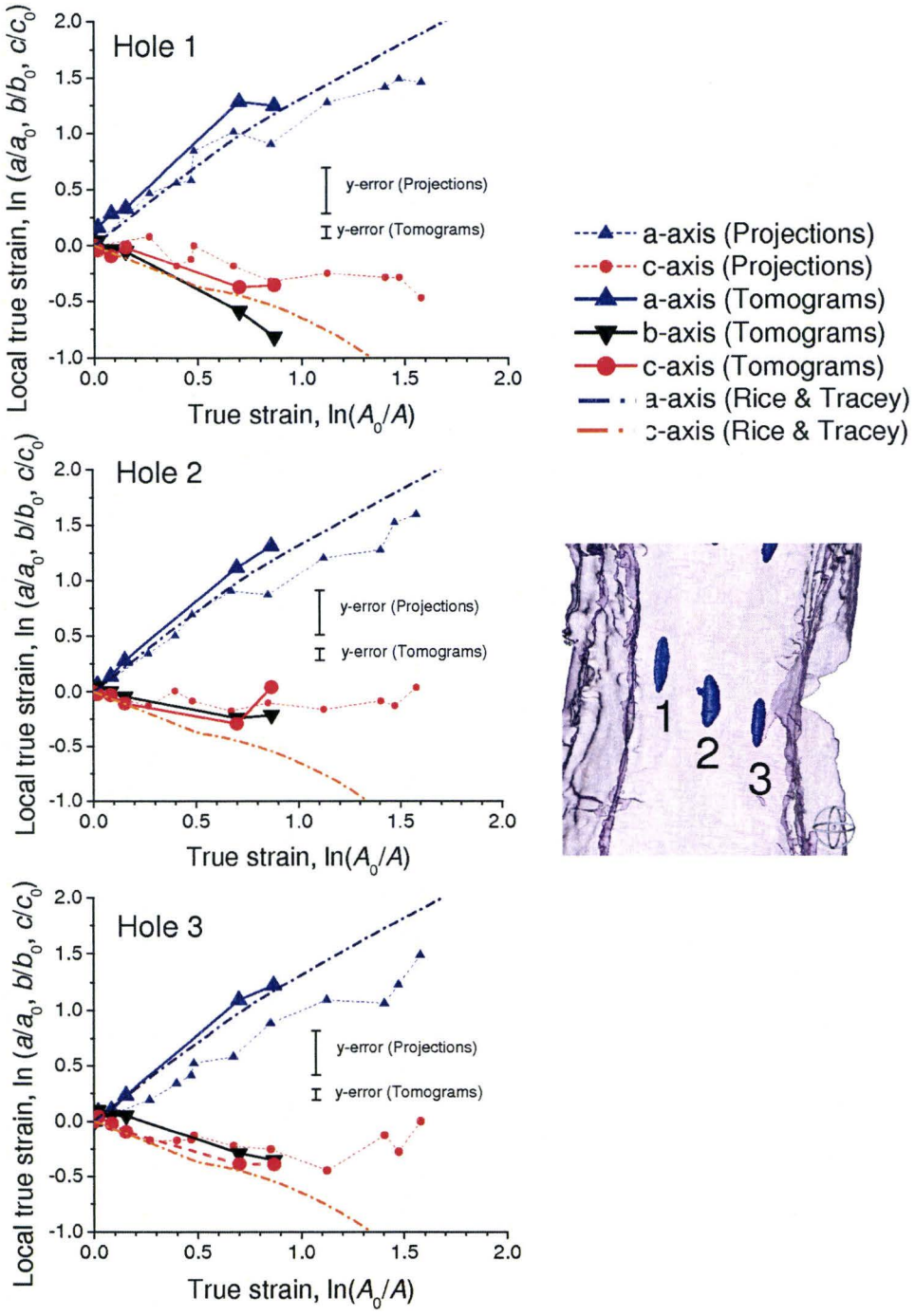

Figure 7.17: The local strain evolution in the Brass Rectangular material due to the void growth plotted as a function of the far field plastic strain.

7.6 Discussion

7.6.1 Assessment of spatial resolution.

The spatial resolution of the current tomography experiment was assessed by the same method explained in section 5.5.1. This beamline is supposed to be capable with the high resolution microtomography experiments with the resolution below 1μm. The estimated spatial resolution from the current experimental result was 0.94 μm, which is about twice as small as the pixel size.

The thickness of the void sheet was also determined as 1.7 μm by a direct measurement in the Glidcop FCC material. The thickness at the onset of void sheeting should be much smaller at the onset of void sheeting, but the current experimental setups is not able to capture those small voids.

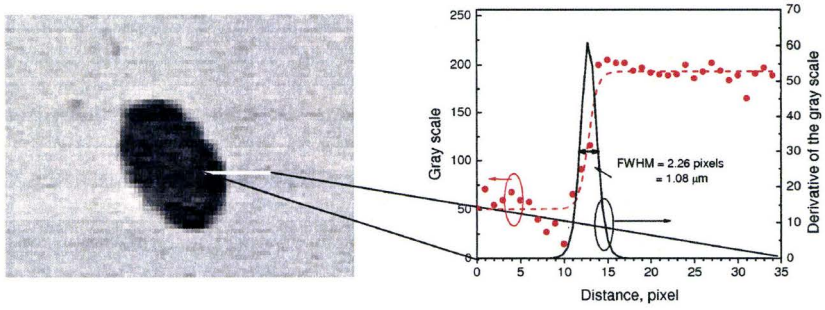

Figure 7.18: The spatial resolution estimated by using the result of the Glidcop FCC model material.

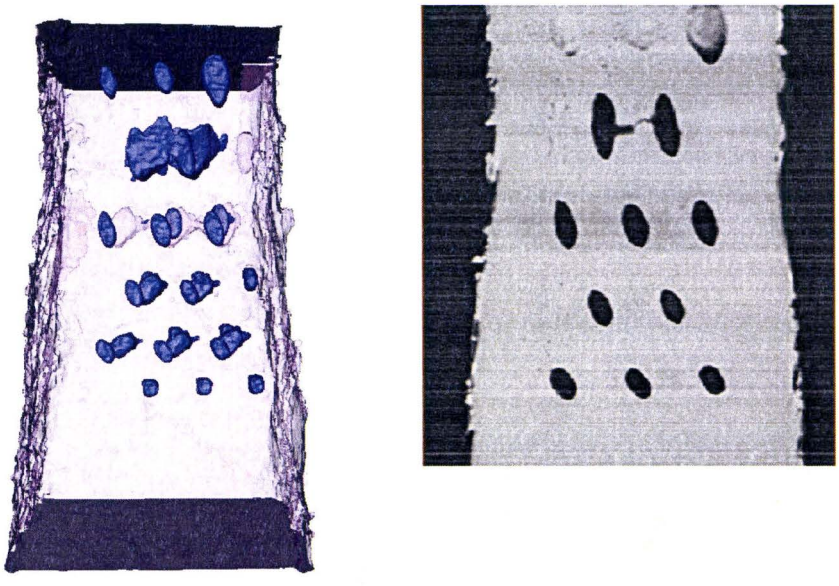

Figure 7.19: The tomogram of the Glidcop FCC model material and its cross section capturing the void sheet at $\varepsilon = 0.30$. The thickness of the void sheet at this stage was 1.7 μm.

7.6.2 Comparison with the void coalescence models

The comparison of the experimentally captured strains at void linkage in individual model materials with the models were performed. Unlike the last chapter, the tensile specimens are simple smooth specimens. Thus, the same methodology addressed in section 5.7 was adopted in this section.

The evolutions of the void length and the intervoid distance during deformation in each model material are shown in Figures 7.20 and 7.21 in order to enable comparison with the void coalescence strain by the Brown and Embury model. The coalescence strain for the Glidcop FCC sample could not be obtained due to delamination. Evolution of the plastic constraint factor for internal necking with respect to individual model materials with far field plastic strain are also shown in Figure 7.22, for the prediction by models by Thomason and Pardoen and Hutchinson.

Table 7.3 summarizes the linkage strains captured from the Glidcop and brass samples experiments, as well as that predicted by the existing models. This table also includes n value, stress triaxiality σ_m/Y, initial void volume fraction V_f^0, strains at coalescence, linkage and fracture ($\varepsilon_{coalescence}$, $\varepsilon_{linkage}$, $\varepsilon_{fracture}$, respectively) together with the predicted void coalescence from the models. The error of the predicted values compared to the $\varepsilon_{coalescence}$, $\varepsilon_{linkage}$ and $\varepsilon_{fracture}$ in the experiments are also shown in the Table. In order to discuss the influence of work hardening behavior on void linkage and coalescence, the results from chapter 5 (pure copper) and the comparable result from Weck et al. (2008b) (pure copper and Glidcop) are also included in such a way that we have more ingredients for comparison.

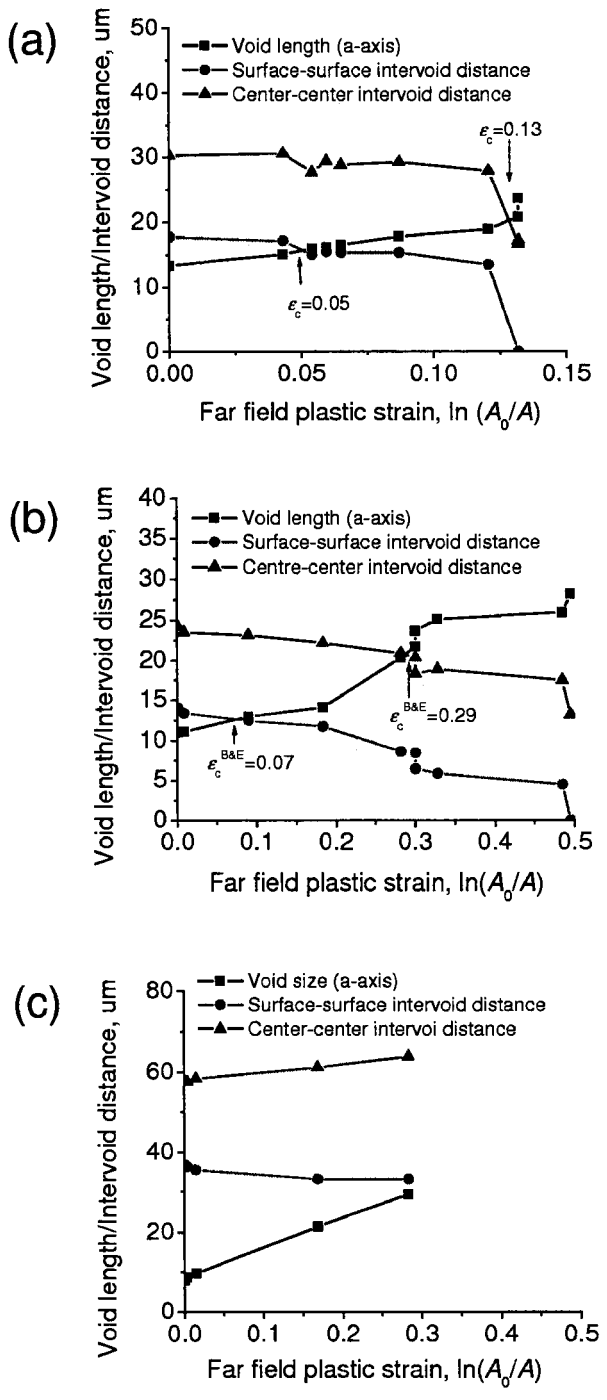

Figure 7.20: Evolutions of the void length and the intervoid distance measured in the Glidcop model materials during the deformation. (a) The Glidcop Rectangular (b) The Glidcop Line (c) The Glidcop FCC.

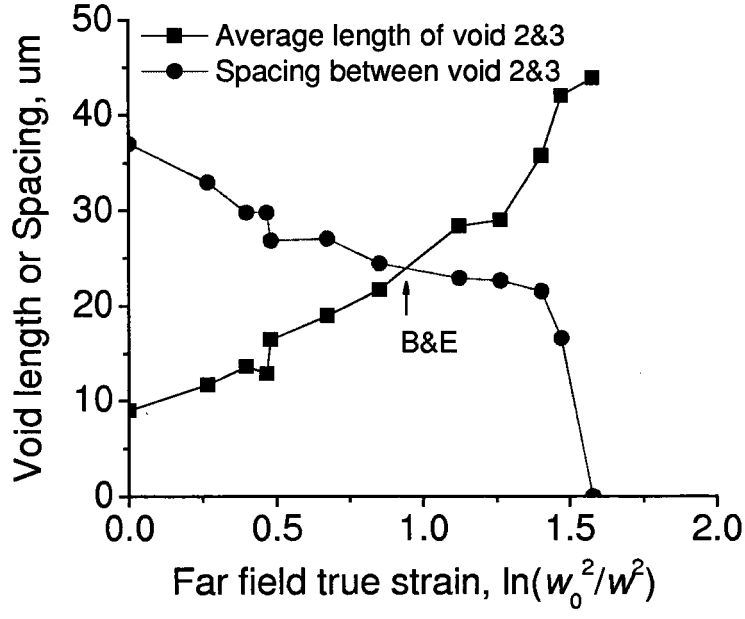

Figure 7.21: Evolutions of the void length and the intervoid distance measured in the Brass Rectangular material.

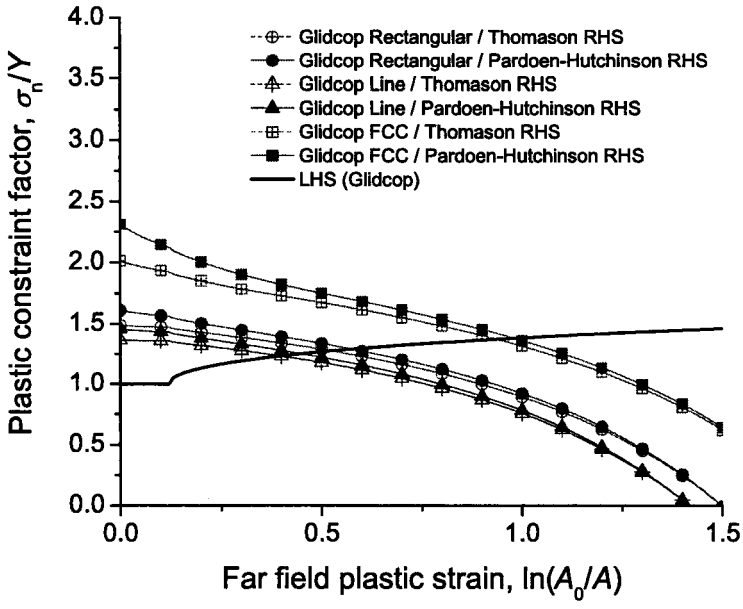

(a) Glidcop model materials

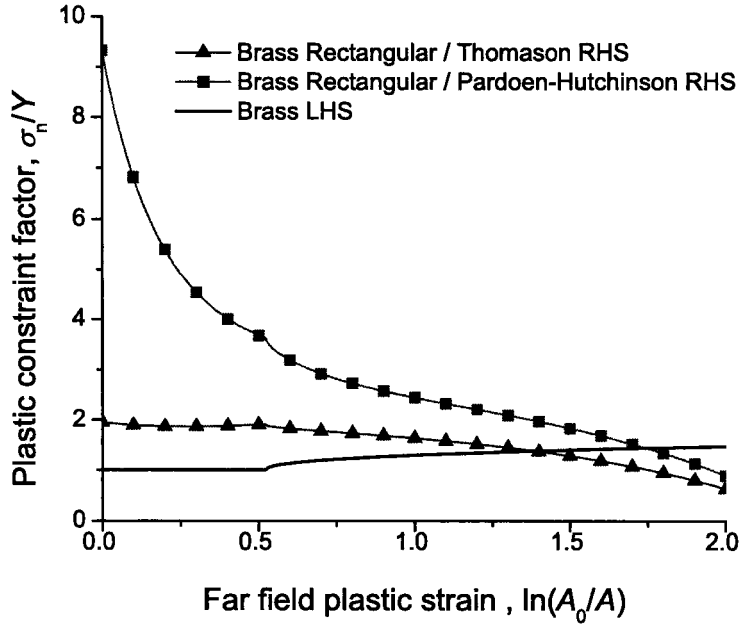

(b) Brass model materials

Figure 7.22: The evolution of the plastic constraint factor for internal necking estimated for the current model materials.

Brown and Embury model

As was observed in Chapter 5, the Brown and Embury model seriously underestimated the experimental results for most of the model materials. We have already concluded that this is because the Brown and Embury model is not capable to predict void coalescence or linkage for voids embedded in a 3D matrix. The only exception is the Glidcop Rectangular sample, which proposes that the Brown and Embury model predicts the experimental linkage strain with 2% error. However, the tomography result confirmed that this material was suffering from some delamination and thus it is considered that the sample behaved like a 2D sample, which can be adequately predicted by the Brown and Embury model.

Thomason model and Pardoen and Hutchinson model

The Thomason model and the Pardoen and Hutchinson model predicted the coalescence strains for the Glidcop Line sample and the Brass Rectangular sample, both of which did not delaminate, with a reasonable accuracy.

One notices that the Thomason model overestimated the void linkage in the Brass Rectangular sample. Since brass has a higher work hardening exponent, it would be expected that the void coalescence or linkage occur at a higher strain than that predicted from the Thomason model, which assumes non-hardening material. The current observation contradicts this, but this does not mean that the models are wrong. This is because the initial volume fraction was too small ($V_f^0 = 0.6\%$) and the void coalescence was suppressed until a very later stage of deformation (i.e. $\varepsilon = 1.74$ as proposed by the Thomason model). However, a macroscopic shear intervened prior to void coalescence.

Thus, it is considered that the coalescence/linkage strain captured in the Brass Rectangular sample is strongly influenced by macroscopic shear and thus it ended up with a even smaller value than that it should be.

Another unexpected observation is that the linkage strain of the Glidcop Line sample is in agreement with the Thomason model and the Pardoen and Hutchinson model. It was expected that the linkage strain in Glidcop would be lower than the values modeled from these 3D models due to void sheeting. To discuss this, we have to consider whether void sheeting precedes shear instability. There are two routes in order for a void sheet to form; shear precedes the nucleation of secondary void population, or the other way around. In the current case apparently the former happens, which is dominated by the concept of work hardening rate, as discussed later in section 7.6.4. The SEM fractograph (Figure 7.4(b)), which exhibits the elongated dimples, also supports this idea. In this situation, it is considered that the deterioration of strains of void coalescence and linkage is not significant.

In contrast, when nucleation of secondary void population precedes shear instability, the strains of void coalescence and linkage would be much smaller.

7.6.3 Effect of void sheeting on linkage strains

A direct comparison in terms of the onset of coalescence cannot be made since the coalescence could not be captured in the Glidcop model materials. The comparison between the linkage strains of pure copper and Glidcop clearly suggests that the void linkage occurred earlier in Glidcop. However, it is quite difficult to say something conclusive because the initial local porosities V_f^0 are different. Furthermore, it is inadequate to use the Glidcop Rectangular

Table 7.3: The comparison of the experimental results with the models.

Experiments									
	n	σ_m/Y	V_f^0	$V_f^{critical}$	$\varepsilon_{coalescence}$	$\varepsilon_{linkage}$	$\varepsilon_{fracture}$	$(WHR/\sigma)_{coalescence}$	$(WHR/\sigma)_{linkage}$
Cu FCC 1	0.4	0.33	4.40%	26.70%	0.88	0.96	1.73	0.27	0.23
Cu FCC 2	0.4	0.33	4.40%	24.30%	0.52	0.85	1.51	0.33	0.07
Glidcop Rectangular**	0.14	0.33	7.30%	N/A	N/A	0.132	0.85	N/A	N/A*
Glidcop Line	0.14	0.33	9.50%	N/A	N/A	0.49	0.58	N/A	0.36
Glidcop FCC**	0.14	0.33	2.90%	N/A	N/A	0.17	0.52	N/A	N/A*
Brass Rectangular	0.52	0.33	0.60%	N/A	1.12	1.56	1.58	0.41	0.25
Pure Cu 1 (Weck et al. (2008))	0.4	0.33	0.90%	N/A	0.5~0.77	1.01	N/A	N/A	N/A
Glidcop1 (Weck et al. (2008))	0.14	0.33	2.90%	N/A	N/A	0.41	N/A	N/A	N/A
Glidcop2 (Weck et al. (2008))	0.14	0.33	5.50%	N/A	N/A	0.45	N/A	N/A	N/A

** Delaminated samples

* Due to delamination

Models											
	Brown and Embury				Thomason				Pardoen and Hutchinson			
		Error (%) compared to				Error (%) compared to				Error (%) compared to		
	Predicted	$\varepsilon_{coalescence}$	$\varepsilon_{linkage}$	$\varepsilon_{fracture}$	Predicted	$\varepsilon_{coalescence}$	$\varepsilon_{linkage}$	$\varepsilon_{fracture}$	Predicted	$\varepsilon_{coalescence}$	$\varepsilon_{linkage}$	$\varepsilon_{fracture}$
Cu FCC 1	0.18	-79.5	-81.3	-89.6	0.9	2.3	-6.2	-48.0	0.95	8.0	-1.0	-45.1
Cu FCC 2	0.05	-90.4	-94.1	-96.7	0.76	46.2	-10.6	-49.7	0.83	59.6	-2.4	-45.0
Glidcop Rectangular**	0.13	N/A*	-1.5	-84.7	0.52	N/A	293.9	-38.8	0.59	N/A	347.0	-30.6
Glidcop Line	0.07	N/A	-85.7	-87.9	0.4	N/A	-18.4	-31.0	0.47	N/A	-4.1	-19.0
Glidcop FCC**	N/A	N/A*	N/A	N/A	0.95	N/A	458.8	82.7	1.1	N/A	547.1	111.5
Brass Rectangular	0.94	-16.1	-39.7	-40.5	1.74	55.4	11.5	10.1	1.77	58.0	13.5	12.0

** Delaminated samples

and the Glidcop FCC model materials for comparison because of delamination. However, the bonding in Glidcop Line material was quite good, and the captured linkage strain was much higher than the other two Glidcop model materials. Within the current results, a direct comparison between pure copper and Glidcop with a fixed local porosity cannot be done. However, the comparison with the linkage strains of Glidcop (V_f^0 =5.5 % in the Glidcop 1 (Weck et al., 2008b)) is comparable with the FCC 1 and FCC 2 pure Cu samples) is possible, showing that the linkage strains in Glidcop are consistently smaller than the pure copper materials, probably due to the void sheeting. This is consistent with the fact that the Thomason model and the Pardoen and Hutchinson model overestimated the coalescence strains for Glidcop 1.

7.6.4 Work hardening exponent vs. work hardening rate

A direct comparison becomes possible between the Pure Cu 1 model material studied by Weck et al. and the Brass Rectangular material, the both of which have the similar initial volume V_f^0, showed that brass ended up with a higher value in linkage strain. This is probably due to the higher value of the work hardening exponent n. It seems clear that the higher work hardening exponent stabilizes the plastic flow in the ligament and slows down the coalescence and linkage. The fact that the linkage strain of the Brass Rectangular sample is in good agreement with the predictions by Thomason's and Pardoen and Hutchinson's model also supports this idea.

Instead of work hardening exponent, work hardening rate (WHR) can also be used for discussion on fracture. WHR beyond diffuse necking (as predicted

by the Considère criterion) cannot be obtained in normal tensile tests, but tomography experiments makes it possible to capture the stress-strain curve after necking.

The use of WHR in discussing plastic instability has been covered by many researchers (e.g. Kocks and Mecking (2003)). WHR can be obtained from the true stress-strain curves in Figure 7.3. Normalizing the WHR by the current flow stress of the ligament provides a fair comparison between materials with different mechanical properties. While the WHR is plotted as a function of the current flow stress in the original the Kocks-Mecking plot, the normalized WHR was plotted as functions of the far field plastic strain in Figure 7.23 for the Brass Rectangular and Glidcop Line samples. This enables us to capture the critical value of normalized WHR at the coalescence or linkage of voids. The results on pure copper samples, which have captured the onset of void coalescence, are also plotted (from Chapter 5) to illustrate the difference between pure copper, Glidcop and brass. The data points after any linkage event were suppressed since the flow stress is significantly degraded by that. For a similar reason, the data of Glidcop FCC 2 and the Glidcop Rectangular samples are suppressed in this figure since they suffered from delamination.

In this figure, the line at $\mathrm{WHR}/\sigma = 1$ is identical to the Considère criterion while the line at $\mathrm{WHR}/\sigma = 1/2$ represents Hill's localized necking condition. This figure clearly shows a significant difference both in coalescence and linkage strains for different materials: a material with higher n value exhibited higher ductility. One also notices that the WHR/σ is always higher than any other materials while that of the Glidcop sample was always lower than the pure copper. It is considered that the WHR in Glidcop reached a saturation value at an early stage of the deformation, mainly around the Al_2O_3 nanoparticles.

The remarkable work hardening rate in brass is attributed to its low stacking fault energy. Nevertheless, the critical values of WHR/σ for all the materials here seem to be approximately the same and independent of material. This roughly estimated value of the critical WHR/σ is 0.07$\sim$0.4, and it is clearly smaller than the Hill's local necking criterion.

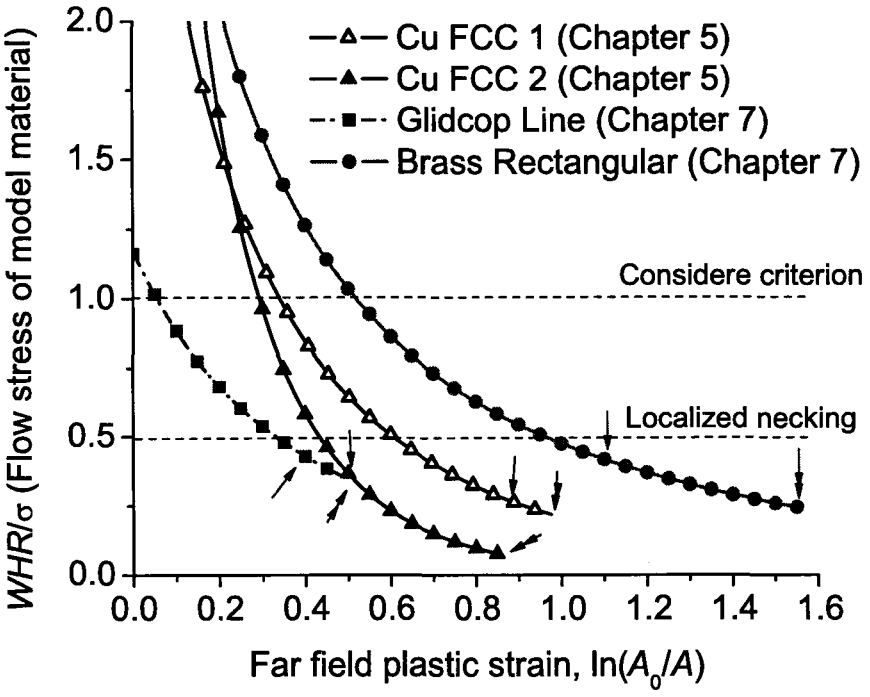

Figure 7.23: Evolution WHR/σ in various model materials during the deformation. Single arrows and double arrows represent the onset of coalescence and linkage, respectively.

7.7 Chapter Summary

A series of model materials made of Glidcop and brass were subject to *in situ* high resolution X-ray tomography coupled with tensile deformation. The outcomes obtained in this chapter are summarized as below.

- Void growth and coalescence (or linkage) in model materials made of Glidcop and brass were visualized successfully.
- Void sheeting was observed and the smallest possible thickness measured in the current experiments was 1.7 μm.
- The spatial resolution was estimated to be 0.94 μm.
- It was found that the void linkage strains in Glidcop are smaller compared to that of pure copper and brass as well as that predicted from the existing models. This is not because of void sheeting, but because of the faster saturation of the work hardening rate around Al_2O_3 nanoparticles dispersed in Glidcop and resultant shear instability.
- It was concluded that a higher work hardening exponent suppresses the void coalescence and linkage events, while the normalized work hardening rate takes a similar value (i.e. $WHR/\sigma = 0.07 \sim 0.4$) no matter how the ductility in individual materials are different.

Chapter 8

Conclusions and Future Work

8.1 Summary and Conclusion

By combining Tables 5.3, 6.3, and 7.3, all the data obtained are summarized in Table 8.1. This table captures the essential results of this study.

The primary aims of the current thesis project were to experimentally visualize the void growth and coalescence/linkage behavior in a class of model materials and to provide a quantitative assessment on the existing void coalescence models. The main contributions by the thesis is summarized as below.

- Following the approach proposed by Weck et al., a methodology was developed to produce a class of model materials containing arbitrary void arrays. The model materials produced for this study were subjected to in-situ X-ray computed tomography coupled with tensile deformation, and the growth and coalescence/linkage of voids were successfully visualized.

- The experiments using continuous tomography enabled us to capture

Table 8.1: The comparison of the experimental results with the models.

Experiments									
	n	σ_m/Y	V_f^0	$V_f^{critical}$	$\varepsilon_{coalescence}$	$\varepsilon_{linkage}$	$\varepsilon_{fracture}$	$(WHR/\sigma)_{coalescence}$	$(WHR/\sigma)_{linkage}$
Cu FCC 1	0.4	0.33	4.40%	26.70%	0.76	0.96	1.73	0.27	0.23
Cu FCC 2	0.4	0.33	4.40%	24.30%	0.52	0.85	1.51	0.33	0.25
Cu Hexagonal	0.4	0.47	0.70%	14.2% ~	N/A	0.68	1.62	N/A	N/A*
Cu Random	0.4	0.47	4.69%	3.57% ~ 60.7%	N/A	0.40	2.6	N/A	0.36
Cu FCC + notch	0.4	0.55	5.15%	24.7% ~ 59.4%	N/A	0.99	1.74	N/A	N/A*
Glidcop Rectangular**	0.14	0.33	7.30%	N/A	N/A	0.132	0.85	0.41	0.25
Glidcop Line	0.14	0.33	9.50%	N/A	N/A	0.49	0.58		
Glidcop FCC**	0.14	0.33	2.90%	N/A	N/A	0.17	0.52		
Brass Rectangular	0.52	0.33	0.60%	N/A	1.12	1.56	1.58		
Pure Cu 1 (Weck et al. (2008))	0.4	0.33	0.90%	N/A	0.5~0.77	1.01	N/A	N/A	N/A
Glidcop1 (Weck et al. (2008))	0.14	0.33	2.90%	N/A	N/A	0.41	N/A	N/A	N/A
Glidcop2 (Weck et al. (2008))	0.14	0.33	5.50%	N/A	N/A	0.45	N/A	N/A	N/A

* due to delamination

Models											
	Brown and Embury				Thomason				Pardoen and Hutchinson			
		Error (%) compared to				Error (%) compared to				Error (%) compared to		
	Predicted	$\varepsilon_{coalescence}$	$\varepsilon_{linkage}$	$\varepsilon_{fracture}$	Predicted	$\varepsilon_{coalescence}$	$\varepsilon_{linkage}$	$\varepsilon_{fracture}$	Predicted	$\varepsilon_{coalescence}$	$\varepsilon_{linkage}$	$\varepsilon_{fracture}$
Cu FCC 1	0.49	-35.5	-49.0	-71.7	0.9	18.4	-6.2	-48.0	0.95	25.0	-1.0	-45.1
Cu FCC 2	0.34	-34.6	-60.0	-77.5	0.76	46.2	-10.6	-49.7	0.83	59.6	-2.4	-45.0
Cu Hexagonal	0.51	N/A	-25.0	-68.5	1.03	N/A	51.5	-36.4	1.29	N/A	89.7	-20.4
Cu Random	0.16	N/A	-60.0	-93.8	0.44	N/A	10.0	-83.1	0.76	N/A	90.0	-70.8
Cu FCC + notch	0.54	N/A	-45.5	-69.0	0.51	N/A	-48.5	-70.7	0.66	N/A	-33.3	-62.1
Glidcop Rectangular**	0.13	N/A*	-1.5	-84.7	0.52	N/A	293.9	-38.8	0.59	N/A	347.0	-30.6
Glidcop Line	0.07	N/A	-85.7	-87.9	0.4	N/A	-18.4	-31.0	0.47	N/A	-4.1	-19.0
Glidcop FCC**	N/A	N/A*	N/A	N/A	0.95	N/A	458.8	82.7	1.1	N/A	547.1	111.5
Brass Rectangular	0.94	-16.1	-39.7	-40.5	1.74	55.4	11.5	10.1	1.77	58.0	13.5	12.0

** Delaminated samples

the onset of the void coalescence in the first void pair to impinge. The experimentally captured plastic strains at the onset of void coalescence were then compared with the void coalescence strains predicted by the existing models. The experiments elucidated several limitations of the existing models.

- In particular, it was experimentally confirmed that the existing models such as those by Thomason (1990) and Pardoen and Hutchinson (2000), which are considered to be one of the most sophisticated void coalescence models, are only able to predict the void coalescence occurring direction normal to the tensile axis. Further development of void coalescence models to take into account the effect of arbitrary void configurations in 3D space is needed.

- The same methodology was also applied to the model materials containing a pair of notches, to investigate the effect of the higher stress triaxiality on the ductile fracture process. The void growth was clearly faster along the direction to which the notches were cut (c-axis using the current thesis's definition). The experimentally captured void growth behavior was simulated by FEM with a relatively good agreement. Because of the anisotropy in void growth, it is expected that the linkage also happens at an earlier stage of the deformation. However, in comparison based on linkage strains (not coalescence strains), no consistent tendency for a notched sample effect was found fractures prematurely.

- Experiments using model materials made from Glidcop and brass were also performed. The experimental results and comparison with the models showed that void sheeting seriously decreased linkage strains, while

the higher work hardening rate in brass slowed down the linkage by stabilizing the plastic flow in the ligament. Nevertheless, the normalized work hardening rate (WHR/σ) took values around 0.07~0.4.

8.2 Future Work

With the view to the missing elements in the current work and literature, it is possible to suggest the tasks to be performed in the next stage of this work.

8.2.1 Void growth and coalescence in HCP materials

The current thesis placed emphasis on f.c.c. material (in a crystallographic sense: essentially copper) due to its simplicity of the interpretation of the data as described in section 3.1.2. However, the demand for light weight materials represented by magnesium and magnesium alloys in automotive industry is remarkable. Also, in order to be ready for the coming inadequate supply of crude oil, the demand from nuclear power plants for zirconium based material is outstanding. The current understanding on void growth and coalescence, however, is far from sufficient. The current methodology can definitely contribute to collect quantitative experimental data on void growth and coalescence/linkage in HCP materials, and provide a mean to assess the validity of models that are to be developed by computational materials scientists.

8.2.2 3D strain mapping

Recent development in 3D strain mapping techniques is also remarkable as proposed by Kobayashi et al. (2008) for example. Their technique traces the

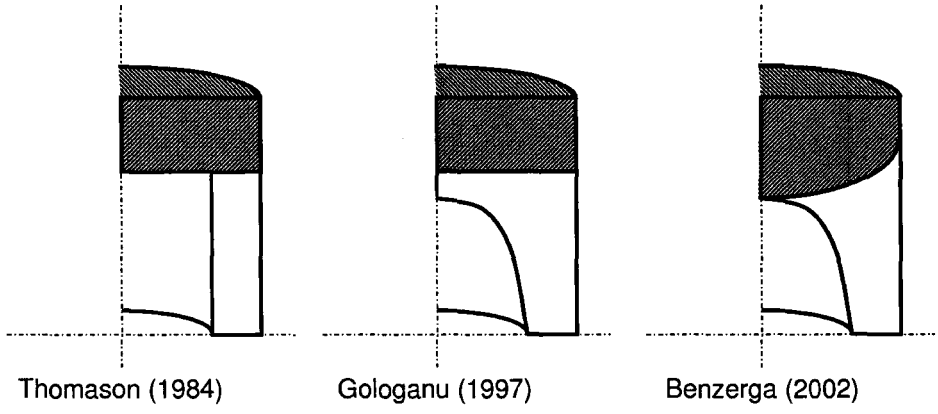

Figure 8.1: Variation of axisymmetric unit cell to model void coalescence in "layer". Assuming that the deformation localized region is sandwiched by rigid blocks, the plastic constraint factor for virtual mode of internal necking is estimated.

movement of the second phase particles or inclusions, the magnitude of strain (all the components in strain tensor) in a tetrahedron formed with its vertices being the 4 neighboring particles. In fact, this type of 3D strain mapping can potentially contribute to the void coalescence modeling. The most serious problem which the modelers are facing in modeling void coalescence of non-cubic arrays is fact that no one knows the exact "shape" of the region where deformation is localized.

Figure 8.1 summarized the "shape" of the deformation localized regions proposed by various researchers. These concepts are perfect in predicting the void coalescence of horizontal void arrays. However, when the void configuration deviates from the horizontal plane, a different shape of the localized region has to be known to estimate the plastic constraint for internal necking. The 3D strain mapping technique might be able to figure out the exact shape

of an arbitrary void configuration. Reproducing the shape of the localized region in FE simulations, we can develop a new generation of void coalescence models that can account for arbitrary void arrays.

It might be useful to start from 2D experiments and FE simulations. A series of 2D strain mappings based on *in situ* SEM observation during tensile deformation enables one to determine the "shape" of the deformation localization on arbitrary void arrays. Estimating the plastic constraint factor for internal necking by FE simulations, we can develop a similar model to that presented in section 5.8.2 more systematically. Then, we can proceed to the 3D situation although the choice of the materials that contain a proper markers for the 3D strain mapping is challenging.

8.2.3 Development of a better method to align holes

Although the current hole alignment method during diffusion bonding in a mold made it quite easy to polish the surfaces to be bonded compared to the method by Weck, the quality of the alignment ended up being slightly worse. Some development to improve the hole alignment is needed.

Appendix A

The comparisons between semi-experimental void coalescence modeling

In Chapter 5, 6, and 7, comparisons between experimentally captured void coalescence strains with those predicted by the Thomason model and the Pardoen and Hutchinson model. In those analyses, the void radii and intervoid spacing that were used as inputs for the void coalescence models are estimated from the Rice and Tracey void growth model. The intervoid spacing was estimated by Equation (5.9) without updating the current void volume fraction.

However, it is also possible to use experimentally captured void radii and the intervoid spacing as inputs for void coalescence models. By doing this, Table 8.1 can be modified as shown in Table A.1. In general, it was found that the predicted values of coalescence are smaller than those predicted by purely theoretical modeling, showing better agreement with experiments.

Table A.1: The comparison of the experimental results with the models. The experimentally measured void radii and intervoid spacing are used as inputs for void coalescence models.

Experiments									
	n	σ_{inf}/Y	V_f^0	$V_f^{critical}$	$\varepsilon_{coalescence}$	$\varepsilon_{linkage}$	$\varepsilon_{fracture}$	$(WHR/\sigma)_{coalescence}$	$(WHR/\sigma)_{linkage}$
Cu FCC 1	0.4	0.33	4.40%	26.70%	0.76	0.96	1.73	0.27	0.23
Cu FCC 2	0.4	0.33	4.40%	24.30%	0.52	0.85	1.51	0.33	0.25
Cu Hexagonal	0.4	0.47	0.70%	14.2% ~	N/A	0.68	1.62	N/A	N/A*
Cu Random	0.4	0.47	4.69%	3.57% ~ 60.7%	N/A	0.40	2.6	N/A	0.36
Cu FCC + notch	0.4	0.55	5.15%	24.7% ~ 59.4%	N/A	0.99	1.74	N/A	N/A*
Glidcop Rectangular**	0.14	0.33	7.30%	N/A	N/A	0.132	0.85	0.41	0.25
Glidcop Line	0.14	0.33	9.50%	N/A	N/A	0.49	0.58		
Glidcop FCC**	0.14	0.33	2.90%	N/A	N/A	0.17	0.52		
Brass Rectangular	0.52	0.33	0.60%	N/A	1.12	1.56	1.58		
Pure Cu 1 (Weck et al. (2008))	0.4	0.33	0.90%	N/A	0.5~0.77	1.01	N/A	N/A	N/A
Glidcop1 (Weck et al. (2008))	0.14	0.33	2.90%	N/A	N/A	0.41	N/A	N/A	N/A
Glidcop2 (Weck et al. (2008))	0.14	0.33	5.50%	N/A	N/A	0.45	N/A	N/A	N/A

** Delaminated samples * due to delamination

Models												
	Brown and Embury				Thomason				Pardoen and Hutchinson			
		Error (%) compared to				Error (%) compared to				Error (%) compared to		
	Predicted	$\varepsilon_{coalescence}$	$\varepsilon_{linkage}$	$\varepsilon_{fracture}$	Predicted	$\varepsilon_{coalescence}$	$\varepsilon_{linkage}$	$\varepsilon_{fracture}$	Predicted	$\varepsilon_{coalescence}$	$\varepsilon_{linkage}$	$\varepsilon_{fracture}$
Cu FCC 1	0.49	-35.5	-49.0	-71.7	0.64	-15.8	-33.3	-63.0	0.67	-11.8	-30.2	-61.3
Cu FCC 2	0.34	-34.6	-60.0	-77.5	0.59	13.5	-30.6	-60.9	0.64	23.1	-24.7	-57.6
Cu Hexagonal	0.51	N/A	-25.0	-68.5	1.03	N/A	51.5	-36.4	1.29	N/A	89.7	-20.4
Cu Random	0.16	N/A	-60.0	-93.8	0.44	N/A	10.0	-83.1	0.76	N/A	90.0	-70.8
Cu FCC + notch	0.54	N/A	-45.5	-69.0	0.51	N/A	-48.5	-70.7	0.66	N/A	-33.3	-62.1
Glidcop Rectangular**	0.13	N/A*	-1.5	-84.7	N/A	N/A*	N/A*	N/A*	N/A*	N/A*	N/A*	N/A*
Glidcop Line	0.07	N/A	-85.7	-87.9	0.23	N/A	-53.1	-60.3	0.25	N/A	-49.0	-56.9
Glidcop FCC**	N/A	N/A*	N/A*	N/A*	N/A*	N/A*	N/A*	N/A*	N/A*	N/A*	N/A*	N/A*
Brass Rectangular	0.94	-16.1	-39.7	-40.5	1.39	24.1	-10.9	-12.0	1.45	29.5	-7.1	-8.2

** Delaminated samples * due to delamination

Bibliography

H. Andersson. *Journal of the Mechanics and Physics of Solids*, 25:217–233, 1977.

Aramis. *Aramis Manual.* Aramis, 2001.

A. S. Argon and J. Im. *Metallurgical Transaction A*, 6A:825–837, 1975.

A. S. Argon, J. Im, and R. Safoglu. *Metallurgical Transaction A*, 6A:825, 1975.

M. F. Ashby, F. J. Blunt, and M Bannister. *Acta Metallurgica*, 37:1847–1857, 1989.

M. F. Ashby, M. F. Gandhi, and D. M. Taplin. *Acta Metallurgica*, 27:699–729, 1979.

L. Babout, E. Maire, J. Y. Buffière, and R. Fougeres. *Acta Materialia*, 49(11): 2055 – 2063, 2001.

M Bannister and M. F. Ashby. *Acta Materialia*, 11:2575–2582, 1991.

A. A. Benzerga. *Journal of the Mechanics and Physics of Solids*, 50(6):1331 – 1362, 2002.

C. A. Berg. *Inelastic Behavior of Solids.* McGraw-Hill Book Company, 1970.

Y. Brechet, J.D. Embury, S. Tao, and L. Luo. *Acta Metallurgica et Materialia*, 39(8):1781 – 1786, 1991.

P. W. Bridgman. *Studies in Large Plastic Flow and Fracture.* McGraw-Hill Book Company, 1952.

L. M. Brown and J. D. Embury. In *Proceedings of the 3rd International Conference on the Strength of Metals and Alloys*, page 164. Institute of Metals, 1973.

L. M. Brown and W. M. Stobbs. *Philosophical Magazine*, 34:351, 1976.

J. Y. Buffière, E. Maire, P. Cloetens, G. Lormand, and R. Fougeres. *Acta Materialia*, 47(5):1613 – 1625, 1999.

W. D. Callister. *Materials Science and Enginering An Introduction.* 2003.

C. W. Chen. *Acta Metallurgica*, 9:68, 1961.

P. Cloetens. *Vrijie Universiteit Brussel, Ph. D. thesis.*, 1999.

A. M. Cormack. *Journal of Applied Physics*, 34:2722–2727, 1963.

A. M. Cormack. *Journal of Applied Physics*, 35:2908–2913, 1964.

T. B. Cox and J. R. J. Low. *Metallurgical Transaction*, 5:1457–1470, 1974.

A. G. Evans and R. M. McMeeking. *Acta Metallurgica*, 34:2435–2441, 1986.

R. K. Everett, K. E. Simmonds, and A. B. Geltmacher. *Scripta Materialia*, 44(1):165 – 169, 2001.

D. Fabregue and T. Pardoen. *Journal of the Mechanics and Physics of Solids*, 56(3):719 – 741, 2008.

J. Faleskog and C. F. Shih. *Journal of the Mechanics and Physics of Solids*, 45(1):21 – 25, 1997.

I. E. French and P. F. Weinrich. *Scripta Metallurgica*, 8:87, 1974.

J. Gammage, D. Wilkinson, Y. Brechet, and D. Embury. *Acta Materialia*, 52 (18):5255 – 5263, 2004.

J. J. Gammage, Wilkinson D. S., J. D. Embury, and E. Maire. *Philosophical Magazine*, 85:26&27, 2001.

W. M. Garrison and N. R. J. Moody. *Journal of Physics and Chemistry of Solids*, 48:1035, 1987.

M. Gologanu, J. Leblond, and J. Devaux. *Jounal of the Mechanics and Physics of Solids*, 41:1723–1754, 1993.

M. Gologanu, J. B. Leblond, G. Perrin, and J. Devaux. *International Journal of Solids and Structures*, 38(32-33):5581 – 5594, 2001a.

Mihai Gologanu, Jean-Baptiste Leblond, and Josette Devaux. *International Journal of Solids and Structures*, 38(32-33):5595 – 5604, 2001b.

S. Goods and L. M. Brown. *Acta Metallurgica*, 27:1–15, 1979.

A. Gurson. *Journal of Enginering Materials and Technology*, 99:2–15, 1977.

J. W. Hancock and A. C. McKenzie. *Journal of the Mechanics and Physics of Solids*, 24:147–169, 1976.

R. Hill. *The Mathematical Theory of Plasticity.* Oxford University Press, 1950.

G. N. Hounsfield. *Patent Specification 1283915*, (1283915), 1972.

E. Hsu. *McMaster University, Master's thesis*, 2007.

F. J. Hunphreys and M. Hatherly. *Recrystallization and Related Annealing Phenom.* Pergamon Press, 1995.

C. Kak, A. *Digital Image Processing Techniques.* Academic Press Inc, 1984.

C. Kak, A. *Principeles of Computerized Tomographic Imaging.* IEEE Press, 1988.

N. Kanetake, M. Nomura, and T. Choh. *Materials Science and Technology*, 11:11246–1252, 1995.

R. J. Klassen, G. C. Weatherly, and B. Ramaswami. *Metallurgical Transactions A*, 23A:3273–3280, 1992a.

R.J. Klassen, G. C. Weatherly, and B. Ramaswami. *Metallurgical Transactions A*, 23A:3281–3291, 1992b.

R.J. Klassen, G. C. Weatherly, and B. Ramaswami. *Materials Science and Engineering A*, 161:181–186, 1993.

M. Kobayashi, H. Toda, Y. Kawai, T. Ohgaki, K. Uesugi, D. S. Wilkinson, T. Kobayashi, Y. Aoki, and M. Nakazawa. *Acta Materialia*, 56(10):2167 – 2181, 2008.

U. F. Kocks and H. Mecking. *Progress in Materials Science*, 48:171–273, 2003.

J. Koplik and A. Needleman. *International Journal of Solids and Structures*, 24(8):835 – 853, 1988.

H Kudo. *International Journal of Mechanical Sciences*, 2:102–127, 1960.

D. E. Kuhl, R. Q. Edwards, A. R. Ricci, and Revich M. *Journal of Nuclear Medicine*, 14:196–200, 1973.

G. Le Roy, J. D. Embury, G. Edwards, and M. F. Ashby. *Acta Metallurgica*, 29:1509, 1981.

C.S. Lee, Y.H. Kim, T. Lim, and K.S. Han. *Scripta Metallurgica et Materialia*, 25(3):613 – 618, 1991.

J. Llorca, A. Martin, J. Ruiz, and M. Elices. *Metallurgical Transaction A*, 24: 1575–1588, 1993.

E. Maire, C. Verdu, Gerard Lormand, and Roger Fougres. *Materials Science and Engineering A*, 196(1-2):135 – 144, 1995.

C. F. Martin, C. Josserond, L. Salvo, J. J. Blandin1, P. Cloetens, and E. Boller. *Scripta Materialia*, 42(4):375 – 381, 2000.

J. W. Martin. *Micromechanisms in particle-hardened alloys.* Cambridge University Press, 1980.

F. A. McClintock. *Journal of Applied Mechanics*, 35:363–371, 1968a.

F. A. McClintock. *The International Journal of Fracture Mechanics*, 4:101–130, 1968b.

C. L. Morgan. *Basic Principles of Computed Tomography.* University Park Press, 1983.

L. E. Murr. *Interfacial Phenomena in Metals and Alloys.* Addison-Wesley, 1975.

A. Needleman and V. Tvergaard. *Journal of the Mechanics and Physics of Solids*, 32(6):461 – 490, 1984.

A. Needleman and V. Tvergaard. *Journal of the Mechanics and Physics of Solids*, 35(2):151 – 183, 1987.

M. Nemcko. *Private Communication*, 2010.

S.R. Nutt and A. Needleman. *Scripta Metallurgica*, 21(5):705 – 710, 1987.

M. Oyane. *Bulletin of JSME*, 15:1507–1513, 1972.

T. Pardoen. *Computers & Structures*, 84(26-27):1641 – 1650, 2006.

T. Pardoen and J. W. Hutchinson. *Journal of the Mechanics and Physics of Solids*, 48(12):2467 – 2512, 2000.

K. E. Puttick. *Philosophical Magazine*, 4:964–969, 1959.

J. Radon. *Berichte ueber die Verhandlungen der Saechsische Akademie der Wissenschaften*, 69:262–277, 1917.

J. Rice and D. Tracey. *Jounal of the Mechanics and Physics of Solids*, 17: 201–217, 1969.

J. W. Rudnicki and J. R. Rice. *Journal of the Mechanics and Physics of Solids*, 23:371, 1975.

F. Scheyvaerts. *Multiscale modelling of ductile fracture in heterogeneous metallic alloys.* 2008.

J. Segurado and J. LLorca. *International Journal of Solids and Structures*, 41 (11-12):2977 – 2993, 2004.

L. S. Sigl, P. A. Mataga, B. J. Dalgleish, R. M. McMeeking, and A. G. Evans. *Acta Metallurgica*, 36:945–953, 1988.

K. Tanaka, T. Mori, and T. Nakamura. *Philosophical Magazine*, 21:267, 1970.

G. I. Taylor. *J. Inst. Met*, 62:307, 1938.

P. F. Thomason. *Journal of the Institute of Metals*, 96:360, 1968.

P. F. Thomason. *Acta Metallurgica*, 33:1079–1085, 1985.

P.F. Thomason. *Acta Metallurgica*, 29(5):763 – 777, 1981.

P.F. Thomason. *Ductile Fracture of Metals.* Pergamon Press, 1990.

V. Tvergaard. *International Journal of Fracture*, 17:389–407, 1981.

R. von Mises. *Zeitschrift Fur Angewandte Mathematik und Mechanik*, 8:161–185, 1928.

A. Weck. *McMaster University, Ph. D. thesis*, 2007.

A. Weck, T. H. R. Crawford, Borowiec A., Wilkinson D. S., and Preston J. S. *Applied Physics A: Materials Science & Processing*, 86:55–61, 2007a.

A. Weck, J. Segurado, J. Llorca, Wilkinson D. S., Boehm, and Helmut. *International Journal of Fracture*, 148:205–219, 2007b.

A. Weck and D.S. Wilkinson. *Acta Materialia*, 56(8):1774 – 1784, 2008.

A. Weck, D.S. Wilkinson, and E. Maire. *Materials Science and Engineering: A*, 488(1-2):435 – 445, 2008a.

A. Weck, D.S. Wilkinson, E. Maire, and H. Toda. *Acta Materialia*, 56(12): 2919 – 2928, 2008b.

H. Yamamoto. *International Journal of Fracture*, 14:347–365, 1978.

D. Zhao, F.R. Tuler, and D.J. Lloyd. *Acta Metallurgica et Materialia*, 42(7): 2525 – 2533, 1994.

Index